Modelling the Effects of Anthropogenic Disturbances on the Evolution of a Mega-Delta

being a thesis submitted in fulfilment of the

requirements for the degree of

Doctor of

Philosophy (PhD)

in the University of Hull

by

Quan Quan Le

February 2025

Acknowledgements

I wish to convey my deepest appreciation to my supervisors, Dr. Grigorios Vasilopoulos, Dr. Christopher Hackney, Prof. Tom Coulthard, and Prof. Daniel Parsons, for their invaluable guidance and motivation throughout my PhD journey, particularly during the more challenging moments. This thesis would not have been possible without their support, and I will remain forever grateful to them.

I would like to extend my sincere thanks to the Energy and Environment Institute (EEI) at the University of Hull for providing me with the opportunity to pursue the funded PhD scholarship. It has been a privilege to live and work in such a supportive research environment, and I am also thankful to my colleagues at EEI for their companionship and support.

I am grateful to Prof. Darby and Assoc. Prof. Nguyen Nghia Hung for their invaluable advice throughout this research project. My sincere thanks also go to the Southern Institute of Water Resources Research (SIWRR), Assoc. Prof. Tran Ba Hoang for providing me with the opportunity to advance my studies abroad and for their unwavering support and encouragement.

Finally, I owe my deepest gratitude to my wife, Hien, who selflessly left behind her own career and personal interests to stand by my side. Her unwavering support throughout my studies and during challenging times has been invaluable. I am also immensely thankful to my parents, Hanh and Tinh, and my beloved daughter, Phuong Thao, for their endless love and encouragement.

Publications and Conferences

[1] Quan, Q.L, Hackney, C.R., Vasilopoulos, G., Coulthard, T., Hung, N.N., Darby, S.E., Parsons, D.R. “Significant Reduction in Tonle Sap Lake's Critical Flood Pulse Caused by Human-Induced Riverbed Lowering”. Status: Submitted to the "Nature Sustainability" journal and currently under review.

[2] Quan.Q.L, G. Vasilopoulos, C. Hackney, T. Coulthard, D.R. Parsons, Hung.N.N , S.E. Darby “Water Level Lowering and Increased Tidal Influence in the Mekong Delta driven by Human-Induced (Sand Mining) Riverbed Degradation” EGU 2024, https://doi.org/10.5194/egusphere-egu24-1296, Conference.

[3] Quan.Q.L, G. Vasilopoulos, C. Hackney, T. Coulthard, D.R. Parsons, N.N. Hung, S.E. Darby, “Water Level Lowering and Increased Tidal Influence in the Mekong Delta Driven by Anthropogenic Riverbed Lowering and Sea-Level Rise” AGU 2023, Conference.

[4] Quan.Q.L, G. Vasilopoulos, C. Hackney, T. Coulthard, D.R. Parsons, N.N. Hung, S.E. Darby, R. Houseago, “Sediment routing though the apex of a mega-delta under future anthropogenic impacts and climate change”, EGU 2022, 10.5194/egusphere-egu22-9871, Conference.

Abstract

River deltas provide ecosystem services that are vital to the world's population, supporting both lives and livelihoods. However, these low-lying areas face heightened vulnerability to the effects of climate change. This is intensified by local resource exploitation including sand mining and hydropower expansion that cause the lowering of riverbeds and modulate freshwater flux. These cumulative impacts, coupled with changes in input hydrological conditions and rising sea levels, have the potential to cause considerable disruptions in the flow dynamics across river deltas. Despite numerous studies into anthropogenic influences in delta evolution, a significant knowledge gap persists regarding how the combination of stressors that drive riverbed lowering influences alterations in hydraulic patterns and sediment transport capacity.

Here the Lower Mekong Basin is used as an exemplar of sediment starved lowland rivers and deltas globally. Long-term hydrological data are combined with a 1D hydrodynamic numerical model and a 2D coupled hydrodynamic – sediment transport model to examine system response to rapid riverbed lowering. Assessing the relationships between riverbed lowering, water level, tidal amplitude and sediment transport across a range of spatiotemporal scales allows the quantification of the effects of riverbed lowering during a historical 20-year period and future projection.

Historical data analysis and hydrodynamic model results suggest that for median freshwater flux conditions, the system's historical average riverbed lowering of approximately 3.06 m (σ = 2.03 m) from 1998 to 2018 has led to simultaneous declines in average annual water levels of approximately 0.65 m (σ = 0.75 m) and an increase in the average annual tidal range by approximately 0.19 m (σ = 0.15 m). The reduction in water level is more pronounced landward, whereas the increased tidal range is more prominent seaward. Under anticipated Future scenario (to the year 2038), where the riverbed lowering is projected to average around 5.92 m (σ = 2.84 m) compared to 1998, declines in mean water level of approximately 1.27 m (σ = 1.5 m) are projected while, the maximum water level reduction landward reaches may reach 4.19 m. Simultaneously, the mean tidal range is expected to increase by approximately 0.46 m (σ = 0.27m), with the maximum rise potentially reaching more than 1 m in seaward areas. Furthermore, model results indicate that riverbed lowering significantly reduces water flux from the river to its floodplain and towards the Tonle Sap Lake, one of the world's most productive lake-wetland systems, with wide implications for food security.

Hydrodynamic and sediment transport model results indicate that riverbed lowering diminishes sediment transport capacity. Specifically, simulated sand transport at the apex of the delta has decreased by approximately 30% over the nine-year period from 2013 to 2022. By 2022,

simulated data at the apex of the delta indicates that sand transport is roughly 10 times lower than the observed total sand extraction volume across the entire Lower Mekong Basin. The significant disparity between sand transport capacity and sand extraction in the delta, coupled with the decrease in sediment supply due to upstream damming and natural reductions in sediment load from shifting tropical cyclones will further exacerbate the adverse effects of sand mining and sediment starvation caused by upstream river impoundment.

Contents

List of Figures

List of Tables

Main symbols

A_r	Delta's aggradation rate
C_A	Accelerated delta compaction rate
C_N	Natural delta sediment compaction rate
d_{50}	The median grain size for suspended sediment (m)
D_{50}	The median grain size for sand (m)
g	The gravitational acceleration (m s^{-2})
M	roughness coefficients ($M = 1/n$) (s^{-1} m$^{1/3}$)
M_r	Downward vertical movement of the land surface rate
n	Manning's n (s m$^{-1/3}$)
p	The pressure (N m^{-2})
Q	Water discharge (m^3 s^{-1})
S	Water slope
V	Velocity (m s^{-1})
$V_x, V_{y,} V_z$	Velocity components in the x, y, x directions, respectively (m s^{-1})
w_s	Settling velocity (kg m^{-1}s^{-1})
W_c	Channel width (m)
ρ	Water density (kg m^{-3})
ρ_s	The density of sediment (kg m^{-3})
τ_0	The critical average bed shear stress (N m^{-2})
τ_b	The bed shear stress (N m^{-2})
τ_{cd}	The critical bed shear stress for deposition (N m^{-2})
τ_{ce}	The critical bed shear stress for erosion (N m^{-2})
$\tau_{xx}, \tau_{xy}, \tau_{xz}, \tau_{yy}, \tau_{yz}, \tau_{zz}$	The weight of the viscous stress tensor in the x, y, z dimension respectively (N m^{-2})
Θ	Shields stress value
Φ	The latitude (degrees)
ζ	Angular rotation of the earth (rad)
Δ_{RSl}	The surface elevation of deltas relative to sea level
Δ_E	Eustatic sea level change rate

List of abbreviations

ADCP	Acoustic Doppler Current Profiler
CMD	Cambodian Mekong Delta
dGPS	Differential global positioning system unit
DEM	Digital Elevation Model
EF	Fredsøe,1976
EH	Engelund and Hansen,1967
EGM	Earth Gravitational Model
GMSL	Global mean sea level rise
GPS	Global positioning system
IPCC	Intergovernmental Panel on Climate Change
LMR	Lower Mekong River
LMB	Lower Mekong Basin
MD	Mekong Delta
MBES	Multibeam Echo Sounder
MM	Meyer-Peter and Müller,1948
MONRE	Ministry of Natural Resources and Environment of Viet Nam
MRC	Mekong River Commission
MSL	Mean Sea level
RHMC	Southern Regional Hydro-Meteorological Centre
SBES	Single Beam Echo Sounding
SIWRR	Southern Institute of Water Resources Research
SLR	Sea level rise
SRHMC	Southern Regional Hydro-Meteorological Center
TSL	Tonle Sap Lake
TSR	Tonle Sap River
VMD	Vietnamese Mekong Delta
VR	Van Rijn,1984
WGS84	World Geodetic System 1984

Chapter 1. Introduction

1.1 Rationale

River deltas are landforms found across the globe, formed where rivers flow into a standing bodies of water such as an ocean or lake basins (Ericson et al., 2006; Syvitski and Saito, 2007; Overeem and Syvutski., 2009). Although, deltas cover only around 1% of the global land area they are home to nearly 339 million people, accounting for approximately 4.5% of the world population (Edmonds et al., 2020) and supporting a diverse range of life species (Stanley and Warne, 1997; Ericson et al., 2006; Best and Darby, 2020). River deltas also are an important source of natural resources, facilitate maritime trade and, because of their fertile lands and relatively flat terrain, hold strategic significance in worldwide agricultural production (Ericson et al., 2006; Best and Darby, 2020). Additionally, deltas act as crucial connectors between terrestrial, riverine and marine ecosystems, serving as diverse habitats for a countless number of species (Overeem and Syvutski, 2009; Hagenlocher et al., 2018).

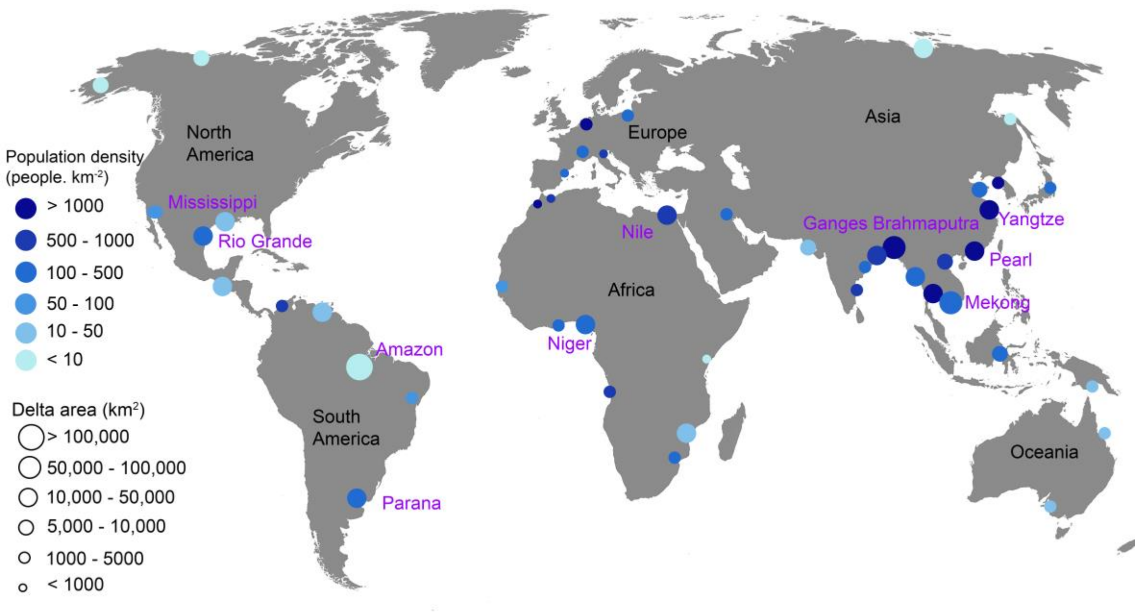

Figure 1-1. Map of major deltas across the globe categorized based on their size and population density, utilizing data sourced from Dunn, (2017)

Since the beginning of the twentieth century, deltas areas have witnessed substantial population growth and accelerating economic development (Krausmann et al., 2017; United Nations, 2018; Best, 2019). This trend has led to the intensification of natural resources exploitation, not only within deltas themselves but also in their feeding basins (Vörösmarty et al., 2009; Lehner et al., 2011; Schandl et al., 2016; Bendixen et al., 2019). Examples include dams constructed in river catchments to harness hydropower, irrigation and the provision of industrial or domestic water supply (Lehner et al., 2011; Xu et al., 2023); extraction of riverine sand for land reclamation or industrial applications, such as cement production (Bendixen et al., 2019); changes in land use to accommodate an increasing food demand and the expansion of urban centers (FAO, 2011); extraction of underground natural resources including water, minerals, and oil to drive economic development within delta regions (Vörösmarty et al., 2009; Best and Darby, 2020) and infrastructure development for navigation and irrigation, as well as flood defences (Vörösmarty et al., 2009; Bucx et al., 2010). The intensified exploitation of resources, coupled with human-induced climate change, results in an array of detrimental effects for deltas, including river and coastal bank erosion (Anthony et al., 2015; Hackney et al., 2020), salinization (Eslami et al., 2021) degrading the health of the river ecosystems (Venson et al., 2017; Torres et al., 2017), and flooding (Arnell and Gosling, 2016; Kondolf et al., 2022). Consequently, modern river deltas find themselves as victims of our economic advancement (Syvitski et al., 2009; Giosan et al., 2014; Ghosh et al., 2019).

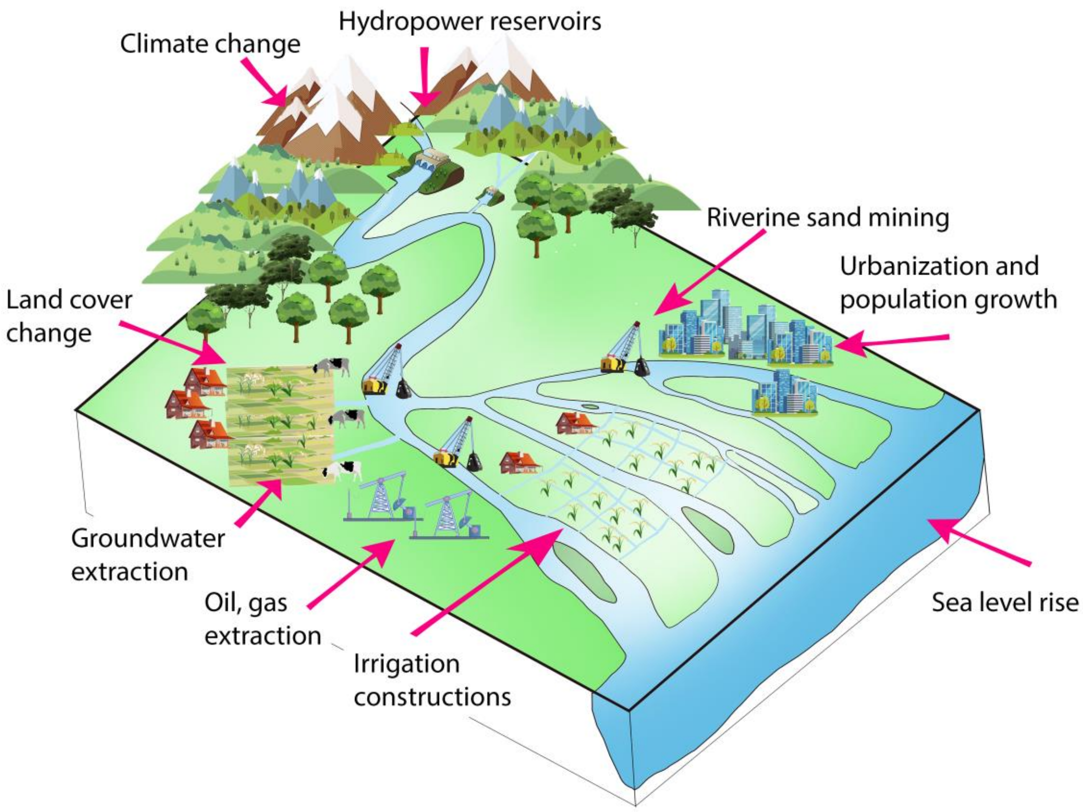

Figure 1-2. Conceptual figure highlights major anthropogenic stresses faced by river deltas globally.

1.2 The Lower Mekong Basin and Delta

The focus of this research is the Lower Mekong Basin (LMB), which extends from Kratie (Cambodia) to the South China Sea, encompassing the Lower Mekong River (LMR) from Kratie to the Chaktomuk Junction, the Tonle Sap Lake (TSL), and the Mekong Delta (MD) from the Chaktomuk Junction to the coast (Figure 1-3) (see section 2.3.1, Chapter 2 for more detail). Within the LMB, the TSL system in Cambodia is one of the most productive lake-wetland ecosystems in the world, ranking fourth in fish productivity (Bonheur and Lane, 2002). The Lake directly supports around two million residents living near the lake (Arias et al., 2013), provides habitat for globally significant populations of endangered amphibians, reptiles, mammals, and birds (UNESCO; Bonheur and Lane, 2002; Campbell et al., 2006; Uk et al., 2018). Additionally, the TSL acts as a massive water reservoir for the Mekong Delta, reducing floodwaters during the flood season and sustaining fresh water flow during the dry season (MRC, 2009). The MD is one of the world's largest deltas (Kondolf et al., 2022), is home to an estimated 23 million people (The General Population Census of Cambodia, 2019; General Statistics Office Of Vietnam, 2024). This delta area plays a vital role in food security and socio-economic development for Viet Nam, Cambodia, and the broader region (Hung, 2011; Balica et al., 2014; Boretti, 2020).

The LMB serves as a prime example of a river-delta system facing multiple anthropogenic pressures (Kondolf et al., 2018; Minderhoud et al., 2019; Hackney et al., 2021; Chua et al., 2022). According to the Intergovernmental Panel on Climate Change (IPCC), this region ranks among the most affected by climate change and sea level rise globally (IPCC, 2007). In recent decades, the LMB has experienced a surge in hydropower dam construction and large irrigation projects (Kummu and Sarkkula, 2008; Hecht et al., 2019; Morovati et al., 2023), with 283 hydropower dams larger than 15 megawatts or reservoirs exceeding 0.5 km^2 currently identified as operational or under construction (WLE Greater Mekong, 2016). These developments are altering the river's hydraulic regime, increasing dry season flows, reducing wet season flood peaks (Blackmore and Stein, 2004; Lauri et al., 2012), and decreasing sediment supply to the downstream delta, with suspended sediment flux projected to drop by 57% from 99 Mt yr^{-1} (1980-2009) to 43 Mt yr^{-1} by 2020-2029 (Bussi et al., 2021) (see section 2.3.2, Chapter 2 for more detail). Sediment deficits are being further worsened by high rates of sand mining in the channels of the Lower Mekong River and its delta. In 2020, sand extraction in Cambodia alone was estimated at 59 million tons (Hackney et al., 2021). Additionally, sand mining in the Vietnamese Mekong Delta from 2015 to 2020 averaged 42 million cubic meters yr^{-1} (approximately 67.2 million tons yr^{-1}) (Gruel et al., 2022). Sand mining and reservoir effects together have led to sediment deficits and subsequent riverbed lowering rates with a median lowering rate of 0.26 m yr^{-1} observed during 2013-2019 period in Cambodia (Hackney et al., 2021) and a mean lowering rate of 0.16 m yr^{-1} observed across the VMD during 2008-2018 (Vasilopoulos et al., 2021) (see section 2.3.2, Chapter 2 for more detail). Additionally, the MD is dealing with land subsidence, occurring at an average rate of 11 mm yr^{-1} (ranging from 7 to 18 mm yr^{-1}), primarily due to groundwater extraction (Minderhoud et al., 2017). Without effective intervention to address the current rates of groundwater extraction in the delta, it is projected that delta subsidence will surpass 1 m by 2100 (Minderhoud et al., 2020). This would effectively amplify the challenges linked to eustatic sea level rise, which is anticipated to be of comparable scale for the region. Such a rise in sea level would submerge about 90% of the delta area, affecting 17 million people, and leading to an annual agricultural loss of $3.2 billion (Kondolf et al., 2022).

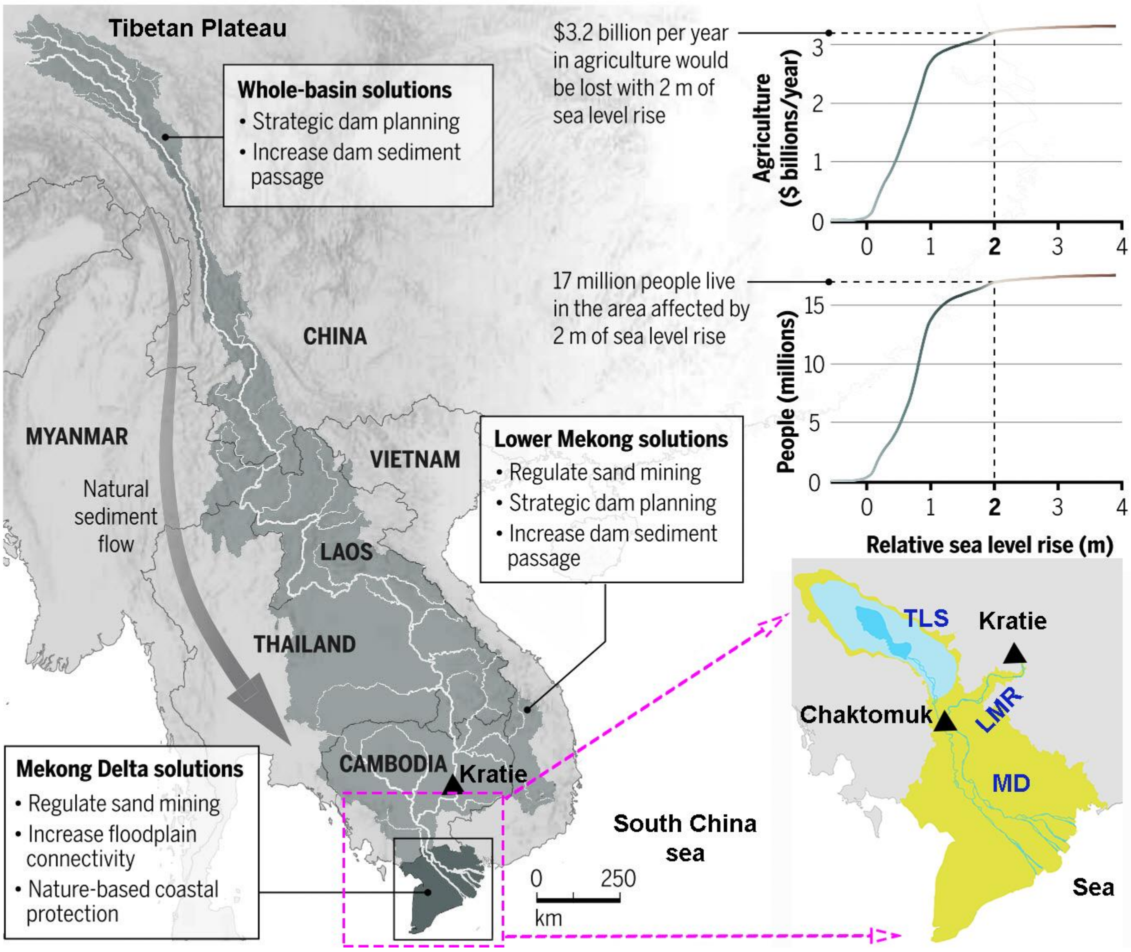

Figure 1-3. Map of South East Asia highlighting the Lower Mekong Basin at Katie and spanning across the TSL in Cambodia and South Viet Nam. The region is facing a considerable risk of drowning and suggested sustainable development solutions for the delta (modified from Kondolf et al., (2022)).

1.3 Problem statement.

Understanding the mechanisms of delta evolution is key to inform decisions and management practices able to mitigate the adverse effects of climate change and local resource exploitation. Over the past century, the demand for sand from river deltas and their adjacent regions has surged dramatically due to population growth, urbanization, and economic development (Torres et al., 2017; Bendixen et al., 2019). Additionally, the construction of upstream hydropower dams has contributed to sediment depletion in many delta systems (Lehner et al., 2011; Xu et al., 2023), leading to riverbed lowering (Huang et al., 2014; Arróspide et al., 2018; Koehnken et al., 2020, Vasilopoulos et al., 2021; Zhang et al., 2022). This is expected to be further exacerbated in the near future due to the heightened demand for sand, hydropower and irrigation driven by population growth and economic development. These combined effects, along with changes in hydrological conditions and sea level rise at the delta front, can alter delta function and impact their future sustainability (Vörösmarty et al., 2009; Syvitski et al., 2009; Best, 2019).

Despite numerous studies addressing delta-related issues caused by riverbed lowering, such as destabilizing riverbanks (Kondolf, 1994; Hackney et al., 2020), increasing coastal erosion (Anthony et al., 2015), intensifying scouring processes that undermine embankments and other riverine infrastructure (Kondolf 1994; Best, 2019), lowering the water table (Chevallier, 2014; Best, 2019), reduced peak water levels (Bao et al., 2022), exacerbating tidal ingress landward (Vasilopoulos et al., 2021), promoting saline intrusion (Eslami et al., 2021), degrading water quality and health of fluvial and riparian ecosystems (Sreebha and Padmalal, 2011; Saviour, 2012; Venson et al., 2017; Torres et al., 2017), there is still a noticeable gap regarding the interplay of changes to water level, discharge and sediment transport capacity due to human-induced riverbed lowering and projected climate change. Using the Lower Mekong Basin as a case study, this research takes a holistic approach quantifying the relationship between riverbed lowering and the resulting changes in water and tidal levels, river-floodplain connectivity including exchanges with the TSL and sediment transport capacity under various projected scenarios of freshwater influx and sea level rise. Gaining an understanding of these dynamics and developing the ability to predict them are critical to pre-empt the initiation of unforeseen hazards, encompassing aspects such as the implementation of flood protection measures (Alphen, 2016; Oppenheimer et al., 2019; Binh et al., 2020), efficiently utilizing water for irrigation in agriculture (Hoang et al., 2016; Salem et al., 2021), facilitation of navigation within the channels of the deltas (Paarlberg et al., 2015; Yang et al., 2017), salinity intrusion (Eslami et al., 2019), and ensuring the stability of river and coastal banks (Anthony et al., 2015, Hackney et al., 2020).

1.4 Research Objectives and Research Questions

The primary aim of the research presented herein is to explore the impacts of anthropogenic-driven riverbed lowering, along with various upstream hydraulic conditions and the influence of sea-level rise at the delta front on the hydraulic, related-water level regime and the sand transport capacity through river deltas, using the LMB as an example. In this study, this anthropogenic-driven riverbed lowering encompasses a combination of factors, including the interplay of sand mining and sediment starvation caused by upstream damming. The main objectives of this study are as follows:

The first Objective (O1) of the study is to assess historical changes in the delta's flow dynamics due to channel bed level lowering. This will be accomplished by statistically analysing the historical record of water discharge and water level collected at different gauging stations and quantifying temporal changes. Assessing these relationships across both spatial and temporal dimensions will improve understanding of the progression of riverbed lowering and offer valuable insights into the impact of riverbed lowering on the delta's water level patterns. The specific Research Question (RQ1) here is: How has historical riverbed lowering affected delta hydraulics?

The second Objective (O2) of the study is to understand the evolution of hydraulic regime in the delta under projected future riverbed lowering and sea level rise. This objective aims to enhance our comprehensive understanding of the modified hydraulic and related-water level regime arising from human-induced riverbed lowering across the entire study region subject to projected changes in freshwater influx and sea level rise. This will be achieved by employing a 1D numerical model capable of simulating the hydraulic regime within the LMB. The Objective seeks to address two research questions (RQ.2): How will hydraulics in the LMB change in the future due to projected riverbed lowering and sea-level rise? and (RQ.3): How will the connection to the Tonle Sap Lake be affected by projected riverbed lowering and sea-level rise?

The final Objective (O3) of the study is to quantify changes in the delta's sand transport capacity due to riverbed lowering. This objective will identify changes to delta's ability to convey the influx of sand supplied from the catchment as a function of the continuous changing channel geometry resulting from the intensification of local sand mining. It aims to develop sustainable solutions for future sand extraction practices in the region. This objective is achieved by developing a two-dimensional coupled hydrodynamic-sediment transport model. It specifically addresses the research question (RQ.4): What are the consequences of riverbed lowering on the sand transport capacity in the apex of the Mekong delta?

1.5 Thesis structure

The work presented in this PhD thesis is organized into eight chapters. Chapter 1 provides the background context of the present study, introduces the challenges that the Mekong region is facing and outlines the Research Objectives and Research Questions. Chapter 2 presents a comprehensive overview of the formation and evolution of river deltas and the impact of human activities on these processes. This chapter also introduces the LMB, the focal point of this research, and explains the principles and underlying theory of numerical modelling, with a specific focus on its application to delta systems. Chapter 3 describes the extensive datasets utilized in this study, including the gauged record, suspended sediment profiles, rates of bedload transport, a suite of riverbed bathymetric datasets, and 1D modelling applied for LMB adopted from existing studies. Chapter 4 addresses the first objective (O1), which involves establishing a relationship between water level and water discharge at a range of gauging stations within the Vietnamese Mekong delta to evaluate historical changes in the water level patterns resulting from ongoing riverbed lowering addressing the first Research Question (RQ.1). In Chapter 5, the 1D numerical model is introduced. The hydraulics of the LMB are modelled numerically and future scenarios of riverbed lowering and climate change are investigated addressing the second Research Question (RQ.2). Chapter 6, focuses on the hydraulic function of the Tonle Sap River and Lake system and their connection to the Mekong River and Mekong delta using the 1D numerical model under future scenarios addressing the third Research Question (RQ3). Chapter 7 develops a calibrated two-dimensional coupled hydrodynamic and sediment transport numerical model, which is employed to explore water and sand transport capacity through the delta apex, under a range of future scenarios of sand mining addressing the fourth Research Question (RQ4). Chapter 8 provides a detailed discussion of the research results, consolidating the key findings and their wider implications for the Mekong and other sediment starved deltas globally, suggesting strategies for the sustainable management of deltaic sediment.

Chapter 2. Literature review

The present Chapter will introduce the broad background theory of the formation and evolution of river deltas (Section 2.1) and how they are impacted by humans (Section 2.2). Section 2.3 will introduce the Mekong River and it's delta, which is the focus of the research. Section 2.4 will introduce the principles and underlying theory of numerical modelling, focusing specifically on its application to delta systems. Finally, Section 2.5 summarizes the gaps in the literature that this thesis aims to address.

2.1 Natural delta evolution

2.1.1 A framework for the classification of river deltas

Modern, stable, river deltas are geologically young and only started to form approximately 6000 years ago when the rapidly rising sea levels, driven by post glacial maximum ice melt and thermal expansion, started to stabilise (Stanley and Warne, 1994; Day et al., 2007; Vörösmarty et al., 2009). Since then, sediment and organic materials from river basins have been transported to deltas through distributary channel systems, shaping dynamic landforms (Pont et al., 2002; Vörösmarty et al., 2009).

Delta morphology is governed by the complex interactions between: (1) water and sediment characteristics, (2) accommodation space, (3) ocean energy and (4) changes in water density (Galloway, 1975; Orton and Reading, 1993; Correggiari et al., 2005; Overeem et al., 2005). The fluvial water and sediment flux is influenced by factors like drainage basin location, climate, and seasonal patterns, and affects delta expansion by altering the volume of sediment supplied (Fisher and McGowen, 1967; Orton and Reading, 1993). The accommodation space pertains to the volume where sediment can accumulate within the delta, primarily influenced by topography and sea level (Bhattacharya and Giosan, 2003; Syvitski et al., 2009). The ocean energy, conveyed through waves, tides, and currents influences sediment transport, deposition patterns, and the shape of delta formations (Wright and Coleman, 1972; Nardin and Fagherazzi, 2012; Hoitink et al., 2017). Differences in temperature and salinity between river water and ocean water result in density variations, causing stratification in estuaries and coastal areas. This stratification affects sediment transport and deposition patterns, consequently affecting the delta evolution (Coleman and Wright, 1971; Kostaschuk and Luternauer, 1989; Gelfenbaum et al., 2009).

While deltas worldwide generally may meet a common definition, they exhibit diverse characteristics influenced by their geographical location and morphology (Hori and Saito, 2007).

The most widely recognized classification system for deltas is the ternary classification proposed by Galloway (1975), which distinguishes three types of deltas based on the interaction among fluvial, tidal, and wave processes (Figure 2-1). Four delta "archetypes" emerge from Galloway's diagram, including elongate, lobate, cuspate, and estuarine deltas. Fluvial-dominated deltas are typically elongated and strongly reliant on sediment input, with the Mississippi Delta serving as a classic example. In contrast, wave-dominated deltas feature cuspate shorelines such as the São Francisco Delta. The interaction between fluvial and wave forces can create lobate deltas, with the Danube Delta being a prime example, whereas tide-dominated deltas exhibit an estuarine-related geometry. Similar to the Ganges-Brahmaputra Delta (Galloway, 1975) (Figure 2-1).

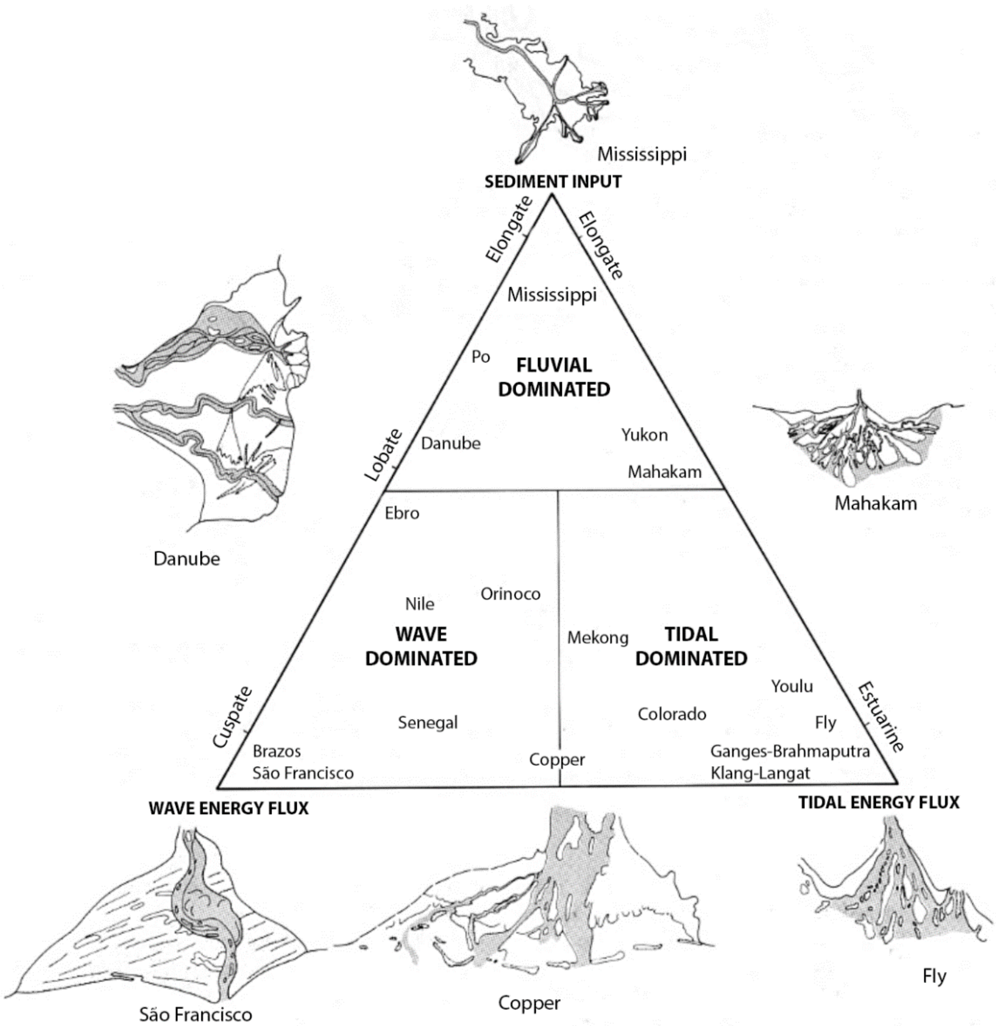

Figure 2-1. The ternary diagram adopted from Galloway, (1975) illustrating the formation of Estuarine, Cuspate, Lobate and Elongated deltas depending on the interactions between fluvial, wave and tidal energy.

2.1.2 Delta progradation

Progradation refers to the seaward extension of a river delta, occurring at the river mouth as sediment-laden flows from distributary channels enter the water body, generating turbulent jets that disperse water and sediment into the receiving basin (Galloway, 1975; Orton and Reading, 1993; Edmonds and Slingerland, 2007). This progradation process can lead to various forms of river mouth deposits, such mouth bars that lead to branching deltaic networks or fan-shaped deltas with a smooth delta front (Figure 2-2, a), or alternatively levees, leading to the formation of elongated, bird's foot-like deltas and tie channels with rugged shorelines (Figure 2-2, b) (Wright, 1977; Orton and Reading, 1993; Rowland et al., 2010).

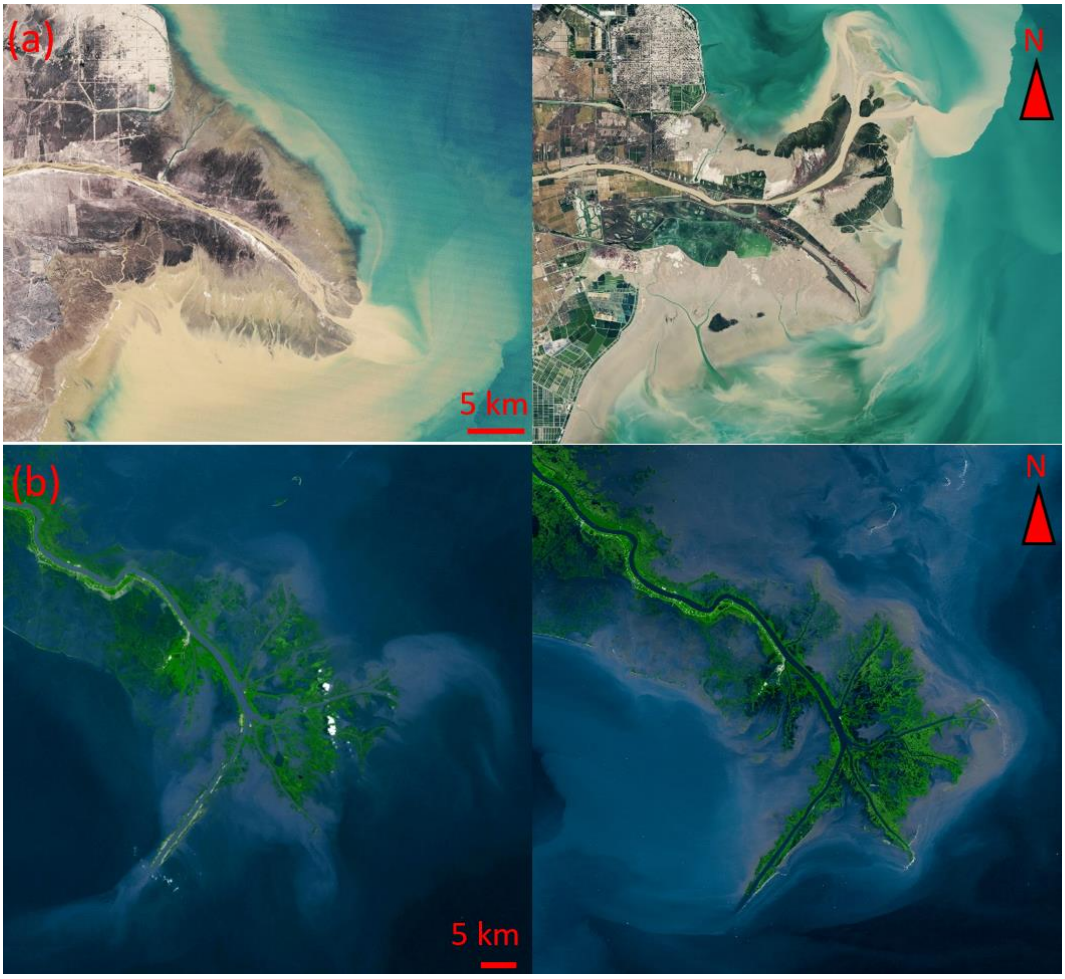

Figure 2-2. (a) The progression of Yellow River Delta captured by Landsat satellites from 1989 (left) to 2020 (right), serving as an example of the evolution branching deltaic networks. (b) Mississippi delta captured by Landsat satellites from 1976 (left) to 2001 (right) showing an elongated morphology ending in a bird's-foot morphology. These images are sourced from NASA Earth Observatory (https://earthobservatory.nasa.gov/).

Under minimal ocean influence, the formation of the river mouth bar and the levees is influenced by several factors. For instance, coarse-grained, noncohesive sediment inputs result in steep topset gradients due to high critical shear stresses, which accelerate the formation of the river mouth bar (Edmonds and Slingerland, 2010; Caldwell and Edmonds, 2014). Conversely, fine-grained, vegetation, cohesive sediment inputs result in shallow topset gradients due to slow settling velocities, allowing suspended sediment deposits to form subaerial levees (Kim et al., 2009; Edmonds and Slingerland, 2010; Caldwell and Edmonds, 2014). In addition, river bed friction, river mouth aspect ratio, and inlet Reynolds number influence the stability or instability of turbulent flow jets at the river mouth (Canestrelli et al., 2014). A stable jet typically leads to the development of a mouth bar, whereas an unstable jet facilitates sediment delivery to the jet margins, thereby promoting the formation of subaerial levees and elongated channels (Canestrelli et al., 2014). The potential vorticity within sediment-laden jet also restricts sediment deposition along the jet's centreline, favouring rapid levees deposition over the formation of frontal mouth bar (Falcini and Jerolmack, 2010). Furthermore, the buoyant effluent constrains lateral spreading of sediment transport, leading to the formation of nearly parallel subaqueous levees (Wright, 1977; Rowland et al., 2010).

Under the influence of wave energy, waves sort and distribute sediments transported by channels, shaping them into various shoreline features such as beaches, barriers, and spits (Wright and Coleman, 1972; Bhattacharya and Giosan, 2003). Waves influence bar development by changing the direction of the river jet, increasing bottom shear stresses at the river mouth, and altering bottom friction, which enhances jet spreading (Nardin and Fagherazzi, 2012). As the result, waves cause mouth bars to form up to 35% closer and 40% quicker to the river mouth compared to scenarios without wave influence (Nardin et al., 2013). Smaller waves, ranging in height up to 0.8 m and with wave periods between 5 s to 10 s potentially fostering deltas with a higher abundance of distributary channels. In contrast, larger waves typically impede mouth bar development, leading to a diminished number of distributary channels (Nardin et al., 2013). The direction of the waves also causes the river mouth to divert, resulting in asymmetrical morphological development around the river in the plan-view configuration of a delta (Nardin and Fagherazzi, 2012; Bhattacharya and Giosan, 2003; Ashton and Giosan, 2011).

In tidal-dominated delta systems, the oscillating flow generated by the tidal prism induces the formation of a central channel, driven by strong ebbing currents in the central part of the river mouth (Gerald et al., 2006; Leonardi et al., 2013). Conversely, the presence of riverine discharge leads to the development of two lateral channels, similar to the fluvial-dominated scenario (Swart and Zimmerman, 2009; Leonardi et al., 2013). Thus, fluctuations in tidal-induced discharge promote the formation of a central channel, while oscillations in basin water level caused by tidal influence encourage the development of two lateral channels cause to the formation of trifurcation at the river mouth (Fagherazzi et al., 2015; Hoitink et al., 2017). The higher tidal amplitudes result in deeper, more stable distributary channels with rougher shoreline patterns (Rossi et al., 2016). The stable channels allow for more efficient sediment by passing across delta plains and seaward channel extension via mouth bar erosion results in sandier deposits in tide-influenced deltas compared to river-dominated ones (Rossi et al., 2016). Additionally, as tidal amplitude increases, the delta-front bathymetry shifts, altering the profile from concave to convex and leading to more complex geometries (Rossi et al., 2016).

2.1.3 Delta avulsion

Avulsion is a natural process responsible for building delta lobes, by which flow diverts out of an established river channel into a new permanent course on the adjacent floodplain (Mackey and Bridge, 1995; Slingerland and Smith, 2004; Reitz and Jerolmack, 2012). Redirecting flow across the delta surface carves out new channels, giving rise to distributaries, which is essential for forming extensive distributary networks on deltas (Jerolmack and Mohrig, 2007; Jerolmack and Paola, 2007). Avulsions can take two main forms, full avulsions where all flow is redirected out of the original channel, often resulting in the abandonment of the original channel downstream of the diversion point and partial avulsions where only a portion of the flow is diverted, leading to the formation of new channels that coexist with the original one (Slingerland and Smith, 2004; Jerolmack, 2009). These types of avulsions can be categorized into: (a) annexation, wherein an active channel is overtaken or a previously abandoned one is reclaimed; (b) avulsion by incision, characterized by the creation of new channels directly on the floodplain surface; and (c) avulsion by progradation, distinguished by significant deposition and the formation of distributary networks with multiple channels (Slingerland and Smith, 2004). The degree of avulsion and the subsequent evolution of new channels are influenced by a long-term setup and a triggering event that causes bank failure and initiates the avulsion (Slingerland and Smith, 2004). Channels and the nearby floodplain accumulate sediment more rapidly compared to the more distant floodplain, this gradual accumulation of sediment raises the channel floor and banks relative to the distal floodplain, eventually leading to a condition known as superelevation. This superelevation condition, characterized by a steeper slope over the floodplain, significantly favours the channel taking an alternate path (Pizzuto, 1987; Smith et al., 1989; Slingerland and Smith, 2004). In a different scenario avulsions can occur at minimal or no superelevation due to upstream-migrating waves of aggradation that result from progradation (Reitz et al., 2010). Avulsions seem to follow cyclical patterns and their frequency appears to be linked to the time needed for sediment aggradation to fill a channel (Bryant et al., 1995; Jerolmack and Mohrig

2007; Reitz and Jerolmack, 2012). Avulsions can also be influenced by downstream processes, such as the development of a river mouth bar resulting in an upstream shift of bed aggradation and overbank flow (Edmonds, 2009). Tectonic tilting, crevasses, delta subsidence, and faulting elevate the likelihood of avulsion, increasing the chances of localized avulsion occurrences (Heller and Paola, 1996; Mackey and Bridge, 1995; Kleinhans et al., 2013). Additionally, the frequency of avulsions is influenced by sea-level rise (Chadwick et al., 2022). When sea level rises slowly (dimensionless sea level rise rate < 0.1 see more detail in Chadwick et al., (2022), the pace of delta progradation into the offshore basin determines avulsion frequency. As sea-level rise accelerates, more frequent avulsions are triggered by the river until a maximum frequency, constrained by the upstream sediment supply, is reached (Chadwick et al., 2022).

In addition, the avulsion mechanism also relies on the stable state of bifurcations within the deltaic system (Edmonds et al., 2010; Salter et al., 2018), which will be discussed in detail in the next section. A bifurcation can either maintain its symmetry or begin to oscillate. As more sediment is directed down one branch, it prograde at a faster rate until the slope advantage triggers an avulsion. The bifurcation continues to prograde, the frequency and magnitude of avulsions tend to increase, with repeated avulsions occurring until the downstream branches encounter an offshore sink (Salter et al., 2018). Tidal-induced backwater effects, which impact water velocity and associated sedimentation or erosion, are considered crucial in the sequence of avulsions (Mackey and Bridge, 1995; Kleinhans, et al., 2010; Reitz et al., 2010). It was highlighted that sedimentation within the channel peaks in the backwater zone, where a preferred location for avulsion initiation is created (Ganti et al.,2016). After an avulsion, one of the shortest routes to the shoreline is typically followed by the newly established flow path, and channel abandonment occurs gradually due to decreased water flow and sediment supply to the main channel over time (Ganti et al.,2016).

Avulsions are predominantly characteristic of floodplains experiencing aggradation, and these phenomena are not limited to specific patterns or sizes of river channels, they can recur in any fluvial system as long as some level of aggradation persists (Slingerland and Smith,2004).

2.1.4 Delta bifurcation

Bifurcations are nodes where water flow from a single channel partitions into two downstream channels (Edmonds and Slingerland, 2008; Kleinhans et al., 2013). In river deltas, bifurcation geometry controls the routing of water and sediment downstream and therefore delta evolution and morphology (Pittaluga et al., 2003; Edmonds and Slingerland, 2007; Kleinhans et al., 2013).

Bifurcations are characterised as stable or unstable, symmetrical or asymmetrical. In stable bifurcations the ratio of water and sediment flux partitioning does not change systematically over time, although it may oscillate due to fluctuations of upstream water flux (Edmonds and Slingerland, 2008; Kleinhans et al., 2013). Unstable bifurcations, where the ratio of water and sediment portioning oscillates, often lead to the abandonment of one of the downstream branches (Pittaluga et al., 2003; Edmonds and Slingerland, 2008). The majority of fluvial bifurcations are asymmetrical in terms of water and sediment flux partitioning, this is also reflected to the geometry of their downstream branches (Pittaluga et al., 2003; Federici and Paola,2003; Bertoldi and Tubino, 2007; Redolfi et al.,2016). Conversely, in tidal environments bifurcations tend towards symmetry (Buschman et al., 2010; Sassi et al., 2011; Iwantoro et al., 2022). The detailed literature on bifurcation evolution will be discussed in the following paragraph.

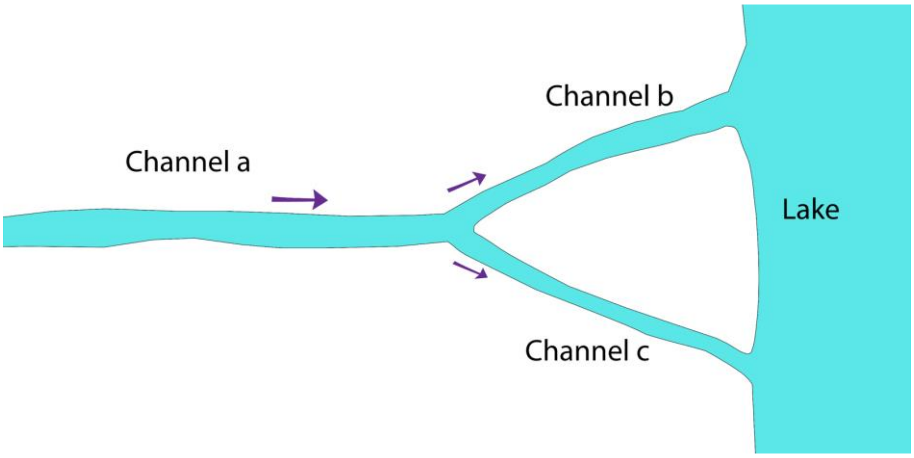

Figure 2-3. A sketch of river bifurcation from Wang et al. (1995) where an upstream channel (labelled as "a") divides into two downstream branches (labelled as "b" and "c"), both flowing within a non-tidal water basin.

Shields stress has been shown to be a good proxy for evaluating bifurcation stability (Pittaluga et al., 2003; Federici and Paola, 2003; Miori et al., 2006; Edmonds and Slingerland, 2008; Pittaluga et al., 2015), it is defined by Equation (1):

$$\Theta = \frac{\tau_0}{(\rho_s - \rho) g D_{50}} \tag{1}$$

Where τ_0 is the critical average bed shear stress, ρ is the water density, g is the gravitational acceleration, ρ_s is the density of sediment and D_{50} is the median grain size for sediment.

In non-tidal deltas with channel beds composed of sand and gravel and typically low values of the Shields parameter, typically smaller than 0.3 (Pittaluga et al., 2003), it has been shown that there exists a threshold value for the Shields stress parameter in the upstream channel. When this threshold is exceeded, the system remains stable only under a symmetrical configuration, however, at Shields stress values lower than the threshold, two additional equilibrium solutions exist for asymmetrical configurations (Pittaluga et al., 2003). For fine-grained channel beds and typically high values of Shields stress, typically ranging from around 0.3 to 6 (Edmonds and Slingerland, 2008). The bifurcations could adopt three different equilibrium solutions, one symmetrical and two asymmetrical configurations, discharge partitioning ratio depends on the Shields stress of the upstream channel (Edmonds and Slingerland, 2008). Non-tidal bifurcations always stabilize in a new configuration if an increase in upstream water flux are less than a threshold of 60% (Edmonds et al., 2010). Beyond this point, instability arises leading to the formation of an avulsion. While, reductions of the upstream water flux increase the system's sensitivity to instability also potentially resulting in channel abandonment (Edmonds et al., 2010). Finer sediments and lower channel slope could influence the total amount of sediment flux, regulating transverse sediment transport and leading to sediment redistribution between downstream branches, facilitating the adoption of a symmetrical, stable configuration (Iwantoro et al., 2021).

In tidal-influenced delta bifurcations, differential water levels from nonlinear interactions between river discharge and tides tend to equalize the discharge division over distributary channels, reducing asymmetric discharge (Sassi et al., 2011; Hoitink et al., 2017). In addition, tidal action, characterized by the erosive nature of tidal currents, promotes channel deepening and enhances the water and sediment transport capacity of both bifurcates to remain morphodynamically active, compared to purely fluvial systems (Ragno et al., 2020). As a result, tides tend to hinder the development of unbalanced distributaries, reducing asymmetries in water and sediment fluxes between branches (Ragno et al., 2020). In addition, the tidal regime could promote the development of bifurcation is more balanced than those in river-influenced systems by governing the bedload transport partitioning between two downstream channels less asymmetrically than suspended load, this process led to stabilizing the bifurcation system and less frequent avulsion (Rossi et al., 2016; Iwantoro et al., 2020).

2.1.5 Delta aggradation

Delta aggradation occurs when sediment accumulates vertically, leading to the raising of the delta’s elevation, an essential process both for the creation and sustenance of river deltas (Evans, 2012; Syvitski and Milliman, 2007; Dunn, 2017). Delta aggradation depends on sediment sinks where net erosive forces are insufficient to remove all the sediment delivered from the upstream fluvial system. Additionally, the accommodation space, or the volume available for sediment accumulation, plays a key role in this process (Galloway 1975; Overeem et al., 2005; Syvitski and Saito, 2007). If sediment supply matches or exceeds the created accommodation space, the delta expands; if not, it shrinks (Syvitski and Saito, 2007; Törnqvist et al., 2008; Syvitski et al., 2009). Delta aggradation is influenced by three key factors (a) sediment delivery to the delta, (b) sediment transport within the delta and (c) sediment retention on the delta plain (Milliman and Syvitski, 1992; Syvitski et al., 2009; Dunn, 2017).

Sediment delivery from rivers into their delta is influenced by climatic factors and catchment attributes (Milliman and Meade, 1983; Overeem et al., 2001; Dadson et al., 2003; Syvitski et al., 2022). Catchment attributes influencing sediment delivery include the size of the drainage basin, the existence of lakes, geological composition, runoff patterns, temperature, and vegetation cover (Wilson 1973; Milliman and Syvitski, 1992). For example, large basins typically having a higher capacity for sediment transport (Syvitski, 2003; Dunn, 2017), while steep basin slopes promote erosion through mechanisms such as landslides and other rapid erosive processes, impacting sediment transport to downstream delta basin (Brozović et al.,1997). Precipitation and temperature enhances soil erosion at hillslopes while also generating the runoff required to transport the eroded sediment to and through the river network (Dadson et al., 2003; Milliman and Kao, 2005; Vrieling et al., 2014). In tropical regions, high rainfall generated from tropical cyclones can play a key role in controlling the magnitude of suspended sediment transport to deltas (Darby et al., 2016).

The main mechanism through which sediment is transported to the deltaic plains is via overbank sedimentation during flooding (Simm and Walling, 1998; Törnqvist and Bridge, 2002; Evans, 2012). This sediment transport process is regulated by the hydraulic connectivity between the distributary channels and their floodplain, which dictates the rate at which material is delivered and deposited on the floodplains (Harvey, 2012; Croke et al.,2013; Strick, 2016). Channel avulsions also play a key role in dispersing sediment to different locations across deltas through overbank sedimentation over time (Piégay et al., 2008; Cabezas et al., 2010; Ibáñez et al., 2014)

The sediment load delivered to a delta is rarely, if ever, fully retained. The ratio of sediment deposited during a flooding event can vary depending on factors like microtopography, flood event characteristics, such as flood magnitude and duration and suspended sediment concentration in the main channel, the flow patterns and stream velocity during the flood (Walling and He, 1998; Asselman et al., 2003; Cabezas et al., 2010). The rate of sediment deposition, layer thickness and mean grain size of overbank deposits typically decreases away from the active channel (Walling and He, 1998). Delta plain topography and the localised nature of flooding also affects sediment delivery which is not uniform across the entire delta (Day et al., 2007; Dunn, 2017). Sediment retention varies across different delta lobes and between subaerial and subaqueous parts of the delta. Subaerial areas retain sediment primarily through flooding or when they temporarily become subaqueous due to channel avulsion, while subaqueous areas, being permanently inundated, can retain sediment continuously. There is a dynamic balance where subaqueous locations that accumulate enough sediment can transition to subaerial forms, which then retain less sediment due to decreased inundation (Dunn, 2017).

2.1.6 Delta subsidence and delta surface elevation change

Delta subsidence stems from various factors influencing the vertical movement of the land surface (Ericson et al., 2006; Vörösmarty et al., 2009; Syvitski et al., 2009). These factors include natural sediment compaction, tectonic activities, and isostatic processes (Vörösmarty et al., 2009; Syvitski et al., 2009). Sediment compaction occurs as sediment particles undergo compression, either under their own weight or the weight of additional sediment deposited on top of them (Meckel et al., 2007; Törnqvist et al., 2008). Tectonic activities, such as uplift and subsidence caused by the shifting of Earth's plates, can also play a significant role in altering delta elevations (Dokka, 2006; Dunn, 2017). Additionally, isostatic processes involve the elastic deformation of the lithosphere in response to changes in mass, this can lead to subsidence when mass is added and uplift when mass is removed (Dunn, 2017). Conversely to aggradation (subsection 2.1.5), subsidence pertains to the reduction of delta plain elevation. The combination of the two counter processes controls the overall delta surface elevation (Ericson et al., 2006; Vörösmarty et al., 2009; Dunn, 2017), which is key for offsetting sea level rise. Syvitski et al., (2009) suggested that the surface elevation of deltas relative to sea level (Δ_{RSl}) can be defined by the following relation:

$$\Delta_{RSl} = \mathrm{A}_r - \Delta_E - \mathrm{C}_N - \mathrm{C}_A \pm M_r \qquad (2)$$

Where, A_r is the delta's aggradation rate, determined by the volume of sediment delivered to and accumulated on the subaerial delta surface as new sedimentary layers. Δ_E represents eustatic sea level changes, which are fluctuations in global sea levels resulting from climatic variations such as ice ages and interglacial periods, as well as ocean water expansion due to temperature changes. C_N denotes natural delta sediment compaction, while C_A is accelerated compaction, which reduces the volume of deltaic deposits due to anthropogenic factors (see

Section 2.2). M_r signifies the typical downward vertical movement of the land surface influenced by the redistribution of Earth's masses, including sea-level fluctuations, delta deposit growth, changes in nearby ice masses, tectonic activity, and deep-seated thermal subsidence (Syvitski et al., 2009).

2.2 Anthropogenic effects on delta evolution

River deltas are home to nearly 339 million people (Edmonds et al., 2020) and throughout history many civilizations preferentially grew around coastlines, rivers and their deltas because of food resources abundance and the facilitation of transport (Stanley and Warne, 1997; Ericson et al., 2006; Best and Darby, 2020). Humans have been exploiting fluvio-deltaic resources for at least 7000 years (Day et al., 2007), however, since the beginning of the twentieth century river and delta exploitation has intensified due to a global population growth and accelerating economic development (Vörösmarty et al., 2009; Overeem and Syvitski, 2009; Bendixen et al., 2019). River deltas are affected by a range of anthropogenic impacts acting on different spatial scales from global to regional to local, all of which will be discussed in the subsections that follow (2.2.1-2.2.3).

2.2.1 Global climate change

Industrial development and population growth have propelled the atmospheric concentrations of greenhouse gases (GHGs) and are the primary cause of the observed global heating since the mid-20th century (IPCC, 2014). Global surface temperatures reached 1.1°C above the 1850-1900 baseline in the 2011-2020 period, cold temperature extremes have been reduced while warm temperature extremes and the frequency of heavy precipitation events have increased in many regions (IPCC, 2023). It is projected that economic development and population growth will continue to be a major contributor to the increase of GHG emissions globally for the near future (IPCC, 2023). It is therefore expected that continuous global heating will result in persistent changes of the Earth's climate. Specifically, heatwaves are projected to become more frequent and prolonged while extreme precipitation events will intensify and become more frequent (Michener et al., 1997; Gu et al., 2011; Day et al., 2016), oceans are becoming more acidic due to warming and mean sea levels are rising because of glacial melt and thermal expansion (IPCC, 2014). The following subsections will discuss the impact of global climate change on delta evolution.

2.2.1.1 Hydroclimatic variability

Intensification of the hydrological cycle as a result of warmer air temperature is associated with changes in precipitation, as well as shifts in the timing and duration of snowmelt (IPCC, 2023; Scown et al., 2023). There are observed trends in streamflow volume, characterized by both increases and decreases across various regions (Kundzewicz et al., 2007). Climate change has led to an increase in annual precipitation in high and mid-latitudes as well as most equatorial regions, but there has been a general decrease in precipitation in the subtropics (Carter et al., 2000). For instance, the discharge of Eurasian rivers draining into the Arctic Ocean has shown an increase since the 1930s, largely in line with heightened precipitation (IPCC, 2007). There is also evidence of more extreme rainfall occurring over much of the world (Best, 2019). It is anticipated that the maximum river water discharges are expected to rise by 11–33% in 49 major deltas by 2100, primarily due to climate change (Scown et al., 2023). Furthermore, it is expected that peak streamflow will shift from spring to winter in many areas due to earlier snowmelt, leading to reduced flows during summer and autumn (Hock et al., 2005; Kundzewicz et al., 2007). Over longer timeframes, ranging from decades to centuries, glacier wasting is forecasted to be exacerbated by positive feedback mechanisms, resulting in a decrease in glacier runoff (Jansson et al., 2003). For instance, the earlier spring snowmelt and increased winter base flow observed in North America and Eurasia are attributed to enhanced seasonal snowmelt associated with climate warming (IPCC, 2007).

In addition to water flux changes, global heating may also impact sediment fluxes into river deltas. Warming could change sediment fluxes to delta through sediment production (Syvitski, 2002). Rising temperatures enhance soil formation and increase freeze-thaw cycles, thereby generating a greater sediment supply, leading to increased fluvial loads (Morehead et al., 2003; Syvitski and Milliman, 2007; Rempel et al., 2016). For example, in Arctic basins, a 2°C rise in mean annual air temperature can result in approximately a 30% increase in river sediment loads, as thawing releases new sediment from its frozen state (Syvitski, 2002). The increased frequency of heavy precipitation events, such as tropical cyclones, results in increased erosion within a catchment area, also leading to higher sediment supply to rivers and subsequently augmenting river discharge and sediment transport (Molnar, 2001; Vrieling et al., 2014; Day et al., 2016). In contrast to the effects of warming-induced increases in sediment supply, rising river temperatures may actually diminish sediment transport. For example, if a river's temperature increases by 25°C, sediment transport for fine sand particles at 62.5 μm could decrease by 90%, while fine silt grains at 10 μm might experience a 300% decrease (Syvitski et al., 2019).

Furthermore, intense rainfall events can lead to considerable flooding in deltas because of their low elevation (Ericson et al., 2006; Overeem and Syvitski, 2009). It is anticipated that, the current 100-year flood would occur at least twice as frequently across 40% of the globe by 2050 (Arnell and Gosling, 2016). This would expose approximately 450 million flood-prone people and 430 thousand km^2 of flood-prone cropland to a doubling of flood frequency, with global flood risk increasing by approximately 187% over the risk in 2050 in the absence of climate change (Arnell and Gosling, 2016). In addition, with anticipated a 1.5 °C rise in temperature, approximately three-quarters of the world's population is likely to face increased flood exposure compared to the 1976–2005 baseline, resulting in a 120% increase in damage costs (Best, 2019).

In contrast with the intense rainfall events, climate change is also anticipated caused more droughts, leading to fresh water shortages in deltas, This, in turn, will reduce coastal and near-shore water quality, cause saltwater intrusion, result in wetland and beach loss, and create socio-economic impacts (Bucx et al., 2010).

2.2.1.2 Sea level rise

Between approximately 21,000 and 11,700 years ago, Earth experienced a warming of about 4°C, causing the global mean sea level (GMSL) to rise by roughly 85 m (NASA, 2022). GMSL continued to rise by an additional 45 m after the warming period ended, resulting in a total increase of 130 m from the pre-warming level, reaching its current level approximately 3,000 years ago (NASA, 2022). From around 3,000 years ago until about 100 years ago, GMSL fluctuated slightly with no significant overall change (NASA, 2022). In the past 100 years, global temperatures have increased by about 1°C, with GMSL rising by approximately 160 to 210 mm, about half of which has occurred since 1993 (NASA, 2022). In 2014, the GMSL was 67 mm higher than the 1993 average and continues to rise at a rate of approximately 3.2 mm yr^{-1} (NASA, 2024). It is projected that the global mean sea level (GMSL) will be 0.20 to 0.29 m by 2050 and 0.63 to 1.01 m by 2100 above the mean sea level of the 1986-2005 period (SSP5-8.5 GHG scenarios) (IPCC, 2023). However, due to uncertainty surrounding ice-sheet processes and their response to global warming these GMSL projections may increase up to 2.5 m by 2100, potentially exceeding 15 m by 2300 (Sweet et al., 2017; Hall et al., 2019; IPCC, 2023).

9.4% of the global deltaic surface, housing approximately 19.8 million people (2017-based estimate), lies at ≤1 m elevation relative to mean sea level, while 50% of global delta area lies at <6.5 m (Edmonds et al., 2020), these low-lying regions are sensitive to even minor changes in sea level (Vörösmarty et al., 2009). Furthermore for many deltas, fluvial sediment supply that acts to aggrade deltaic plains (see section 2.1.5) is currently inadequate to mitigate the consequences of sea level rise (Giosan et al., 2014) and when coupled with the impact of land subsidence, it is contributing to delta sinking (Syvitski et al., 2009; Kondolf et al., 2022). Reduced sediment fluxes, land subsidence, and eustatic sea level rise (SLR) are collectively causing the drowning of 46 of the world's largest deltas, with average rates of contemporary submersion estimated at an average of 6.8 mm yr^{-1} (Tessler et al., 2018). Delta sinking has the potential to exacerbate flood occurrences within delta regions. In the absence of eustatic SLR, existing rates of subsidence would lead to flooding of approximately 26 % of deltaic surfaces by 2100, however, considering different scenarios of eustatic SLR, the affected surface area is projected to range between 45 % and 61 % by 2100 (Aguilar et al., 2012). These finding is further supported by Syvitski et al., 2009), who estimate that by 2100, relative SLR (i.e. the combination of eustatic SLR, delta subsidence and sediment supply reduction) will increase the areas at risk of flooding in the world's deltas by more than 50 %. Under the projected RCP8.5 scenario until 2100, more than 85 % of delta land loss is anticipated to be attributed to SLR, resulting in approximately a 5 % reduction in global delta land area (Nienhuis and Wal, 2021). Relative SLR also contributes to the expansion of tides (Ensign and Noe, 2018; Vasilopoulos et al., 2021), which in turn exacerbate saline intrusion (Chang et al., 2011; Herbert et al., 2015; Ensign and Noe, 2018). Increased salinity content imposes physiological stress on wetland biota, potentially leading to significant alterations in wetland communities and their respective ecosystem functions (Herbert et al. 2015). In addition, SLR could lead to a relative amplification of wave and tide influence on the delta front (Arns et al., 2017). These changes could alter the evolutionary trajectory of deltas (Nienhuis et al., 2020).

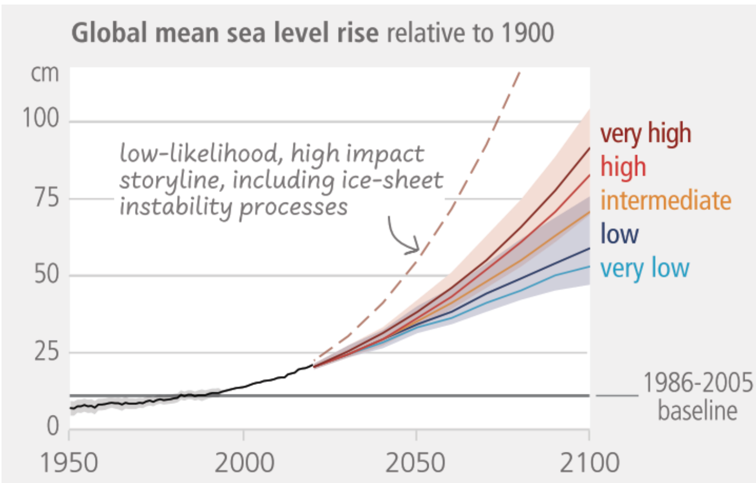

Figure 2-4. Future projected Global Mean Sea Level (IPCC, 2023).

2.2.2 Regional perturbations

Section 2.2.1 discussed the global-scale impact of human activities affecting the evolution of river deltas. This section will delve into the effects of human activities on the large-scale catchments that feed river deltas, with a focus on how these activities influence deltaic systems. Key aspects include river impoundment, such as the construction of dams and reservoirs, which disrupt the natural flow and sediment transport of rivers, leading to changes in delta formation and stability. Additionally, land use changes, including deforestation, urbanization, and agricultural practices, can considerably impact the hydrology and sediment load of river catchments.

2.2.2.1 River impoundment

It is estimated that approximately 16.7 million reservoirs larger than 100 m^2 exist globally amounting to a total storage volume of 8069 km^3 and a combined area covering 305,723 km^2 (Lehner et al., 2011). There is estimated that only 37% of rivers longer than 1,000 km remain free-flowing along their entire length, with merely 23% flowing uninterrupted to the ocean (Grill et al., 2019). River hydropower accounts for 16% of the global electricity generation and 69% of the global renewable electricity (Xu et al., 2023). It is estimated that river reservoirs have a combined economic benefit of $265 billion annually (Hogeboom et al., 2018). Over 3,700 hydropower dams with capacities exceeding 1 MW were in the planning or construction stages globally in 2015 which when fully executed will increase global hydroelectric capacity by 73% and reduce the number of remaining free-flowing rivers by 21% (Zarfl et al., 2015). The focus of future hydropower development lies predominantly in developing nations and emerging economies across Southeast Asia, South America, and Africa (Zarfl et al., 2015; Winemiller et al., 2016; Adams, 2017).

While reservoir construction offers various advantages to humans, it also carries numerous negative impacts on the environment and river deltas in particular (Vörösmarty et al., 2003; Best, 2019; Edmonds et al., 2020). Large river dams have caused a substantial increase in the retention of water within rivers, by as much as 600–700%, while the duration for a water parcel to travel from land to sea has extended threefold (Vörösmarty et al.,2009). Consequently, dams have induced modifications in the hydrological cycle of rivers and their delta systems, including the reduction of flood peaks and the increase of base flow during dry seasons (Dunn, 2017; Kondolf et al., 2018). Flow regulation, resulting from reservoirs, is seen as a major ecological issue, causing a swift decrease in aquatic biodiversity, obstructing species migration and leading to reduced species diversity (Petts, 1984; Nilsson et al., 2005; Dudgeon et al., 2006; Winemiller et al., 2016). Furthermore, dams act as sediment traps, which in turn affects the quantity of sediment transported from land to river deltas (Vörösmarty et al., 2003). Since 1950, worldwide large dams have trapped approximately 3,200 gigatonnes of sediment (Syvitski et al., 2022). A portion of this sediment consists of sand, as emphasized by UNEP (2019), which highlights that large rivers have lost 50% to 95% of the global sand flux and the construction of dams has played a role in reducing this amount. This sediment supply reduction has destabilised the natural process of delta progradation (Syvitski et al., 2005), resulting in delta sediment starvation (Vörösmarty et al., 2003; Syvitski et al., 2009; Edmonds et al., 2020), triggering riverbed incision and increasing river and costal erosion (Marchesiello et al., 2019; Best and Darby, 2020; Vasilopoulos et al., 2021), further exacerbating the threat of delta sinking (Syvitski et al., 2009) posed by relative sea level rise (Vörösmarty et al., 2009; Best, 2019) and imperilling the future sustainability of numerous deltas (Vörösmarty et al., 2009; Best, 2019; Syvitski et al., 2022). Moreover, river dams may exacerbate the risk of catastrophic floods through dam failures (Xu et al., 2023) and can impose substantial costs for human societies, leading to displacement and resettlement, social upheaval (Scudder, 2012).

2.2.2.2 Land use change

Changes of land cover within river basins, mainly due to activities like deforestation, intensification of agriculture, and urban expansion can influence delta evolution (Watson et al., 1996; Syvitski et al., 2005; Overeem and Syvutski, 2009; Best and Darby, 2020). Forest areas retain and regulate surface and groundwater movement, maintain water quality and modulate soil erosion (Watson et al., 1996; FAO, 2011). However, from 1990 to 2000, approximately 13 million hectares of forest were either converted to alternative purposes or lost annually (FAO, 2011). In the following decade, extensive tree planting initiatives significantly mitigated the net decrease of forested areas with average forest lost estimated at 5.2 million hectares yr^{-1}. The primary loss of forested land has been concentrated in regions such as South America, sub-Saharan Africa, Southeast Asia, and Oceania (FAO, 2011).

Soil that is bare or partially vegetated and compacted tends to shed water at a much higher rate compared to vegetated and uncompacted soils (Watson et al., 1996), consequently altering soil erosion rates (Routschek et al., 2014). Deforestation exposes the soil surface to erosional forces such as wind, sun and water (Vrieling et al., 2014), and it diminishes soil cohesion by removing stabilizing roots (Zhang, et al., 2014), therefore increased catchment erosion rates, considerably impacting the transport of fluvial sediment (Watson et al., 1996; Syvitski et al., 2005). It is estimated that around 75 billion tonnes of soil are lost annually from arable lands worldwide

(GSP, 2016). Nearly all catchments that have transitioned from natural vegetation to agricultural land uses show increased sediment fluxes (Watson et al., 1996). For instance, bed load transport in the Araguaia River, Brazil, increased by 31% from the 1970s to 2000, rising from 6.7 million tonnes of sandy sediments to 8.8 million tonnes, largely in response to deforestation (Latrubesse et al., 2009). Similarly, sediment load at the basin outlet of the Rio Magdalena river in Colombia potentially increased by 40–45% between 1975 and 1995 due to forest clearance, intensified land use, and gold mining activity (Walling, 2006).

Moreover, the impact of land use changes on fluvial systems often interacts with and is influenced by climate change and variability (Watson et al., 1996). On one hand, alterations in land cover can exacerbate the greenhouse effect (Houghton, 1990; Shukla, 2012). For instance, FAO, (2011) reports that agriculture and deforestation combined contribute up to a third of total anthropogenic greenhouse gas emissions, contributing to climate change. On the other hand, the direction and timing of climatic shifts can significantly affect the resulting sediment response. In cases where climatic changes occur gradually, adjustments in vegetation cover and land use may occur (Watson et al., 1996; Syvitski, et al., 2005).

2.2.3 Local perturbations

Section 2.2.2 discussed the impact of human activity on a regional scale. In this section, the direct effects of human activities on the deltas themselves will be examined. These include riverine sand mining, which depletes sediment resources critical for maintaining delta stability; groundwater and hydrocarbon extraction, which can lead to land subsidence and increase the vulnerability of deltas to flooding; and infrastructure development, which alters natural water flow patterns, disrupts sediment transport, and often contributes to the degradation of deltaic environments.

2.2.3.1 Sand mining

Sand plays a crucial role in the construction industry, land reclamation and a myriad of other industrial applications including the production of electronics, cosmetics, and glass (UNEP, 2019; Bendixen et al., 2019), ongoing rapid urban expansion and economic growth has lead to increasing demands for sand (Torres et al., 2017; Krausmann et al., 2017; UNEP, 2019; Bendixen et al., 2019). Since 1950, the global urban population has increased from 751 million to 4.2 billion. As a result, between 1900 and 2010, there was a remarkable 23-fold increase in the global utilization of natural resources for building and transportation infrastructure (Krausmann et al., 2017). Sand and gravel emerged as the leading contributors to this surge, establishing them as two of the most heavily extracted resources worldwide (Schandl et al., 2016). A large portion of aggregates is used for land reclamations or cement production. China produced approximately 2.4 billion tonnes of cement in 2017 (UNEP, 2019) while India followed with a production of 270 million tonnes, and the USA produced 86.3 million tonnes in the same year (UNEP, 2019). Singapore, known as the world's top sand importer, increased its land area by more than 20% over the last forty years, equating to an addition of 130 km^2. During the past two decades alone, Singapore has imported an estimated 517 million tonnes of sand, sourced mainly from Indonesia, Malaysia, Thailand, Cambodia, and Viet Nam, to support its land expansion initiatives (UNEP, 2019; Filho et al., 2021).

In concrete production, fluvial sand, characterized by its angularity, is favoured over rounded particles sourced from coastal beaches or desert dunes (Bendixen et al., 2019). Consequently, this preference has prompted the expansion of sand extraction operations from rivers and floodplains (Best, 2019; Bendixen et al., 2019). Most sand and gravel extracted from natural environments are used locally due to the high cost of transportation (UNEP, 2019). The increasing demand for sand has resulted in illegal extraction activities in various regions (WWF, 2018), such as South Africa (Chevallier, 2014), China (Xiqing et al., 2006) and Mekong (Eco-Business, 2017). On a global scale, the extraction of sand is estimated to range between 32 and 50 billion tons annually, this estimate exceeds twofold the estimated total annual sediment supply from continents to the global ocean, which is approximately 19 billion tons yr^{-1} (Bendixen et al., 2019). By 2050, it is projected that approximately 66% of the global population will reside in urban areas (United Nations, 2014). The demand for sand and gravel for construction purposes is escalating at a rate surpassing the capacity of natural sources to replenish, leading to an anticipated surge in prices in the foreseeable future (Figure 2-5) (Bendixen et al., 2019).

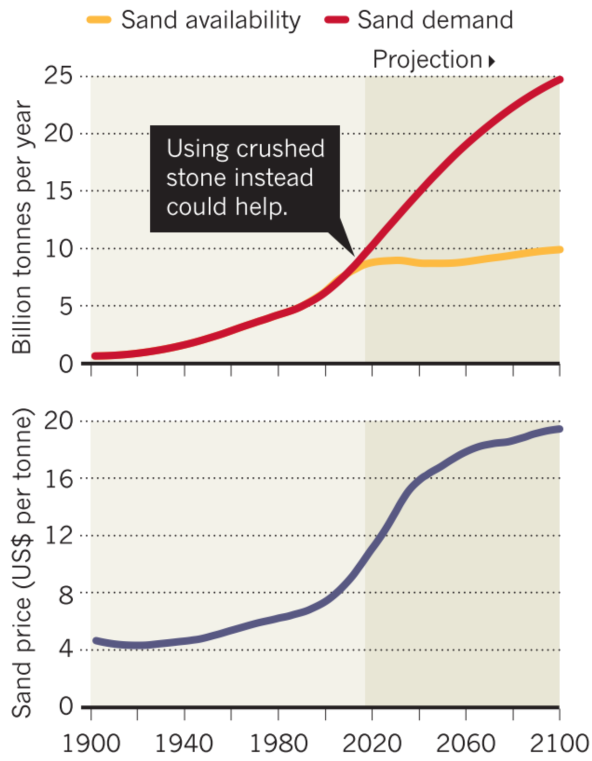

Figure 2-5. Predicted demand for sand for construction compared to natural sources, along with associated prices, as sourced from Bendixen et al., (2019)

While sand mining provides some economic benefits, it also inflicts considerable harm on rivers and their deltas (Syvitski et al., 2009; Best, 2019; Bendixen et al., 2019; Kondolf et al., 2022). Sand mining combined with reduced fluvial sediment supply has resulted in sediment deficits in many large deltas contributing to delta sinking (Syvitski et al., 2009; Kondolf et al., 2022). Sand mining is the primary contributor to river lowering in many deltas (Kondolf 1994; Chevallier, 2014; Huang et al., 2014; Arróspide et al., 2018; Koehnken et al., 2020, Vasilopoulos et al., 2021; Zhang et al., 2022). Riverbed lowering caused by sand mining considerably alters water level regimes within delta regions. For example, riverbed lowering in the Pearl River Delta has led to reduced peak water levels in upstream areas (Bao et al., 2022). In the northern outlet channel of Poyang Lake, located in the middle reaches of the Yangtze River, an average riverbed lowering of 3 m has resulted in approximately 0.3-m reductions in water levels during low-water periods in central lake regions (Yao et al., 2019). Additionally, extensive sand mining in the Dongjiang River's lower reaches and its delta has caused riverbed lowering, which has subsequently led to decreased tidal water levels in the delta's upper sections (Jia et al., 2007). In addition to altering hydrodynamics, sand mining destabilizes riverbanks, increasing the risk of erosion and bank collapse (Kondolf 1994; Hackney et al., 2020) and contributes to coastal erosion (Anthony et al., 2015). For instance, in the Vietnamese Mekong Delta, the Vietnamese government estimates that nearly 500,000 people will need relocation due to riverbank collapsing caused by in-channel sand mining (Bendixen et al., 2019; Hackney et al., 2020). Sand mining also intensifies scouring processes that undermine embankments and other built infrastructure (Kondolf 1994; Best, 2019), lowers the water table (Chevallier, 2014; Best, 2019), exacerbates tidal ingress landward (Vasilopoulos et al., 2021; Talke et al., 2021) and promotes saline intrusion (Eslami et al., 2021). It can also degrade water quality and the overall health fluvial and riparian ecosystems (Sreebha and Padmalal, 2011; Saviour, 2012; Venson et al., 2017; Torres et al., 2017). For example, in the Ganges River in northern India, eroded river banks caused by sandmining have obliterated the nesting and breeding habitats of fish-eating gharial crocodiles, a critically endangered species with only around 200 adults remaining in the wild in northern India and Nepal (Bendixen et al., 2019).

2.2.3.2 Underground water and hydrocarbon extraction

Land subsidence as a natural processes of delta evolution have been discussed in Section 2.1.6. However, rates of subsidence can be considerably intensified by the extraction of groundwater and hydrocarbons (Erkens et al., 2015; Minderhoud et al., 2017; Best and Darby, 2020). This human-exacerbated rates of delta subsidence often outpace natural delta-building processes, causing significant sinking in many major delta's worldwide (Syvitski et al., 2009; Vörösmarty et al., 2009; Kondolf et al., 2022). The estimated rate of land subsidence in most river deltas exceeds 2.5 mm yr^{-1} and becomes especially severe in urban lowland areas, reaching over 20 mm yr^{-1} (Hooijer and Vernimmen, 2020). For example, the natural subsidence rate for the Po Delta was about 2-4 mm yr^{-1}, but since the 1950s, it has surged to 40-60 mm yr^{-1} due to increased groundwater extraction and natural gas mining (Overeem and Syvitski, 2009). In Suzhou city, located in the Yangtze River Delta, excessive groundwater extraction has caused rapid subsidence, with rates reaching 90 mm yr^{-1} between 1984 and 1987 (Shi et al., 2012).

Land subsidence has led to various environmental problems, for example, considerable wetland losses in coastal Louisiana, US, are mainly due to accelerated land subsidence and fault reactivation caused by reduced reservoir pressures from extensive gas and oil extraction (Morton et al., 2006). In the Mississippi River Delta, oil and gas extraction has resulted in spills that harm estuarine organisms and, combined with altered surface hydrology and induced subsidence, has intensified the negative effects (Day et al., 2020). Similarly, in Delta State, Nigeria, oil and gas extraction operations have caused oil spills, soil degradation, hindered vegetation growth, adverse health effects, and the displacement of local residents (Omorede, 2014). Furthermore, land subsidence driven by water and hydrocarbon extraction causes significant economic losses due to structural damage and high maintenance costs, impacting roads and transportation networks, hydraulic infrastructure, river embankments, sluice gates, flood barriers, pumping stations, sewage systems, buildings, and foundations (Ericson et al., 2006; Galloway and Burbey, 2011). The global damage associated with subsidence is estimated to amount to billions of dollars annually (Erkens et al., 2015)

2.2.3.3 Infrastructure development

Over the past century, a range of engineering structures have been built in river deltas (Vörösmarty et al., 2009) including channels for navigation and irrigation, flood defences, dikes, culverts, and pumping stations, among others that constrain the natural movement of water and sediment (Revenga et al., 2000; Vörösmarty et al., 2009; Bucx et al., 2010). Seasonal flood waves would overtop natural levees every few years, depositing nutrient-rich sediment on the delta surface promoting delta aggradation (Evans, 2012; Syvitski and Milliman, 2007; Syvitski et al., 2009). However, the construction of dikes, levees, and other flood-control structures, while mitigating floods, has disrupted river-floodplain connectivity, preventing overbank flooding and confiding the flow within delta channels (Syvitski and Saito, 2007; Hung, 2011). Consequently, there is a decrease in the sediment delivery from river to deltas, resulting in diminished delta aggradation and heightened delta subsidence (Syvitski and Saito, 2007; Vörösmarty et al., 2009; Syvitski et al., 2009; Evans 2012). For example, In the Mississippi Delta, extensive levee systems isolating the river from much of the delta plain, along with hydrological changes, and reduced sediment discharge have led to a 25% loss of delta wetlands over the past century (Day et al., 2007). If these trends continue, most of the remaining wetlands could vanish by 2100 (Day et al., 2007).

In addition, the river-floodplain disconnect driven by Infrastructure development can lead to a rapid decline in biodiversity and essential ecosystem services, including the provision of breeding and feeding grounds for various fish and bird species (Revenga et al. 2000; Pringle, 2003; Cardinale et al., 2012; Grill et al., 2019). For example, the implementation of irrigation systems, road networks, and terrestrial urban development has gradually transformed the delta terrain into a more terrestrial environment in the Chao Phraya Delta, Thailand (Morita, 2016). Large-scale water engineering projects including dams and flood embankments in the Waza-Logone floodplain of northern Cameroon reduced flooding across substantial areas of the plain, leading to the collapse of fisheries, loss of grazing lands, a decline in biodiversity, and a substantial migration of both human populations and livestock out of the region (Revenga et al., 2000).

2.3 The Mekong

2.3.1 The Mekong River and Delta

The Mekong River originates from the Tibetan plateau, located at approximately 5,160 m above sea level. The river stretches approximately 4,800 km in length and runs through 5 countries; China, Myanmar, Lao PDR, Thailand and Cambodia where it bifurcates forming the Mekong Delta (MD) which then flows through South Cambodia and into Viet Nam (Figure 2-6, a). The river ranks 10th in the world in terms of total flow (475 km^3 annually), 25th in terms of catchment area (795,000 km^2) and transports around 87 million metric tons of sediment annually (MRC, 2005; Darby et al., 2016).

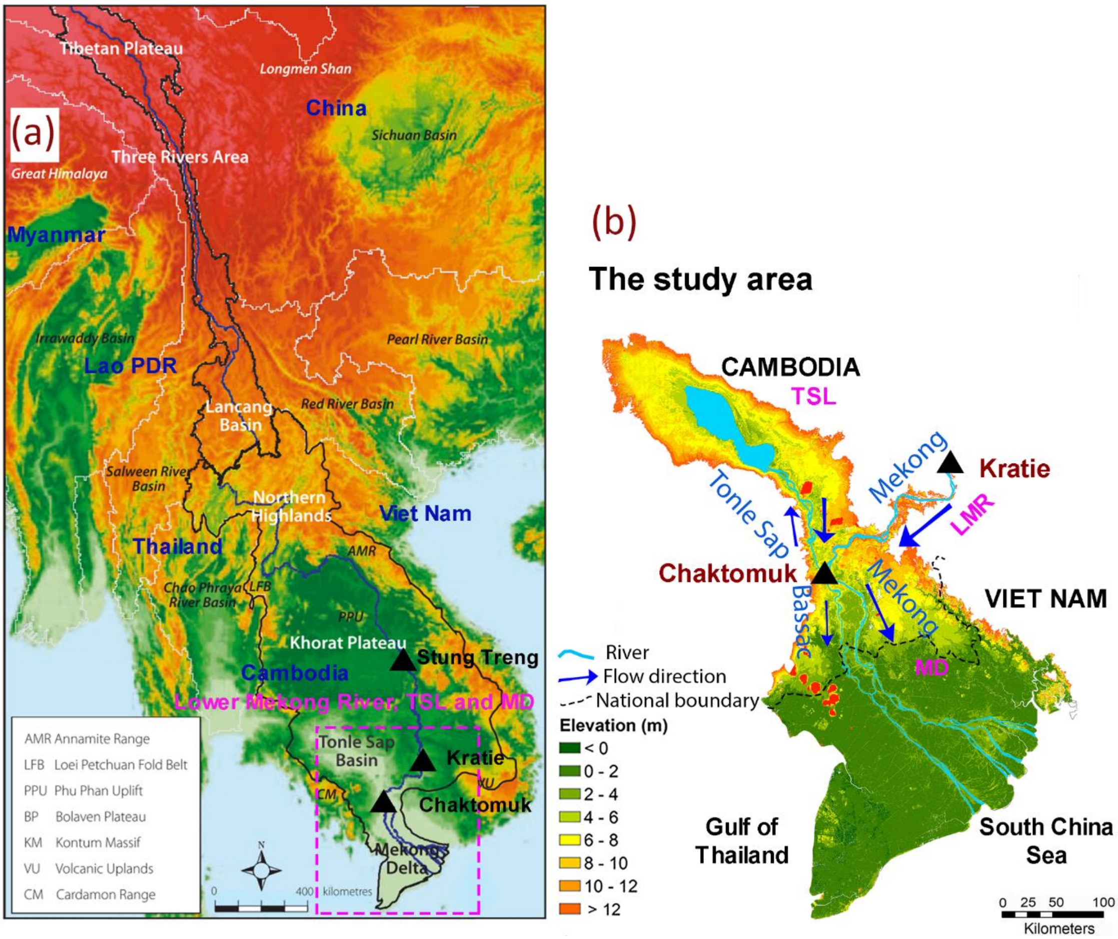

Figure 2-6. (a) Map of Southeast Asia highlighting the Mekong Basin. (b) The study area, Lower Mekong Basin (LMB) extends from upstream at Kratie to the South China Sea in southern Viet Nam, encompassing the Lower Mekong River (LMR), Tonle Sap Lake system (TSL), and Mekong delta (MD).

For the majority of its course, the Mekong River flows almost entirely through a succession of mountainous and hilly regions, confined by the underlying bedrock (MRC, 2010). This changes when the river reaches Kratie (Figure 2-6, a), the northmost boundary of the present study, Lower Mekong Basin (LMB), where the river starts to flow through alluvium. Upon reaching the junction of Chaktomuk in Phnom Penh (Figure 2-6, b), the Mekong River splits into three separate branches; the Tonle Sap River (TSR) that connects with the Tonel Sap Lake (TSL) and the two primary distributary channels that form the Mekong Delta (MD), namely Mekong and Bassac. The Mekong and Bassac channels flow south-southeast reaching the Vietnamese Mekong delta (VMD), where they divide further into a system of seven distributary channels before reaching the South China Sea (MRC, 2010). The present study focuses on the region extending from Kratie to the South China Sea, encompassing three main reaches here dubbed as the Lower Mekong River (LMR), which includes the stretch of the Mekong River from Kratie to the Chaktomuk Junction; the TSL system which includes the Tonle Sap Lake and Tonle Sap River; and the Mekong Delta (MD), stretching from the Chaktomuk Junction in Cambodia to the South China Sea in Viet Nam (Figure 2.6).

The floodplains of the LMR in Cambodia are home to around 1.8 million people and cover approximately 15,000 km², with approximately 4,100 km² dedicated to cereal agriculture (The General Population Census of Cambodia, 2019; Census of Agriculture of the Kingdom of Cambodia, 2013). The TSL system in Cambodia, ranks among the most productive lake-wetland ecosystems globally, placing it fourth in fish productivity (Bonheur and Lane, 2002). The lake has an estimated annual fish yield of over 537,000 tons (Pin et al., 2020), directly supports approximately two million people (Arias et al., 2013). Surrounding the lake is a mosaic of diverse habitats, including flooded forests, scrublands, grasslands, and agricultural areas. The flooded forests, consisting of tree species adapted to prolonged submersion, play a vital role in preserving biodiversity and delivering critical ecosystem services such as carbon sequestration, water regulation, and soil stabilization (Bonheur and Lane, 2002; Campbell et al., 2006; Arias et al., 2013). Since 1997, the TSL has been recognized as a UNESCO World Heritage Biosphere Reserve, serving as a habitat for globally significant populations of endangered amphibians, reptiles, mammals, and birds, spanning a diverse array of 885 species (UNESCO; Bonheur and Lane, 2002; Campbell et al., 2006; Arias et al., 2013; Uk et al., 2018).

The MD covers approximately 49,700 km², with roughly 8,700 km² located in Cambodian Mekong Delta (CMD) and approximately 41,000 km² in Vietnamese Mekong delta (VMD). The delta is home to an estimated population of 23 million, with 5 million residents in Cambodia and about 18 million in VMD (The General Population Census of Cambodia, 2019; General Statistics Office Of Vietnam, 2024). In the CMD around 3,570 km² are dedicated to rice agriculture, while fresh water fish from rivers and aquaculture totalled 30,500 tons according to the 2010 estimates (CEIC, 2010; The General Population Census of Cambodia, 2019). In the VMD, approximately 39,230 km^2 delta plain area is allocated to rice agriculture, while around 7,720 km^2 of deltaic terrain is designated for aquaculture. Agriculture in this area contributes an output of nearly 23.5 million tons, while the aquaculture sector contributes nearly 3.4 million tons according to estimates from 2021 (General Statistics Office Of Vietnam, 2024).

The study region's climate is tropical and influenced by a monsoon pulse, characterized by distinct dry and wet seasons. The wet season, normally spanning from mid-May to October, accounts for more than 90% of the annual precipitation in the region (Kingston at al., 2011) and contributes to 80-90% of the total annual flow of the River (Triet et al., 2017). The hydrological pattern in the Mekong River aligns with the climatic trends of the area. Starting around May, the monsoon-generated rainfall in the basin leads to a gradual rise in river discharge, typically peaking towards the end of September. This is followed by a gradual decline in discharge, reaching its lowest point around March (MRC, 2009). Due to the pronounced seasonality of the flow, the monthly water discharge at Kratie averages around 36,000 m^3s^{-1} during the flood season, whereas it drops to approximately 3,000 m^3s^{-1} in the dry season (MRC, 2009).

The hydraulics of the TSL are primarily influenced by the monsoonal flood pulse of the Mekong River. Specifically, during the rising limb of the monsoon flood season (typically June – October), water from the Mekong flows into TSL through two main pathways: (1) the water levels in the Mekong at Chaktomuk Junction rise above those in the lake, creating a hydraulic gradient that reverses the flow of the TSR, directing water from the Mekong into TSL (MRCS/WUP-FIN, 2007); and (2) the Mekong also floods the Tonle Sap floodplain, with nearly half of this water flowing directly into the lake and the rest reaching it via the TSR (Fujii et al., 2003; MRC, 2005). This flow reversal results in a typical increase of the lake's water level from a mean low level of 1.32 m (σ = 0.10 m) during the dry season to a mean peak water level of 9.14 m (σ = 1.00 m) during the flood season (Kummu et al., 2014). Consequently, the lake's surface area expands by an order of magnitude - from 2,210 km^2 (σ = 118 km^2) to approximately 13,260 km^2 (σ = 1,714 km^2), with the volume of the lake experiencing an even greater increase from around 1.6 km^3 (σ = 0.2 km^3) up to 59.7 km^3 (σ = 13.0 km^3) (MRCS/WUP-FIN, 2007; Kummu et al., 2014). In total, at peak levels, approximately 57 % of the water in the TSL originates from the Mekong River - around 52% entering through the TSR and ~ 5% directly through the Tonle Sap floodplain, the tributaries that feed directly into the lake contributing a further 30%, and direct inputs of precipitation accounting for the remainder (13 %) (MRCS/WUP-FIN, 2007). As the flood season subsides, the direction of water in the TSR undergoes a reversal, and the water stored in the TSL drain back into the Mekong River and flow towards the MD (MRC, 2005).

This unique flow reversal along the TSR into the TSL governs the timing and duration of the annual floods in the region, playing a crucial role in shaping the overall hydrology, and ecology, of both the TSL floodplain and the MD downstream (MRC, 2009). The flow reversal and TSL effectively act as a vast water capacitor for the Lower Mekong, storing sufficiently large volumes of the Mekong's seasonal floodwater to modulate down delta flood season water levels across the MD, and then releasing the stored water during the dry season maintaining water fluxes to the downstream delta at precisely the point when agricultural water demand is greatest. Indeed, the TSL outflows could accounts for 20-50 % of the Mekong fluxes at the apex of the delta during the period from October–March (Fujii et al., 2003; Kummu et al., 2014). As such the lake's flood pulse functioning is not just critical in terms of the lake's biological productivity and biodiversity, but it is also integral to water systems and water levels across the entire lower Mekong system (Cochrane at al., 2014; Wen and Park, 2021; Dang et al., 2022; Morovati et al., 2023).

In the MD front, the observed tidal patterns exhibit a combination of characteristics, primarily following a semidiurnal cycle with a range of 2.5 to 3.8 m in the South China sea and 0.5 to 1.0 m in the Gulf of Thailand (Figure 2-6, b) (Nguyen et al., 2000). In the flood season, the impact of tides is evident at monitoring stations located more than 203 km from the channel mouths. During the dry season, the tidal signal reaches as far as the delta apex at the junction of Chaktomuk, which is around 400 km away from the coast (Gugliotta et al., 2017).

2.3.2 Anthropogenic challenges

In recent decades, global climate change and human activities within the greater Mekong region have exacerbated the vulnerability of the system (Anthony et al., 2015; Lu et al., 2014; Kondolf et al., 2018; IPCC 2023). The region is predicted to become warmer in the future, with longer and dryer dry seasons, which will negatively affect agricultural and aquacultural productivity (MONRE, 2016). Additionally, extreme events like tropical storms are anticipated to become more frequent (Delgado et al., 2010; Delgado etal., 2012; MONRE, 2016; IPCC, 2023; Wood et al., 2023) . The Intergovernmental Panel on Climate Change (IPCC) projects future sea level rise (SLR) for the Mekong coast, specifically at Vung Tau stations (see Figure 3.1, Chapter 3). By 2050, under the SSP1-1.9 scenario, SLR is expected to reach 0.2 m (0.1 m; 0.4 m) for the 50% (5%; 95%) percentile ranges. In the SSP8.5 low-confidence scenario, this rises to 0.3 m (0.1 m; 0.6 m) (NASA, 2021). By 2100, SLR values are projected to increase further to 0.4 m (0.1 m; 0.8 m) under SSP1-

1.9 and 0.5 m (0.9 m; 2.5 m) under SSP8.5 low-confidence scenarios (NASA, 2021). A 1 m rise in sea level could result in the loss of half of the Mekong Delta's mangrove area (2,500 km^2), the conversion of nearly 1,000 km^2 of agricultural and aquaculture land into salt marshes, and the flooding of 15,000 to 20,000 km^2 of delta area (IPCC, 2007).

Furthermore, the greater Mekong region has seen a surge in hydropower dam construction and infrastructure development, including projects for irrigation, flood control, domestic water supply, and navigation (Kummu and Sarkkula, 2008; Hecht et al., 2019; Morovati et al., 2023). Currently, 283 hydropower dams with capacities greater than 15 megawatts or reservoirs larger than 0.5 km^2 have been identified as either in operation or under construction (WLE Greater Mekong, 2016). These constructions are altering the hydraulic regime of the lower Mekong River. For instance, hydropower dam resulting in increased water flow during the dry season and reduced flood peaks during the wet season (Lauri et al., 2012; Hecht et al., 2019). Comparing the baseline period (1982–1992) to the projected period (2032–2042) with the planned dams, water discharge at Kratie is anticipated to be 25–160 % higher during the dry season and 5–24 % lower during flood peaks (Lauri et al., 2012). The combined with the impact of upstream dams, infrastructure development in the Mekong basin is also affecting the flood pulse from the Mekong River into the TSL and altering the hydraulic regime in the MD (Cochrane et al., 2014; Arias et al., 2014; Hecht et al., 2019; Morovati et al., 2023). For instance, there has been a 36.2 % decline in the average annual reverse flow from the Mekong River to the TSL, decreasing from 49.7 billion m^3 during the period 1962-1972 to 31.7 billion m^3 during the period 2010-2018 (Chua et al., 2022).

Additionally, hydropower dams have a well-documented effect on the sediment flux through the basin, with the suspended sediment flux in the Lower Mekong River projected to drop from 99 Mt yr^{-1} (in 1980-2009) to 43 Mt yr^{-1} by 2020-2029, a 57 % decrease (Bussi et al., 2021). If all planned dams in the Mekong basin are constructed, a sediment load reduction could be up to 96% (Kondolf, et al., 2014). Sediment deficits are further exacerbated by the escalating rates of sand mining in the channels of the lower Mekong River and its delta. In 2020 sand extraction was calculated at 59 Mt in Cambodia alone (Hackney et al., 2021), compared to the 32 Mt for the same stretch of the Mekong in 2011 (Bravard et al., 2013). Meanwhile, a volume of 42 Mm^3 yr^{-1} (around 67.2 Mt yr^{-1}) for sand mining over the period from 2015 to 2020 in the VMD (Gruel et al., 2022). Sand extraction typically exceeds the total amount of sand influx to the Lower Mekong which has been suggested to be as little as 6.18 ± 2.01 Mt yr^{-1} (Hackney et al., 2020). The combined resulting sediment deficit has led to substantial riverbed lowering rates, with a median lowering rate of 0.26 m yr^{-1} observed for the 2013-2019 period in Cambodia (Hackney et al., 2021) and a mean lowering rate of 0.16 m yr^{-1} observed in VMD for the 2008-2018 period (Vasilopoulos et al., 2021). Looking ahead, with the mounting pressures of population growth and urbanization, the demand for energy, water supply, and construction sand is expected to continue rising. Consequently, the anticipated increase in the lowering of the riverbed in the mainstream Mekong River is expected to intensify in the future. Such channel deepening has caused an extension of the tidal limit landward (Vasilopoulos et al., 2021), linked to salt-water intrusion (Eslami et al., 2019), and also triggers riverbank instability (Hackney et al., 2020) and coastal zone erosion (Anthony et al., 2015; Tu et al., 2019).

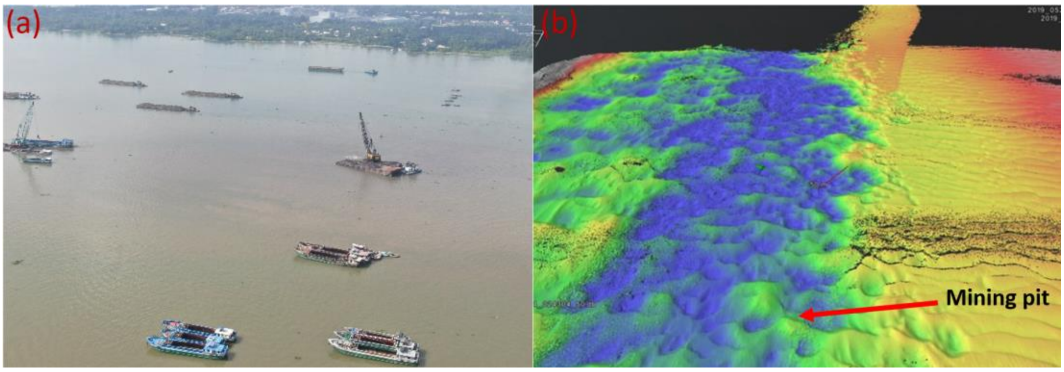

Figure 2-7. (a) Sand mining operations in the VMD, 10 km upstream from the My Thuan gauging station (see figure 3.1, Chapter 3), (b) the noticeable existence of mining pits, at coordinates 10.809, 105.284 in upper VMD, is a result of sand mining activities as measured by a Multibeam Echo Sounder in 2019 (Vasilopoulos, G., personal communication).

Furthermore, the MD is confronted with the issue of land subsidence, occurring at an average rate of 11 mm yr^{-1}, primarily attributed to groundwater extraction (Minderhoud et al., 2017). If the current rates of ground water extraction in the delta are not effectively addressed, delta subsidence is projected to surpass 1 m by 2100 (Minderhoud et al., 2020) effectively doubling challenges associated with eustatic SLR which for the region is projected to be of similar magnitude. This related SLR (combined SLR and land subsidence) would lead to the inundation of approximately 90% of the delta area, impacting 17 million people and resulting in an annual agricultural loss of 3.2 billion US dollars (Kondolf et al., 2022).

While the Cambodian floodplain (Lower Mekong River and Cambodian Mekong delta) remains relatively natural (Manh et al., 2014; Horton et al., 2022), the dykes in the VMD were primarily constructed after the devastating flood of 2000 to prevent floodwaters from entering the floodplain and to enable continuous cultivation during the flood season (Fujihara et al., 2016; Triet et al., 2017). The introduction of high dykes was said to benefit the population by providing safety and increasing farmers' income (Triet et al., 2017). However, the construction of dykes has disrupted the connection between the floodplain and channels, preventing floodplain inundation and reducing the sediment and nutrient levels in fields, which serve as natural fertilizers for paddy fields (Käkönen, 2008; Hung, 2011). This channel-floodplain disconnection has led to decreased crop yields (Manh et al., 2014), resulting in increased reliance on agrochemicals and higher production costs. Moreover, the separation between the floodplain and channels has led to additional social and environmental problems, including water pollution, increased stress and exhaustion for farmers due to the absence of a "resting period," and more severe damage during extreme events that result in dyke breaches and flooding of the third summer crops (Käkönen, 2008). Furthermore, dyke systems have contributed to higher maximum water levels in downstream areas, potentially exacerbating flooding in downstream VMD regions (Triet et al., 2017).

2.4 Numerical Modelling

Given the complex nature of deltaic change and the drivers outlined earlier in the present Chapter, coupled with the large number of people living on deltas, there is an increasing demand for accurate forecasts of water and sediment -related challenges within deltaic areas. Such forecasts can be accomplished through the utilization of sophisticated numerical models (Chow, 1959; Edmonds, 2009; Novak et al., 2010). Over the past few decades, there has been a remarkable expansion in numerical modelling of rivers and deltas, primarily driven by the progress made in computational technology (Olsen, 2012; Nicholas et al., 2012). Numerical modelling has become a widespread tool in water related research, with numerous software programs developed over time. Some of these programs have gained considerable popularity in the global scientific community, such as Delft3D, MIKE, HEC-RAS, CAESAR-Lisflood (see details in Table 2-2). These modelling software predominantly seek to simulate the movement of water, often referred to as the hydraulic numerical module, and sediment through a model domain (Toombes and Chanson, 2011; Nicholas, 2013; Qian et al., 2016). The forthcoming subsections will elucidate the underlying theoretical foundation that governs the simulations of these physical processes within numerical models.

2.4.1 Numerical Modelling of Open Channel Hydrodynamics

Fluid motion is governed by the conservation of mass and momentum, which can be described by equations (3-6) also known as the Navier-Stokes equations. Specifically, the conservation of mass is given by

$$\frac{\partial V_x}{\partial x} + \frac{\partial V_y}{\partial y} + \frac{\partial V_z}{\partial z} = 0 \qquad (3)$$

where V_x, V_y , V_z are velocity components in the x, y and z direction, respectively, and the momentum conservation in the three-dimensional space is given by

$$\left(\frac{\partial}{\partial t}(\rho V_x) + \frac{\partial}{\partial x}(\rho V_x^2) + \frac{\partial}{\partial y}(\rho V_x V_y) + \frac{\partial}{\partial z}(\rho V_x V_z)\right) - 2\rho V_x \zeta \sin \Phi + \frac{\partial p}{\partial x} - \frac{\partial \tau_{xx}}{\partial x} - \frac{\partial \tau_{xy}}{\partial y} - \frac{\partial \tau_{xz}}{\partial z} = 0 \qquad (4)$$

$$\left(\frac{\partial}{\partial t}(\rho V_y) + \frac{\partial}{\partial x}(\rho V_x V_y) + \frac{\partial}{\partial y}(\rho V_y^2) + \frac{\partial}{\partial z}(\rho V_y V_z)\right) - 2\rho V_y \zeta \sin \Phi + \frac{\partial p}{\partial y} - \frac{\partial \tau_{xy}}{\partial x} - \frac{\partial \tau_{yy}}{\partial y} - \frac{\partial \tau_{yz}}{\partial z} = 0 \qquad (5)$$

$$\left(\frac{\partial}{\partial t}(\rho V_z) + \frac{\partial}{\partial x}(\rho V_x V_z) + \frac{\partial}{\partial y}(\rho V_y V_z) + \frac{\partial}{\partial z}(\rho V_z^2)\right) + \rho g + \frac{\partial p}{\partial z} - \frac{\partial \tau_{xz}}{\partial x} - \frac{\partial \tau_{yz}}{\partial y} - \frac{\partial \tau_{zz}}{\partial z} = 0 \qquad (6)$$

where ρ is the water density, ζ is the angular rotation of the earth, Φ is the latitude, p is pressure, g is the acceleration of gravity. τ_{xx}, τ_{xy}, τ_{xz}, τ_{yy}, τ_{yz}, τ_{zz}, are the components of the stress tensor in the x, y, z dimension, respectively.

The Navier-Stokes equations mentioned above cannot be solved analytically, instead they are typically solved iteratively. To reduce model complexity and computational requirements simplifying approximations are often introduced. These include spatial averaging in fewer dimensions, steady flow assumptions (where flow does not vary over time), or neglecting certain fluid properties that would have a minor effect (e.g. assuming a constant fluid density, temperature and viscosity). These simplifications allow for the development of generic formulas that describe specific flow properties (Toombes and Chanson, 2011).

Hydrodynamic numerical models use variations of the Equations (3-6) introduced above to simulate open channel flow. These models can be categorized based on the number of dimensions employed to represent fluid motion. One-dimensional models (1D) are confined to considering flow in a single dimension, usually along a conduit or channel. Two-dimensional models (2D) simulate flow in two dimensions, typically by depth-averaging. Three-dimensional models (3D) simulate flow in all three dimensions. Increasing the number of dimensions in these models improves model detail but also increases the computational requirements to solve the more complex equations. As such model selection depends on strengths and limitations associated with each model type, as well as the nature of the problem under examination and the availability of computational resources (Hunter et al., 2007; Olsen, 2012).

In the context of 1D modelling, the underlying assumption is that fluid movement takes place solely in a single direction (e.g. up or down stream). In these models, the depiction of the channel's physical structure is achieved by employing a sequence of fixed cross-sectional profiles (Toombes and Chanson, 2011). This depiction makes 1D models less complex than their multi-dimensional counterparts and suitable for situations where flow behaviour predominantly occurs in one direction (Olsen, 2012). The strength of 1D models lies on their reduced computational requirements which allows the representation of expansive and often complex channel networks (Benjankar, 2009; Dung et al., 2011; Betsholtz, 2017). 2D modelling methodologies are useful in applications where fluid motion on the lateral dimension is also important, especially when considering overbank floodplain flow (Horritt and Bates, 2002; Edmonds 2009; Benjankar et al., 2014). 2D models utilise the depth averaged approximation of the Navier-Stokes Equations. This approach assumes that the vertical length scale is considerably smaller than the horizontal length scale (Lane, 1998), which is often true as for example in large rivers. However, the depth-averaging employed in 2D models can limit their applicability in certain scenarios, such as those involving hydrostatic pressure, viscous shear stresses and bed friction (Toombes and Chanson, 2011; Lane, 1998). 3D models are not constrained by such limitations as they solve the Navier-Stokes equations across all three spatial dimensions but this incurs an increased computational expense, which hinders their application to large model domains and/or long durations of simulation (Mackey and Bridge, 1995; Olsen, 2012).

2.4.2 Numerical Modelling of Sediment transport

In geomorphological numerical modelling, sediment transport and hydrodynamic models interact closely in a feedback system. The movement of sediment, influenced by the hydrodynamics, changes the domain morphology which in turn alters the hydrodynamics (Dade and Friend, 1998; Bridge and Best, 1988). Sediment transport is usually calculated according to two different processes, namely bed load and suspended load transport (Einstein, 1950; Engelund, 1967; Rijn, 1984a). In general, the distinction between bed load transport and suspended load transport is based on the movement of sediment particles, which is primarily governed by particle size and the flow conditions (Engelund and Fredsoe, 1976; Rijn, 1984a; Rijn, 1984b). Bed load transport involves the rolling and sliding of bed material, such as sand and gravel, along the streambed (Meyer-Peter and Müller, 1948; Rijn 1984a), whereas suspended load transport involves sediment particles (i.e. sand, silt and clay) being carried by the fluid for a period of time before settling (Rijn, 1984b; Church, 2006). Bedload is typically defined as bed material with grain diameters larger than 63 µm, while suspended load generally includes silt, clay and bed material with grain diameters smaller than 63 µm (Engelund and Hansen, 1967; Rijn, 2013). Figure 2.2 illustrates these sediment transport categories.

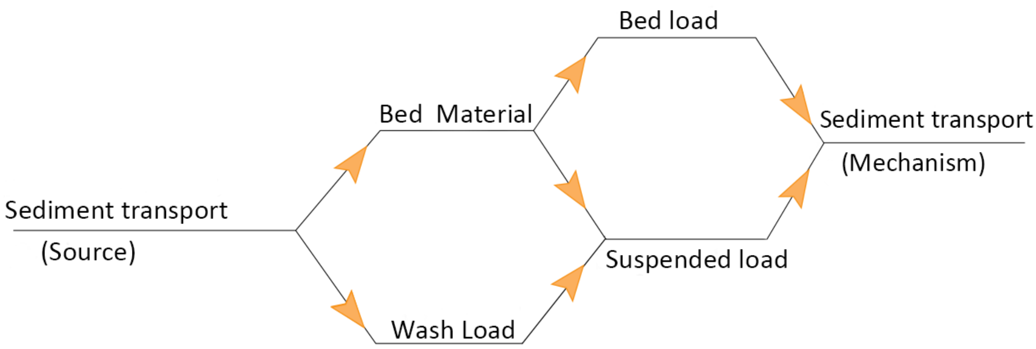

Figure 2-8. The classification of sediment transport modified from Jansen et al., (1979)

Estimating the amount and properties of sediment that a specific flow can transport has been a major focus of scientific research. Over the years, many sediment transport models have been introduced, including those by Meyer-Peter and Müller, (1948); Einstein, (1950); Bagnold, (1960); Yalin, (1963); Colby, (1964) Engelund and Hansen, (1967); Shen, (1970); Ackers and White, (1973); Engelund and Fredsøe, (1976); Yang, (1984); Rijn, (1984a, 1984b). Among these sediment transport theories, the most widely used and applied in numerical modelling include those by Meyer-Peter and Müller, (1948); Engelund and Hansen, (1967); Rijn, (1984a, 1984b); and Engelund and Fredsøe, (1976). The following paragraph will briefly discuss the advantages and disadvantages of these sediment transport equations and their applications in natural channels.

Meyer-Peter and Müller, (1948) developed an empirical equation to predict bed load transport in natural streams by correlating sediment discharge with shear stress. Their equation is based on flume experiments with non-uniform sand grains ranging from 0.4 mm to 30 mm. The calibration data for the Meyer-Peter and Müller formula primarily came from flows with minimal or no suspended load. The application of this formula to flows with minimal or no suspended load and sediment diameters larger than 2.0 mm (Habibi, 1994; Stevens and Yang 1989)

Engelund and Hansen, (1967) employed a correlation between the sediment discharge rate and the stream power. The sediment transport is influenced by parameters such as mean flow velocity, water surface slope, hydraulic radius, median diameter, and relative density of sediment particles (Engelund and Hansen, 1967). However, the research did not confirm their method for situations where the median size of the bed material is less than 0.15 mm, as this could considerably alter the velocity distribution. Additionally, for highly graded sediments containing unusually high proportions of finer fractions, the actual sediment discharge appears to be substantially greater than predicted, especially for low sediment transport rates (Engelund and Hansen, 1967). Stevens and Yang, (1989) recommended that the Engelund and Hansen, (1967) formula is best suited for streams with sandy beds and subcritical flow conditions.

Engelund and Fredsøe, (1976) established bed load transport through experiments focusing on the motion and transport velocities of individual particles along the bed. This approach was applied to simulate both bed load transport and suspended load in straight alluvial rivers. The model is assumed have two advantages that it is grounded in a description of physical processes and it provides insights into the quantity and size of sand particles in suspension as well as bed particles (Engelund and Fredsøe, 1976).

Rijn, (1984a) developed a bed load transport equation by combining the saltation height, the velocity of bed load particles, and the concentration of sediment materials in the bed layer. Rijn, (1984b) estimating suspended load by integrated the depth of the product of vertical velocity profiles and sediment concentration. These equations were calibrated with data from various natural rivers and laboratory flumes to enhance the accuracy and predictability of the proposed equations. However, it has been demonstrated that the calculation of bed and suspended loads is limited to a specific range of sediment grain sizes in natural streams. Specifically, Rijn, (1984a) proposed that the expressions for bed load concentration and transport rate are suitable for sand grains with diameters ranging from 0.2 mm to 2.0 mm, while Rijn, (1984b) expression for suspended load is applicable to sediment particles within the range of 0.1 mm to 0.5 mm.

These sediment transport formulas mentioned above have undergone extensive testing in laboratory settings and have been applied in natural river environments. However, the results have varied, influenced by the specific conditions of each river. The present paragraph will elaborate on this variability. White et al., (1973) examined sediment transport models using approximately 1000 flume experiments and field data collected from 11 diverse fluvial river sites across America and Europe. These river sites encompassed sediment sizes ranging from 0.04 mm to 4.94 mm and relative densities (sediment and water) ranging from 1.07 to 2.65. The results showed that the equation derived from Meyer-Peter and Müller, (1948) aligns well with observations for fine sediments but less so for coarse sediments. The equation proposed by

Engelund and Hansen, (1967) demonstrated consistent performance across the entire spectrum of sediment sizes and densities. Nonetheless, Engelund and Hansen's theory is most reliable in situations where viscosity exerts minimal influence, albeit it tends to overestimate transport rates when sediment transport rates are low. Fattah et al., (2004) tested different sediment transport theories using observed sediment transport loads at four sites in the Nile River in Egypt, from Aswan to Cairo. The results suggest that the Rijn, (1984a) formulas provided the best fit among them. Haddadchi et al., (2013) evaluated the effectiveness of various bed load sediment transport equations by comparing field data with predicted data in the Narmab river, Iran, by considering two types of grain sizes: bed load (mean d_{50} = 2.11 mm) and bed material (mean d_{50} = 18 mm). Their findings indicated that the Meyer-Peter and Müller, (1948) equations provided the best results for bed load, while the Engelund and Hansen, (1967) and Rijn, (1984a) equations performed well for bed material. Macedo et al., (2017) tested different sediment transport theories, including Rijn, (1984a); Meyer-Peter and Müller, (1948) and Bagnold, (1960) bedload transport, applied to the alluvial Paraná River, South America. Among the three formulas, the Rijn, (1984a) calculation was the closest to the measured sediment transport load, with a ratio difference (ratio of computed to measured sediment transport rate) of only 1.65 times. In comparison, the Meyer-Peter and Müller, (1948) formula showed a difference of 2.48 times. Olaniyan et al., (2020) emphasized that Meyer-Peter and Müller, (1948) equation yielded satisfactory outcomes when compared with observed sediment transport data from the River Osun in Southwestern Nigeria. The summarized findings of research utilizing these sediment transport equations and applied across various river environments are presented in Table 2-1.

Table 2-1. The application of different sediment transport theories across various river environments, with the checkmark (✓) indicating the most accurate alignment between predicted outcomes and observed results.

No	River/ Formulas	Meyer-Peter and Müller, (1948);	Engelund and Hansen, (1967)	Engelund and Fredsøe, (1976).	Rijn, (1984a, 1984 b)	Study
1	11 rivers in America, and Europe	✓	✓			White et al., (1973)
2	5 alluvial rivers, Western Jutland			✓		Thomsen (1982)
3	Sacramento River, USA		✓			Nakato, (1990)
4	5 rivers, Bangladesh		✓			Hossain and Rahman, (1998)
5	Nile River, Egypt				✓	Fattah et al., (2004)
6	Fraser River, British Columbia	✓				Martin and Ham, (2005)
7	Kulim River, Malaysia		✓			Chang et al. (2008)
8	Narmab River, Iran	✓	✓		✓	Haddadchi et al., (2013)
9	Karun River, Iran		✓			Najafpour et al., (2016)
10	Flume experiment				✓	Prajapati et al., (2016)
11	Paraná River, South America				✓	Macedo et al., (2017)
12	Omi River, Nigeria		✓			Olaniyan and Adegbola, (2018)
13	River Osun, Southwestern Nigeria	✓				Olaniyan et al., 2020)
14	Euphrates River in Iraq		✓			Sulaiman et al., (2021)

The results from Table 2-1 demonstrates that each mathematical model is suited to specific river conditions, making it challenging to determine which sediment transport formula performs best overall. Sediment-discharge rates are influenced by various factors, including flow velocity, energy slope, water temperature, the size, gradation, shape of bed material and suspended-sediment particles (Stevens and Yang, 1989) and other factors include channel geometry and pattern, the extent of bed surface covered by coarse material, the rate of fine material supply, and bed configuration (Stevens and Yang, 1989). Additionally, large-scale variables such as hydrologic, geologic, and climatic conditions impact sediment transport rates. Due to the wide range and number of variables, it is not feasible to select a single sediment transport formula that satisfactorily addresses all the conditions an investigator might encounter, as each formula is suited to specific conditions (Stevens and Yang, 1989; Gomez and Church, 1989; Macedo et al., 2017). The potential accuracy of a formula can be evaluated by examining the similarity between the experimental conditions used to develop its parameters and their relevance to real field conditions, as well as through direct comparison with field measurements (Stevens and Yang, 1989). Hence, there is a requirement for comprehensive, on-site measurements of sediment transport in natural streams to establish a more reliable foundation for model calibration (Thomsen, 1982).

2.4.3 Modelling software and their applications to river deltas

Diverse numerical modelling software tools have been developed and utilized to address issues associated with deltas, encompassing both open-source and commercial options. Examples include the MIKE, HEC-RAS, Delft3D, SOBEK, CAESAR-Lisflood modelling suite and additional software listed in Table 2-2.

Table 2-2. The well-known modelling suite for delta-related issues

No.	Software	The creator	Status	Applicable domain	Dimensions
1	Delft3D	Delft University of Technology, Netherlands	Open-source	Rivers, Delta, Estuaries, Coastal areas, and urban drainage systems.	1D, 2D, 3D
2	ADCIRC	United States Army Corps of Engineers, USA	Open-source	Rivers, Delta, Estuaries, Coastal areas	2D and 3D
3	CAESAR-Lisflood	Thomas J. Coulthard et al., Hull University, UK	Open-source	Rivers, Delta, Estuaries, Coastal areas	2D
4	MIKE	Danish Hydraulic Institute (DHI), Denmark	Commercial	Rivers, Delta, Estuaries, Coastal areas, and urban drainage systems.	1D, 2D, 3D and combined 1D-2D
5	HEC-RAS	US Army Corps of Engineers, US	Commercial	Rivers, Delta, Estuaries, Coastal areas, and urban drainage systems.	1D and 2D and combined 1D-2D
6	SOBEK	Deltares, Netherlands	Commercial	Rivers, Delta, Estuaries, Coastal areas, and urban drainage systems.	1D and 2D and combined 1D-2D
7	SWMM	United States Environmental Protection Agency (EPA), US	Commercial	Rivers, Delta, Estuaries, Coastal areas, and urban drainage systems.	1D and 2D
8	TELEMAC	National Laboratory of Hydraulics and Environment (LNHE), France	Commercial	Rivers, Delta, Estuaries, Coastal areas, and urban drainage systems.	2D and 3D

Numerical models are valuable tools for understanding delta evolution and response to different perturbations. They have been frequently used in various studies to address a range of delta-related issues, as discussed herein. Instances employing modelling to explore delta flooding include Lin et al., (2020), who utilized the FLUS model to evaluate flood risk in the Guangzhou Metropolitan Area within the Pearl River Delta. Their findings indicate that inundation is projected to increase by approximately 31.32 km² by 2030 and 48.49 km² by 2050 compared to 2015 condition, influenced by urbanization and climate change.

Rai et al., (2018) utilized a coupled SWAT-SWMM and IRIC hydraulic model effectively performing flood simulations for the Baitarani River delta. Samantaray et al. (2015) employed the MIKE FLOOD model to effectively generate flood hazard maps for the Mahanadi River Basin in Odisha, India. These maps, coupled with flood vulnerability data for different rice crops, were utilized to construct an optimal rice allocation. Triet et al., (2017) using the MIKE 1D model, highlighted that the functionality of the dyke system in the Mekong Delta has led to an increase in maximum water levels in downstream areas. Lyddon et al. (2024) used the Caesar-Lisflood model to study how flood extent responds to river discharge magnitude, tides, and surges in Conwy estuary, North Wales, UK. The results indicated considerable amplification in flood extent due to these combined factors. Additionally, a shift in the timing of peak river discharge relative to high tide with a 3-hour time lag (peak river discharge occurring 3 hours before high tide and coinciding with a rising tide that traps fresh water) resulted in 7.7% more flooding compared to a 0-hour time lag (Lyddon et al., 2024).

Examples utilizing modelling to investigate delta evolution include the research conducted by Edmonds et al., (2010), who used Delft3D model to examine the stability of delta bifurcations under disturbances caused by variations in upstream discharge. Their findings showed that the bifurcations consistently transitioned to a new stable configuration as long as the upstream water flux increased but remained below 60% of the initial magnitude. Beyond this threshold, the bifurcation system became unstable, resulting in the formation of a new channel. Nardin and Fagherazzi, (2012) used Delft3D to demonstrate that wave characteristics, such as height, period, and direction, control the formation of mouth bars in deltas. Sassi et al. (2011) using the SLIM model to demonstrated the tidal oscillations can equalize the net discharge ratio between the two downstream bifurcation channels, which stabilizing the delta bifurcation.

In addressing other challenges within river deltas Vasilopoulos et al., (2021) utilized the 2D hydrodynamic MIKE model to demonstrate that tidal extension into the Mekong delta could surge by up to 56 km due to the anticipated riverbed lowering within the next two decades. Zhu et al. (2016) used the EFDC model to demonstrate that the construction of navigation training works in the North Passage significantly impacted the hydrodynamics of the Changjiang Estuary in the Yangtze River Delta, resulting in an erosion trend in the estuary. Ysebaert et al., (2016) utilized the SOBEK model to simulate various management options for restoring estuarine dynamics in the Rhine-Meuse-Scheldt Delta. The study found that combining increased water flow from the basin with limited management of downstream sluice gates could partially aid in the recovery of the estuarine transition zone and improve fish migration routes. Manh et al., (2015) used a MIKE 11 model to study changes of sediment transport in the Mekong delta under various scenarios of hydropower development, climate change, deltaic subsidence and sea level rise, the results showed that floodplain sedimentation can be reduced between 40% and 90% for the various scenario combinations. Examples encompassing diverse modelling suites to investigate various delta issues are summarized in Table 2-3.

Table 2-3. Examples of research employing numerical modelling for deltaic challenges

Model software	**Objectives/location**	**Finding**	**Study**
Delft3D	Morphological changes in the channel-shoal complex in a mega Fluvial-Tidal Delta, Yangtze Delta	When the suspended sediment concentration (SSC) from the Changjiang River decreased due to the construction of the Three Gorges Dam—falling from 0.53 kg m^{-3} (1965–1988) to 0.35 kg m^{-3} (1989–2003), 0.16 kg^{-3} (2004–2013), and 0.12 kg m^{-3} (2014–2022). The net suspended sediment deposition in the area decreased by 3.13%, 7.35%, and 8.67%, respectively.	Wang et al., 2024)
Delft3D	Morphological changes in anthropogenically controlled estuaries, coastal Yellow Sea, China	The location of control gates is crucial in influencing siltation patterns. Long channels result in intense siltation, whereas short channels tend to support undisturbed sediment transport and are less prone to increased siltation.	Zhu et al., 2017)
MIKE 21 FM	Modelling the impact of typhoons on morphological changes in the Beinan Estuary, Taiwan	The morphology of the Beinan Estuary is mainly control by typhoon events, resulting in rapid processes of erosion, sediment transport, and deposition.	Huang, (2017)
MIKE 11	Applied hydrodynamic modelling in the data-poor countries with large flood-prone river system, India	The model is capable of representing the hydraulics in the study area and is useful for studying flooding in the region.	Patro et al., (2009

Model software	Objectives/location	Finding	Study
Caesar-Lisflood	Simulated the extreme flood in a Tonle Sap Lake, Mekong River	The extreme water level of 1% chance (100-year flood return period) exceeding the annual maximum water level at Prek Kdam station was approximately 11.38 m resulting in the largest inundation area of 15193 km^2 in the Lake basin areas.	Siev et al., (2020)
Caesar-Lisflood	Simulating tidal and storm surge in the Humber Estuary, UK	Successfully establishing modelling within the Humber Estuary has enabled the ability to accurately reproduce flood inundation extents in the study area.	Skinner et al., (2015)
TELEMAC and TOMAWAC	The Impact of seasonal climate on the morphology of the mouth-bar in the Yangtze Estuary, China	The stability of shallow shoal morphology in the estuary is closely linked to the seasonal presence of wind-driven waves. During summer, deposition prevails, while erosion dominates in winter. In contrast, deep channels act as conduits for water and sediment transport, facilitating sediment export throughout the year.	Zhang et al., (2018)
STREAM -2D	Flow Dynamics in the Tidal Delta of the Northern Dvina River.	Variations in roughness coefficients within delta channels and floodplains have minimal influence on delta flow dynamics. However, changes in tidal range during neap-spring cycles and shifts in mean sea level are considered highly considerable factors affecting delta flow dynamics.	Alabyan and Lebedeva, (2018)
SELFE	Study inundation in the Tsengwen River basin, southern Taiwan, under the influence of storm surge, fresh water discharge, and their combination	The combination of extreme storm surge and high upstream river discharges could worsen flood severity compared to individual drivers.	Chen and Liu, (2014)

Each modelling software possesses its unique strengths and limitations. The selection of a specific model depends on various factors, such as the capacity to simulate sediment transport, the research objectives related to scale, hydrological conditions, hydraulic patterns, and the topography of the study area (Wester et al., 2018). In the present study, the MIKE modelling suite (DHI, 2012) is utilized. Specifically, the 1D hydrodynamic numerical model MIKE 11 is employed in Chapters 5 and 6 to simulate water level and discharge through the Lower Mekong Basin considering a range of historical and Future scenarios. In Chapter 7, the 2D numerical model MIKE21 is used to develop a coupled hydrodynamic and sediment transport solution, calibrated against observations, and applied to the apex of the Mekong delta at the junction of Chaktomuk, Cambodia.

2.5 Chapter Summary

In the present Chapter, the fundamental principles and underlying theories of natural delta evolution have been reviewed, emphasizing three key factors that shape delta architecture namely upstream water and sediment input, tidal energy and wave dynamics. The conveyance of water and sediment across a river delta through channels and floodplains, via channel-floodplain connectivity, combined with the tidal energy and wave characteristics govern delta progradation and aggradation processes, the likelihood of avulsions and bifurcation dynamics. Aggradation and progradation processes serve as a natural defence against delta subsidence and rising sea levels. However, the factors driving deltaic evolution are rapidly changing, primarily due to anthropogenic disturbances resulting from significant population growth and accelerated economic development since the early twentieth century. These primary anthropogenic disturbances span a range of scales, from global (such as climate change-induced hydroclimatic shifts and sea level rise) to regional (including dam construction and land use change) to local (such as sand mining, underground water and oil/gas extraction, and infrastructure development) and have had substantial impacts on delta evolution and the communities residing within them.

The Lower Mekong Basin extends from upstream at Kratie to the South China Sea in VMD, is an exemplar of river deltas system affected by human-induced disruptions and serves as a central focus in the present study. Over the past century, sediment deficits caused by sand mining and sediment starvation due to upstream damming have become the main factors behind the degradation of the Mekong delta. This problem is anticipated to worsen in the near future due to the increased demand for sand, hydropower, and irrigation, driven by population growth and economic development. These trends, along with changes in upstream hydroclimate variability and rising sea levels at the delta front, can alter delta functions and impact future sustainability. Although many studies have examined delta-related issues, there remains a noticeable gap in quantifying the impacts of human-induced riverbed lowering, upstream water flux variation and the concurrent rise in sea levels at delta fronts on hydraulic dynamics, water-level dynamics, and sediment transport capacity within deltas. In this study, 1D hydraulic modelling will be used to simulate various scenarios of ongoing and future riverbed lowering, along with changes in upstream water flux and anticipated sea level rise at the delta front. These simulations aim to assess the impacts on the flood pulse in Tonle Sap Lake (TSL), the hydraulic connection between the river and its floodplain, water level patterns throughout the Lower Mekong Basin (LMB). Additionally, a 2D coupled hydrodynamic and sediment transport numerical model will be employed for the apex of the Mekong Delta to evaluate how riverbed lowering and upstream water flux affect sand transport capacity. Understanding these dynamics and developing predictive capabilities are essential for anticipating unforeseen hazards concerning the delta's future sustainability and its ability to adapt to ongoing and future in riverbed levels, sea level rise, and climate change.

Chapter 3. Materials

In the previous chapter, the fundamental principles and underlying theories of natural delta evolution were discussed, emphasizing how the factors driving deltaic evolution are rapidly shifting, mainly due to anthropogenic disturbances. The Lower Mekong Basing (LMB), extending from Kratie to the South China Sea is the VMD, serves as a prime example of river delta systems affected by human-induced disruptions and is the central focus of the modelling work presented in this PhD thesis. In the present Chapter, a range of already existing data sets that describe the hydrological records and channel bathymetries utilized in the models developed is provided. Specifically, these data are utilized as follows: (1) The historical hydrological records, including water level and discharge measurements, particularly from various gauging stations within the Vietnamese Mekong Delta (VMD) (taken from the Southern Institute of Water Resources Research (SIWRR)), are utilized to achieve the first objective (O1) of the study. This objective focuses on assessing historical changes in the delta's flow dynamics caused by channel bed level lowering by addresses the first research question (RQ1): How has historical riverbed lowering affected delta hydraulics*?* The detailed analysis of this objective is presented in Chapter 4; (2) The historical water discharge and water level records across the entire Lower Mekong Basin (LMB), combined with large-scale mainstream bathymetry data (taken from Mekong River Commission (MRC), Vasilopoulos et al., (2021) and Hackney et al., (2021)), are used to set up, calibrate, and validate a one-dimensional (1D) numerical model covering the entire LMB. These data also underpin the development of 1D model scenarios, including variations in upstream water flux, riverbed lowering, and downstream sea-level rise (detailed in Chapter 5, Sections 5.1 and 5.2). This work contributes to Objective 2: understanding the evolution of the hydraulic regime in the delta under projected future riverbed lowering and sea-level rise. It addresses two specific research questions: (RQ.2) How will hydraulics in the LMB change in the future due to projected riverbed lowering and sea-level rise? and (RQ.3) How will the connection to the Tonle Sap Lake be affected by projected riverbed lowering and sea-level rise?; (3) The velocity data, combined with high-resolution bathymetry for the Chaktomuk Junction (Delta apex) (taken from Hackney et al., (2020)), are used to set up, calibrate, and validate a two-dimensional (2D) numerical model. This is driven by the fact that a 2D model requires more precise bathymetric details across all four channels at Chaktomuk Junction (Lower Mekong River, Tonle Sap River, and the Mekong and Bassac channels downstream) to accurately simulate water partitioning and sand transport between the channels. This level of detail cannot be achieved using the lower-resolution data from SBES. This 2D model is employed to address the final objective (O3) of the study: quantifying changes in the delta's sand transport capacity resulting from riverbed lowering. This work specifically aims to answer the final research question (RQ.4): What are the consequences of riverbed lowering on the sand transport capacity at the apex of the Mekong Delta?

Section 3.1 will introduce the archive of water level and flow discharge measurements collected at a range of locations that cover the LMB, which include the Lower Mekong River (LMR), the Tonle Sap River (TSR) and Lake system and the Mekong delta (MD) as well as flow velocity data for the Chaktomuk Junction (Figure 3-1). Section 3.2 will introduce datasets collected through hydrographic surveys, adopted from the literature, that describe channel bed elevations across the study area, obtained at different times and with various resolutions. Finally, Section 3.3 will discuss the quality and effectiveness of the datasets presented and address uncertainties.

3.1 Hydrological data

3.1.1 Historical water discharge and water level data

Data on flow, discharge and water level have been recorded regularly at a range of locations (Figure 3-1) across the main channels of the study area, and for long durations, in some cases starting from the early 1930's, However, the useful and consistent time series data for both water discharge and water level for all stations are from 2000 to 2021, synchronized with the adopted bathymetry data (presented in the following paragraphs). Despite the longevity of these records there are some variations in meta-data and resolution that requires addressing before these datasets, the details of which are presented in Table 3-1, can be effectively employed within the modelling frameworks developed in this thesis. For example, the water level time series data has variable temporal resolutions, with only daily or twice per day data available in Cambodian gauges compared to higher resolution hourly data in VMD gauges, and these water levels are referenced to different vertical datums (Table 3-1). The approaches used to standardise these datasets are described herein.

Data from the Cambodian gauges (Table 3-1) were obtained from the Mekong River Commission (MRC: https://portal.mrcmekong.org/). They include mean daily water flow discharge (m^3 s^{-1}) measured at Katie and mean daily water levels (m) measured at the remaining eight gauges (Figure 3-1 and Table 3-1). The daily water level measurements are manually recorded from gauges, with staff readings taken once per day before 2006, and twice per day for all Cambodian gauge stations starting from 2006. These water level measurements are referenced to a local vertical datum that is unique for each gauge location (MRC, 2023). To synchronize the water level dataset, the daily water level data from 2006 onwards is obtained by averaging the twice-daily readings from all Cambodian gauges. In addition, to align these water level records to a single datum, a conversion to the MRC's chosen vertical datum, Ha Tien Mean Sea Level (MSL), was applied by adding the offset between the local vertical datum at each gauge and the Ha Tien MSL (See MRC, 2023 and Appendix, Table. 1). In the final step, in order to align the water level recordings measured in Cambodian gauges with those measured in VMD gauges that will be introduced below, the water level measurements from Cambodian gauges are further converted from the Ha Tien MSL to the national vertical datum used in Viet Nam (Hon Dau MSL) by subtracting 0.167 m from each recording, that is the vertical offset between Ha Tien MSL and Hon Dau MSL (TCVN: 8478, 2010).

The daily water discharge at Kratie gauge is derived from a rating curve (stage-discharge relationship) based on the daily water level at Kratie gauge, which is referenced to the Ha Tien MSL vertical datum (MRC, 2004).

In the VMD, water levels in the mainstream Mekong and Bassac channels, Mekong coastal zone, and water discharge data are recorded at hourly intervals (Table 3-1, Figure 3-1). Prior to 2005, hourly water levels at these stations were manually recorded by staffs using measuring rules placed at each station along the river or coast. Later, beginning in 2005 (exact date unspecified), automatic sensors were employed for monitoring water levels referenced to the Hon Dau Mean Sea Level (MSL) vertical datum.

Hourly flow discharge is measured at four gauges (Tan Chau and My Thuan on the Mekong and Chau Doc and Can Tho on the Bassac) using both the Current Meters Method and Acoustic Doppler Current Profilers (ADCP). In more detail, since 1996 up to the present, the Current Meter Method has been used to manually measure water velocity, with staff recording data based on propeller rotations. The Five-Point method was used for measuring water velocity, involving measurements at 0.0, 0.2, 0.6, and 0.8 times the depth from the surface, and 0.2 m above the riverbed, at an only fixed representative vertical location within the measured cross-section to calculate the average velocity along the representative vertical. Alongside detailed measurements taken at least four times a year across multiple verticals of the entire measured cross-section (the number of verticals is unspecified) to calculated the average velocity for the entire measured cross-section. The relationships were established between the velocity at representative vertical and the average velocity for the entire measured cross-section. Water discharge is calculated by multiplying the average velocity of the measured cross-section by its wetted area. The wetted areas are determined based on the corresponding water level and the riverbed elevation, which is updated at least twice a year. Later, starting from 2005 (exact date unspecified), the Acoustic Doppler Current Profiler (ADCP) was used in parallel with the Current Meters Method to update and verify each other's data. The RDI Teledyne RioGrande 600kHz, combined with an RTK differential-GPS unit (dGPS), is used to measure water discharge at these stations. However, due to budget for each year, the ADCP is typically used only for a few months during the flood or dry seasons each year. The exact date of ADCP implementation for each year is not specified. The available water discharge data at these gauges have been obtained using both the Current Meters Method and ADCP Method. These water level and discharge gauges are operated by the Southern Regional Hydro-Meteorological Centre (SRHMC) and have been provided by the Southern Institute of Water Resources Research (SIWRR). It is also noteworthy that although the water level and water discharge data in the Vietnamese Mekong Delta are managed by SRHMC, this data is also shared and used by both SRHMC and MRC. Therefore, the water level and water discharge datasets described above are considered a consistent data source for the entire Lower Mekong River, Tonle Sap Lake system and MD.

Table 3-1. Information on gauge stations and data availability

No	Gauges (code)	Latitude (^{0}N)	Longitude (^{0}E)	Available data period		Resolution	Channel	Region
				Discharge	Water level			
1	Kraite (KH_014901)	12.481	106.018	2000-2021		Daily/ twice per day	Mekong River	Cambodia
2	Kompong Cham (KH_019802)	11.909	105.338		1930-2021	Daily/ twice per day	Mekong River	Cambodia
3	Chroy Chang Var KH_019801	11.58	105.939		1960-2022	Daily/ twice per day	Mekong River	Cambodia
4	Chaktomuk (KH_033401)	11.563	104.935		1960-2021	Daily/ twice per day	Mekong River	Cambodia
5	Prek Kdam (KH_020102)	11.811	104.807		1960-2021	Daily/ twice per day	Tonle Sap	Cambodia
6	Kompong Luong (KH_020106)	12.577	104.207		1998-2021	Daily/ twice per day	Tonle Sap	Cambodia
7	Neak Luong (KH_019806)	11.261	105.284		1926-2023	Daily/ twice per day	Mekong	Cambodia
8	Koh Khel (KH_033402)	11.242	105.036		1990-2023	Daily/ twice per day	Bassac	Cambodia
9	Tan Chau (TC)	10.801	105.248	1996-2021	1996-2021	Hourly	Mekong	VMD
10	My Thuan (MT)	10.275	105.926	2000-2021	2000-2021	Hourly	Mekong	VMD
11	Chau Doc (CD)	10.705	105.134	1996-2021	1996-2021	Hourly	Bassac	VMD
12	Can Tho (CT)	10.053	105.787	2000-2021	2000-2021	Hourly	Bassac	VMD
13	Vung Tau (VT)	10.34	107.071		1996-2021	Hourly	Coastal Mekong	VMD

No	Gauges (code)	Latitude (^{0}N)	Longitude (^{0}E)	Available data period		Resolution	Channel	Region
				Discharge	Water level			
14	Vam Kenh (VK)	10.274	106.737		1996-2021	Hourly	Coastal Mekong	VMD
15	Binh Dai	10.197	106.711		1996-2021	Hourly	Coastal Mekong	VMD
16	An Thuan	9.967	106.605		1996-2021	Hourly	Coastal Mekong	VMD
17	Ben Trai (BT)	9.861	106.533		2000-2021	Hourly	Coastal Mekong	VMD
18	My Thanh (MT)	9.425	106.171		1996-2021	Hourly	Coastal Mekong	VMD
19	Ganh Hao	9.031	105.42		1996-2021	Hourly	Coastal Mekong	VMD
20	Song Doc	9.037	104.831		1996-2021	Hourly	Coastal Mekong	VMD
21	Xeo Ro	9.887	105.083		1996-2021	Hourly	Coastal Mekong	VMD
22	Rach Gia	10.023	105.082		1996-2021	Hourly	Coastal Mekong	VMD

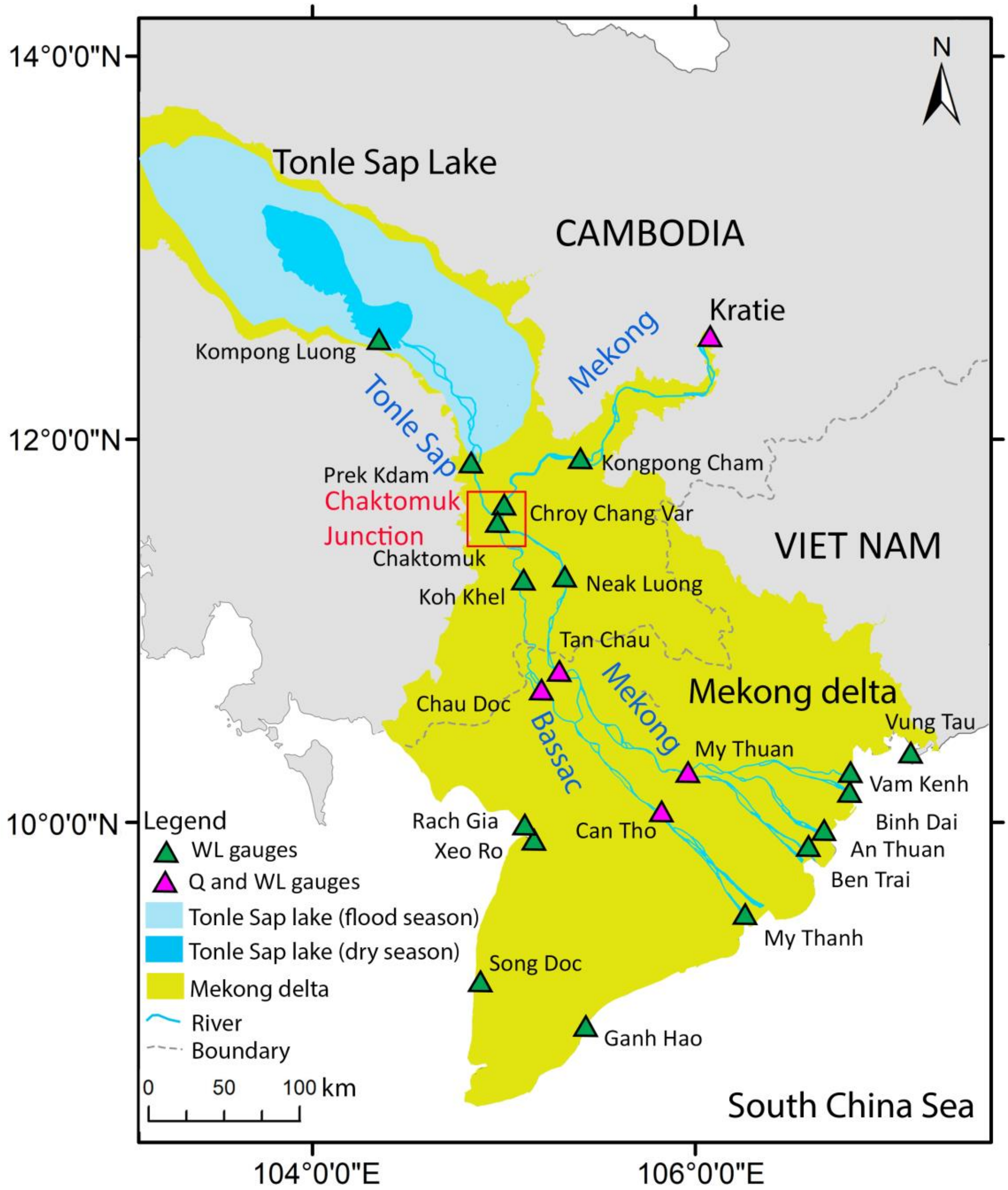

Figure 3-1. Map of the study area and the location of the hydrological gauging stations.

3.1.2 Flow velocity data

Three-dimensional velocity was surveyed at the apex of the delta (Chaktomuk, Figure 3-1), using an Acoustic Doppler Current Profiler (ADCP) (Figure 3-2). This dataset was provided by Christopher R. Hackney, Newcastle University (personal communication). Flow measurements were taken at five predetermined cross-sections, with the survey conducted twice, on 12 September 2013 and 27 October 2013 (Figure 3-2). Due to instrument availability and flow conditions at the time, two RDI Teledyne RioGrande 600kHz units and one RDI Teledyne

RioGrande 1200kHz unit were employed. At each cross-section, four repeat surveys were conducted to resolve the time-averaged flow field (Szupiany et al., 2007). Each ADCP unit was coupled with the same dGPS used in the Multibeam Echo Sounder (MBES) surveys to determine the position and velocity of the survey vessel. Boat speed and trajectory were continuously monitored during the survey to minimize associated errors (Szupiany et al., 2007). The transect ensemble was averaged using the Velocity Mapping Toolbox v4.08 (Parsons et al., 2013) which also estimates of a flow discharge value for each transect at a given time and also the decomposes the flow velocity field into its longitudinal (U_x) and Lateral (U_y) components, from the averaged flow data.

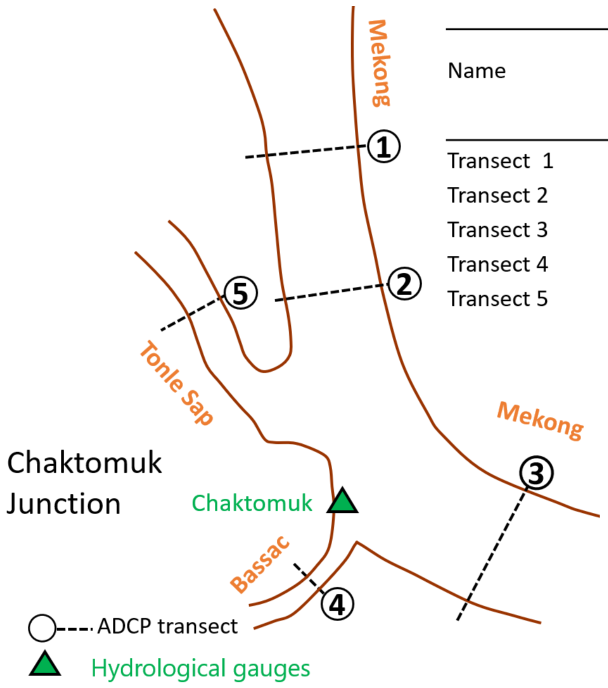

Name	Left bank		Right bank	
	Latitude (⁰N)	Longitude (⁰E)	Latitude (⁰N)	Longitude (⁰E)
Transect 1	11.592	104.947	11.592	104.938
Transect 2	11.572	104.950	11.571	104.941
Transect 3	11.554°	104.962	11.545	104.955
Transect 4	11.543	104.943	11.545	104.942
Transect 5	11.572	104.934	11.570	104.931

Figure 3-2. Map and coordinate locations of the ADCP transects

3.2 River bathymetric data

3.2.1 Large scale bathymetric data

Multiple bathymetric surveys have been undertaken in the region at different times, covering different parts of the Lower Mekong River and Delta. Here, surveys undertaken in 1998, 2013 and 2018 (Figure 3-3) were chosen to represent a 20 year period of bathymetric change that covers a period of observed increase in anthropogenic activity (hydropower expansion and sediment extraction) across the Lower Mekong Basin (Bravard et al., 2013; Hecht et al., 2019).

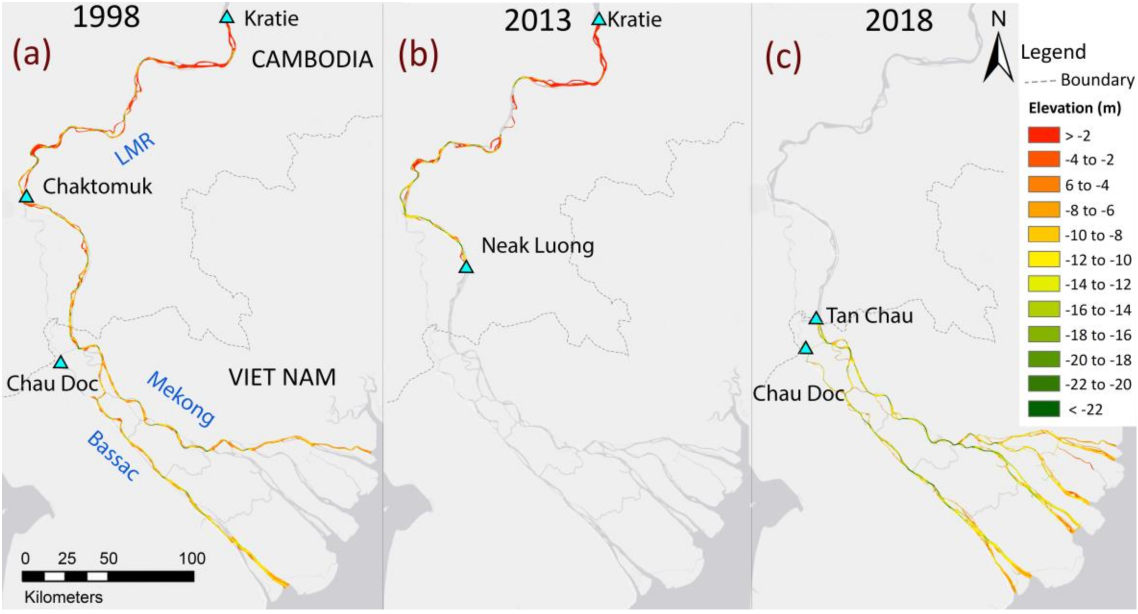

Figure 3-3. The bathymetric dataset utilized in this study for the LMR and MD covers the years 1998, 2013, and 2018. These datasets are referenced to the WGS84 coordinates and are aligned with the Hon Dau MSL vertical datum

Specifically, in 1998 an extensive bathymetric survey was undertaken that covered the Lower Mekong River from Kratie to the delta apex, the main Mekong channel seaward of the delta apex and the Bassac channel seaward of Chau Doc, spanning approximately 700 km in length (Figure 3-3, a). The riverbed depths were acquired using a bi-frequency echosounder, but specific characteristics of the echosounder were not further specified (Brunier et al., 2014). These data incorporate elevation measurements with a measurement uncertainty of ±0.2 m per 10 m, leading to an average vertical error of approximately 0.19 m (Brunier et al., 2014). These 1998 bathymetry data are provided from the Mekong River Commission (MRC, https://www.mrcmekong.org/) and consist of geographic coordinates in WGS1984 and elevations above the Ha Tien MSL. In this study, the Digital Elevation Models (DEM) bathymetry data with a resolution of 50 m for the VMD territory in 1998 were sourced from Vasilopoulos et al. (2021), while the DEM bathymetry data with the same resolution for the Cambodian part in 1998 were adopted from Hackney et al., (2021).

In September 2013, The Lower Mekong River and Mekong Channal in Cambodia, from Kratie to Neak Luong over approximately 275 km in length, was surveyed using a single-beam echo sounder (SBES) by Hackney et al., (2021) (Figure 3-3, b) . A Garmin Fishfinder was linked to a Trimble differential-GPS unit, which had a positional accuracy of ~0.4 m, and bathymetric data were recorded at a frequency of 1 Hz. Survey lines were arranged in a saw-tooth pattern, covering cross-sections of the channel at intervals of one channel width (Hackney et al., 2021).

The water slope between the two nearest gauges was computed for each hour, assuming a linear gradient along the river centerline. This water surface slope was applied to the water level readings of the nearest gauges, generating varying water levels for each survey date, which were subsequently used to convert water depths into channel bed elevations (Hackney et al., 2021). The bathymetry data are referenced to the Ha Tien MSL and using WGS1984 coordinates. Then, the elevation data were utilized to create a raster DEM at a resolution of 50 meters using a Kriging interpolant (Figure 3-3, b). Both of the 1998 and 2013 bathymetry datasets were converted from Ha Tien MSL to the Hon Dau MSL by subtracting the vertical offset between the two datums (0.167 m) (Figure 3-3, a and b).

Finally, in 2018, a survey of the VMD was conducted by Vasilopoulos et al., (2021), covering all major distributary channels between Tan Chau, Chau Doc, and the coast, with a total length of approximately 681 km (Figure 3-3, c). The survey was participated by myself, contributing to the data collection for this research. The survey employed two vessels equipped with identical single-beam echo-sounding (SBES) systems, each featuring a Garmin GT20-TM sonar transducer fully submerged below the water surface (~0.5 m) (Vasilopoulos et al., 2021). These systems were connected to a global positioning system (GPS). The sonar pulse frequencies ranged between 800 kHz and 455 kHz, with beam angles of 1.6° and 2.5°, respectively, depending on the depth of the channel below the water surface (Vasilopoulos et al., 2021). The depth data were recorded at a frequency of 1 Hz, while the vessel speed was maintained below 20 km h^{-1} to minimize air entrainment and data noise (Vasilopoulos et al., 2021). The reported mean vertical error for this dataset is 0.25 m. The depth recordings were converted into projected WGS1984 coordinates, and total water depth measurements were derived. These depths were then converted to riverbed elevations using hourly water level recordings from the Vietnamese hydrological agency's network of water level monitoring stations, referenced to the Hon Dau MSL. The elevation data were then used to generate a raster DEM with a 50-m resolution, employing a Kriging interpolation method (Vasilopoulos et al., 2021) (Figure 3-3, c).

Importantly, the stretch of main Mekong channel between Neak Luong and Tan Chau (50 km) was only surveyed in 1998, while the stretch of Bassac between the delta apex and Chau Doc has never been surveyed. These data gaps will be addressed later in Section 5.2.1, Chapter 5.

3.2.2 High resolution bathymetric data

In addition to the large-scale bathymetric surveys outlined above, High-resolution bathymetric surveys covering the area of the Chaktomuk Junction were undertaken by Hackney et al., (2020) using a Multibeam Echo Sounder (MBES). Surveys were undertaken on 12 September 2013, 27 October 2013 (Figure 3-5, a and b). A RESON SeaBat 7125 multibeam echo sounder operating at 400 kHz and forming 512 equal-angle beams across a 140° swath were employed (Hackney et al., 2020). A Leica 1230 differential global positioning system (dGPS) was used in real-time kinematic mode, providing positions at 1 Hz with an accuracy of ±0.02 m in the horizontal plane and ±0.03 m in the vertical plane. The dGPS was coupled with an Applanix POS MV WaveMaster inertial motion unit, providing real-time, three-dimensional (3D) motion and heading data correction at 100 Hz for the MBES. It also synchronized all survey data streams using the dGPS time stamp and a pulse-per-second signal (Hackney et al., 2020). After the survey, the MBES data underwent post-processing steps including calibration, correction for angular offsets, and adjustment for temporal variations in water-surface elevation using CARIS HIPS and SIPS software version 9. Additionally, extraneous data points within the water column (false targets) and secondary bed returns were manually eliminated prior to conducting 3D surface analysis in CloudCompare (https://www.danielgm.net/cc/) (Hackney et al., 2020). Identical survey methods, equipment, and post-processing techniques as described earlier were employed to cover the area of the Chaktomuk Junction in May 2022 (Figure 3-5, c). These three MBES bathymetric datasets (September 2013, November 2013, and May 2022) were then used to generate a raster DEM with a 0.5-m resolution, employing a Kriging interpolation method and referenced to the WGS1984 coordinate system. The channel bed elevations are referenced to the Earth Gravitational Model (EGM 2008).

However, the EGM2008 is a geoid, whereas the Hon Dau MSL is a flat datum, this makes elevation conversions from EGM2008 to Hon Dau MSL difficult. Here, the fact that in September 2013 two bathymetric datasets, covering a common area, were simultaneously obtained - an SBES dataset referenced to the Hon Dau MSL and an MBES dataset referenced to EGM2008 (Figure 3-4, a) - is exploited in order to convert MBES derived elevations from EGM2008 to the Hon Dau MSL. First, an MBES-derived DEM with resolution of 50 m was generated in GIS, these cells coordinates were extracted and using the online tool provided by the Geodetic Facility for the Advancement of Geoscience (GAGE:https://www.unavco.org/software/geodetic-utilities/geoid-height-calculator/geoid-height-calculator.html) the geoid undulation was calculated for each coordinate. The results showed that the mean geoid undulation across the region of the MBES survey is approximately 0.10 m (σ = 0.05 m) (Figure 3-4, a). Because of the small mean (and σ) of the geoid undulation calculated and because the MBES survey covered a relatively small area, the curvature of the geoid can be neglected and EGM2008 can be assumed to be flat within this limited area. In the next step, a 10m wide x 12,380 m long area of the MBES dataset was outlined on ArcGIS to match the SBES survey lines (Figure 3-4, b). DEMs of 10 m resolution were generated from the SBES and MBES data within this band, using ordinary kriging interpolation. Comparison of the two surfaces showed a mean vertical offset of 19.77 m (σ = 0.42 m) (Figure 3-4, c) with SBES elevations being higher than the corresponding MBES elevations. This conversion factor was applied to all three MBES datasets thus converting the MBES-based elevations of all three surveys from EGM2008 to the Hon Dau MSL (Figure 3-5).

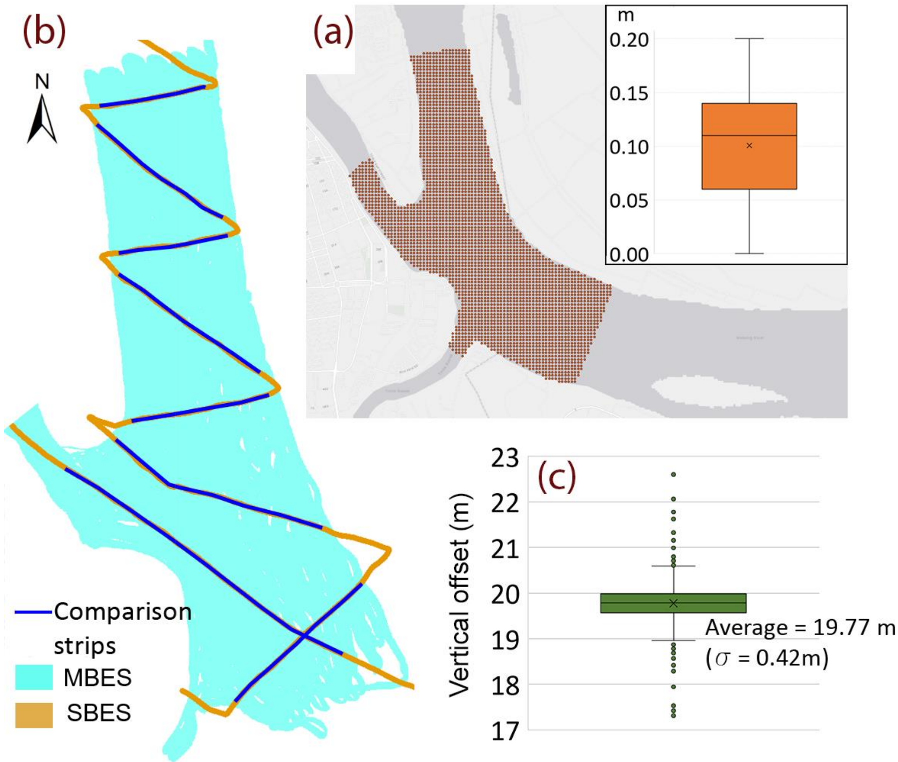

Figure 3-4. (a) Variations in the EGM2008 geoid across the study area, (b) The region where the MBES (Multi-Beam Echo Sounder) and SBES (Single-Beam Echo Sounder) datasets intersect and the location of strip DEM used to compare two surfaces MBES and SBES, (c) The difference between SBES elevations (referenced to Hon Dau MSL vertical datum) and MBES elevations (referenced to EGM2008 vertical datum) revealed a discrepancy of 19.77 m (σ = 0.42 m)

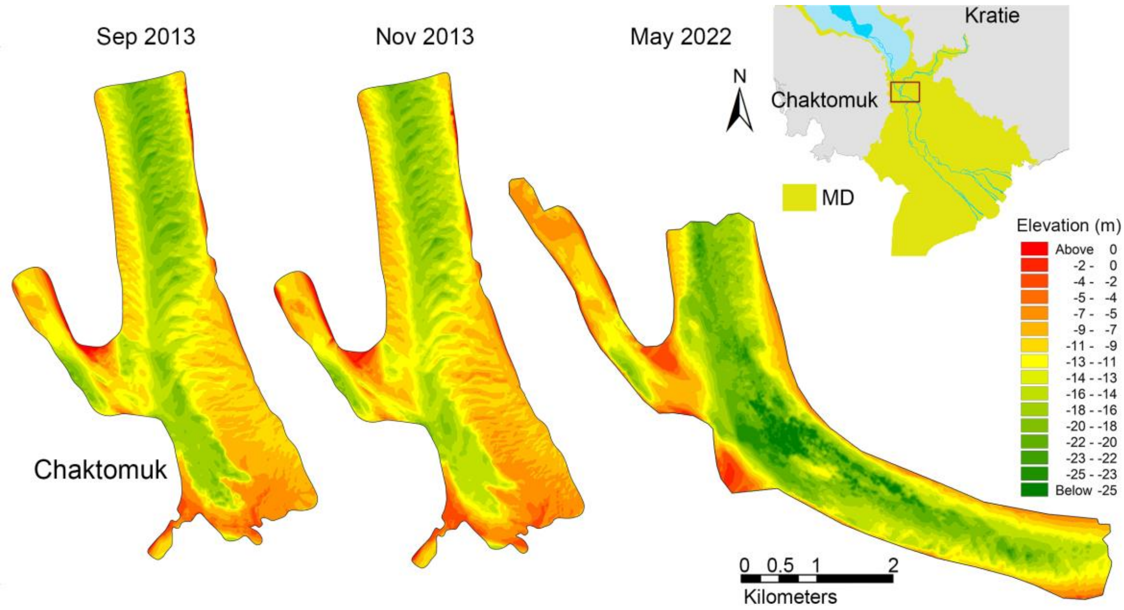

Figure 3-5. Three MBES bathymetry datasets surveyed on September 12, 2013, October 27, 2013 and May, 2022. These bathymetry datasets reference the WGS84 coordinates and are converted to align with the Hon Dau MSL

3.3 Chapter Summary

The present Chapter introduced the datasets that will be utilised in the result Chapters (4-7) that follow and have been obtained from various sources, including previous studies. Datasets include flow discharge, flow velocity and water level recordings, channel bed topography. While they offer valuable information, they also come with certain limitations that present challenges to the research. The archive of water levels includes measurements spanning the entire area of interest and many decades (Table 3-1). However, data for Cambodia only provide daily and twice per day measurements. A similar problem exists for the flow discharge data, although the record for VMD is at hourly resolution, for Cambodia, a long-term flow discharge is measured only at Kratie and at a daily interval (Table 3-1). This daily water level data from the Cambodian gauges lacks the temporal resolution required to capture the tidal signal along these parts of the system and temporal changes in the freshwater flux from the upper reaches of the Mekong and Bassac channel. Moreover, the daily water discharge at Kratie is computed using a rating curve (stage-discharge relationship) derived from the daily water level data. Consequently, this dataset inherently incorporates uncertainties in the discharge calculations.

The DEM generated using Kriging interpolation for the SBES dataset may introduce uncertainties in elevation. These uncertainties result from the interpolation process and the inherent variability in riverbed morphology, such as scour and fill features (Heritage et al., 2009; Milan et al., 2011; Glenn et al., 2016). Furthermore, except for the widest coverage area provided by the

1998 bathymetric dataset, the remaining datasets of channel bed elevations, though extensive, are fragmented in both space and time (Figure 3-3). For example, the 1998 bathymetry lacks coverage for areas between the Chaktomuk Junction in Cambodia and Chau Doc in VMD for the Bassac channel. The 2013 bathymetry covers only a portion of the Lower Mekong River, from Kratie to Neak Luong, while the 2018 bathymetry covers only the channels in the VMD (Figure 3-3). This fragmentation in space and time makes difficult to quantify the impact of temporal changes in riverbed morphology under anthropogenic activities. The high-resolution riverbed bathymetry data obtained via MBES is limited to a small area around the Chaktomuk Junction (Figure 3-5). Finally, the vertical datum conversion from MBES riverbed bathymetry from the geoid EGM 2008 to Hon Dau MSL vertical datum may involve some minor inaccuracies, with a range of approximately 0.10 m (σ = 0.05 m).

To address the issue of low-resolution data (daily or twice daily) at the Cambodian gauging stations, which cannot capture tidal ingress, a one-dimensional (1D) hydrodynamic model for the entire Lower Mekong Basin will be used to understand the evolution of water levels and tidal amplitude across the basin, as presented in section 5.1, Chapter 5. To reduce reliance on the calibration at a single gauge point (at Kratie), the 1D model will be validated and calibrated across a range of gauges spanning the entire study area. The stretch of the main Mekong channel between Neak Luong and Tan Chau (50 km) lacks bathymetry data for both 2018 and 2013. This data gap will be addressed through linear interpolation between the two observed bathymetry data sets, as detailed in Section 5.2.1 of Chapter 5. Meanwhile, the stretch of the Bassac River between the delta apex and Chau Doc has never been surveyed. This is a small channel, accounting for only 20% of the Mekong River's flow (Fujii et al., 2003). An assumption was made that it is the same as the stretch from Chaktomuk to the Viet Nam border in the Mekong River, also detailed in Section 5.2.1 of Chapter 5.

In this chapter, a range of data sets describing the hydrological records and channel bathymetry used in the research are presented. The quality and effectiveness of these datasets are evaluated, and uncertainties are addressed. Observed hourly water level and discharge data from gauging stations along the VMD will be used to quantify historical changes in water levels and tidal range across the VMD, as detailed in Chapter 4. The water level and discharge data for gauging stations in the entire Lower Mekong Basin will be employed for model calibration, validation, and scenario simulations, as discussed in Sections 5.1 and 5.2 of Chapter 5. The large-scale bathymetry dataset is used to build the 1D modelling mainstream bathymetry and develop river lowering scenarios, as described in Sections 5.1 and 5.2 and utilised in Chapters 5 and 6.

High-resolution bathymetry data will be used to develop 2D modelling and 2D bathymetry scenarios for the Chaktomuk Junction, as detailed in section 7.3 Chapter 7. Flow velocity data will be employed for the calibration and validation of the 2D modelling, as described in Section 7.3 of Chapter 7.

Chapter 4. Historical changes of water level and tidal range across the Vietnamese Mekong Delta

In the previous chapter, various datasets detailing hydrological records and channel bathymetry relevant to this research were introduced. Building on that foundation, this Present chapter focuses on analysing observed hourly water level and discharge data collected from gauging stations across the VMD. The chapter aims to systematically explore the relationships between mean water levels, tidal range, and corresponding mean water discharge values to assess historical changes influenced by anthropogenic factors, particularly riverbed lowering. This analysis addresses the first objective (O1) of the study, which is to assess historical changes in the delta's flow dynamics resulting from channel bed level lowering and responds to the specific Research Question (RQ1): How has historical riverbed lowering affected delta hydraulics? In more detail, Section 4.1 introduces the response of delta hydrology to anthropogenic activities and highlights the research gap in understanding historical changes in water level and discharge relationships under these influences. Section 4.2 outlines the methodology used to analyse these relationships, Section 4.3 presents the results of this analysis, Section 4.4 discusses the broader implications of the findings and Section 4.5 will summary the finding of the Chapter.

4.1 Introduction

Human activities affect natural delta processes and have the potential to cause substantial alterations in delta hydrology in various ways (Cochrane et al., 2014; Lu et al., 2014; Räsänen et al., 2017; Hoang et al., 2019), which have been discussed in detail in Section 2.2, Chapter 2. For example, within river basins, river flow may be regulated by dams (Lauri et al., 2012), and changes in land cover (Watson et al., 1996). Locally within deltas, riverbed lowering driven by sand extraction and upstream dams or channel dredging for navigation purposes has been found to be a major driver of tidal amplification in deltas (Vellinga et al.,2014; Cox et al., 2021; Vasilopoulos et al., 2021), destabilising riverbanks (Hackney et al., 2020) and contributing to coastal erosion (Anthony et al. 2015). Dyke systems often built for flood protection have been demonstrated to increase the in-channel water level during the flood season (Dang et al., 2016; Triet et al., 2017) by concentrating all flow into the channel while also hindering channel floodplain connectivity. Rising sea levels in the delta front elevate the risk of flooding (Overeem and Syvitski, 2009; Takagi et al., 2015; Becker et al., 2020).

In order to understand the response of delta hydrology to a combination of aforementioned anthropogenic activities, the present Chapter will explore the relationship between mean water level, tidal amplitude and mean water discharge throughout the Vietnamese Mekong Delta (VMD), utilizing consistent historical observations from 2000 to 2021 for all of monitoring gauges situated within the region, including Tan Chau (distance between the gauge location and corresponding channel mouth: 203 km) and My Thuan (101 km) on the Mekong channel, and Chau Doc (186 km) and Can Tho (78 km) on the Bassac channel (Figure 3-1, Chapter 3). Dynamically changing water levels as a function of fresh water flux and tidal conditions play a key role in delta functioning, thus, changes in these relationships could have diverse effects on delta-related issues. It is important to emphasize that the analysed dataset, spanning from 2000 to 2021 in these gauging stations encompasses the period following the commencement of anthropogenic activities (Bravard et al., 2013; Hecht et al., 2019). The completion of the first hydropower plant on the main stream Mekong river in China was in 1993 (Fan et al., 2015) (see Appendix, Fig 1 for the cumulative total water storage of major dams in the Mekong basin), and riverine sand extraction began before 2000 (Bravard etal., 2013). Therefore, this dataset cannot provide any 'baseline' data for comparison with those driven solely by natural processes. The Cambodian gauge record is of a daily resolution and, with the exception of Kratie, only contains water levels (As described in section 3.1, Chapter 3), which is not sufficient for the type of analysis undertaken here, where high temporal resolution data are needed to capture tidal range. Hence Chapter 4 will focus only on the VMD while a numerical modelling approach will be undertaken to explore changes across the entire system encompassing the Lower Mekong River and MD in Chapters 5 and 6.

4.2 Methods

To assess historical changes in the relationship between water level, tidal range, and corresponding water discharge, two methods have been employed, including (a) developing a mean water level and tidal range to mean water discharge relationship, which provides a comprehensive understanding of the spatial and temporal historical evolution of these relationships; and (b) utilizing the "Specific-Gage" method, introduced by Blench (1969). This "Specific-Gage" method involves choosing a reference flow discharge and tracking the corresponding water level trend over time. If the water level for the reference discharge decreases over time, it suggests that the channel capacity has increased, possibly due to riverbed lowering, widening, or decreased roughness. Conversely, an increase in water level indicates a decrease in channel capacity, potentially due to riverbed aggradation, narrowing, or increased roughness (Pinter and Heine, 2005; Slater, 2014). Data from the gauging stations along the VMD that record both hourly water level and flow discharge (Table 3-1, Chapter 3) are used in the analysis. The details of these methods are provided in Sections 4.2.1 and 4.2.2 below.

4.2.1 Establishing a water level to water discharge relationship

The VMD experiences a semi-diurnal tidal regime, with a tidal oscillation lasting approximately 25 hours (Hak et al., 2016). Hence, when examining the hydrograph, it is more suitable to consider two specific parameters: the mean water level ($\overline{WL}$) and the tidal range (TR) over the 25-hour tidal cycle. The $\overline{WL}$ value represents the water level unaffected by tidal variations and is calculated by averaging the instantaneous hourly data throughout the tidal oscillation. On the other hand, the TR value is a measurement of the amplitude of the water level and is calculated by subtracting the minimum water level from the maximum water level during a tidal cycle. Similarly, the determination of the corresponding mean water discharge ($\bar{Q}$) is obtained by averaging the instantaneous hourly discharge data collected over a 25-hour tidal cycle. This approach is based on the understanding that water discharge is a function of velocity and volume. As tides rise, velocity decreases due to changing water surface slope, leading to a reduction in water discharge. Conversely, as tides fall, increasing velocity contributes to a rise in water discharge.

In addition to tidal forcing, the VMD is strongly influenced by a monsoon pulse, which exhibits two distinct periods; a dry and a flood season. Due to climatic patterns, the start and end of each season can vary, therefore in the present Chapter, the MRC, (2011) definition of the flood and dry periods for a water year is adopted, where the water year typically begins and ends in December. The dry season is then defined as the period when the $\bar{Q}$ value falls below the long-term mean annual discharge value, while the flood season is defined as the period when the $\bar{Q}$ value exceeds the long-term mean annual discharge value. These periods are established by calculating the long-term mean discharge value using entire gauged record for the four monitoring stations examined here (Figure 4-1, a). Specifically, the long-term mean water discharge value at Tan Chau, My Thuan, Chau Doc, Can Tho stations is 10,061 m^3s^{-1}, 6,522 m^3s^{-1}, 2,358 m^3s^{-1}, and 5,989 m^3s^{-1}, respectively, for the period from 2000 to 2021.

Delta hydrology is also affected by the ability of the floodplain to store water. During a median (low; high) fresh water flux year the total water volume at Kratie is estimated at 416 billion m^3 (301 billion m^3; 500 billion m^3), the flood volume flowing from channel into the VMD floodplain account for 21% (17%;24%) of the water volume at Kratie (Manh et al., 2014). Floodplain storage removes water volume from the channel during the rising limb of the flood which is then returned into the channel during the receding limb of the flood season (Fujii et al., 2003) and results in a hysteresis in the water-discharge relationship. Hence, for an equivalent discharge value, water levels are greater during the receding limb of the flood period season compared to the rising limb (Figure 4-1, b). To account for this discrepancy between rising limb and receding limb periods, the year-on-year flood hydrograph in each water year is further divided into two distinct periods: a rising limb, before the water discharge reaches its maximum value for a given year, and a receding limb after the maximum discharge value has been reached (Figure 4-1, b). The $(\overline{WL}, TR)$ are plotted against the $\bar{Q}$ to visualize stage-discharge relationship for each consecutive year from 2000 to 2021. Different plots are generated for the dry, rising limbs, and receding limb periods of the hydrograph (Figure 4-2 and Figure 4-4 for $\overline{WL}$ and TR, respectively).

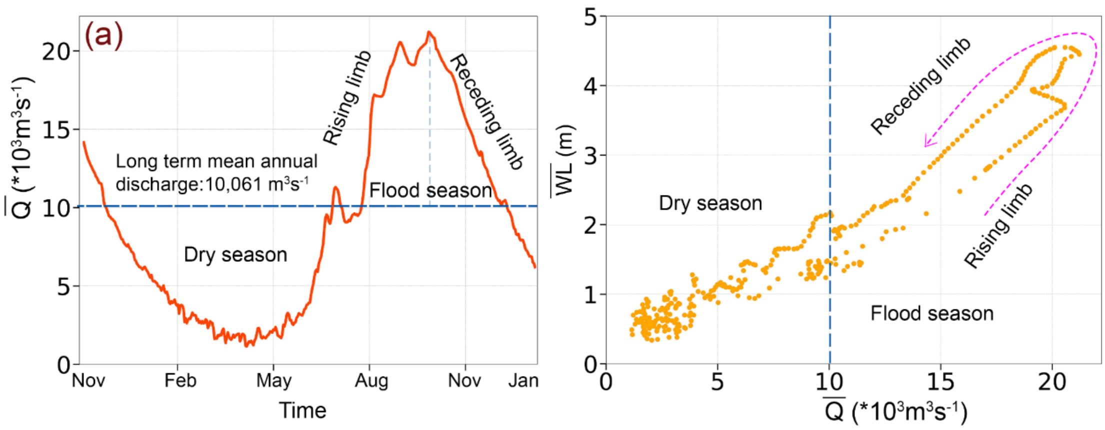

Figure 4-1. (a) Mean water discharge for the Tan Chau station for the water year of 2004 (red), also showing the long-term mean annual discharge for 2000-2021 (dashed blue). In this hydrograph, the dry season extends from 22 November 2003 to 20 July 2004, while the flood season encompasses the period from 21 July 2004 to 3 December 2004 and is split to a rising limb from 21 July 2004 to 23 September 2004 and receding limb from 24 September 2004 to 3 December 2004. (b) The impact of water floodplain storage causes a hysteresis in the stage-discharge relationship here illustrated from the $\bar{Q}$, $\overline{WL}$ data recorded at the Tan Chau gauge for the water year of 2004.

4.2.2 Choosing representative water discharge rates

To quantify historical changes in mean water level and tidal range under different water flow conditions, temporal changes of $\overline{WL}$ and TR corresponding to specific water discharge levels are analysed. The representative water discharge rates at each gauging station are specified by the probability frequencies at the 95% (Q_{95}), 75% (Q_{75}), 50% (Q_{50}), 25% (Q_{25}) and 5% (Q_5) percentiles within the normal distribution of the entire historical mean water discharge ($\bar{Q}$) time series data at each gauging station. The Q_{75}, Q_{50} and Q_{25} statistics represent the conditions of low-water discharge, median-water discharge, and high-water discharge, respectively, while the Q_{95} and Q_5 percentiles represents instances of extreme low-flow and high-flow discharge occurring during the lowest dry season and the peak of the flood season, respectively (Table 4-1). However, the exact mean water level for each percentile discharge value was rarely recorded. Therefore, a buffer with an uncertainty of ±1% around each quartile range was applied. The mean water level ($\overline{WL}$) and tidal range (TR) are obtained by averaging the corresponding water level values and tidal range values within this discharge buffer, respectively (see Table 4-1). Datasets for the $\overline{WL}$ and TR values corresponding to each different quantiles of flow discharge Q_{75}, Q_{50}, Q_{25}, Q_5 for each water year are then visually represented in consecutive annual patterns in Figure 4-3 and Figure 4-5 respectively.

Table 4-1. The indicative quantiles of water discharge at the hydrological stations of the VMD. The values in parentheses represent the buffer of ±1% around each quartile range.

Gauges		The probability of water flow $(*\ 10^3 m^3 s^{-1})$			
	Q_{95} $(Q_{94}; Q_{96})$	Q_{75} $(Q_{74}; Q_{76})$	Q_{50} $(Q_{49}; Q_{51})$	Q_{25} $(Q_{24}; Q_{26})$	Q_5 $(Q_4; Q_3)$
Tan Chau	2.23 (2.14; 2.32)	3.98 (3.90; 4.07)	8.24 (7.98; 8.51)	16.41 (16.10; 16.63)	21.20 (20.81; 21.65)
My Thuan	1.06 (0.97; 1.13)	2.37 (2.30; 2.45)	5.14 (4.97; 5.35)	10.44 (10.26; 10.66)	14.95 (14.63; 15.31)
Chau Doc	0.36 (0.35; 0.38)	0.65 (0.64; 0.67)	1.57 (1.51; 1.62)	3.93 (3.80; 4.03)	6.28 (6.11; 6.42)
Can Tho	0.82 (0.74; 0.91)	2.04 (1.98; 2.10)	4.52 (4.38; 4.65)	9.76 (9.55; 10.04)	14.49 (14.16; 14.83)

4.3 Results

4.3.1 Relationship between mean water level and mean water discharge

Figure 4-2 shows the linear relationship between the mean water level ($\overline{WL}$) and the mean flow discharge ($\bar{Q}$) for different periods (dry season, rising, and receding limb of the flood season) of each water year from 2000 to 2021 for all stations within the VMD: Tan Chau (203 km) and My Thuan (101 km) in the Mekong channel, and Chau Doc (186 km) and Can Tho (78 km) in the Bassac channel. The regression slope, intercept, and coefficient of determination R^2, which indicates the strength of the relationship; ranging from 0 to 1 with higher values reflecting a better fit and less error variance with values greater than 0.5 generally considered acceptable for hydrological studies (Moriasi et al., 2007), as well as the $P - value$ for each linear regression between the $\overline{WL}$ and the corresponding $\bar{Q}$ for the dry season, rising limb, and receding limb of the flood season for each gauge, is presented in the Appendix, Table 2, Table 3, and Table 4, respectively. Figure 4-3 presents temporal changes of $\overline{WL}$ for different quantiles of flow discharge at the four gauges for the same periods mentioned above. These figures will be discussed in paragraphs 4.3.1.1 and 4.3.1.2 that follow.

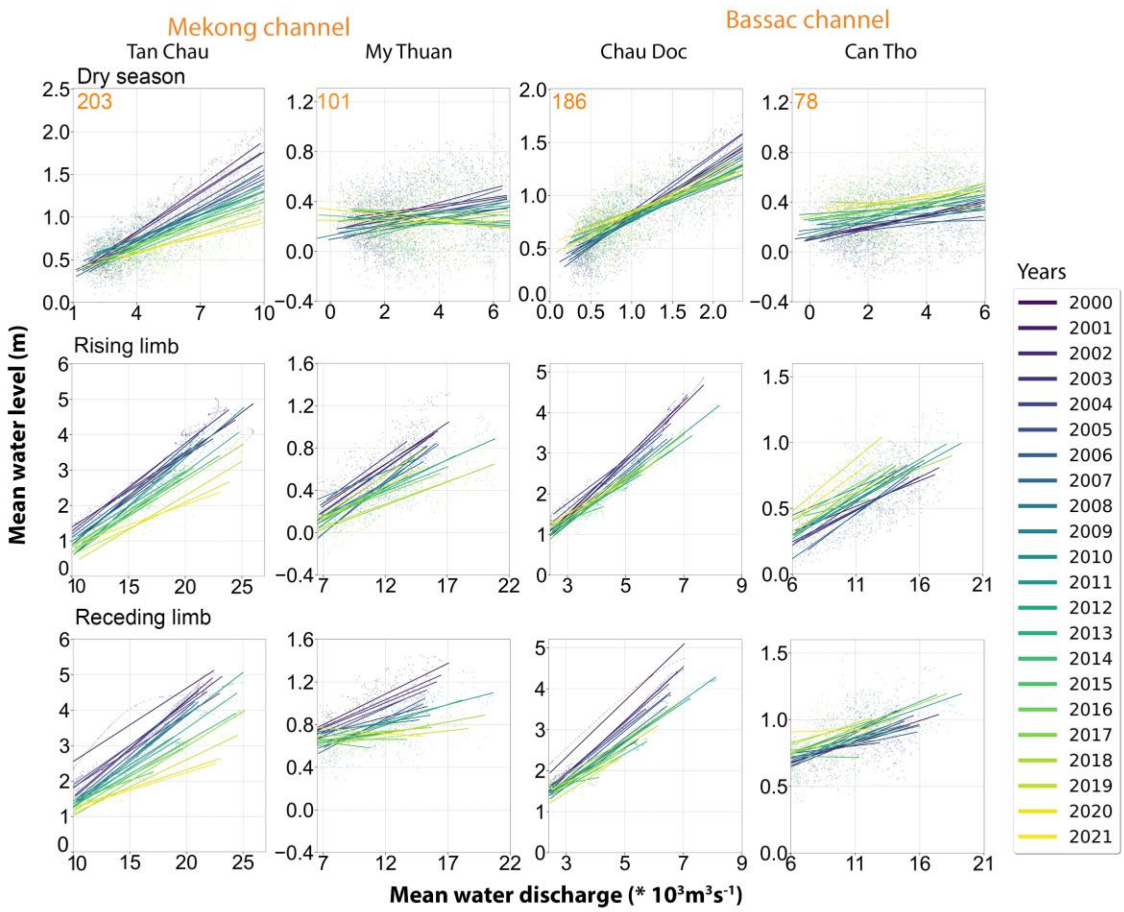

Figure 4-2. Mean water level –discharge linear relationship at four gauging stations of the VMD, covering the period from 2000 to 2021 for Tan Chau and My Thuan in the Mekong channel, Chau Doc and Can Tho in the Bassac channel. The number on the top left of each panel indicates the distance between the gauge and the corresponding channel mouth in km. The axis scale differs for each panel base on the difference hydraulic conditions at each gauge. All of mean water level are referenced to Hon Dau Mean Sea Level (MSL).

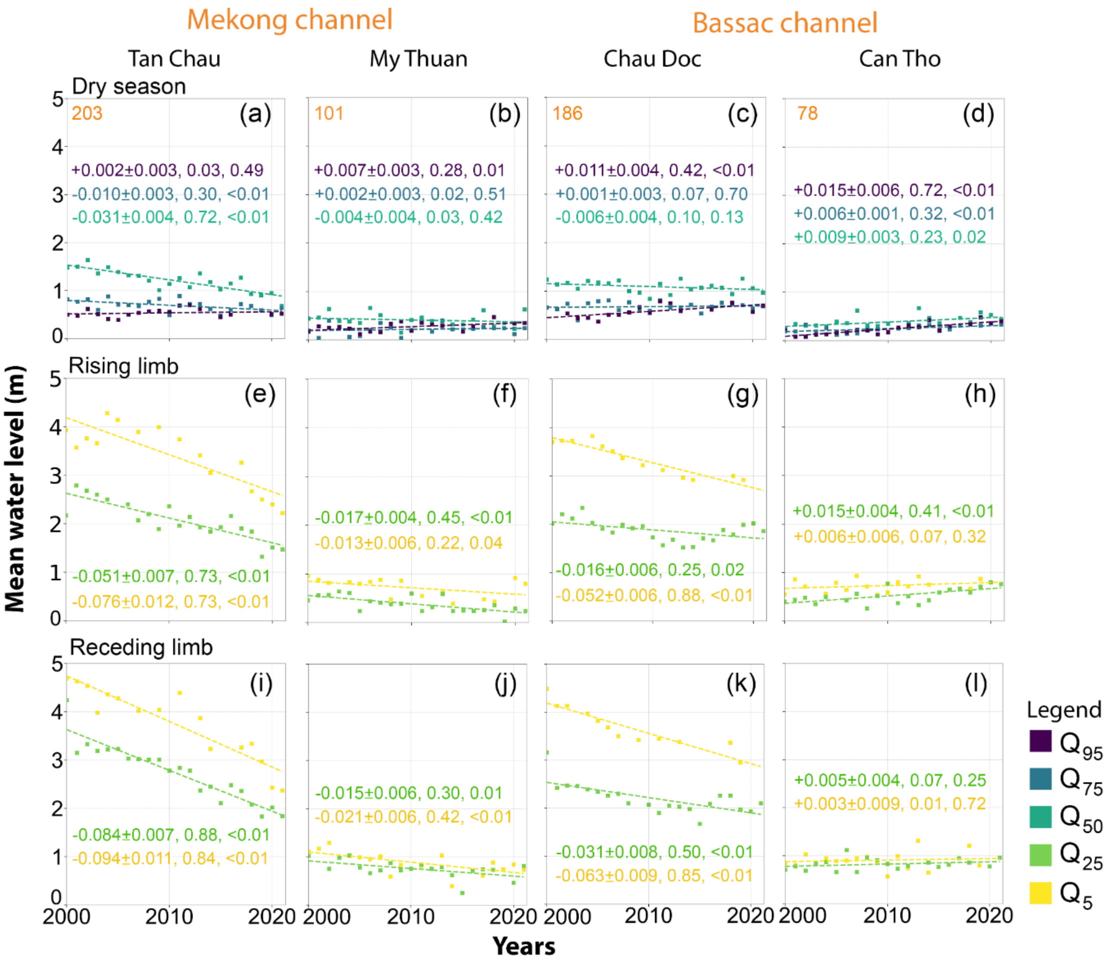

Figure 4-3. Change of mean water level for given quantiles of mean water discharge in the VMD, from 200 to 2021 for Tan Chau and My Thuan in the Mekong channel, Chau Doc and Can Tho in the Bassac channel. The linear regression shows the long-term trajectory of change with numbers indicating the regression slope, R^2 and P-value.

4.3.1.1 Dry season

During the dry season, the mean water level ($\overline{WL}$) showed overall decreasing trends as it approached the seaward direction in both Mekong and Bassac channels (Figure 4-2, Dry season). An increase in mean flow discharge ($\bar{Q}$) leads to a more pronounced rise in the $\overline{WL}$ (indicated by the slope value of the linear regression) in the upstream regions of the VMD, particularly at the Tan Chau (203 km) and Chau Doc (186 km) stations, however, this trend is less pronounced (as shown by the smaller slope value of the linear regression) at the My Thuan (101 km) and Can Tho (78 km) stations, which are located further seaward (Figure 4-2, and Appendix, Table 2). The smaller rise in the $\overline{WL}$ despite increasing $\bar{Q}$ at the seaward stations, is due to the influence not only by freshwater flux but also by seasonal variations of mean sea level. Additionally, the presence of a high number of irrigations channels can affect the way that the volume of water is distributed in these seaward stations.

Regarding the temporal variation of the mean water level- discharge relationship, the results indicate an overall year-on-year decrease in the slope of the linear regression across all gauging stations from 2000 to 2021, with the linear regression of the water-discharge relationship tending to flatten over time (Figure 4-2, and Appendix, Table 2). This temporal reduction in the slope of the linear regression of the mean water level- discharge relationship has led to an overall decrease in the $\overline{WL}$ for the same discharge conditions, particularly noticeable at high mean water discharge values compared to lower discharge levels. An exception is noted at the lowest freshwater flux stage during the dry season at Tan Chau, My Thuan, and Chau Doc, as well as throughout most of the dry season at the Can Tho station, where despite a tendency towards a smaller slope of these linear regression, the water level shows a temporal increase. This phenomena of temporal rise in $\overline{WL}$ will be discussed in detail in Section 4.4. These results of reduced slope for the linear regression demonstrate that the temporal change of the $\overline{WL}$ tends to be less dependent on the magnitude of fresh water, particularly in the seaward gauging stations.

Looking at the temporal $\overline{WL}$ values corresponding to specific quantiles of water discharge (Figure 4-3, Dry season). Overall, the temporal trend shows a smaller slope of the linear regression of the water-discharge relationship as upstream water flux rises (from Q_{95} to Q_{50}) at all stations. In addition, the temporal trend shows a transition from an increasing $\overline{WL}$ (positive slope of the linear regression) to a decreasing $\overline{WL}$ (negative slope of the linear regression) as upstream water flux rises (from Q_{95} to Q_{50}) at Tan Chau, My Thuan in Mekong channel and Chau Doc in Bassac channel. At the Can Tho station shows an overall increase in $\overline{WL}$ across all quantiles of water discharge: Q_{95}, Q_{75}, Q_{50}. The increase in $\overline{WL}$ at low water discharge in Tan Chau, Chau Doc, and My Thuan, as well as at all water discharge levels in Can Tho, will be discussed in detail in Section 4.4.

In more detail, in the Mekong channel, at the Tan Chau station, for water flow at Q_{95}, the temporal linear relationship indicating an increase in $\overline{WL}$ is statistically insignificant, with a value of 0.002 m ± 0.003 m yr^{-1} ($R^2 = 0.03, P = 0.49$). For water flow at Q_{75}, there are a decreasing trend in $\overline{WL}$ at 0.01 m ± 0.003 m yr^{-1} ($R^2 = 0.30, P < 0.01$) leading to an accumulated water decrease of 0.21 m ± 0.06 m for the 21-year period from 2000 to 2021. At Q_{50} the $\overline{WL}$ reduction rate is higher, at 0.031 m ± 0.004 m yr^{-1} ($R^2 = 0.72, P < 0.01$), resulting in an accumulated water decrease of 0.65 m ± 0.08 m for the same period (Figure 4-3, a). At the My Thuan station, for water flow at Q_{95}, there is an increasing trend in $\overline{WL}$ is 0.007 m ± 0.003 m yr^{-1} ($R^2 = 0.28, P = 0.01$), resulting in an accumulated water rise of 0.15 m ± 0.06 m from 2000 to 2021. For water flow at Q_{75}, the temporal linear relationship indicating an increase in $\overline{WL}$ is statistically insignificant, with a value of 0.002 m ± 0.003 m yr^{-1} ($R^2 = 0.02, P = 0.51$). For water flow at Q_{50}, the temporal linear relationship indicating an reduce in $\overline{WL}$ is statistically insignificant, with a value of 0.004 m ± 0.004 m yr^{-1} ($R^2 = 0.03, P = 0.42$) (Figure 4-3, b).

In the Bassac channels, at Chau Doc station, there is slight increase in $\overline{WL}$ at Q_{95}, with increase rate of 0.011 m ± 0.004 m yr^{-1} ($R^2 = 0.42, P < 0.01$) resulting in an accumulated water rise of 0.21 m ± 0.08 m for the 21-year period. However, at the higher discharge, Q_{75}, The temporal linear relationship trend in $\overline{WL}$ is not statistically significant, with an increase rate of 0.001 m ± 0.003 m yr^{-1} ($R^2 = 0.07, P = 0.70$) for the same period. For water flow at Q_{50}, the temporal linear relationship indicating an reduce in $\overline{WL}$ is statistically insignificant, with a value of 0.006 m ± 0.004 m yr^{-1} ($R^2 = 0.10, P = 0.13$). (Figure 4-3, c). At the Can Tho station, the $\overline{WL}$ tends to exhibit a slight increase at all given discharges. In more detail, for water flow at Q_{95}, there is an increasing trend in $\overline{WL}$, calculated at 0.015 m ± 0.006 m yr^{-1} ($R^2 = 0.72, P < 0.01$), resulting in an accumulated water rise of 0.32 m ± 0.13 m from 2000 to 2021. At the Q_{75} and Q_{50}, the water increase rate of 0.006 m ± 0.001 m yr^{-1} ($R^2 = 0.32, P < 0.01$) and 0.009 m ± 0.003 m year^{-1} ($R^2 = 0.23, P = 0.02$), respectively, leading to an accumulated water increase of 0.13 m ± 0.02 m at Q_{75} and 0.19 m ± 0.06 m at Q_{50}, respectively, over for the 21-year period from 2000 to 2021. (Figure 4-3, d).

4.3.1.2 Flood season

For both the rising and receding limbs of the flood season a general trend of decreasing $\overline{WL}$ seaward is observed in both the Mekong and Bassac channels (Figure 4-2, rising limb and receding limb). It is observed that the $\overline{WL}$ at a given mean discharge during the receding limb is higher than that during the rising limb, with this distinction in water level being more notable in the landward direction, this is explained by the hysteresis triggered by floodplain storage discussed in 4.2.1. Increasing $\bar{Q}$ is associated to increasing $\overline{WL}$ with the trend being more pronounced in the landward direction in all gauging stations (Figure 4-2, rising limb and receding limb and Appendix, Table 3, Table 4). An exception occurs at the seaward stations of My Thuan (101 km) and Can Tho (78 km) during the receding limb for several recent lowest water discharge years (year 2015, 2016, 2021), where the trends show a reduction in $\overline{WL}$ despite an increase in water discharge (Figure 4-2 and Appendix, Table. 3, Table. 4), which will be discussed in detail in Section 4.4.

Regarding year-on-year changes, an overall temporal decrease in the slope of the linear regression of the mean water-discharge relationship across all gauging stations from 2000 to 2021, with the linear regression of the mean water-discharge relationship tending to flatten over time (Figure 4-2, rising limb and receding limb and Appendix, Table. 3, Table. 4). Again, the results showed that the temporal change of the $\overline{WL}$ tends to be less dependent on the magnitude of fresh water discharge as showed during the dry season. The overall temporal decrease in the slope of the linear regressions of the mean water level -discharge relationship indicates a decline in $\overline{WL}$ for the same discharge conditions, evident at all gauging stations with an exception is observed at Can Tho in the Bassac channel, where the opposite trend occurs, which will be discussed in detail in Section 4.4.

Considering temporal changes of the relationship between $\overline{WL}$ for specific flow discharge quantiles (Figure 4-3), There is a temporal decrease in $\overline{WL}$ at given discharge conditions at the Tan Chau, My Thuan, and Chau Doc stations, with the water reduction trend being more pronounced at the landward stations and at higher fresh water discharge levels. An exception is observed at Can Tho in the Bassac channel, where the opposite trend occurs. In more detail, at Tan Chau (203 km) in the Mekong channel, there is a substantial and consistent decrease in $\overline{WL}$ over consecutive years from 2000 to 2021, for both limbs of the flood season. At Q_{25}, the $\overline{WL}$ reduction rate in $\overline{WL}$ is 0.051 m ± 0.007 m yr^{-1} $(R^2 = 0.73, P < 0.01)$ and 0.084 m ± 0.007m yr^{-1} $(R^2 = 0.88, P < 0.01)$ in rising limb and receding limb, respectively. These reduction rates in $\overline{WL}$ result in an accumulated water decrease of 1.07 m ± 0.15 m and 1.76 m ± 0.15 m for the rising limb and receding limb periods, respectively, over the 21-year period from 2000 to 2021. However, the $\overline{WL}$ reduction is more pronounced at higher water discharge levels. For the higher discharge value at Q_5, the reduction rate in $\overline{WL}$ is 0.076 m ± 0.012 m yr^{-1} $(R^2 = 0.73, P < 0.01)$ during the rising limb and 0.094 m ± 0.011 m yr^{-1} $(R^2 = 0.84, P < 0.01)$ during the receding limb. These reduction rates in $\overline{WL}$ result in an accumulated water decrease of 1.60 m ± 0.25 m and 1.95 m ± 0.23 m for the rising limb and receding limb periods, respectively, from 2000 to 2021 (Figure 4-3, e and i). A similar trend persists but is less prominent further seaward at My Thuan. For Q_{25}, the $\overline{WL}$ reduction rate is 0.017 m ± 0.004 m yr^{-1} $(R^2 = 0.45, P < 0.01)$ during the rising limb and 0.015 m ± 0.006 m yr^{-1} $(R^2 = 0.30, P = 0.01)$ during the receding limb. This leads to an accumulated water decrease of 0.36 m ± 0.08 m and 0.32 m ± 0.13 m during the rising limb and receding limb, respectively, from 2000 to 2021. For higher water discharge at Q_5, the $\overline{WL}$ reduction rate is 0.013 m ± 0.005 m yr-1 ($R^2 = 0.22, P = 0.04$) during the rising limb and 0.021m ± 0.006 m yr-1 ($R^2 = 0.42, P < 0.01$) during the receding limb. This results in an accumulated water level decrease of 0.27 m ± 0.13 m during the rising limb and 0.44 m ± 0.13 m during the receding limb from 2000 to 2021. (Figure 4-3, f and j).

In the Bassac channel, a distinct pattern of declining $\overline{WL}$ for a given discharge is noticeable solely at the Chau Doc gauge. In more detail, for Q_{25}, the reduction rate in $\overline{WL}$ is 0.016 m ± 0.006 m yr-1 ($R^2 = 0.25, P < 0.02$) during the rising limb and 0.031 m ± 0.008 m yr-1 ($R^2 = 0.50, P < 0.01$) during the receding limb. These reduction rates in $\overline{WL}$ result in an accumulated water decrease of 0.34 m ± 0.13 m and 0.65 m ± 0.17 m for the rising limb and receding limb periods, respectively, over the 21-year period from 2000 to 2021. The reduction in $\overline{WL}$ is more pronounced at higher water discharge levels, at Q_5, the reduction rate in $\overline{WL}$ is 0.052 m ± 0.006 m yr-1 ($R^2 = 0.88, P < 0.01$) during the rising limb and 0.063 m ± 0.009 m year-1 ($R^2 = 0.85, P < 0.01$) during the receding limb. These reduction rates in $\overline{WL}$ result in an accumulated water decrease of 1.09 m ± 0.13 m and 1.32 m ± 0.19 m for the rising limb and receding limb periods, respectively, from 2000 to 2021 (Figure 4-3, g and k). At Can Tho, a opposite trend is observed with an increase in $\overline{WL}$ for a given water discharge for both the rising limb and receding limb. Specifically, for Q_{25}, the rate of increase in $\overline{WL}$ is 0.015 m ± 0.004 m yr-1 ($R^2 = 0.41, P < 0.01$), result in an accumulated water increase of 0.32 m ± 0.08 m from 2000 to 2021 during the rising limb. While the established temporal linear relationship increasing water level is not statistically significant for the receding limb, at 0.005 m ± 0.004 m yr-1 ($R^2 = 0.07, P = 0.25$). For the higher Q_5, the established temporal linear relationship increasing water level is not statistically significant for rising limb and receding limb, at 0.006 m ± 0.006 m yr-1 ($R^2 = 0.07, P = 0.32$) and 0.003 m ± 0.009 m yr-1 ($R^2 = 0.01, P = 0.72$), respectively. (Figure 4-3, h and l). The temporal rise in $\overline{WL}$ for Can Tho station at the given discharge condition will be discussed in detail in Section 4.4.

4.3.2 Relationship between tidal range and water discharge

Figure 4-4 depicts the linear relationship between the tidal range (TR) and the corresponding mean water discharge ($\bar{Q}$) for different periods (dry season, and the rising and receding limbs of the flood season) of each water year, covering the period from 2000 to 2021 for stations in both Mekong and Bassas channels. The regression slope, intercept, R^2, and $P - value$ for each linear regression between the TR and the corresponding $\bar{Q}$ for the dry season, rising limb, and receding limb of the flood season for each gauge, is presented in Appendix, Table 5, Table 6 and Table 7, respectively. Figure 4-5 showcases the changes in tidal range stages at different quantiles of flow discharge at the four gauges for the same mentioned periods. These figures will be discussed in paragraphs 4.3.2.1 and 4.3.2.2 that follow.

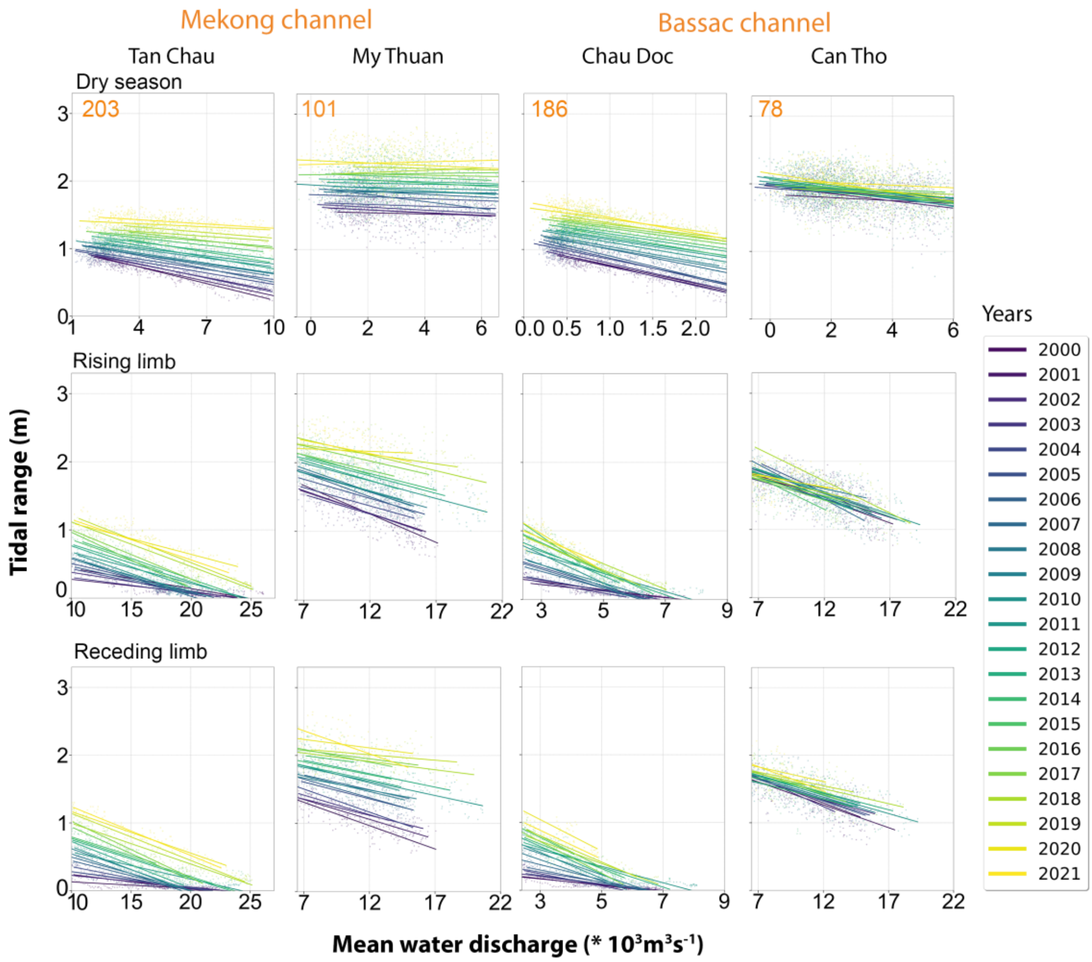

Figure 4-4. Tidal range – mean water discharge linear relationship at four gauging stations of the VMD, covering the period from 2000 to 2021. The number on the top left of each panel indicates the distance between the gauge and the corresponding channel mouth in km. The axis scale differs for each panel base on the difference hydraulic conditions at each gauge.

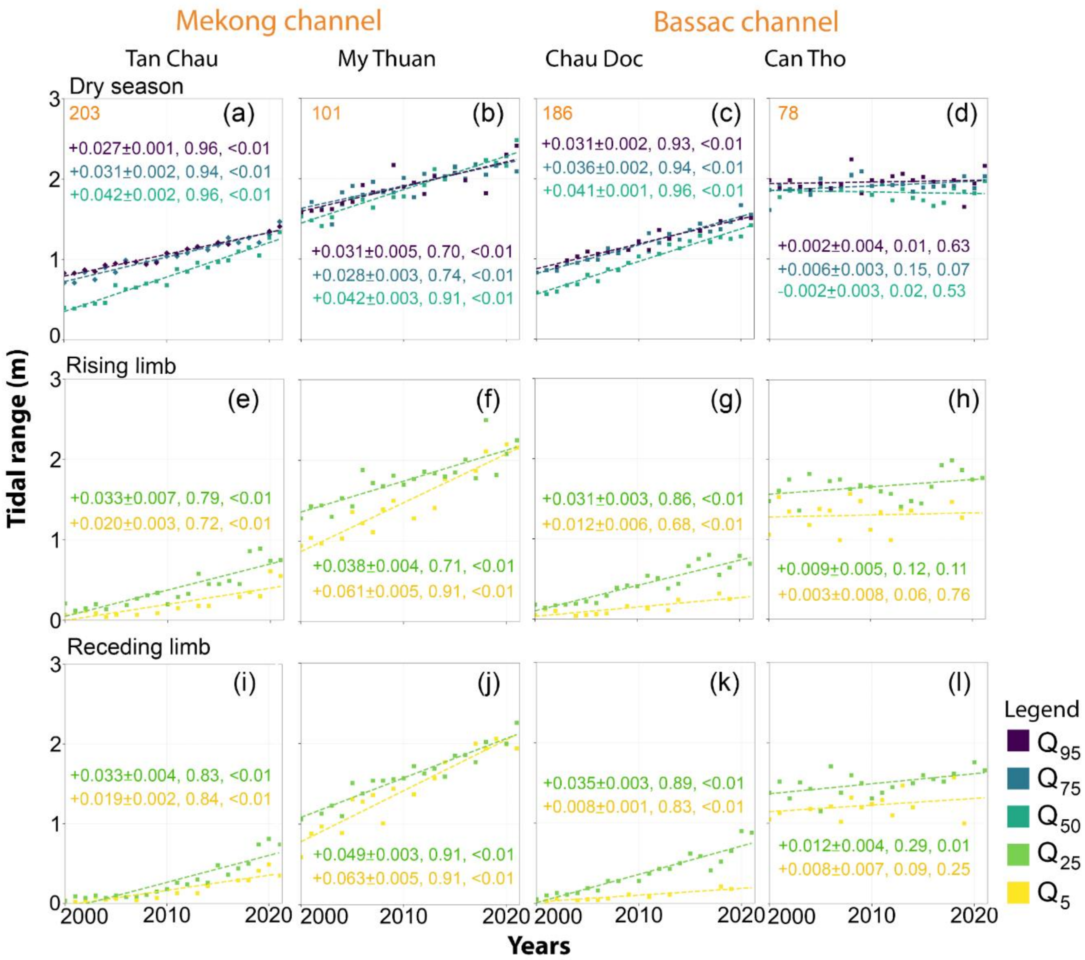

Figure 4-5. The alteration of tidal range for given quantiles of water at four gauging stations of the VMD from 2000 to 2021. The linear regression shows the long-term trajectory of change with numbers indicates the regression slope, R^2 and P-value**.**

4.3.2.1 Dry season

During the dry season, the TR showed increasing trends as it approached the seaward direction in both the Mekong and Bassac channels. The increases in flow discharge causes a reduction in the TR at all stations (Figure 4-4, Dry period). Regarding the temporal variation of the tidal range-discharge relationship, results indicate a consistent year-on-year increase in TR for the same discharge conditions throughout the 2000-2021 period for Tan Chau (203 km), My Thuan (101 km) in Mekong Channel and Chau Doc (186 km) on Bassac channel. The rising temporal trend in TR at Can Tho (78 km) in the Bassac channel is considerably smaller in magnitude compared to the other stations (Figure 4-4, Dry period).

Examining the TR values corresponding to specific quantiles of water discharge reveals a rising temporal trend in TR at all stations with the smallest magnitude observed at Can Tho station

(Figure 4-5, a, b, c and d). The overall rate of increase TR in these gauges, represented by the slope of the linear regression in the tidal range-discharge relationship, is particularly slightly higher at high water discharge values compared to lower discharge.

In more detail, in the Mekong channel, at Tan Chau station, for water flow at Q_{95}, the increase rate of TR is 0.027m ± 0.001 m yr^{-1} $(R^2 = 0.96, P < 0.01)$, leading to an accumulated increasing TR of 0.57 m ± 0.02 m for the 21-year period from 2000 to 2021. For water flow at Q_{75}, the increase rate of TR is 0.031m ± 0.004 m yr^{-1} $(R^2 = 0.94, P < 0.01)$, leading to an accumulated increasing TR of 0.65 m ± 0.04 m from 2000 to 2021. At Q_{50} the increase rate of TR is higher, at 0.042 m ± 0.002 m yr^{-1} $(R^2 = 0.94, P < 0.01)$, resulting in an accumulated TR rise of 0.88 m ± 0.04 m for the same period (Figure 4-5, a). At My Thuan, the increase rate of TR values at Q_{95} is 0.031m ± 0.005 m yr^{-1} $(R^2 = 0.97, P < 0.01)$, resulting in an accumulated increasing of TR is 0.65 m ± 0.11 m over the 21-year period from 2000 to 2021. The increase rate of TR values at Q_{75} and Q_{50} are 0.028m ± 0.003 m yr^{-1} $(R^2 = 0.74, P < 0.01)$ and 0.042 m ± 0.003 m yr^{-1}, $(R^2 = 0.91, P < 0.01)$, respectively, resulting in an accumulated increasing of TR is 0.59 m ± 0.06 m and 0.88 m ± 0.06 m), respectively, for the same period from 2000 to 2021 (Figure 4-5, b).

In the Bassac channel, at Chau Doc, the increase rate of TR at Q_{95} is 0.031m ± 0.002 m yr^{-1} $(R^2 = 0.93, P < 0.01)$ resulting in an accumulated increase of 0.65 m ± 0.04 m over the 21-year period from 2000 to 2021. The increase rate of TR at Q_{75} is 0.036m ± 0.002 m yr^{-1} $(R^2 = 0.94, P < 0.01)$ resulting in an accumulated increase of 0.76 m ± 0.04 m from 2000 to 2021. The increase rate of TR for higher discharge at Q_{50} is slightly higher, at 0.041m ± 0.001 m yr^{-1} $(R^2 = 0.96, P < 0.01)$ leading to an accumulated increase in TR of 0.86 m ± 0.04 m over the same period (Figure 4-5, c). At the Can Tho station, the temporal linear relationship indicating an increase in TR is not statistically significant across all percentile water discharge values. In more detail, at Q_{95}, Q_{75}, Q_{50}, the rise rate of TR are 0.002 m ± 0.004 m yr^{-1} $(R^2 = 0.01, P = 0.63)$, 0.006 m ± 0.003 m yr^{-1} $(R^2 = 0.15, P = 0.07)$, -0.002 m ± 0.003 m yr^{-1} $(R^2 = 0.02, P = 0.53)$, respectively (Figure 4-5, d).

4.3.2.2 Flood season

For both the rising and receding limbs of the flood season a general trend of increasing TR seaward is observed in both the Mekong and Bassac channels. Additionally, an increase in flow discharge causes a reduction in the observed TR at all stations (Figure 4-4, rising limb and receding limb). Regarding the temporal variation of the tidal range-discharge relationship, the results indicate a consistent year-on-year increase in TR for the same discharge conditions at all stations, except during the rising limb period at the Can Tho station, where there is no clear year-on-year trend in TR values (Figure 4-4, rising limb and receding limb, and Appendix, Table 6, Table 7), which will be discussed in detail in Section 4.4. It is observed that the temporal slope of the linear regression for the tidal range-discharge relationship in the landward areas, particularly at Tan Chau (203 km) and Chau Doc (186 km), was small (flattened) in historical years (approximately around 2000) for both the rising and receding limbs of the flood season (Figure 4-4, rising limb and receding limb and Appendix, Table 6, Table 7), which will discussed in detail in section 4.4.

Considering temporal changes of the relationship between tidal range for specific flow discharge quantiles (Figure 4-5), there is a temporal increase in TR across all discharge quantiles for all stations. A rise in TR is observed at the Can Tho station, albeit of a smaller magnitude compared to the other stations. In more detail, in Mekong channel, at Tan Chau (203 km), at Q_{25}, the increase rate in TR is 0.033 m ± 0.007 m yr^{-1} $(R^2 = 0.79, P < 0.01)$ and 0.033 m ± 0.004 m yr^{-1} $(R^2 = 0.83, P < 0.01)$ in rising limb and receding limbs, respectively. These increase rates in TR result in an accumulated rise of 0.69 m ± 0.15 m and 0.69 m ± 0.08 m for the rising limb and receding limb periods, respectively, over the 21-year period from 2000 to 2021 (Figure 4-5, e and i). The corresponding TR rise values for the higher discharge Q_5 are relatively smaller for both the rising limb and receding limb in compared with those for Q_{25}, at 0.020 m ± 0.003 m yr^{-1} $(R^2 = 0.72, P < 0.01)$ during the rising limb and 0.019 m ± 0.002 m yr^{-1} $(R^2 = 0.84, P < 0.01)$ during the receding limb. These increase rates in TR result in an accumulated TR rise of 0.42 m ± 0.06 m and 0.40 m ± 0.04 m for the rising limb and receding limb periods, respectively, from 2000 to 2021 (Figure 4-5, e and i). A comparable trend continues but becomes more noticeable farther seaward at the My Thuan station (101 km). For Q_{25}, the increase rate in the TR is 0.038 m ± 0.004 m yr^{-1} $(R^2 = 0.71, P < 0.01)$ during the rising limb and 0.049m ± 0.003 m yr^{-1} $(R^2 = 0.84, P < 0.01)$ during the receding limb. These increase rates result in an accumulated TR rise of 0.80 m ± 0.08 m and of 1.03 m ± 0.06 m for the rising limb and receding limb periods, respectively, from 2000 to 2021 (Figure 4-5, f and j). At the higher discharge Q_5, the increase rate in the TR is 0.061 m ± 0.005 m yr^{-1} $(R^2 = 0.91, P < 0.01)$ during the rising limb and 0.063 m ± 0.005 m yr^{-1} $(R^2 = 0.91, P < 0.01)$ during the receding limb. These increase rates in TR result in an accumulated TR rise of 1.28 m ± 0.11 m and 1.32 m ± 0.11 m for the rising limb and receding limb periods, respectively, from 2000 to 2021 (Figure 4-5, f and j).

In the Bassac channel, at the Chau Doc (186 km), at Q_{25}, the increase rate of TR is 0.031 m ± 0.003 m yr^{-1} $(R^2 = 0.86, P < 0.01)$ during the rising limb and 0.035m ± 0.003 m yr^{-1} $(R^2 =$

$0.89, P < 0.01)$ during the receding limb. These increase rates in TR result in an accumulated TR rise of 0.65 m ± 0.06 m and of 0.74 m ± 0.06 m for the rising limb and receding limb periods, respectively, from 2000 to 2021 (Figure 4-5, f and j). At the higher discharge Q_5, the increase rate of TR is smaller than those value for Q_{25} for both rising limb and receding limb, at 0.012 m ± 0.006 m year^{-1} $(R^2 = 0.68, P < 0.01)$ and 0.008m ± 0.001 m yr^{-1} $(R^2 = 0.83, P < 0.01)$ for rising limb and receding limb, respectively. These increase rates in TR result in an accumulated TR rise of 0.25 m ± 0.13 m and of 0.17 m ± 0.02 m for the rising limb and receding limb periods, respectively, from 2000 to 2021 (Figure 4-5, f and j). However, there is a considerable smaller increase in TR observed at the Can Tho station (78 km) in the Bassac channel compared to other stations (Figure 4-5, h and l). In more detail, the temporal linear relationship trend in TR is not statistically meaningful for both Q_{25} and Q_5 during the rising limb, at 0.009 m ± 0.005 m yr^{-1} $(R^2 = 0.12, P = 0.11)$ and 0.003 m ± 0.008 m yr^{-1} $(R^2 = 0.06, P = 0.76)$. During the receding limb, at Q_{25}, the increase rate of TR is 0.012 m ± 0.004 m yr^{-1} $(R^2 = 0.29, P = 0.01)$ resulting in a cumulative increase in TR of 0.25 m ± 0.08 m over the 21-year period from 2000 to 2021. However, at Q_5, the temporal linear relationship trend in TR is not statistically significant, with a rise rate of 0.008 m ± 0.007 m yr^{-1} $(R^2 = 0.09, P = 0.25)$ (Figure 4-5, h and l).

4.4 Discussion

In the present chapter, historical changes in the relationship between mean water levels, tidal range and the corresponding mean water discharge values across the VMD gauging stations from 2000 to 2021 for Tan Chau (203 km), My Thuan (101 km) in the Mekong channel and Chau Doc (186 km) and Can Tho (78 km) in the Bassac channel are presented in section 4.3.1 and 4.3.2. The analyses result from section 4.3.1 indicate the slope of the linear regression relationship between mean water levels and discharge has been decreasing (flattening) over time across all gauging stations during both the dry season and both limbs of the flood season, from 2000 to 2021. This suggests that changes in mean water levels ($\overline{WL}$) have become less dependent on the magnitude of freshwater flux and more influenced of mean sea level in the coast. An overall trend of decreasing $\overline{WL}$ at a given mean water discharge ($\bar{Q}$) is observed across all VMD gauging stations, with the decline is relatively small in seaward areas but more pronounced landward, and is more substantial at high discharge than at lower discharge.

The reduction of $\overline{WL}$ for a given $\bar{Q}$ could be explained by the increase in channel capacity following the definition of the "specific-gage" method, (Blench, 1969), which can be attributed to (i) decreased roughness, (ii) channel widening and (iii) channel deepening. However, decreased roughness of the riverbed does not seem to be the case here because riverine sand mining within the channel could contribute to riverbed coarsening, thereby increasing the riverbed roughness (Yang et al., 2017). Regarding channel widening, it is noted that historical Google Earth satellite images for these gauging stations show stable riverbanks around the measured cross-section areas (Appendix, Figure 2). Although the available historical Google Earth satellite images do not cover entire period of the analysis (2000-2021), from 2007 to 2021, the width of the measured cross-section at Tan Chau station narrowed by 10 m (1.5 % channel width reduction), while the channel width at Chau Doc station narrowed by 14 m (4.0 %) during the same period. From 2003 to 2021, My Thuan station's width narrowed by 18 m (1.1 %). However, from 2001 to 2021, My Thuan station's width increased by 2 m (0.2 %). Hence, the observed consistent trend of decreasing mean water levels at given discharge in gauging stations within the VMD is primarily linked to the modification of the river shape, particularly riverbed lowering. This riverbed lowering is estimated to be approximately 2.5 m (σ= 3.9 m) in the VMD for the 1998-2018 period (Vasilopoulos et al., 2021). Riverbed lowering increases channel depth and capacity, reducing water levels for a given discharge, with the effect being more pronounced during high water flux conditions (flood season) as enhanced channel capacity dampens the rise in $\overline{WL}$ relative to $\bar{Q}$. During low water flux conditions (dry season), this impact is less noticeable as channel capacity is not fully utilized, and relatively stable coastal water levels (Nguyen et al., 2023) play a greater role in influencing $\overline{WL}$. As a result, the effect of riverbed lowering on $\overline{WL}$ reduction is more evident during high water flux conditions than during low water flux conditions, leading to the temporal flattening of the linear regression relationship between mean water levels and discharge.

An exception is noted where the mean water level-discharge relationship shows a tendency for the $\overline{WL}$ to decrease with increasing mean water discharge in the seaward stations. This pattern has been observed at My Thuan station during the dry season since 2009 (see Figure 4-2, and Appendix, Table 1) and during the receding limb of the flood season in recent lowest water discharge years (year 2015, 2016, 2021) at both the My Thuan and Can Tho stations (see Figure 4-2, and Appendix, Table 2). This phenomenon is likely due to $\overline{WL}$ at this gauge station being more influenced by seasonal variations in mean sea level within the Mekong coastal zone. In more detail, the highest mean sea levels along the Mekong coast typically occur in December-January, reaching around 0.25 m relative to Hon Dau MSL at Vam Kenh station, Mekong channel coast (see Figure 3-1, Chapter 3 for the location), this peak of mean water level coincides with the start of the dry season (see Fig. 4, Nguyen et al., 2023). These mean sea levels gradually decrease to a lowest value of approximately -0.3 m relative to Hon Dau MSL (at Vam Kenh station) around June-July, at the end of the dry season, based on long-term sea level observations from 1997 to 2015 (Fig. 4, Nguyen et al., 2023). As a result, the impact of seasonal mean sea level causes the $\overline{WL}$ to gradually decrease during the dry season, despite the influence of fresh water discharge, which typically decreases from the beginning of the dry season (around December) to mid-dry season (around March) and then rises from March to the end of the dry season (around June) (see Figure 4-1). Similarly, the decrease of $\overline{WL}$ during the receding limbs of the flood season in recent lowest water flux years (2015, 2016, 2021) (see Figure 4-2), when water discharge is low, the influence of seasonal variations in mean sea level at seaward stations (My Thuan, Can Tho) becomes more pronounced. Since seasonal mean sea levels along the coast generally rise from June to July and typically peak in December to January (Nguyen et al., 2023), the mean water levels at these stations may gradually increase during the receding limb (typically from September to December) in tandem with rising sea levels, despite the gradual decrease in water discharge during this period.

The findings from section 4.3.2 also revealed a consistent temporal trend of increasing tidal range across the region, with a relatively smaller increase in Can Tho compared to other stations. This trend of increasing landward tidal propagation could be attributed the riverbed lowering, which increases channel capacity and promotes the tidal signal from the sea to the landward direction (Vasilopoulos et al., 2021). The relatively smaller increase in tidal amplitude observed at Can Tho station (78km), compared to other stations, could be attributed to its closer proximity to the river mouth. Additionally, one potential reason for this observation could be the relatively minor reduction in the riverbed elevation at the mouth of the Bassac channel based on observed bathymetric data from 1998 to 2018 (see Figure 5-6, Chapter 5), which could reduce the impact of increasing tidal signals caused by riverbed lowering (Eslami et al., 2019). However, the observed riverbed lowering between 1998-2018 indicates a substantial deepening of channel bed levels upstream of Can Tho (see Figure 5-6, Chapter 5), which explains the higher increase in tidal range observed at Chau Doc (187 km). In addition, the increasing sea level could potential increasing tidal ingress in Can Tho station (Fujihara et al., 2016).

It is observed that the temporal slope of the linear regression for the tidal range-discharge relationship in the landward areas, particularly at Tan Chau (203 km) and Chau Doc (186 km), is considerable small (flattened) in historical years (approximately around 2000) for both the rising and receding limbs of the flood season (Figure 4-4, rising limb and receding limb and Appendix, Table 6, Table 7). This could be explained by the fact that the tidal range values, which measure the amplitude of the water level by subtracting the minimum water level from the maximum water level during a 25-hr tidal cycle, can be affected by changes in the mean water level caused by high fresh water flux during both limbs of the flood season. This is especially true in historical years during both limbs of the flood season when the tidal range was considerable smaller across all water discharge conditions (tidal range < 0.4m) compared to recent observations. As a result, the tidal range values may have been affected by these uncertainties led to a reduction in the slope of the linear regression for the tidal range-discharge relationship. This uncertainty in tidal range calculation will be addressed in Section 5.3, Chapter 5, where the tidal range for the entire Lower Mekong River and MD will be calculated.

There are also uncertainties associated with this method and the utilized observed dataset. These constraints arise from the accuracy of the dataset for water level and water discharge used at the gauging stations (see section 3.1.1, Chapter 3). They can be attributed to variations in the instruments used for measurement, changes in cross-section, or errors in the velocity measurements used to calculate water discharge (Brauer and River, 2009; Slater, 2014) as well as land subsidence. All of the above could potentially cause errors on the water level record. In more detail, land subsidence has been estimated to be 0.34 m at Can Tho, (Figure 2, location H, Erban et al., 2014), 0.09 m at Tan Chau, 0.08 m at Chau Doc, and 0.13 m at My Thuan between 2000 to 2021 (Figure 6, Minderhoud et al., 2017). Although this may have impacted the water level record, these cumulative changes are much smaller than the quantified amount of channel incision which is approximately 3 m for the Bassac at Can Tho and Chau Doc and approximately 2.5 m for the Mekong at My Thuan and Tan Chau (see Figure 1, Vasilopoulos et al., 2021 and also Figure 5-6, Chapter 5 of this Thesis).

In addition, the recorded sea level rise along the coast of the VMD has been estimated at approximately 0.0022 ± 0.0003 m yr^{-1} over the past 40 years since 1980 (Nguyen et al., 2023). This could result in an increase of around 0.05 ± 0.006 m over the period of 2000-2021, which is similar to the sea level rise values estimated by NASA, (2021) at the Vung Tau station in Mekong coast (0.06 m in 2020 compared to the 1995-2014 baseline). Although this could potentially also increase the mean water level and tidal range recorded in gauging stations the magnitude of change is much smaller compared to the quantified mean channel incision of 2.5 m (σ = 3.9 m) for the VMD (Vasilopoulos et al., 2021).

The results outlined above demonstrate that riverbed lowering has altered the historical relationships between mean water level, tidal range, and water discharge in the delta at both spatial and temporal scales. This includes a pronounced reduction in water levels inland and an increase in the tidal range across the VMD delta. Moreover, water dynamics are now more influenced by mean sea level and less by fresh water flux, particularly in seaward regions, indicating that the impact of sea level is becoming more pronounced in the delta.

Dynamically changing water levels, influenced by fresh water flux and tidal conditions, are crucial to delta function. Therefore, alterations in these relationships could have varied impacts on delta-related issues. For example, the decrease in water levels during both the dry season and the flood season has both positive and negative implications. On the positive side, this reduction in water level is anticipated to alleviate future flood risks in the upstream part, especially in the face of the growing frequency of high-water discharge events associated with extreme climate phenomena, such as typhoons and heavy rain (MONRE, 2016). For example. at Tan Chau (203km) at high water discharge value Q_5 = 21,200 m^3s^{-1}, the decrease in accumulated water could reach 1.63 m ± 0.28 m during the rising limb period and 1.83 m ± 0.33 m during the receding limb period from 2000 to 2021. In contrary, the decline in water levels also gives rise to a range of adverse consequences. These include the disconnection of the river and its floodplain (Strick, 2016), reduced efficiency of irrigation systems (Figure 4-6), and challenges in navigation within the river delta networks (Paarlberg et al., 2015).

Furthermore, the increase in tidal range driven by both riverbed lowering and sea level rise, compounded by factors like land subsidence and elevated sea levels, has the potential to heighten the risk of tidal, storm surges (Wood et al., 2023). The details of how riverbed lowering and sea level rise have impacted water level dynamics, along with the implications of these changes, will be discussed further in Section 5.5, Chapter 5.

Figure 4-6. A recent decrease in water levels in the upper part of VMD has resulted in reduced efficiency of infrastructure elements like pumps and sluice systems. The photo took place in 2019 and provided by SIWRR

4.5 Chapter Summary

In the present Chapter, historical changes in the relationship between mean water levels, tidal range, and corresponding discharge values at the VMD gauging stations are presented. This analysis addresses the first objective (O1) of the study, which is to assess historical changes in the delta's flow dynamics resulting from channel bed level lowering and responds to the specific Research Question (RQ1): How has historical riverbed lowering affected delta hydraulics?

The analysis indicates that the slope of the linear regression relationship between mean water levels and discharge has been decreasing (flattening) over time at all gauging stations, during both the dry season and both limbs of the flood season, from 2000 to 2021. Additionally, an overall trend of declining mean water levels at a given mean water discharge is evident, with the decrease being less significant in seaward areas but more pronounced in landward regions and more substantial during high-discharge conditions compared to lower discharge. Furthermore, there is a consistent temporal trend of increasing tidal range across the region. These observed changes are primarily driven by riverbed lowering, which has significantly altered the channel's capacity and hydrodynamic behaviour, emphasizing its critical role in shaping the evolving flow dynamics of the Vietnamese Mekong Delta.

However, limitations exist regarding the observed data used, and these findings are constrained to the VMD region. To address these limitations and extend the analysis of water level evolution to the Lower Mekong River and Cambodian Mekong delta, where data is limited, Chapter 5 will utilize 1D modelling to quantify the relationship between riverbed lowering and the subsequent changes in water level patterns across spatial and temporal scales of the Lower Mekong River and the Mekong Delta.

Chapter 5. Modelling the effects of riverbed lowering and sea level rise on delta hydrology

Chapter 4 utilized the historical gauge record across the Vietnamese Mekong delta (VMD) to demonstrate how riverbed lowering has contributed to substantial changes in mean water level and tidal range over the past 21 years from 2000 to 2021. However, data limitations did not allow the same analysis to be performed for the Cambodia part, which includes the Lower Mekong River (LMR) and Cambodian Mekong Delta (CMD) and it is uncertain how riverbed lowering there might be affecting local water levels and tidal amplitudes. For the Cambodian part, this difficulty is further exacerbated by the additional complexity added by the connection to the Tonle Sap Lake (TSL). In order to better understand ongoing changes of flow dynamics across the entire LMR and Mekong Delta (MD) and project them into the future under different scenarios of future riverbed lowering and sea level rise, this Chapter utilizes a one-dimensional (1D) hydrodynamic model, (MIKE 11) to provide insights into the changes of water level and tidal amplitude across the LMR and Mekong delta (MD), with implications for channel-floodplain connectivity. It is noted here that water exchanges between the Mekong and the Tonle Sap Lake will be the specific focus of Chapter 6 and so are not discussed in the present Chapter. This chapter addresses the second objective (O2) of the research, which aims to understand the evolution of the hydraulic regime in the LMR and MD under projected future scenarios of riverbed lowering and sea-level rise, and to answer the specific research question: (RQ.2) How will hydraulics in the Lower Mekong Basin (LMB) change in the future due to projected riverbed lowering and sea-level rise? The present Chapter is structured as follows; Section 5.1 will introduce the 1D model, along with the calibration and validation processes. Section 5.2 will describe the scenarios investigated, including various levels of river bed lowering, sea level rise and upstream fresh water flux. This model scenarios will be used for both Chapter 5 and Chapter 6. The approach to analysing model results will be outlined in Section 5.3 and results will be presented in Section 5.4. Section 5.5 will discuss the broader implications of hydrodynamic changes in delta function. Finally, Section 5.6 will summarize the key findings of the Chapter.

5.1 1D hydraulic model

5.1.1 Model setup

A 1D hydrodynamic model, MIKE 11, is used to simulate the hydraulics across the entire river network of the alluvial Lower Mekong Basin extending from Kratie in Cambodia, to the Mekong delta shoreline. The model domain encompasses the channel network, TSL, and the floodplains within the LMR and MD (Figure 5-1). The model was initially set up for this region by the

Southern Institute of Water Resources Research (SIWRR) in Viet Nam and has been widely used to understand the hydraulics of the TLS, LMR and MD and assess flood risk (Dung et al., 2011; Manh et al., 2014). The model employs the WGS84 coordinate system and elevations are in reference to the Hon Dau MSL. The topographic data for the mainstream Mekong channels and Tonle Sap River are gathered and updated through various projects with different levels of accuracy Dung et al., (2011). The floodplains in CMD lack significant channels and dikes, therefore, they are represented by channels using wide cross-sections (Dung et al., 2011). In contrast, the floodplains in VMD, which are divided into numerous flood cells to protect agricultural activities, are depicted as channels with wide cross-sections enclosed by dikes (Dung et al., 2011). The topography of these floodplains is derived directly from the Shuttle Radar Topography Mission (SRTM) Digital Elevation Model (DEM) from 2000, which features a horizontal resolution of 90 m and has been thoroughly calibrated and validated against observed inundation data in the floodplain for the years 2008 and 2009, respectively (Dung et al., 2011). The upstream model boundary is forced with daily water discharge ($m^3 s^{-1}$) at Kratie. Rainfall data within the Tonle Sap basin has been transformed into daily discharge at 11 boundary points for the Tonle Sap Lake by using the rainfall-runoff model NAM (Dung et al., 2011). To define downstream boundary conditions along the coastal area of the Mekong, tidal stage measurements from 10 coastal stations named: Vung Tau, Vam Kenh, Binh Dai, An Thuan, Ben Trai, My Thanh, Ganh Hao, Song Doc, Xeo Ro, Rach Gia are utilized (Figure 5-1), providing tidal data at an hourly resolution (Dung et al., 2011). The tidal levels at these boundaries are taken from the nearest tidal stations (Dung et al., 2011).

Given that the river bathymetry dataset is an essential component of the modelling, the bathymetric data used in existed 1D models, as sourced from various outlets with varying degrees of error and lacking temporal synchronization (Dung et al., 2011). Therefore, in this study, the main bathymetry in the mainstream of the Mekong channels is updated, as described herein. Elevation data for the reaches in Cambodia and parts of Viet Nam was obtained from bathymetry data collected by hydrographic surveys in 1998 by the Mekong River Commission (MRC) (here adopted from Vasilopoulos et al., 2021) and the Mekong Atlas survey in 1998, which were obtained from the ISIS model developed by MRC (here adopted from Dung et al., 2011) (Figure 5-2). The historical analogue for the spatially missing data in 1998 within the VMD (Figure 5-2, a) is adopted from Vasilopoulos et al., (2021). A total of 419 cross-section datasets is then extracted at approximately 3 km intervals along the entire 1998 Mekong channel bathymetry elevation surface, combining both the observed 1998 data and the analogous 1998 topography data in missing sections. This cross-sectional dataset is then integrated into the 1D model. Dyke crest elevations are adjusted to match the elevation of the floodplain, allowing water from side channels to flow onto the floodplain during the flood season. This adjustment reflects the condition of the dyke system in the VMD in 2000 (Triet et al., 2017).

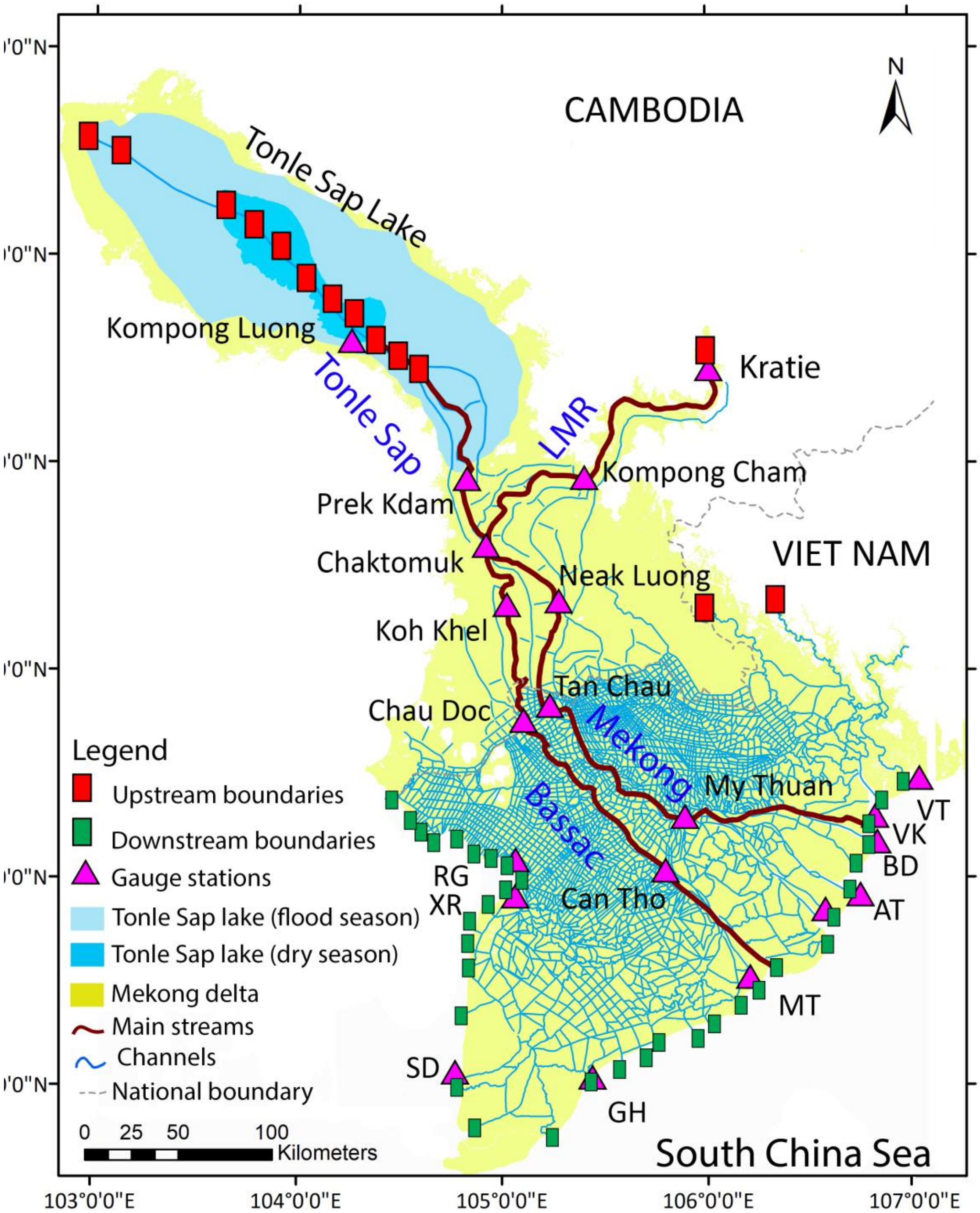

Figure 5-1. 1D model domain including the Lower Mekong River (LMR), Tonle Sap River and Lake and the Mekong Delta, also highlighting the location of the hydrological gauging stations.

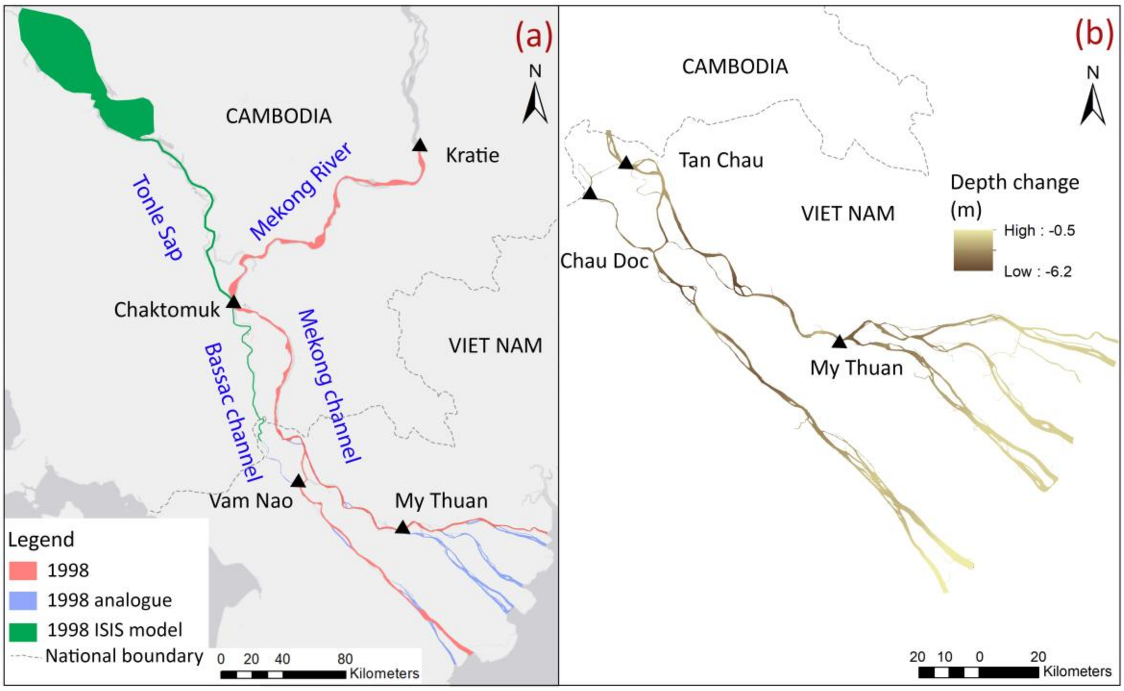

Figure 5-2. (a) The coverage areas of different mainstream river bathymetry datasets employed in generating a cross-sectional dataset for 1D modelling, (b) The spatial progression of main channels deepening in VMD from 1998 to 2018 adopted from Vasilopoulos et al., (2021)

5.1.2 Model calibration and validation

Calibration is the process of adjusting input parameter and initial settings within acceptable ranges until the simulated outcomes closely align with observed data (Ritter and Muñoz-carpena, 2013; Moriasi et al., 2015; Knoben et al., 2019) and validation is the process of demonstrating that a calibrated model can accurately replicate a set of field observations or predict future conditions without additional adjustments to the calibrated parameters (Moriasi et al., 2015). The calibration and validation processes require the use of model performance measures along with corresponding evaluation criteria (Gupta et al., 2009; Moriasi et al., 2015; Duc and Sawada, 2023). Model performance measures refer to the statistical and graphical techniques employed and the associated quantitative thresholds for the statistical measures of interest, while the corresponding evaluation criteria pertain to qualitative ratings of model performance (e.g. very good, good, satisfactory, or unsatisfactory) (Ritter and Muñoz-carpena, 2013; Moriasi et al., 2015; Clark et al., 2021).

Some model performance measures are commonly used in hydrological modelling, including the Root Mean Squared Error ($RMSE$), referred to as the standard error of the estimate in regression analysis. The $RMSE$ is expressed in the same units as the model's output variable and represents the typical error magnitude, with a value of 0 indicating a perfect fit (Moriasi et al., 2007). The coefficient of determination (R^2) represents the proportion of variance in the observed data that is explained by the model. R^2 ranges from 0 to 1, with higher values indicating less error variance. Generally, values greater than 0.5 are considered acceptable (Moriasi et al., 2007). The dimensionless Nash-Sutcliffe efficiency coefficient (NSE) is a normalized statistic that quantifies the complement to unity of the ratio between the mean squared error of observed versus predicted values and the variance of the observations (Nash and Sutcliffe, 1970). This dimensionless metric (NSE) assesses how well the plot of observed versus simulated data aligns with the 1:1 line and ranging from $-\infty$ to 1, where NSE of 1 signifies perfect agreement between the model simulation and the observations (Nash and Sutcliffe, 1970). Kling–Gupta efficiency (KGE) is calculated as the Euclidean distance using the coordinates of bias, standard deviation, and correlation between model simulations and observations (Gupta et al., 2009). In general, positive KGE values indicate satisfactory model simulations, while negative KGE values are considered unsatisfactory (Siqueira et al., 2018; Towner et al., 2019)

However, these model performance measures have both strengths and limitations. For instance, R^2 is highly sensitive to extreme values and does not adequately account for additive or proportional differences between model predictions and observed data (Legates and McCabe, 1999). The extremely skewness of daily streamflow observations (particularly during high flow events) lead to uncertainty in both NSE and KGE metrics (Clark et al., 2021; Duc and Sawada, 2023). A limitation of the KGE metric is that it combines many hydrologically important aspects of model performance—such as the shape of rising limbs and recessions, and the timing of peak flows—into a single correlation component (Knoben et al., 2019). A detailed discussion on the advantages and disadvantages of each model performance measure listed in Table 5 of Moriasi et al., (2015), and further explored in Clark et al., (2021). Therefore, it is crucial to understand the theoretical behaviour and limitations of system-scale performance metrics as well as evaluating uncertainties in model inputs is essential (Clark et al., 2021).

In this study, the Nash-Sutcliffe model efficiency coefficient (NSE; Eq. 7) (Nash and Sutcliffe, 1970), which has been widely recognized and utilized in hydrological modelling (Moriasi et al., 2007; Gupta et al., 2009; Ritter and Muñoz-carpena, 2013; Duc and Sawada, 2023) was used to assess the quality of the comparison between the calibrated predictions and the observed data. This metric was chosen because the flow data in the study area—comprising alluvial and delta regions (LMR, TSL, and MD)—does not exhibit extreme skewness, as exanimated from observed water discharges and levels in the gauging stations across the region (see Table 3-1, Chapter 3). Therefore, the NSE is deemed suitable for this application.

$$NSE = 1 - \frac{\sum_{t=1}^{T}(X_m^t - X_0^t)^2}{\sum_{t=1}^{T}(X_0^t - \overline{X_0})^2} \quad (7)$$

Where X_m^t is the calibrated value at time t and X_0^t is the observed data at time t, $\bar{X}_0$ represents the mean of observed values. NSE values below 0.5 indicate a calibration that is not performing well, while values exceeding 0.5 suggest satisfactory model performance. NSE values higher than 0.65 indicate a well-performing calibration, and values exceeding 0.8 indicate a highly accurate calibration (Ritter and Muñoz-carpena, 2013; Moriasi et al., 2015).

The 1D model is calibrated using timeseries data from the year 2000 (from 1 January 2000 to 31 December 2000). This was a very high fresh water flux year with the total volume of water flowing through Kratie being approximately 523 billion m^3, much higher than the 2000-2021 average of 390 billion m^3 (a volume exceedance frequency of ~3% in the in the range data from 2000 to 2021; Figure 5-3, a). Model validation was subsequently conducted using timeseries data from water year 2003 - a low fresh water flux year (from 1 December 2002 to 31 November 2003) with a total volume of water flowing through Kratie equal to 328 billion m^3 (a volume exceedance frequency of ~72%) (Figure 5-3, a). The selected years of high and low fresh water flux are also evident from the series of discharge records at gauging stations along the VMD (Figure 5-3, a). In addition, both the 2000 and 2003 water years are temporally close to the elevation data from 1998 that are used to define the model domain, which minimizes the impact of riverbed morphology changes on the hydraulic regime. The simulated daily water discharge at the 11 Tonle Sap tributary boundaries, obtained from the NAM model, was incorporated into the modelling for the years 2000 and 2003. The total water volume for these years was estimated at 37.3 billion m^3 for 2000 and 24.3 billion m^3 for 2003. These estimates are in close agreement with those reported by Kummu et al., 2014, which are 42.1 billion m^3 for 2000 and 20.9 billion m^3 for 2003.

The simulated hourly water levels and discharge are extracted at gauging stations in LMR, TSL system and MD (Figure 5-4) for calibration and validation purposes. The available water level data was provided as daily data for the LMR and CMD stations, and as hourly data for the VMD station (see Table 3-1, Chapter 3). Therefore, the simulated daily water level data for the LMR and CMD gauging stations was derived though averaging the hourly simulated data. The hourly simulated water level and water discharge for VMD will be retained for calculating the NSE and for comparison purposes.

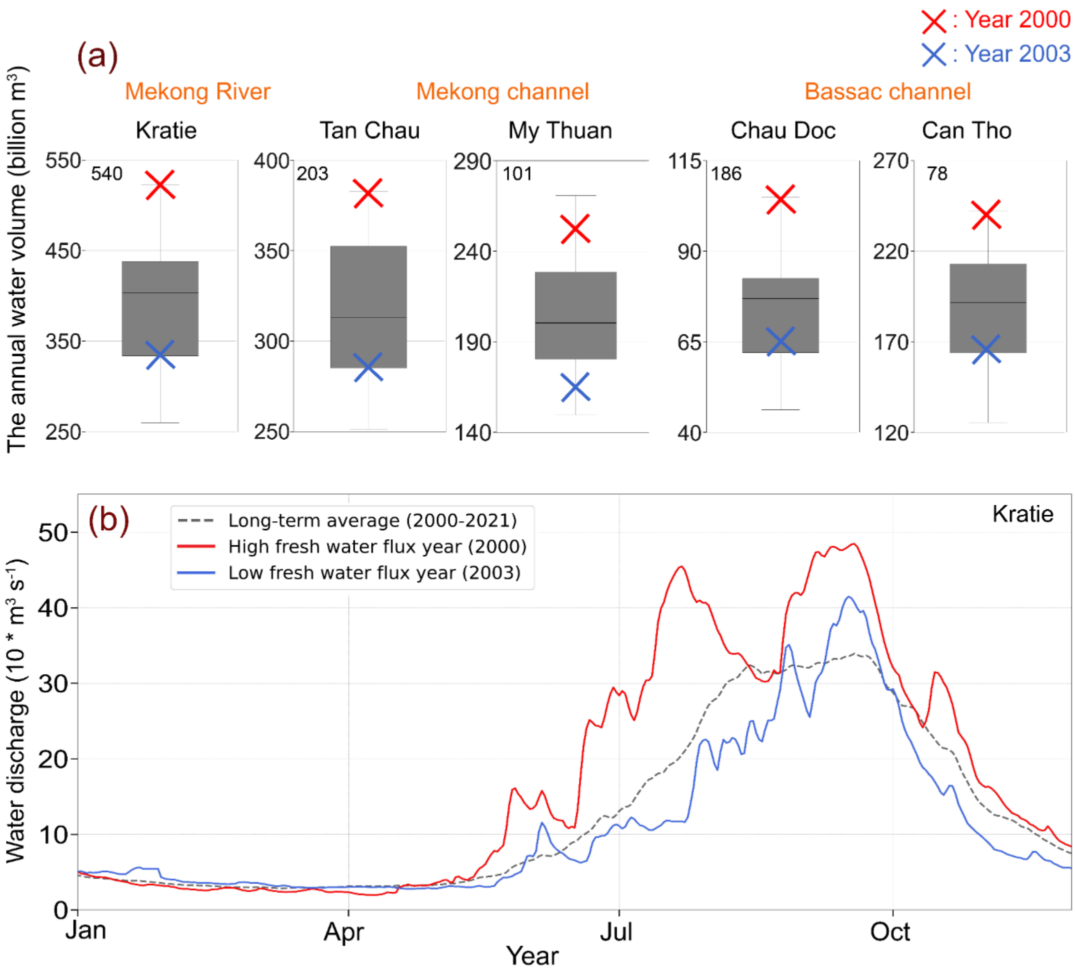

Figure 5-3. (a) Boxplots showing range of annual flow volume in range gauging station within LMR and MD as estimated from MRC and SRHMC monitoring gauges (see Table 3-1, Chapter 3) for 2000-2021 highlighting the distinct years chosen to simulate high (2000) and low (2003) flow discharge conditions to calibrate and validate the numerical model. The number situated at the upper left corner of each panel specifies the distance from the gauge to the channel mouth; (b) Observed long-term average hydrograph for Kratie for 2000-2021 (black) also showing hydrographs for 2000 (red) and 2003 (blue) used in model calibration and validation.

The calibration process involved adjusting the Manning roughness parameter until modelled depths best matched observed values, which is a standard procedure in hydraulic models. The hydraulic roughness for the model was adopted by Manh et al., (2014), who divided the model domain into distinct zones and assigned a different Manning's value on each zone. This division ensures that the selected roughness coefficient accounts for the distinct hydraulic characteristics of each zone. Manning's n values were systematically adjusted until the best match between water level and water discharge outputs were generated (Table 5-1). The model's predictions results were extracted and compared to the corresponding observed data. If the model's performance was considered unsatisfactory, the roughness coefficient in these zones was adjusted, and the model was rerun until optimal results were achieved through several iterations. The duration of each model run was 7 hours per scenario.

Simulated timeseries of water level and water discharge were compared against observations recorded from the existing network of gauging stations (see Figure 5-1 and Table 3-1, Chapter 3 for the locations). The results (Figure 5-4, Table 5-2) reveal a strong overall agreement between the simulated outcomes and the corresponding observed water level and water discharge throughout the gauging stations across the entire channel network. The NSE values for water level in all gauging stations exceeds 0.8 indicating a highly accurate calibration, with the exception of the My Thuan station during the dry season, for which the NSE value is only slightly lower at 0.75, which still indicates a well-performing calibration (Table 5-2). The NSE values for discharge in gauging stations within the VMD also exceeds 0.8 during the dry season, with the exception of the Can Tho station, which stands slightly lower at 0.73. However, during the flood season, the NSE values tend to decrease with the lowest NSE value at the Tan Chau station being 0.53, indicating satisfactory performance, while values for the remaining stations and all higher than 0.7, indicating a good overall performance. The reduced NSE values for water discharge may lead to inaccuracies in simulating the exchange of water flow between the floodplain and the main river stream, particularly during periods of high-water discharge stage (Manh et al., 2014).

Table 5-1. The Manning roughness coefficient (n) is categorized based on different zones using in the modelling. The Manning roughness in the channel changing for different cross-sections within the same zone

Zone	Description	Manning's coefficient (n)
1	Mekong River: Kratie to Phnom Penh	0.032 to 0.035
2	Mekong channel: Phnom Penh to Tan Chau	0.031 to 0.032
3	Mekong channel: Tan Chau to My Thuan	0.025 to 0.032
4	Mekong channel: My Thuan to River months	0.018 to 0.025
5	Bassac channel: Phnom Penh to Chau Doc	0.031 to 0.032
6	Bassac channel: Chau Doc to Can Tho	0.022 to 0.031
7	Bassac channel: Can Tho to River months	0.017 to 0.022
8	Side channels	0.035

9	Floodplains	0.037

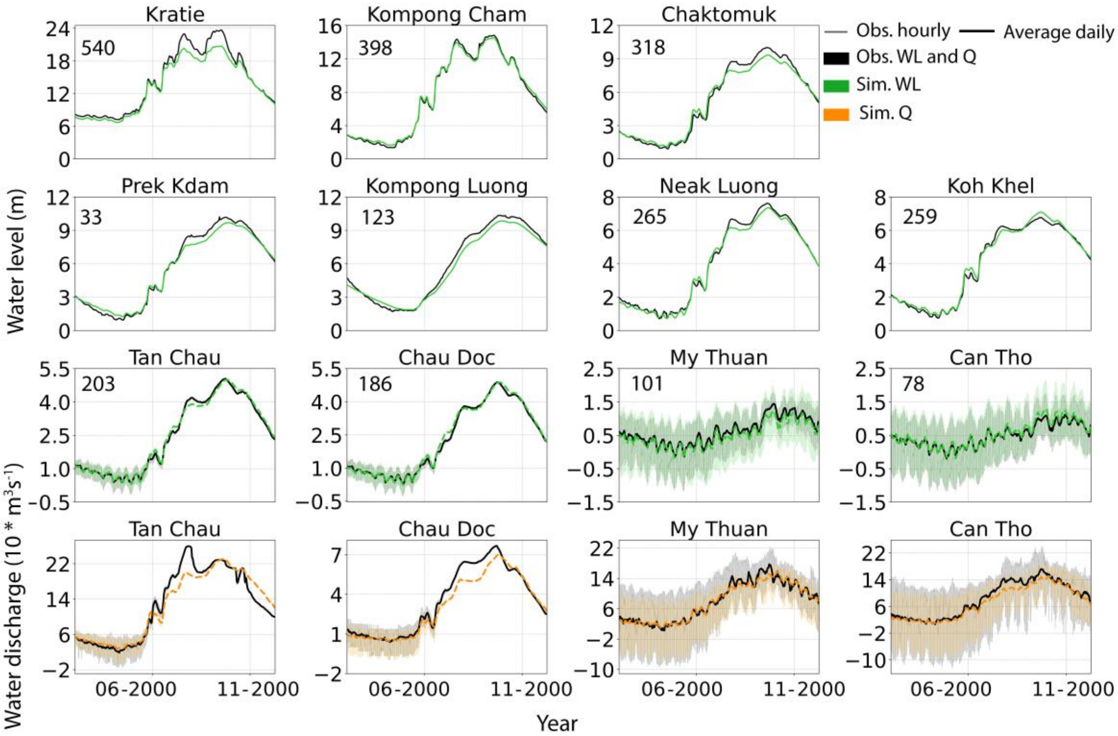

Figure 5-4. Comparison of model predictions and observed values for water level and water discharge at monitoring stations throughout the model domain during the calibration run in high fresh water flux year of 2000. It is noted monitoring stations within Cambodia territory (Kratie, Kompong Cham, Chaktomuk, Prek Kdam, Kompong Luong, Neak Luong, and Koh Khel) only provide recordings at a daily resolution, therefore, the hourly simulated data in these gauges is converted into mean daily values to facilitate comparison. In contrast, the data from the monitoring stations within VMD are at hourly intervals. The figure panels for the VMD gauges present both hourly data but also daily means.

Table 5-2. The NSE coefficient was calculated across a range of gauge stations throughout model domain for distinct dry and flood periods during the calibration step for the high fresh water flux condition

No	Water level (WL)		Water discharge (Q)	
	Dry	Flood	Dry	Flood
Kratie	0.93	0.86		
Kompong Cham	0.98	0.99		
Chaktomuk	0.86	0.93		
Prek Kdam	0.88	0.95		
Kompong Luong	0.91	0.95		
Neak Luong	0.87	0.97		
Koh Khel	0.94	0.96		
Tan Chau	0.94	0.98	0.82	0.56
Chau Doc	0.95	0.98	0.84	0.73
My Thuan	0.87	0.75	0.93	0.83
Can Tho	0.96	0.93	0.73	0.76

The model parameter set was then validated by assessing its performance for a low flood year by simulating the conditions of 2003. Comparison between observed and simulated data (Figure 5-5, Table 5-3), demonstrate a robust overall model performance for the entire region. There is a persistent trend of high agreement in water level values and also overall strong agreement in term of water discharge for all stations with NSE values for water level and water discharge surpassing 0.8, indicate highly accurate performance. The only exception is found for the Chaktomuk station during the dry season, with an NSE of 0.67, indicating good performance (Table 5-3).

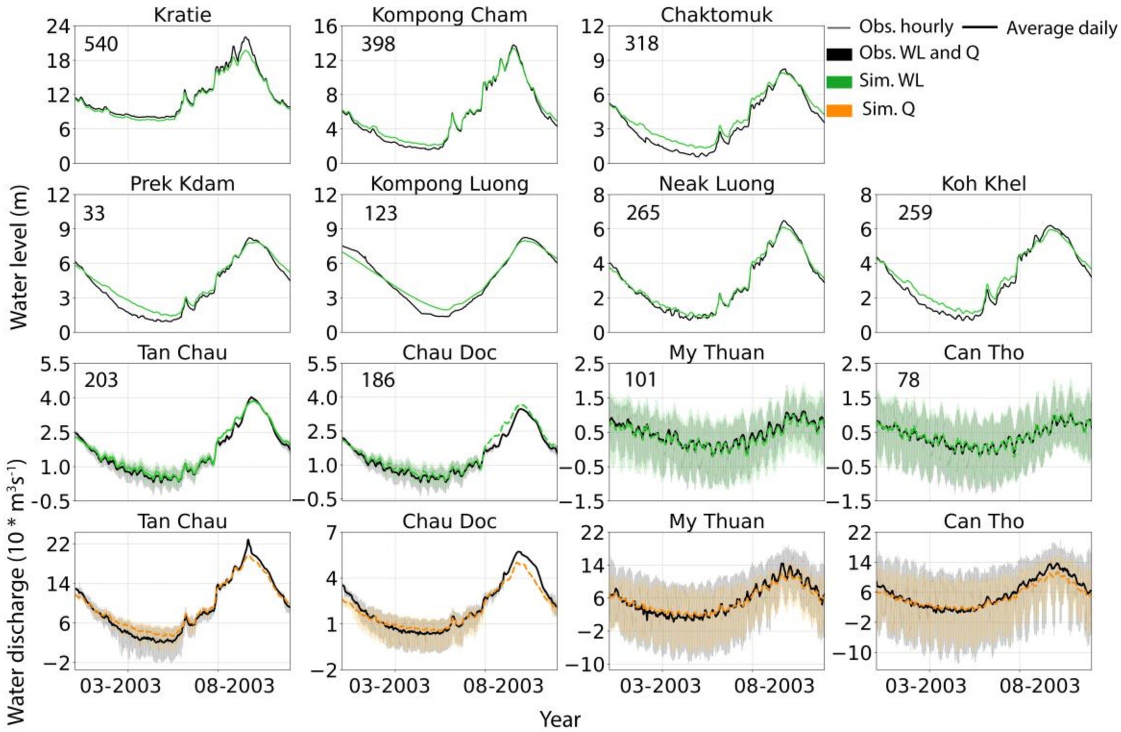

Figure 5-5. Comparison of model predictions and observed values for water level and water discharge at monitoring stations throughout the model domain during simulation of low-fresh water flux year of 2003.

Table 5-3. The NSE was calculated by taking into account various gauge stations throughout the model domain the validation step. The values were separately for distinct dry and flood periods in the low fresh water flux condition

No	Water level (WL)		Water discharge (Q)	
	Dry	Flood	Dry	Flood
Kratie	0.9	0.88		
Kompong Cham	0.9	0.99		
Chaktomuk	0.67	0.94		
Prek Kdam	0.80	0.98		
Kompong Luong	0.92	0.98		
Neak Luong	0.96	0.98		
Koh Khel	0.83	0.95		
Tan Chau	0.96	0.97	0.85	0.95
Chau Doc	0.94	0.88	0.85	0.85
My Thuan	0.89	0.82	0.94	0.85
Can Tho	0.97	0.97	0.83	0.82

In summary, the model shows robust performance in both the calibration and validation stages, confirming its suitability for developing various model scenarios to analyse the hydraulic evolution in the LMB.

5.2 Model scenarios

To examine the potential future response of the system to a range of anthropogenic perturbations a series of scenario combinations where designed which are described below.

5.2.1 Future channel bed levels

To assess the influence of channel bed level lowering on the hydrology of the system, two additional scenarios of channel bathymetry were constructed. The Contemporary scenario closely matches channel bed elevations surveyed in 2018 (see section 3.2.1, Chapter 3) while the Future scenario presents hypothetical bathymetries 20 years into the Future (year 2038) assuming a linear future trajectory of channel bed level lowering. Both scenarios use the 1998 model domain as their basis which is then vertically offset in a way that reflects observed and future trajectories of channel bed level lowering, which are spatially variable. Details are described herein.

For the TSR and TSL previous studies have indicated that sedimentation in the TSL remains minimal, with the net sedimentation accumulation in the TSL totalling only 0.5–0.7 m over the period from approximately 5500 years BP to the present (Tsukawaki, 1997; Penny et al., 2005; Kummu et al., 2008). Furthermore, there is little-to-no sand extraction occurring on the TSR (Hackney et al., 2021). Therefore, the model cross-sections from the 1998 model domain for these reaches were retained for both Contemporary and Future bathymetry scenarios.

To create a contemporary bathymetric scenario for the Lower Mekong River and the Delta, the first step involved calculating the cumulative riverbed lowering from 1998 to 2018. This calculation was based on the range of bathymetric data for the LMR and MD from 1998, 2013, and 2018, as detailed in Chapter 3 (3.2.1). However, since the available riverbed data is not continuous across the entire LMR and MD but instead covers different sections of the LMR and MD system at different times, so the riverbed lowering from 1998 to 2018 was calculated separately for each part of the LMR and MD system, as described below.

For the LMR from Kratie to Chaktomuk and the Mekong delta channel from Chaktomuk to Neak Luong, two DEMs of river bathymetry in 1998 and 2013, covering the river reach from Kratie to Neak Luong (Figure 3-3, Chapter 3) were differenced using the spatial analyst toolbox (Raster

Calculator) in ArcGIS. The laterally averaged depth difference between the 1998 and 2013 bathymetry DEMs was then calculated at 1 km intervals along the main channels.

To calculate the riverbed lowering in this reach (LMR and Mekong channels from Chaktomuk to Neak Luong) from 2013 to 2018, several steps are undertaken. First, the upstream region of the LMR, from Kratie to Kompong Cham (see Figure 5-1), experiences significantly lower rates of sand and gravel extraction, approximately 10 times less than those in the area from Kompong Cham to the Cambodia-Viet Nam border (see Figure 5-1) (Bravard et al.,2013). In contrast, the observed riverbed lowering rates from 1998 to 2013 indicate that the area from Kratie to Kompong Cham had only experienced slight shallowing. Therefore, it was assumed that there was no change in the riverbed from Kratie to Kompong Cham during the period from 2013 to 2018. According Hackney et al., (2021), in the LMR and Mekong channel, stretching from Kompong Cham to the Chaktomuk and from Chaktomuk to Cambodia- Viet Nam border (see Figure 5-2, a), a net negative sand budget has led to substantial riverbed lowering, with a median rate of 0.26 m yr^{-1} between 2013 and 2019. Consequently, the estimated riverbed lowering from 2013 to 2018 is 1.3 m across the entire reach of the LMR from Kompong Cham to Chaktomuk, and the Mekong channels from Chaktomuk to Neak Luong. Finally, the laterally averaged depth data from 1998 to 2013 are then merged with the accumulated riverbed lowering data from 2013 to 2018 to calculate a record of riverbed lowering with 1 km intervals spanning in LMR and Mekong channel from Chaktomuk to Neak Luong for the period from 1998 to 2018.

To estimate the accumulated riverbed lowering in Mekong channel, where data is lacking, spanning from Neak Luong to the Cambodia- Viet Nam border during the same period from 1998 to 2018, linear interpolation is applied between the two sets of averaged riverbed lowering value at Neak Luong and at Cambodia- Viet Nam border, which is adopted from Vasilopoulos et al., (2021) from 1998 to 2018 (see Figure 5-2, b). For the Bassac channel, spanning from Chaktomuk to the Cambodia- Viet Nam border, there is a lack of riverbed lowering information. Therefore, the accumulated riverbed lowering in the Bassac channel in this area is assumed to be the same as that from Chaktomuk to the Cambodia- Viet Nam border in the Mekong channel. The laterally averaged depth difference between 1998 and 2018 bathymetry DEMs in the Mekong and Bassac channel within VMD, as adopted from Vasilopoulos et al., (2021) (Figure 5-2, b), was calculated at 1 km intervals along the main channels.

The riverbed lowering data in the LMR, Mekong and Bassac channel spanning from Chaktomuk to Cambodia- Viet Nam border, is integrated with the riverbed lowering information within

VMD, collected at 1 km intervals from 1998 to 2018. These depth difference data were further categorized into 10 km sections by averaging the 1 km data to delineate a more gradual trend in riverbed lowering, thereby reducing the impact of sand pits caused by sand mining activity. This resulted in an average riverbed lowering of 2.38 m (σ = 2.22 m) in the LMR from Kratie to Chaktomuk, 3.19 m (σ = 1.39 m) in the Mekong channel from Chaktomuk to the coastal zone and 3.45 m (σ = 1.64m) in the Bassac channel from Chaktomuk to the coastal zone. The overall average riverbed lowering across the entire system was 3.06 m (σ = 2.03 m) (Figure 5-6, a).

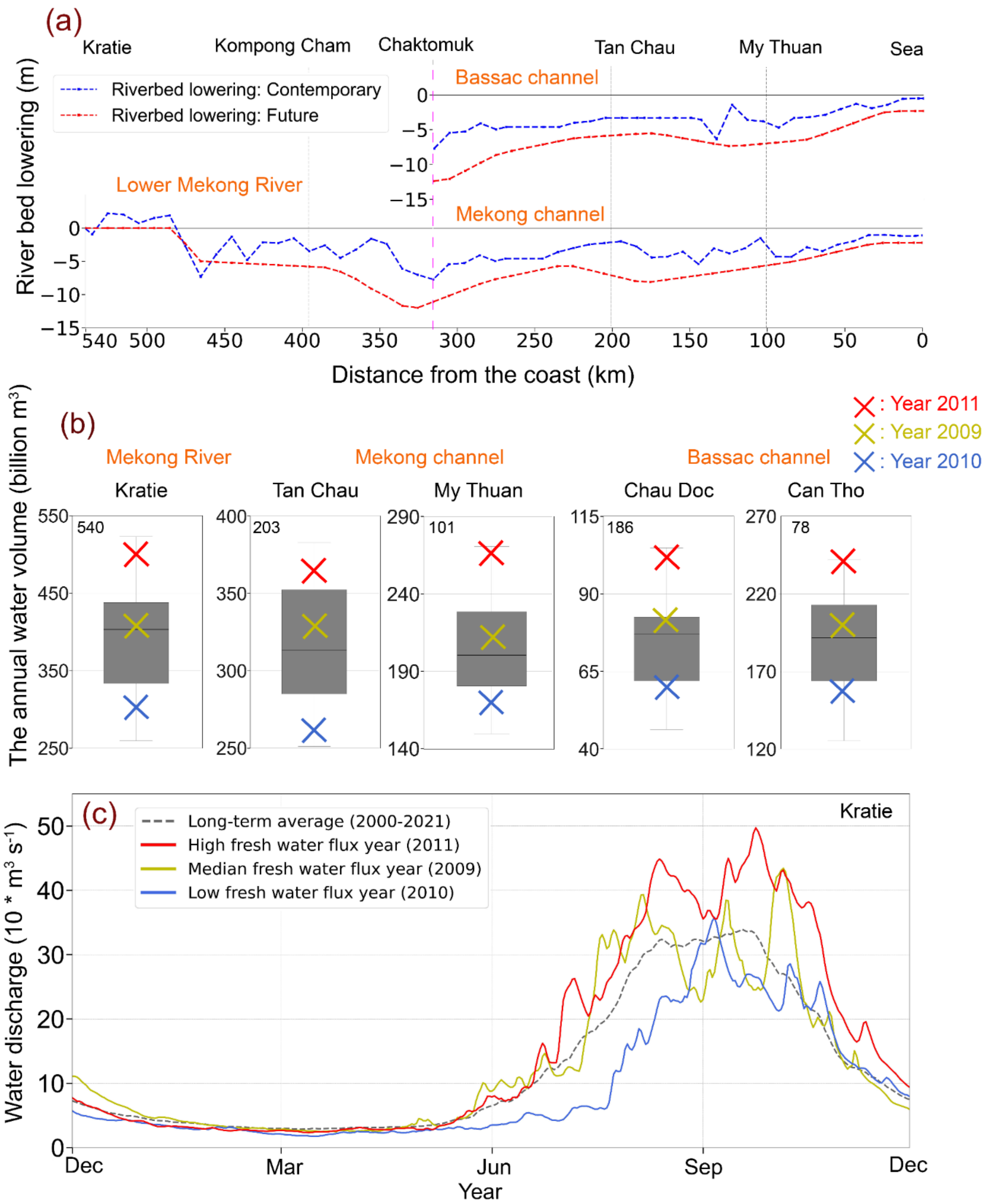

Figure 5-6. (a) Development of two scenarios for the accumulated average riverbed lowering: one comparing the Baseline historical scenario with the Contemporary scenario (1998-2018), and the other comparing the Baseline scenario with Future projections (1998-projected 2038), along the longitudinal axis of the LMR and two main Mekong and Bassac channels. The outcomes show an average riverbed lowering of 3.06 m (σ = 2.03 m) from 1998 to 2018 and 5.92 m (σ = 2.84 m) for the 1998 to 2038 scenarios for system. (b) Boxplots of total annual water volume recorded at different gauges across the LMR and MD system for the 2000-2021 period highlighting datasets high- (2011) median- (2009) and low-(2010) fresh water flux years; (c) Discharge hydrographs as estimated at Kratie for the years 2009 (median flow scenario; yellow), 2010 (low flow scenario; blue) and 2011 (high flow scenario; red) in relation to the long term mean hydrograph for the period 2000-2021.

To forecast the future topography of riverbeds, a situation is hypothesized where the trend in riverbed incision observed between 1998 to 2018 would continue until 2038. This long-term observed rate subtracted from the bathymetry data of 2018. The difference riverbed between 1998 and the projected future bathymetry of 2038 shows an average lowering of 5.20 m (σ = 3.86 m) in the LMR, 6.06 m (σ = 2.29 m) in the Mekong channel, and 6.45 m (σ = 2.45 m) in the Bassac channel. The combined average riverbed lowering for entire system was calculated to be 5.92 m (σ = 2.84 m) (Figure 5-6, a).This scenario assumes substantial sand deposits on the river bed, supported by evidence that the spatial variation in the thickness of sand beneath the channel across the alluvial reaches of the Mekong, which can range from up to 45 m near Kampong Cham to 25 m south of Phnom Penh (Uhlemann et al., 2017) and the alluvial sediment deposits in and around the Mekong delta channel are estimated at approximately 28 m (Hackney et al., 2020). It is observed that in a small area near Kratie in the Lower Mekong River, the depth differences exhibit positive values, indicating a shallower trend from 1998 to 2018 (Figure 5-6, a). Therefore, in the depth differences from 1998 to the projected 2038, the positive values of depth difference change were set to 0 m, indicating no change in riverbed elevation between 1998 and the future 2038 in the upper LMR of the domain, close to Kratie. The elimination of positive values in the difference in riverbed elevation between 1998 and 2038 in this zone is supported by the anticipation that the riverbed will continue to descend in the future, owing to the effects of sand mining and sediment starvation caused by upstream dams. Finally, a series of cross-sections are extracted at approximately 3-km intervals along the entire Contemporary and Future scenarios bathymetries to integrate into the 1D model.

5.2.2 Eustatic sea-level rise scenarios

Future scenarios of sea level rise (SLR) have been presented in Chapter 2 both in a global context (Section 2.2.1) and for the Mekong specifically (Section 2.3.2). Taking into account these future projections, the eustatic sea-level rise scenarios employed in the model adopt an SLR of 0 m, 0.5m and 0.5 m, to replicate baseline/historical (1998), and mid-century (approx. 2050, similar to the projected Future riverbed lowering scenarios) and end of century (approx. 2100) projected sea levels (NASA, 2021). Two additional scenarios of 2.0 m and 2.5 m mean sea level rise are also considered, these reflect a pathway with very high rates of emissions (RCP8.5) that could trigger rapid ice sheet collapse (NASA, 2021). These scenarios of sea level rise are applied in the model by utilizing the hourly tidal record at a series of gauging stations along the Mekong's coastal area from 1998 (Table 3-1, Chapter 3). Sea level rise values are then added to these records to replicate the effects under various future projections.

5.2.3 Scenarios of water flux.

Finally, three scenarios of water fluxes are chosen from the hydrograph record of Kratie to represent a low (2009), median (2010), and high (2011) water year, covering the period from December to the following December. 2011 was a year of high fresh water flux, with the total volume of water flowing through Kratie estimated at approximately 500 billion m^3. This is above the 2000-2021 estimated average of 390 billion m^3. The exceedance frequency of water volume in 2011 was approximately 7%. 2009 was a year of average fresh water flux, with the total volume of water flowing through Kratie estimated at approximately 415 billion m^3. The exceedance frequency of water volume in 2009 was approximately 37%. 2010 was a low fresh water year with the total volume of water flowing through Kratie estimated at approximately 301 billion m^3, below the 2000-2021 estimated average of 390 billion m^3. The exceedance frequency of water volume in 2010 was approximately 88% (Figure 5-6, b). The simulated daily water discharge at the 11 Tonle Sap tributary boundaries, derived from the NAM model for selected years, was incorporated into the modelling. The total water discharge contributed to the lake from the Tonle Sap basin tributaries is estimated at 27.6 billion m^3 for 2011 (a high-water flux year), 22.5 billion m^3 for 2009 (a median-water flux year), and 16.5 billion m^3 for 2010 (a low-water flux year). These values highlight the hydrological variability across different water flux years. For comparison, the average total discharge from the Tonle Sap basin tributaries was reported as 23.8 billion m^3 from 1997 to 2003 (MRCS/WUP-FIN, 2007).

5.3 Analysis method

The combination of three riverbed lowering scenarios: Baseline historical (referencing the 1998 bathymetry condition), Contemporary (2018), and Future (projected 2038) scenarios, three scenarios of fresh water flux and five scenarios of eustatic sea-level rise generated a total of 45 scenarios to be investigated. The present chapter will focus on three key reaches from the model domain; the Lower Mekong River (LMR) from Kratie to the delta apex at the Chaktomuk Junction; the principal Mekong distributary delta channel from Chaktomuk to the coast via Tan Chau and My Thuan and the Bassac distributary delta channel from Chaktomuk to the coast via Chau Doc and Can Tho (Figure 5-7).

Figure 5-7. (a) Map of the lower Mekong and delta highlighting (red) the selected reaches for which model result are extracted and analysed in the present Chapter.

Model outputs include simulated water level and discharge at hourly intervals for an entire water year. These are extracted at location intervals of approximately 10 km along the reaches investigated (Figure 5-7). From the timeseries predictions the annual minimum, maximum is calculated, while mean water level ($\overline{WL}$) are calculated for the dry season, rising limb and receding limb separately. To calculate the predicted tidal range (TR), the method described in Section 4.2.1, Chapter 4 was adopted, however, this approach may introduce some uncertainty in the TR values due to changes in the mean water level, which can be affected by high upstream flow during both phases of the flood season, as discussed in Section 4.4, Chapter 4. To mitigate the impact of these changes on TR values, several steps were implemented. Firstly, a 25-hour tidal cycle window was initially used to extract the minimum, maximum, and mean water level predictions from the time series. The change in the mean water level ($\overline{WL}_{change}$) during a tidal cycle is calculate by Eq. 8 and see Figure 5-1.

$$\overline{WL}_{change\_tc1} = \left|\frac{(\overline{WL}_{tc1} - \overline{WL}_{tc0}) + (\overline{WL}_{tc2} - \overline{WL}_{tc1})}{2}\right| \quad (8)$$

Where, $\overline{WL}_{change\_tc\ 1}$ represents the mean water level change during 25-hour tidal cycle 1 (see Figure 5-8).

$\overline{WL}_{tc0}, \overline{WL}_{tc1}, \overline{WL}_{tc2}$ are the mean water level during tidal cycle 0, 1 and 2 respectively (see Figure 5-8)

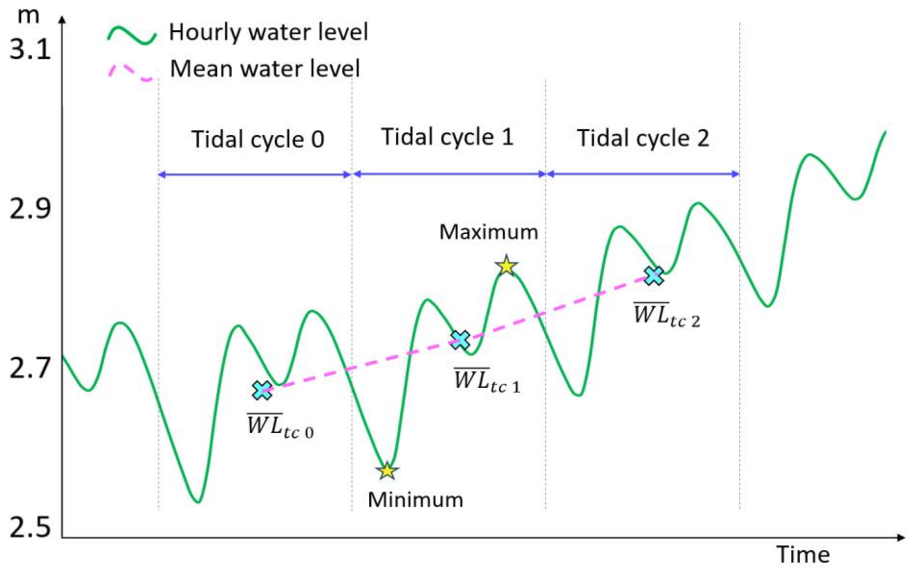

Figure 5-8. A representation of the method used to calculate the tidal range.

The $\overline{WL}_{change}$ is minimal in the downstream areas of the LMB system but more pronounced in the upstream regions. For instance, during the high fresh water flux year scenarios, at Tan Chau (203 km from the coast) in the Mekong Channel the average $\overline{WL}_{change}$ are minor, at around 0.02 m, 0.03 m, and 0.03 m for the dry season, rising limb, and receding limb, respectively. Similar values are observed at Chau Doc station (178 km) in the Bassac Channel as in Tan Chau station. However, these changes become more noticeable upstream. At Kompong Cham (398 km) in LMR (see Figure 5-1), the average $\overline{WL}_{change}$ are approximately 0.05 m, 0.12 m, and 0.11 m during the dry season, rising limb, and receding limb periods, respectively.

To mitigate the impact of upstream flow on tidal range calculation, it is assumed that, if the amplitude of fluctuation of water level, calculated by the maximum water level subtracts the minimum water level during a 25-hour tidal cycle, exceeds the change in the mean water level ($\overline{WL}_{change}$) in a tidal cycle period, there is a tidal signal present. Conversely, if the fluctuation does not exceed the $\overline{WL}_{change}$, we consider the area to have no tidal signal and assign it a value of 0 m. The tidal range is calculated by Eq. 9.

$$TR_{tc1} = \begin{cases} WL_{\mathrm{max\_tc1}} - WL_{\mathrm{min\_tc1}} - \overline{WL}_{change\_tc1} & if\ (WL_{\mathrm{max\_tc1}} - WL_{\mathrm{min\_tc1}}) > \overline{WL}_{change\_tc1} \\ 0 & if\ (WL_{\mathrm{max\_tc1}} - WL_{\mathrm{min\_tc1}}) \leq \overline{WL}_{change\_tc1} \end{cases} \quad (9)$$

TR_{tc1} is the tidal range during tidal cycle 1

$WL_{\mathrm{max\_tc\,1}}$, $WL_{\mathrm{min\_tc\,1}}$ is the maximum and minimum water level during tidal cycle 1 respectively

Subsequently, the tidal range is grouped ($\overline{TR}$) for the dry season, and both limbs of flood season.

5.4 Results

The present Section will explore the impact of riverbed lowering, sea level rise, and the combination of both on water levels (mean, maximum, and minimum) and tidal range in the LMB system. Section 5.4.1 will focus on the effects of riverbed lowering, Section 5.4.2 will address the effects of sea level rise, and Section 5.4.3 will examine the combined impact of riverbed lowering and sea level rise.

5.4.1 Changes in water level and tidal amplitude due to riverbed lowering

To isolate the effects of riverbed lowering, the present Section will provide a detailed description of changes in water level and tidal amplitude under the investigated scenarios of riverbed lowering for 0 m sea level rise.

5.4.1.1 Effects of riverbed lowering on mean water level

Table 5-4 shows that for a high fresh water flux year, compared to the Baseline historical scenario, in the Lower Mekong River (LMR), the $\overline{WL}$ for the Contemporary scenario is lower than the Baseline historical scenario by an average of 1.05 m (σ = 1.19 m), for the dry season. However, there is some seasonality in the magnitude of these impacts, with riverbed lowering reducing water levels less during the dry season than the flood season (rising and receding limbs), with the highest reduction observed at the receding limb of the flood season (Table 5-4). In more detail, during the rising and receding limbs of the flood season, these average of $\overline{WL}$ decrease is higher, by 1.58 m (σ = 0.71 m) and 1.92 m (σ = 0.86 m), respectively. The $\overline{WL}$ reductions are further exacerbated in the Future scenario, where they amount to an average of 2.43 m (σ = 0.78 m), 3.44 m (σ = 0.80 m), and 3.96 m (σ= 0.77 m) for the dry season, rising and receding limbs, respectively. The simulated decrease of $\overline{WL}$ is smaller in areas close to the coast compared to those in the landward part in LMR. More specifically, in the Mekong channel, under the Contemporary scenario, the $\overline{WL}$ is reduced by an average of 0.29 m (σ = 0.28 m), 0.44 m (σ = 0.37 m), and 0.74 m (σ = 0.60 m) during the dry season, rising limb, and receding limb, respectively. These reductions in $\overline{WL}$ are more pronounced in the Future scenario, where they amount to an average reduction of 0.41 m (σ = 0.38 m), 0.87 m (σ = 0.75 m), and 1.31 m (σ = 1.10 m) for the dry season, rising limb, and receding limb, respectively. In the Bassac channel, under the Contemporary scenario, the $\overline{WL}$ decreases by an average of 0.40 m (σ = 0.39 m) during the dry season, 0.43 m (σ = 0.40 m) during the rising limb, and 0.75 m (σ = 0.60 m) during the receding limb. These reductions in $\overline{WL}$ are more pronounced in the Future scenario, where they amount to an average reduction of 0.55 m (σ = 0.49 m), 0.90 m (σ = 0.65 m), and 1.39 m (σ = 0.99 m) for the dry season, rising limb, and receding limb, respectively, compared to the Baseline historical scenario (Table 5-4). Similar trends have been found for simulations using the median and low fresh water flux conditions and are included in Table 5-4.

Figure 5-9 shows the seaward areas for both Mekong and Bassac channels extending from the coast up to approximately 100 km landward show a minimal reduction in $\overline{WL}$ (<0.2 m) regardless of the extent of riverbed lowering, which could reach up to 5.92 m (σ = 2.84 m) in the Future scenario (Figure 5-6, a). In reaches further landward, the impact of riverbed lowering on reducing $\overline{WL}$ is more pronounced. For example, at 480 km from the coast in LMR, the largest decrease in $\overline{WL}$ for the Contemporary scenario is showed, with reductions of 2.40 m, 2.32 m, and 2.59 m compared to the Baseline historical scenario during the dry season, rising limb, and receding limb periods, respectively (Figure 5-9). In the Future scenario, the decrease in $\overline{WL}$ is more pronounced, with a reduction of 3.60 m at 500 km from the coast in LMR during the dry season, and reductions of 4.34 m and 4.71 m at 410 km from the coast during the rising limb and receding limb periods, respectively, compared to the Baseline scenario (Figure 5-9). It should be noted that for the Contemporary scenario, in the reaches from 490 km landward from the coast to Kraite (540 km), the $\overline{WL}$ becomes higher than in the Baseline historical scenario. This is because of a local shallowing of the Contemporary bathymetry compared with Baseline historical bathymetry there (see Figure 5-6, a). Similar trends have been found for simulations using the median and low fresh water flux conditions and are included in the Appendix, Figure 3 and Figure 4.

Table 5-4. Average changes in mean water level ($\overline{WL}$) along the LMR, Mekong and Bassac distributary delta channels under Contemporary and Future bathymetric scenarios compared to the Baseline historical scenario are presented for all fresh water flux scenarios investigated with 0 m of sea level rise. Positive values indicate an increase in water level (m), while negative values indicate a decrease (m). The values in parentheses represent the standard deviation.

Fresh water flux scenarios/ Riverbed bathymetry scenarios		Lower Mekong River			Mekong channel			Bassac channel		
		Dry	Rising limb	Receding limb	Dry	Rising limb	Receding limb	Dry	Rising limb	Receding limb
Low fresh water flux year	Contemporary (-3.06 m)	-0.99 (1.21)	-1.67 (0.85)	-1.79 (0.98)	-0.29 (0.28)	-0.40 (0.38)	-0.55 (0.52)	-0.40 (0.39)	-0.41 (0.40)	-0.60 (0.53)
	Future (-5.92 m)	-2.34 (0.78)	-3.61 (0.81)	-3.75 (0.72)	-0.41 (0.37)	-0.79 (0.76)	-0.95 (0.90)	-0.54 (0.48)	-0.86 (0.69)	-1.08 (0.88)
Median fresh water flux year	Contemporary (-3.06 m)	-1.10 (1.18)	-1.66 (0.81)	-1.89 (0.99)	-0.29 (0.28)	-0.45 (0.40)	-0.68 (0.60)	-0.39 (0.39)	-0.46 (0.42)	-0.73 (0.60)
	Future (-5.92 m)	-2.53 (0.80)	-3.55 (0.80)	-3.88 (0.72)	-0.42 (0.39)	-0.87 (0.79)	-1.13 (1.02)	-0.56 (0.50)	-0.92 (0.69)	-1.26 (0.96)
High fresh water flux year	Contemporary (-3.06 m)	-1.05 (1.19)	-1.58 (0.71)	-1.92 (0.86)	-0.29 (0.28)	-0.44 (0.37)	-0.74 (0.60)	-0.40 (0.39)	-0.43 (0.40)	-0.75 (0.60)
	Future (-5.92 m)	-2.43 (0.78)	-3.44 (0.80)	-3.96 (0.77)	-0.41 (0.38)	-0.87 (0.75)	-1.31 (1.10)	-0.55 (0.49)	-0.90 (0.65)	-1.39 (0.99)

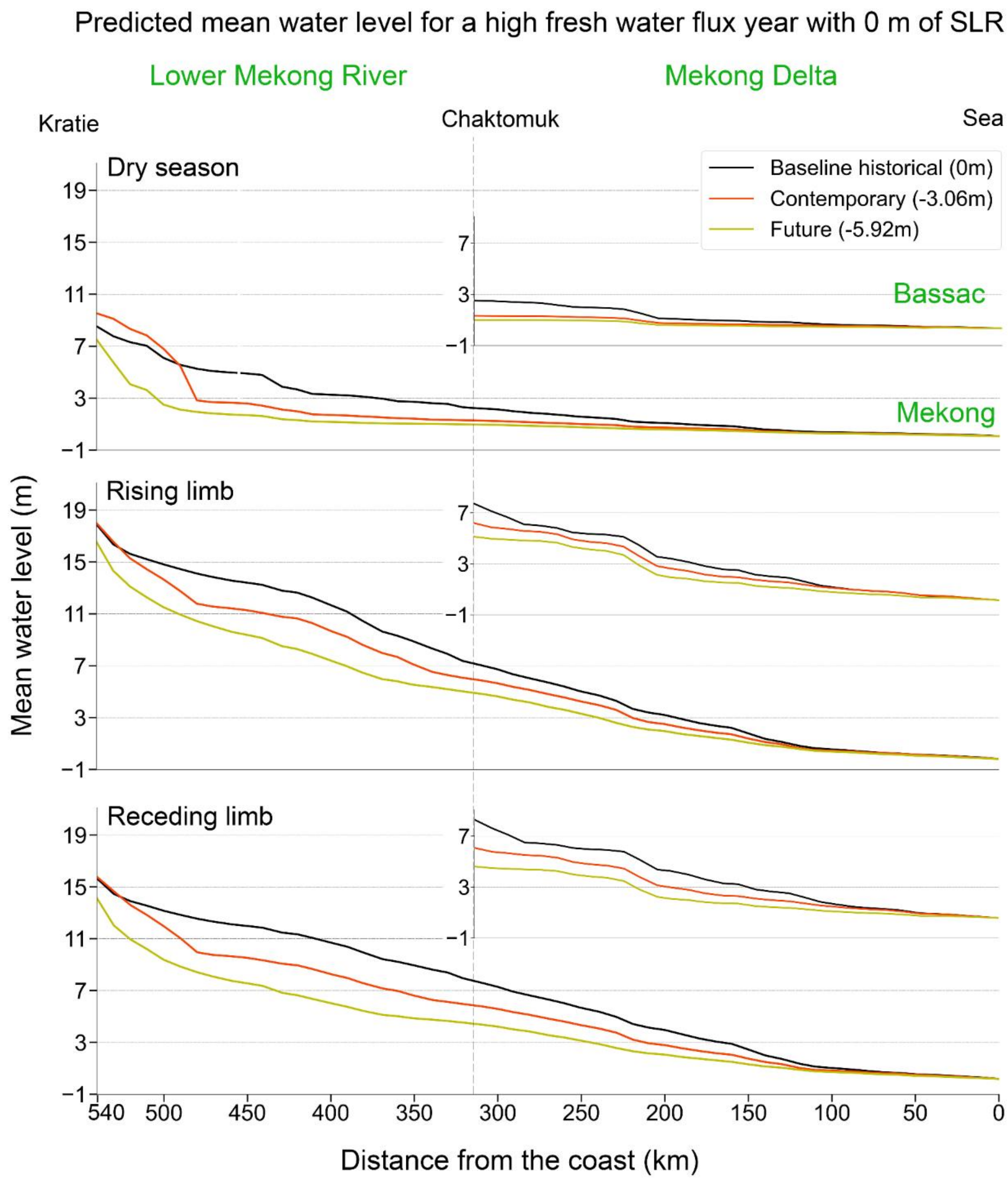

Figure 5-9. Longitudinal profile of mean water level ($\overline{WL}$) along the LMR, Mekong and Bassac distributary delta channels for the bathymetric scenarios investigated under high fresh water flux year and 0 m of sea level rise. The main panel focuses on the LMR and Mekong channel, while the insert panel shows the Bassac channel. All water levels are referenced to Hon Dau Mean Sea Level (MSL).

5.4.1.2 Effects of riverbed lowering on mean tidal amplitude

Table 5-5 shows under low water flux year conditions in the LMR, compared to the Baseline historical scenario, the Contemporary scenario exhibits an average increase in $\overline{TR}$ of 0.15 m (σ = 0.13 m) during the dry season and no change during both limbs of the flood season. Average increases in $\overline{TR}$ are more pronounced in the Future scenario, amounting to 0.41 m (σ = 0.23 m), 0.02 m (σ = 0.03 m), and 0.06 m (σ = 0.06 m) for the dry season, rising limb, and receding limb, respectively. The simulated increasing of $\overline{TR}$ is higher in areas close to the coast compared to those in the landward parts. In more detail, in the Mekong channel, the Contemporary scenario shows an average increase in $\overline{TR}$ of 0.31 m (σ = 0.14 m), 0.21 m (σ = 0.12 m), and 0.26 m (σ = 0.16 m) for the dry season, rising limb, and receding limb, respectively. In the Future scenario, the average increase of $\overline{TR}$ are more pronounced, amounting to 0.58 m (σ = 0.27 m), 0.51 m (σ = 0.27 m), and 0.59 m (σ = 0.32 m) for the dry season, rising limb, and receding limb of the flood season, respectively (Table 5-5) In the Bassac channel, the Contemporary scenario shows an average increase in $\overline{TR}$ of 0.24 m (σ = 0.22 m), 0.09 m (σ = 0.14 m), and 0.13 m (σ = 0.18 m) for the dry season, rising limb, and receding limb, respectively. In the Future scenario, the average increases in $\overline{TR}$ are more pronounced, amounting to 0.59 m (σ = 0.29 m), 0.43 m (σ = 0.35 m), and 0.50 m (σ = 0.38 m) for the dry season, rising limb, and receding limb of the flood season, respectively (Table 5-5). A similar pattern of projected increases of $\overline{TR}$ resulting from riverbed lowering is also evident for the median and high fresh water flux simulations, albeit to a lesser extent as the increased flow discharge at the upstream boundary acts to further control the propagation of the tidal signal (see Table 5-5).

Figure 5-10 shows that in the Baseline historical scenario, the simulated tidal signal (TR> 0.1 m) reaching the apex of the delta at Chaktomuk (318 km) during the dry season. During the flood season, the tidal signal is dampened by the increased water flux reaching only to approximately 190 km landward of the coast near Tan Chau (203 km) in the Mekong channel. In the Bassac the tidal signal appears to attenuate at 230 km landward of the coast during the dry season and is further constrained to approximately 180 km during the flood season. In the Contemporary scenario the tidal signal reaches further landward to approximately 430 km into the LMR during the dry season and is constrained to less than 250 km landward during the flood season, for both rising and receding limbs of the hydrograph in the Mekong channel. The Bassac is tidal all the way to its source at Chaktomuk (318 km) in the dry season but it does not appear to have a tidal signal landward of 220 km in the flood season. In the Future scenario, the tidal signal extends even further inland, reaching approximately 500 km into the LMR during the dry season and is limited to less than 310 km inland during the flood season, for both the rising and receding limbs of the hydrograph in the Mekong channel. The Bassac channel remains tidal up to its source at Chaktomuk during the dry season, but does not exhibit a tidal signal beyond 230 km inland during the flood season.

A substantial increase of the tidal range ($\overline{TR}$) is also observed in the Contemporary and Future scenarios, in comparison to the Baseline historical scenario (Figure 5-10). For instance, at Tan

Chau (203 km) on the Mekong channel, during the dry season $\overline{TR}$ rises from 0.72 m in the Baseline scenario to 1.27 m and 1.66 m for the Contemporary and Future scenarios, respectively. Similarly, there is an observed increase in $\overline{TR}$ at Tan Chau (203 km) during the rising limb period, from 0.1 m in the Baseline scenario to 0.39 m and 0.93 m for the Contemporary and Future scenarios, respectively. The $\overline{TR}$ at Tan Chau (203 km) for the receding limb period tend to be slightly higher than those observed during the rising limb, increasing from 0.1 m in the Baseline scenario to approximately 0.46 m and 1.09 m for the Contemporary and Future scenarios, respectively (Figure 5-10). At Chau Doc (186 km) on the Bassac channel, during the dry season, the mean tidal range $\overline{TR}$ increases from 0.73 m in the Baseline scenario to 1.30 m and 1.74 m in the Contemporary and Future scenario, respectively. Similarly, during both limbs of the flood season, $\overline{TR}$ rises from 0.1 m in the Baseline scenario to 0.32 m and 0.95 m in the Contemporary and Future scenarios, respectively (Figure 5-10).

Table 5-5. The average changes in mean tidal range ($\overline{TR}$) along the LMR, Mekong and Bassac distributary delta channels under Contemporary and Future bathymetric scenarios compared to the Baseline scenario are presented for all fresh water flux scenarios investigated with 0 m sea-level rise. Positive values indicate an increase in $\overline{TR}$ (m), while negative values indicate a decrease (m). The values in parentheses represent the standard deviation.

Fresh water flux scenarios/Riverbed bathymetry scenarios		Lower Mekong River			Mekong channel			Bassac Channel		
		Dry	Rising limb	Receding limb	Dry	Rising limb	Receding limb	Dry	Rising limb	Receding limb
Low fresh water flux year	Contemporary (-3.06 m)	0.15 (0.13)	0.00 (0.00)	0.00 (0.01)	0.31 (0.14)	0.21 (0.12)	0.26 (0.16)	0.24 (0.22)	0.09 (0.14)	0.13 (0.18)
	Future (-5.92 m)	0.41 (0.23)	0.02 (0.03)	0.06 (0.06)	0.58 (0.27)	0.51 (0.27)	0.59 (0.32)	0.59 (0.29)	0.43 (0.35)	0.50 (0.38)
Median fresh water flux year	Contemporary (-3.06 m)	0.12 (0.10)	0.00 (0.00)	0.00 (0.00)	0.28 (0.13)	0.19 (0.22)	0.24 (0.15)	0.24 (0.21)	0.08 (0.13)	0.14 (0.18)
	Future (-5.92 m)	0.34 (0.21)	0.02 (0.02)	0.06 (0.05)	0.55 (0.28)	0.45 (0.23)	0.54 (0.28)	0.60 (0.30)	0.44 (0.37)	0.53 (0.41)
High water flux year	Contemporary (-3.06 m)	0.14 (0.12)	0.00 (0.00)	0.00 (0.00)	0.30 (0.14)	0.19 (0.13)	0.21 (0.17)	0.23 (0.21)	0.05 (0.11)	0.08 (0.11)
	Future (-5.92 m)	0.38 (0.22)	0.01 (0.01)	0.02 (0.02)	0.57 (0.27)	0.43 (0.24)	0.50 (0.28)	0.57 (0.29)	0.37 (0.32)	0.42 (0.35)

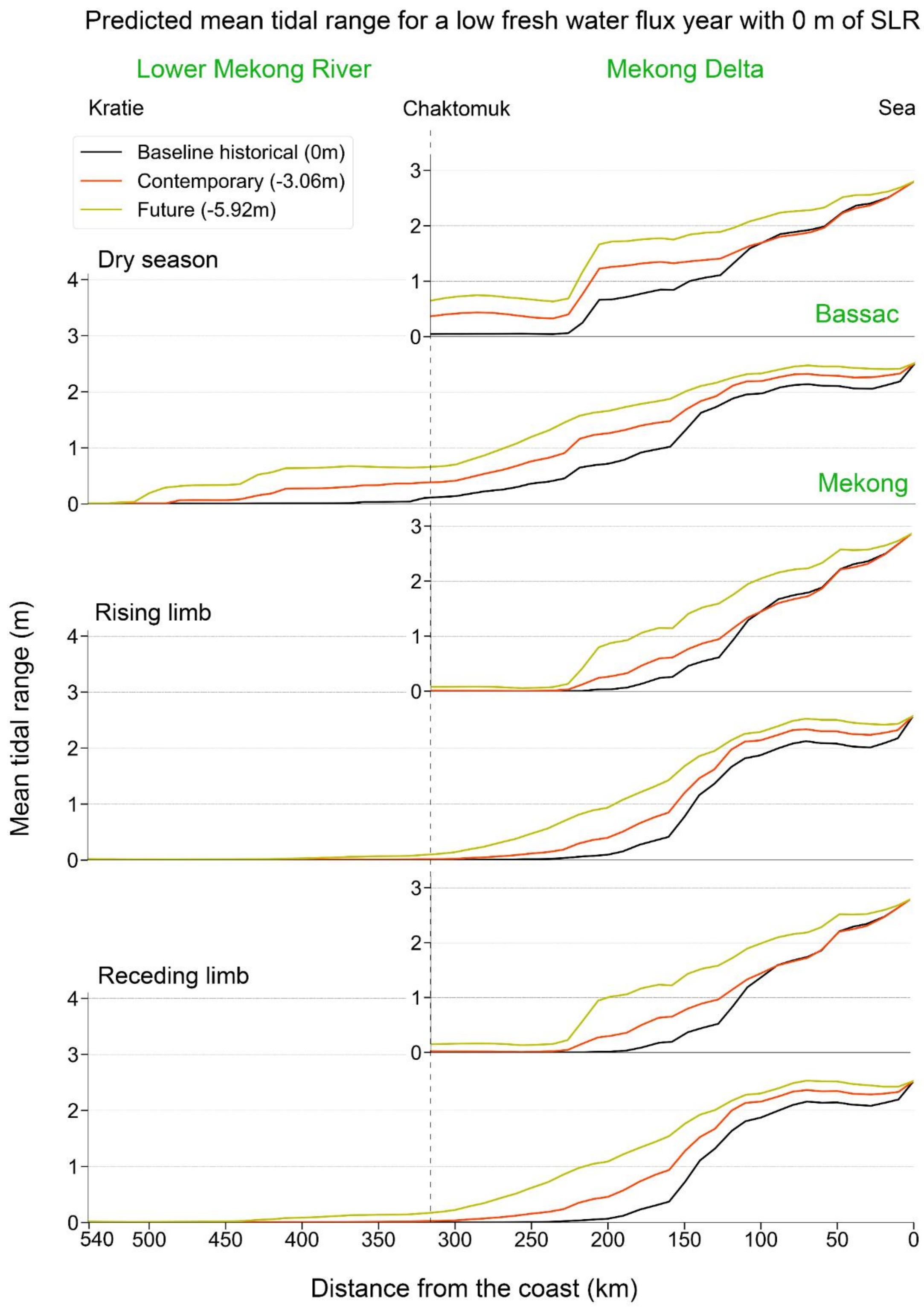

Figure 5-10. The longitudinal profile of mean tidal range ($\overline{TR}$) along the LMR, Mekong and Bassac distributary delta channels for the bathymetric scenarios investigated under low fresh water flux year and 0 m sea level rise. The main panel focuses on the LMR and Mekong channel, while the insert panel shows the Bassac channel.

5.4.1.3 Effects of riverbed lowering on extreme water levels

This section will examine how riverbed lowering affects the maximum and minimum water levels, considering that the maximum water level indicates the potential for flood hazards, while the minimum water level reflects the potential for drought hazards.

Table 5-6 indicates that for the median fresh water flux condition, compared to the Baseline historical scenario, in the LMR, the Contemporary scenario shows a decrease in simulated maximum water levels and minimum water levels by an average of 1.52 m (σ = 0.67 m) and 0.87 m (σ = 1.28 m), respectively. These reductions in maximum and minimum water levels become more substantial in the Future scenario, where they decrease by an average of 3.34 m (σ = 0.78 m) and 2.33 m (σ = 0.80 m), respectively. The simulated decrease in both maximum and minimum water levels is lower in areas close to the coast compared to those in the landward parts of the delta system. In more detail, in the Mekong channel, the Contemporary scenario shows a decrease in simulated maximum water levels and minimum water levels by an average of 0.43 m (σ = 0.42 m) and 0.34 m (σ = 0.21 m), respectively. These reductions in maximum and minimum water levels become more substantial in the Future scenario, where they decrease by an average of 0.78 m (σ = 0.79 m) and 0.56 m (σ = 0.30 m), respectively. In the Bassac channel, the Contemporary scenario demonstrates a decrease in simulated maximum water levels and minimum water levels by an average of 0.49 m (σ = 0.41 m) and 0.40 m (σ = 0.39 m), respectively. These reductions in maximum and minimum water levels become more pronounced in the Future scenario, decreasing by an average of 0.79 m (σ = 0.70 m) and 0.71 m (σ = 0.41 m), respectively. Similar trends are evident across low and high fresh water flux scenarios (see Table 5-6).

Figure 5-11 shows that under median fresh water flux conditions, the most substantial decreases in maximum water level occur in landward reaches in riverbed lowering scenarios. At 430 km from the coast, the largest decrease in maximum water level with reductions of 2.30 m and 4.19 m is observed for the Contemporary and Future scenarios, respectively, compared to the Baseline historical scenario. The decrease in minimum water levels is most pronounced at approximately 500 km from the coastline, with a reduction of 2.01 m and 3.2 m for the Contemporary and Future scenarios, respectively compared to the Baseline historical scenario. Moving seaward, the decrease in both maximum and minimum water levels appear to be dampened, with regions approximately 100 km from the sea showing a minimal variation (<0.2 m) of extreme water levels between scenarios. Similar trends are evident across low and high fresh water flux scenarios (Figure 5-11).

Table 5-6. The average changes in the Maximum and minimum water level along the LMR, Mekong and Bassac distributary delta channels for all of bathymetric and fresh water flux scenarios investigated under 0 m of sea level rise. Positive values indicate an increase in water level (m), while negative values indicate a decrease (m). The values in parentheses represent the standard deviation.

Fresh water flux scenarios /Riverbed bathymetry scenarios		Lower Mekong River		Mekong channel		Bassac channel	
		Maximum water level	Minimum water level	Maximum water level	Minimum water level	Maximum water level	Minimum water level
Low fresh water flux year	Contemporary (-3.06 m)	-1.58 (0.72)	-0.74 (1.24)	-0.30 (0.37)	-0.36 (0.20)	-0.32 (0.34)	-0.40 (0.37)
	Future (-5.92 m)	-3.48 (0.86)	-2.10 (0.70)	-0.56 (0.76)	-0.61 (0.30)	-0.61 (0.65)	-0.75 (0.39)
Median fresh water flux year	Contemporary (-3.06 m)	-1.52 (0.62)	-0.87 (1.28)	-0.43 (0.42)	-0.34 (0.21)	-0.49 (0.41)	-0.40 (0.39)
	Future (-5.92 m)	-3.34 (0.78)	-2.33 (0.80)	-0.78 (0.79)	-0.56 (0.30)	-0.79 (0.70)	-0.71 (0.41)
High fresh water flux year	Contemporary (-3.06 m)	-1.36 (0.54)	-0.77 (1.23)	-0.45 (0.45)	-0.37 (0.20)	-0.48 (0.42)	-0.40 (0.37)
	Future (-5.92 m)	-3.20 (0.71)	-2.21 (0.73)	-0.82 (0.85)	-0.63 (0.30)	-0.85 (0.73)	-0.74 (0.40)

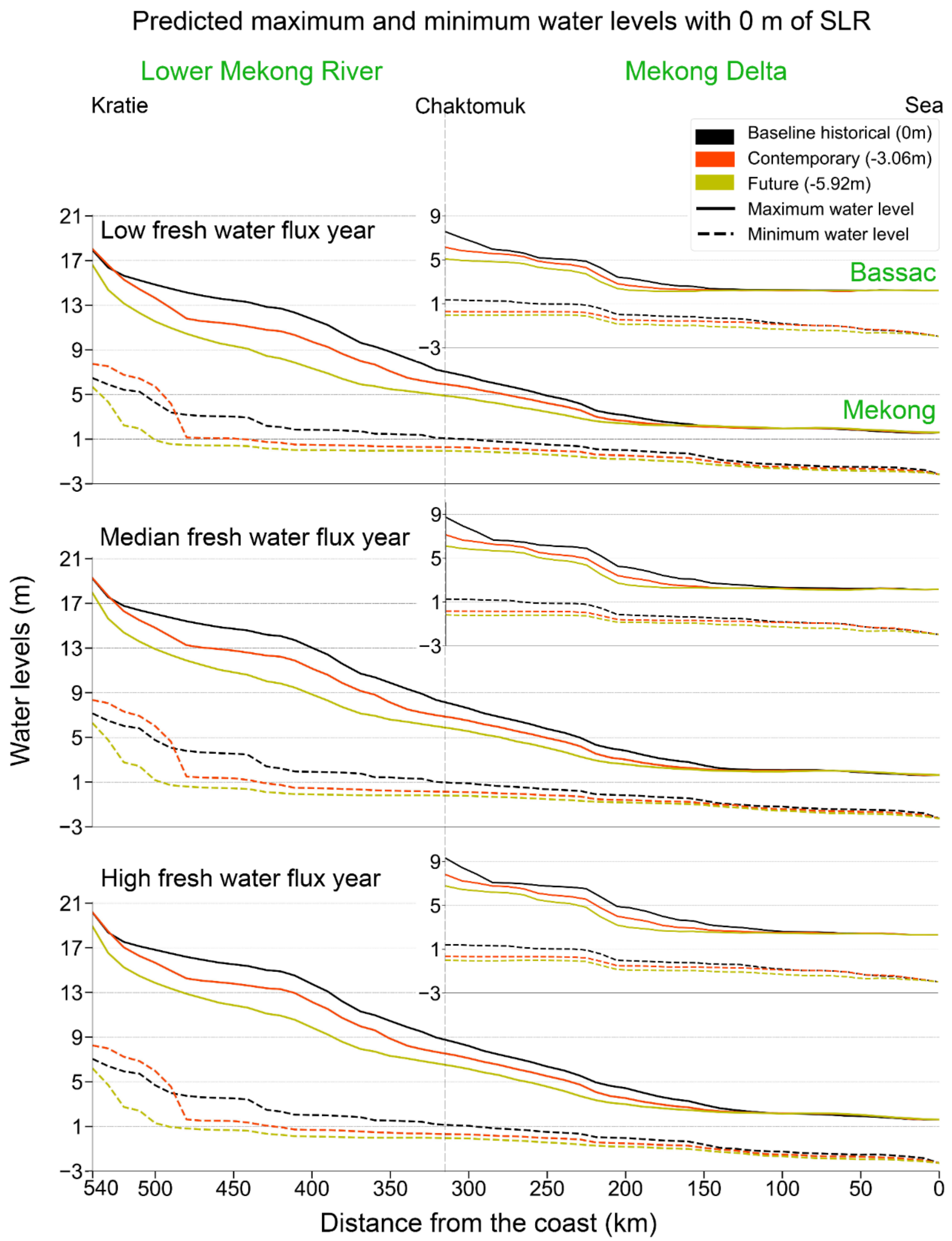

Figure 5-11. The longitudinal profile of maximum and minimum water levels along the LMR, Mekong and Bassac distributary delta channels, for the Baseline historical, Contemporary and Future bathymetric conditions, across all fresh water flux scenarios and with 0 m sea-level rise. The main panel focuses on the LMR and Mekong channel, while the insert panel shows the Bassac channel.

5.4.2 Changes in water level and tidal amplitude due to sea level rise

To isolate the effects of sea level rise, the present Section will provide a detailed description of changes in water level and tidal amplitude under the investigated scenarios of rising sea levels using only the Baseline historical (1998) bathymetry.

5.4.2.1 Effects of sea-level rise on mean water level

Table 5-7 shows for a high fresh water flux year, compared to the Baseline 0 m SLR scenario, in the LMR, the $\overline{WL}$ for the 0.5m SLR scenario increases by an average of 0.12 m (σ = 0.09 m), 0.03 m (σ = 0.01 m), and 0.03 m (σ = 0.01 m) for the dry season, rising limb, and receding limb, respectively. The simulated increase of $\overline{WL}$ is higher in areas close to the coast compared to those in the landward parts of the LMB system. In more detail, in the Mekong channel, the $\overline{WL}$ increases by an average of 0.42 m (σ = 0.07 m), 0.30 m (σ = 0.16 m), and 0.29 m (σ = 0.16 m) for the dry season, rising limb, and receding limb, respectively. In the Bassac channel, the $\overline{WL}$ increases by an average of 0.40 m (σ = 0.09 m), 0.26 m (σ = 0.16 m), and 0.26 m (σ = 0.15 m) for the dry season, rising limb, and receding limb, respectively. The $\overline{WL}$ gradually increases with rising sea levels such that in the 2.5 m SLR scenario. In more detail, in the LMR, the $\overline{WL}$ increases by an average of 0.81 m (σ = 0.50 m), 0.13 m (σ = 0.09 m), and 0.19 m (σ = 0.09 m) for the dry season, rising limb, and receding limb, respectively, compared to the 0m SLR scenario. In the Mekong channel, the $\overline{WL}$ increases by 2.19 m (σ = 0.28 m), 1.67 m (σ = 0.73 m), and 1.57 m (σ = 0.73 m) for the dry season, rising limb, and receding limb, respectively. In the Bassac channel, the $\overline{WL}$ increases by 2.07 m (σ = 0.38 m), 1.46 m (σ = 0.76 m), and 1.42 m (σ = 0.74 m) for the dry season, rising limb, and receding limb, respectively. These trends persist for both low and median fresh water flux scenarios, with the increase in water levels being more notable in low fresh water flux year (Table 5-7). Figure 5-12 show an increase in $\overline{WL}$ for subsequent SLR scenarios that is more pronounced seaward and gradually attenuates landward under high fresh water flux. Although on reaches close to the sea no seasonality is observed, in landward reaches, SLR appears to have a greater effect in the dry season rather than the flood season. Additionally, the effect of SLR on increasing $\overline{WL}$ appears to propagate further landward for higher values of SLR. For example, compared to the Baseline 0 m SLR scenario, in the 2.5 m SLR scenario, the increase in $\overline{WL}$ extends up to 520 km inland ($\overline{WL}$ rise > 0.1 m) during the dry season, however, this effect extends only up to 440 km during both the rising and receding limbs of the flood season. Similar trends are observed for both low and median fresh water flux scenarios and the increase of $\overline{WL}$ due to sea level rise is more pronounced for low fresh water flux conditions (Appendix, Figure 7 and Figure 8).

Table 5-7. The average changes of mean water level ($\overline{WL}$) along the LMR, Mekong and Bassac distributary delta channels under sea level rise scenarios of 0.5 m, 1.0 m, 2.0 m and 2.5m compared to the Baseline 0 m of sea level rise scenario are presented for all fresh water flux scenarios investigated with historical bathymetric. Positive values indicate an increase in water level (m), while negative values indicate a decrease (m). The values in parentheses represent the standard deviation.

Fresh water flux scenarios/Sea level rise scenarios		Lower Mekong River			Mekong channel			Bassac channel		
		Dry	Rising limb	Receding limb	Dry	Rising limb	Receding limb	Dry	Rising limbs	Receding limb
Low fresh water flux year	0.5m SLR	0.13 (0.09)	0.02 (0.01)	0.04 (0.02)	0.42 (0.07)	0.31 (0.16)	0.34 (0.14)	0.40 (0.09)	0.28 (0.16)	0.30 (0.15)
	1m SLR	0.28 (0.19)	0.04 (0.03)	0.08 (0.05)	0.86 (0.13)	0.64 (0.30)	0.68 (0.27)	0.81 (0.17)	0.58 (0.32)	0.61 (0.30)
	2m SLR	0.63 (0.40)	0.11 (0.09)	0.20 (0.13)	1.75 (0.23)	1.35 (0.56)	1.42 (0.51)	1.65 (0.3)	1.22 (0.61)	1.27 (0.58)
	2.5m SLR	0.84 (0.51)	0.15 (0.12)	0.28 (0.17)	2.20 (0.27)	1.72 (0.68)	1.80 (0.62)	2.09 (0.37)	1.55 (0.75)	1.63 (0.70)
Median fresh water flux year	0.5m SLR	0.12 (0.09)	0.02 (0.02)	0.04 (0.02)	0.42 (0.07)	0.31 (0.15)	0.32 (0.15)	0.40 (0.09)	0.28 (0.16)	0.29 (0.15)
	1m SLR	0.27 (0.19)	0.05 (0.04)	0.09 (0.04)	0.85 (0.13)	0.64 (0.30)	0.65 (0.29)	0.81 (0.17)	0.57 (0.31)	0.58 (0.30)
	2m SLR	0.61 (0.40)	0.12 (0.10)	0.19 (0.11)	1.74 (0.23)	1.32 (0.57)	1.34 (0.55)	1.65 (0.31)	1.20 (0.59)	1.21 (0.58)
	2.5m SLR	0.80 (0.51)	0.16 (0.13)	0.26 (0.14)	2.19 (0.28)	1.69 (0.69)	1.71 (0.67)	2.07 (0.38)	1.53 (0.73)	1.55 (0.71)
High water flux year	0.5m SLR	0.12 (0.09)	0.03 (0.01)	0.03 (0.01)	0.42 (0.07)	0.30 (0.16)	0.29 (0.16)	0.40 (0.09)	0.26 (0.16)	0.26 (0.15)
	1m SLR	0.27 (0.18)	0.05 (0.02)	0.06 (0.03)	0.85 (0.13)	0.61 (0.31)	0.60 (0.31)	0.80 (0.17)	0.54 (0.31)	0.54 (0.31)
	2m SLR	0.61 (0.39)	0.10 (0.07)	0.14 (0.07)	1.74 (0.23)	1.27 (0.60)	1.24 (0.60)	1.64 (0.31)	1.14 (0.62)	1.12 (0.60)
	2.5m SLR	0.81 (0.50)	0.13 (0.09)	0.19 (0.09)	2.19 (0.28)	1.62 (0.73)	1.57 (0.73)	2.07 (0.38)	1.46 (0.76)	1.42 (0.74)

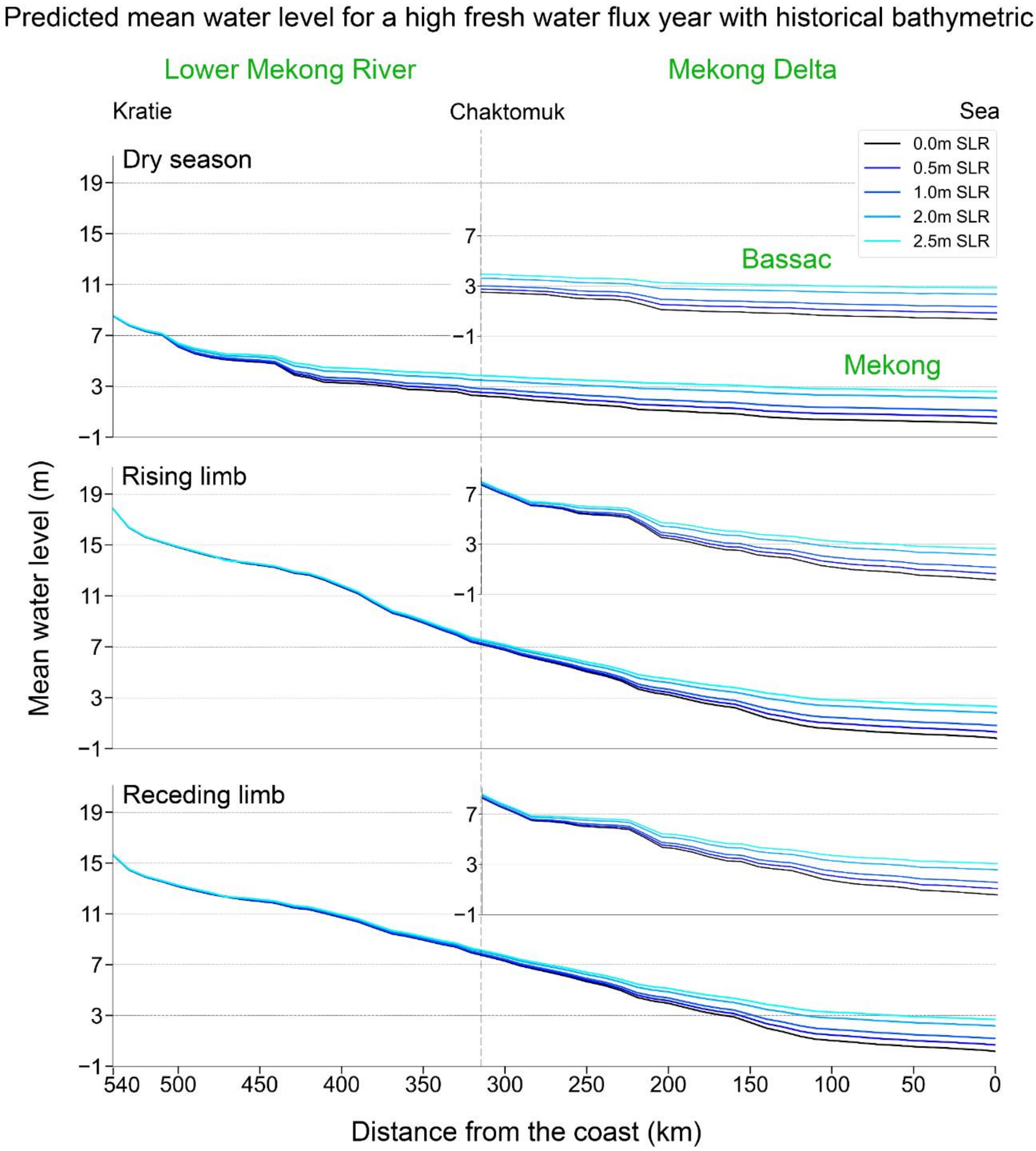

Figure 5-12. The longitudinal profile of mean water level $\overline{WL}$ along the LMR, Mekong and Bassac distributary delta channels for the sea level rise scenarios investigated under high fresh water flux and Baseline historical bathymetric scenarios. The main panel focuses on the LMR and Mekong channel, while the insert panel shows the Bassac channel.

5.4.2.2 Effects of sea-level rise on mean tidal range

Both Table 5-8 and Figure 5-13 show that the influence of SLR causes only a small increase in tidal range (< 0.35 m; 2.5 m SLR) and tidal expansion (< 318 km; 2.5 m SLR) in LMR and Mekong delta. The SLR appears to have a greater effect of increasing tidal range in the flood season rather than the dry season. In more detail, the LMR remains non-tidal for all Future scenarios investigated, while the maximum increase in $\overline{TR}$ only reaches around 0.35 m in an area approximately 160 km from the sea in the Mekong Channel during the receding limb for the 2.5 m SLR scenario compared to the 0 m SLR scenario (Figure 5-13). Results for the median and high fresh water flux simulations are presented in Table 5-8 and the Appendix, Figure 9 and Figure 10. The minor impact of SLR on tidal range will be discussed further in Section 5.1: Discussion.

Table 5-8. The average of mean tidal range ($\overline{TR}$) along the LMR, Mekong and Bassac distributary delta channels under sea level rise scenarios of 0.5 m, 1.0 m, 2.0 m and 2.5m compared to the Baseline 0 m of sea level rise scenario are presented for all fresh water flux scenarios investigated with historical bathymetric. Positive values indicate an increase in $\overline{TR}$ (m), while negative values indicate a decrease (m). The values in parentheses represent the standard deviation.

Fresh water flux scenarios/Sea level rise scenarios		Lower Mekong River			Mekong channel			Bassac channel		
		Dry	Rising limb	Receding limb	Dry	Rising limb	Receding limb	Dry	Rising limbs	Receding limb
Low fresh water flux year	0.5m SLR	0.00 (0.00)	0.00 (0.00)	0.00 (0.00)	0.03 (0.03)	0.04 (0.04)	0.03 (0.03)	0.00 (0.00)	0.02 (0.02)	0.02 (0.02)
	1m SLR	0.01 (0.01)	0.00 (0.00)	0.00 (0.00)	0.04 (0.05)	0.08 (0.06)	0.06 (0.05)	-0.02 (0.05)	0.04 (0.04)	0.04 (0.04)
	2m SLR	0.01 (0.01)	0.00 (0.00)	0.00 (0.00)	0.06 (0.09)	0.16 (0.11)	0.13 (0.10)	-0.03 (0.09)	0.08 (0.08)	0.09 (0.08)
	2.5m SLR	0.02 (0.01)	0.00 (0.00)	0.00 (0.00)	0.07 (0.11)	0.19 (0.13)	0.17 (0.12)	-0.04 (0.12)	0.10 (0.10)	0.11 (0.10)
Median fresh water flux year	0.5m SLR	0.00 (0.00)	0.00 (0.00)	0.00 (0.00)	0.02 (0.03)	0.04 (0.04)	0.03 (0.03)	0.00 (0.00)	0.02 (0.02)	0.02 (0.02)
	1m SLR	0.00 (0.00)	0.00 (0.00)	0.00 (0.00)	0.04 (0.05)	0.08 (0.06)	0.07 (0.06)	-0.02 (0.05)	0.05 (0.04)	0.05 (0.05)
	2m SLR	0.01 (0.00)	0.00 (0.00)	0.00 (0.00)	0.06 (0.09)	0.15 (0.11)	0.14 (0.11)	-0.03 (0.09)	0.10 (0.09)	0.10 (0.10)
	2.5m SLR	0.01 (0.00)	0.00 (0.00)	0.00 (0.00)	0.07 (0.10)	0.18 (0.13)	0.17 (0.13)	-0.03 (0.10)	0.12 (0.12)	0.13 (0.13)
High fresh water flux year	0.5m SLR	0.00 (0.00)	0.00 (0.00)	0.00 (0.00)	0.02 (0.03)	0.05 (0.04)	0.04 (0.04)	0.00 (0.00)	0.03 (0.03)	0.03 (0.03)
	1m SLR	0.00 (0.00)	0.00 (0.00)	0.00 (0.00)	0.04 (0.05)	0.09 (0.07)	0.08 (0.08)	-0.02 (0.05)	0.05 (0.05)	0.06 (0.06)
	2m SLR	0.01 (0.00)	0.00 (0.00)	0.00 (0.00)	0.06 (0.08)	0.16 (0.13)	0.15 (0.14)	-0.03 (0.09)	0.10 (0.09)	0.11 (0.12)
	2.5m SLR	0.01 (0.00)	0.00 (0.00)	0.00 (0.00)	0.07 (0.10)	0.20 (0.15)	0.19 (0.16)	-0.03 (0.11)	0.13 (0.12)	0.14 (0.14)

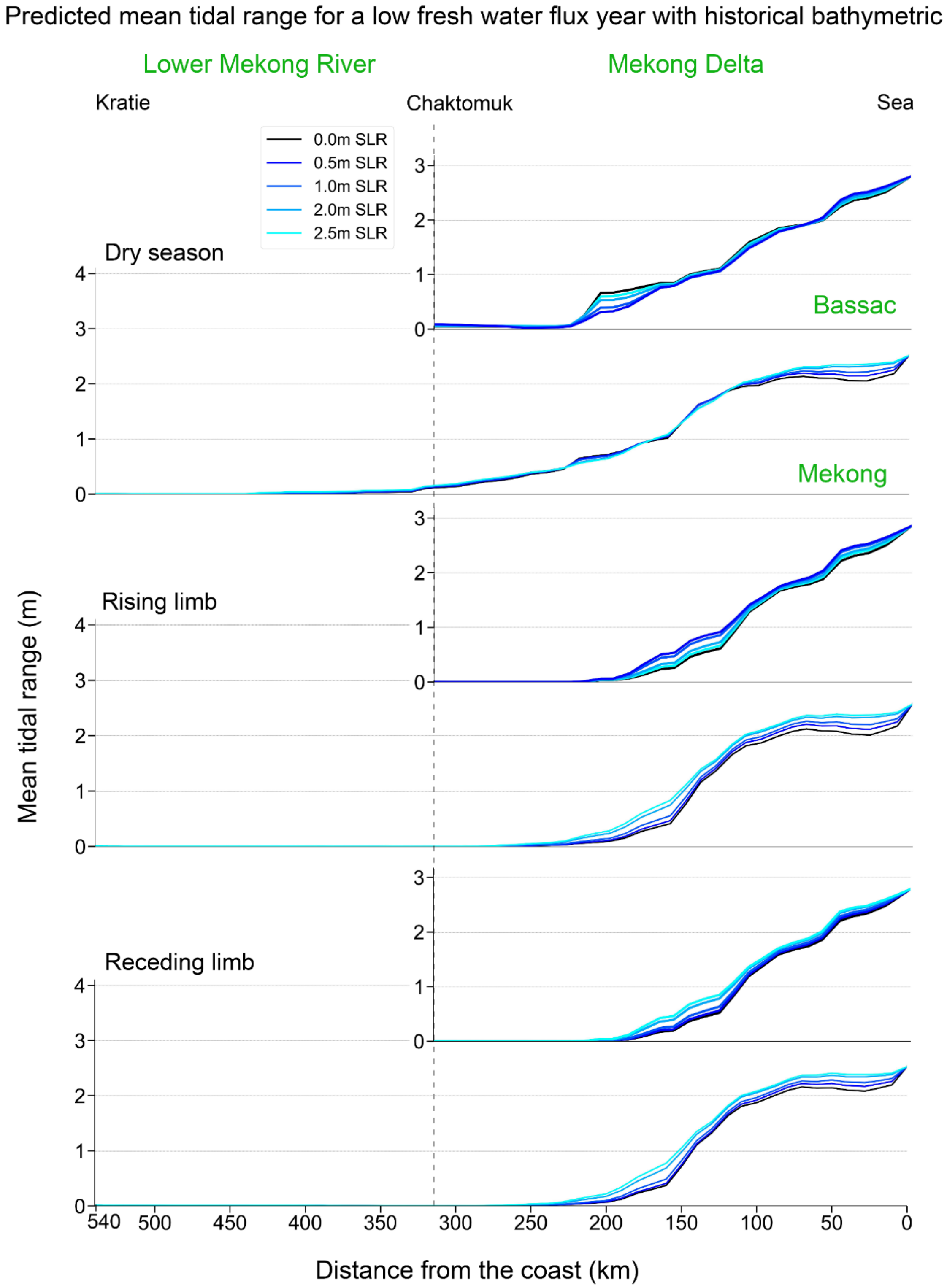

Figure 5-13. The longitudinal profile of mean tidal range ($\overline{TR}$) along the Lower Mekong River and Mekong and Bassac distributary delta channels for sea level rise scenarios investigated under low fresh water flux and Historical bathymetric scenarios. The main panel focuses on the LMR and Mekong channel, while the insert panel shows the Bassac channel.

5.4.2.3 Effects of sea-level rise on water level extremes

Table 5-9 shows that for the median fresh water flux condition, compared to the Baseline 0 m SLR scenario, in the LMR, the 0.5 m SLR shows a rise in simulated maximum water levels and minimum water levels by an average of 0.04 m (σ = 0.0.01 m) and 0.16 m (σ = 0.11 m), respectively. These increases in maximum and minimum water levels become more pronounced in higher sea level rise scenarios. For example, in 2.5 m SLR scenarios, these water level increase by an average of 0.16 m (σ = 0.07 m) and 1.04 m (σ = 0.60 m), respectively. The simulated increase in both maximum and minimum water levels is higher in areas close to the coast compared to those in the landward parts of the system. In more detail, in the Mekong channel, the 0.5 m SLR scenario shows a rise in simulated maximum water levels and minimum water levels by an average of 0.31 m (σ = 0.17 m) and 0.41 m (σ = 0.04 m), respectively, compared to 0 m SLR scenarios. In the 2.5 m SLR scenarios, these values increase by an average of 1.62 m (σ = 0.82 m) and 2.25 m (σ = 0.17 m), respectively, compared to 0 m SLR scenarios. Similar values are observed in the Bassac channel as in the Mekong channel (Table 5-9). These trends persist for both low and high fresh water flux scenarios, with the overall increase in maximum water levels and minimum water levels being more notable in low fresh water flux year (see Table 5-9). Figure 5-14 shows that the most substantial increases in water level occurs in seaward reaches, with the rise in minimum water levels being higher and propagating considerably further inland than the increase observed in maximum water levels. The notable rises in minimum water level compared to those for maximum water level are attributed to the minimum level is recorded during the low water stage in the dry season, when the influence of sea level rise is more pronounced in elevating water levels further inland. In contrast, the maximum water level is recorded during the peak water stage in the flood season, when the effect of sea level rise in raising water levels is relatively lower in the inland sections.

Table 5-9. The average changes in the average of Maximum and minimum water level along the LMR, Mekong and Bassac distributary delta channels under all sea level rise in compared with Baseline 0m of sea level rise, across all fresh water flux scenarios and Historical bathymetric scenarios. Positive values indicate an increase in water level (m), while negative values indicate a decrease (m). The values in parentheses represent the standard deviation.

Fresh water flux scenarios /Sea level rise scenarios		Lower Mekong River		Mekong channel		Bassac channel	
		Maximum water level	Minimum water level	Maximum water level	Minimum water level	Maximum water level	Minimum water level
Low fresh water flux year	0.5m SLR	0.02 (0.01)	0.17 (0.11)	0.32 (0.18)	0.42 (0.03)	0.28 (0.17)	0.42 (0.06)
	1m SLR	0.03 (0.02)	0.37 (0.24)	0.66 (0.35)	0.87 (0.07)	0.58 (0.33)	0.87 (0.12)
	2m SLR	0.08 (0.06)	0.84 (0.49)	1.38 (0.65)	1.80 (0.12)	1.22 (0.65)	1.87 (0.22)
	2.5m SLR	0.11 (0.08)	1.11 (0.62)	1.75 (0.80)	2.27 (0.14)	1.56 (0.80)	2.27 (0.25)
Median fresh water flux year	0.5m SLR	0.04 (0.01)	0.16 (0.12)	0.31 (0.17)	0.42 (0.04)	0.27 (0.16)	0.42 (0.06)
	1m SLR	0.07 (0.02)	0.34 (0.25)	0.63 (0.34)	0.88 (0.08)	0.56 (0.33)	0.89 (0.12)
	2m SLR	0.11 (0.05)	0.79 (0.2)	1.30 (0.66)	1.85 (0.15)	1.16 (0.65)	1.85 (0.22)
	2.5m SLR	0.13 (0.06)	1.05 (0.66)	1.65 (0.81)	2.33 (0.17)	1.48 (0.81)	2.33 (0.26)
High fresh water flux year	0.5m SLR	0.04 (0.01)	0.16 (0.11)	0.31 (0.17)	0.41 (0.04)	0.27 (0.17)	0.42 (0.06)
	1m SLR	0.07 (0.03)	0.34 (0.23)	0.63 (0.34)	0.85 (0.08)	0.55 (0.33)	0.87 (0.13)
	2m SLR	0.13 (0.05)	0.78 (0.47)	1.28 (0.66)	1.78 (0.15)	1.13 (0.65)	1.80 (0.23)
	2.5m SLR	0.16 (0.07)	1.04 (0.60)	1.62 (0.82)	2.25 (0.17)	1.43 (0.80)	2.27 (0.27)

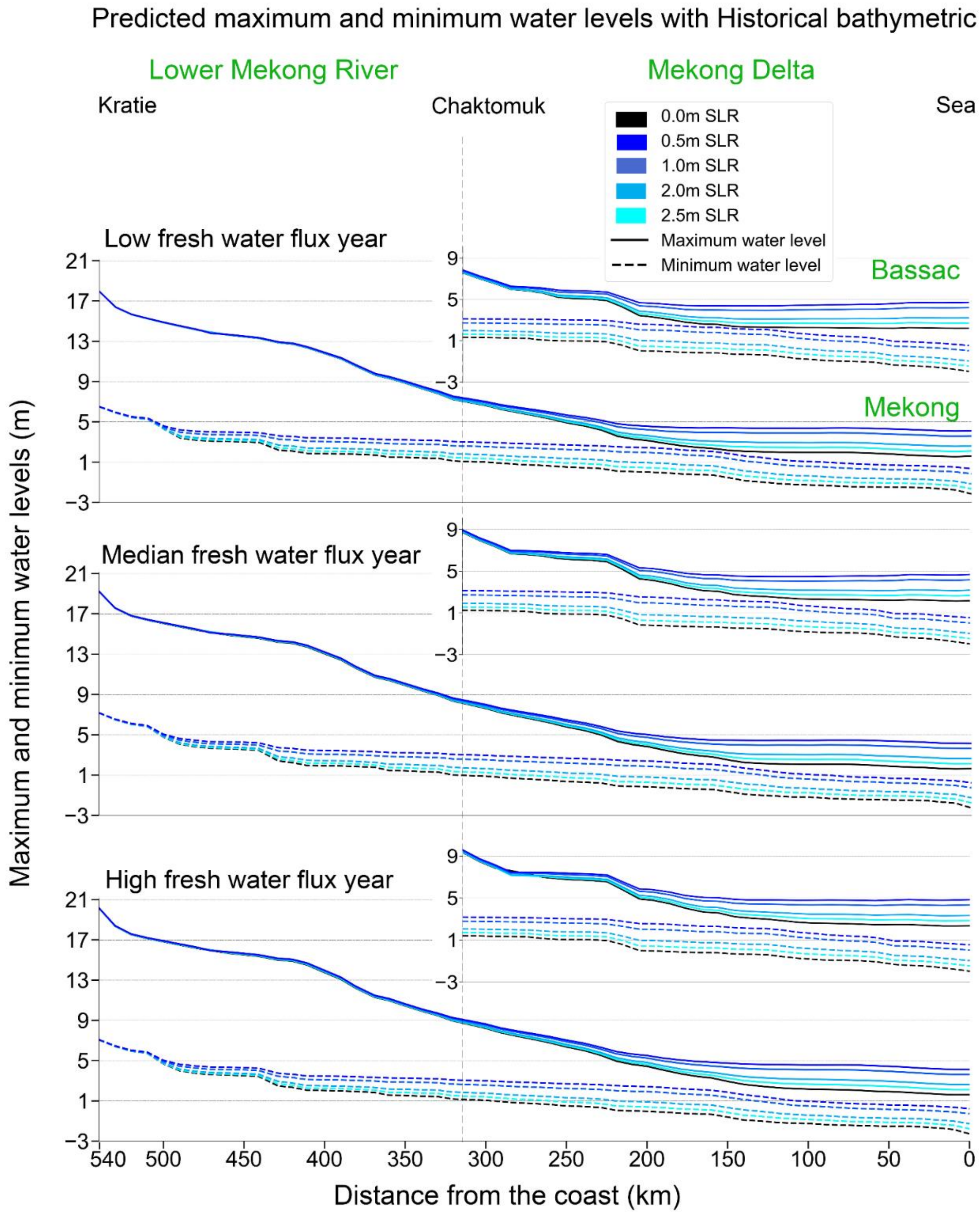

Figure 5-14. The longitudinal profile of maximum and minimum water levels along the LMR, Mekong and Bassac distributary delta channels for sea level rise of 0.0 m, 0.5 m, 1.0m, 2.0 m and 2.5 m scenarios investigated, across all fresh water flux scenarios and with Historical bathymetric scenarios. The main panel focuses on the LMR and Mekong channel, while the insert panel shows the Bassac channel.

5.4.3 Future projections of the combined effects of riverbed Lowering and sea level rise

Sections 5.4.1 and 5.4.2 highlighted changes in water level and tidal range due to riverbed lowering or sea level rise, respectively, in isolation. The present Section will assess the combined impact of projected future changes in riverbed levels and sea level on the system. Here, Baseline conditions are represented as assuming the Baseline historical (1998) bathymetry scenarios and a sea level rise of 0 m (Baseline historical_0m SLR). The Contemporary conditions are representing by adopting the Contemporary bathymetric and a sea level rise of 0.5 m (Comtemporary_0.5m SLR) while three potential Future scenarios are explored that adopt the Future bathymetric scenario in combination with sea level rise scenarios of 0.5, 1 and 2.5 m (Future_0.5m SLR, Future_1.0m SLR, Future_2.5m SLR, respectively). These combinations cover a range of hypothetical Future trajectories of riverbed lowering and sea level rise for the region.

5.4.3.1 Future changes in mean water levels

Table 5-10 shows for a high fresh water flux year, compared to the Baseline scenarios, in the LMR, the $\overline{WL}$ for the Contemporary scenario decreases by an average of 0.8 m (σ = 1.08 m), 1.54 m (σ = 0.7 m), and 1.85 m (σ = 0.84 m) for the dry season, rising limb and receding limb of the flood season, respectively. In the Future_2.5m SLR scenario, the $\overline{WL}$ is reduced by an average of 0.64 m (σ = 1.07 m), 2.96 m (σ = 0.77 m), and 3.20 m (σ = 0.61 m) for the dry season, rising, and receding limbs of the flood season, respectively. In the Mekong channel, for the Contemporary scenario, the $\overline{WL}$ increases by an average of 0.17 m (σ = 0.31 m) during the dry season. However, the $\overline{WL}$ decreases by an average of 0.11 m (σ = 0.51 m) and 0.40 m (σ = 0.74 m) during the rising and receding limbs of the flood season, respectively. In the Future_2.5m SLR scenario, the $\overline{WL}$ increases by an average of 2.00 m (σ = 0.45 m), 1.07 m (σ = 1.25 m), and 0.74 m (σ = 1.49 m) for the dry season, rising, and receding limbs, respectively (Table 5-10). In Bassac channel, for the Contemporary scenario, the $\overline{WL}$ increases by an average of 0.06 m (σ = 0.43 m) during the dry season. However, the $\overline{WL}$ decreases by an average of 0.14 m (σ = 0.52 m) and 0.44 m (σ = 0.72 m) during the rising and receding limbs of the flood season, respectively. In the Future_2.5m SLR scenario, the $\overline{WL}$ increases by an average of 1.84 m (σ = 0.58 m), 0.90 m (σ = 1.21 m), and 0.53 m (σ = 1.45 m) for the dry season, rising, and receding limbs, respectively, compared to the Historical baseline. These trends of $\overline{WL}$ persist for both low and median fresh water flux scenarios, with the overall trend of reduce $\overline{WL}$ more notable in high fresh water flux year (Table 5-10).

Figure 5-15 shows that $\overline{WL}$ are projected to be higher in the future in seaward reaches but lower in landward areas. The location (km point) where this switch from increase to decrease occurs varies between scenarios and different parts of the hydrograph. The switch for the contemporary scenario and Future 0.5 m and 1.0 m SLR scenarios seems to happen at the same location around 200 km during the dry season and around 150 km during the flood season, but an SLR of 2.5 m appears to push the switch location further landward. For example, in the Future_2.5m SLR scenario, the switch occurs at 400 km during the dry season and around 200 km during both limbs of flood season. In addition, both Table 5-10 and Figure 5-15 underscores that the influence of riverbed lowering on reducing $\overline{WL}$ is notably more pronounced in the upstream section during the flood season compared to the dry season. In contrast, the impact of sea level rise on increasing $\overline{WL}$ is more pronounced in the seaward section during the dry season compared to the flood season (Table 5-10 and Figure 5-15), as presented in section 5.4.1.1 and section 5.4.2.1

Table 5-10. The average changes in the mean water level ($\overline{WL}$) along the LMR, Mekong and Bassac distributary delta channels under Contemporary bathymetric with sea level rise of 0.5 m and Future bathymetric with sea level rise of 0.5 m, 1 m and 2.5 m scenarios compared to Baseline historical bathymetry with a sea level rise of 0 m scenarios, considering all fresh water flux conditions. Positive values indicate an increase in water level (m), while negative values indicate a decrease (m). The values in parentheses represent the standard deviation.

Fresh water flux scenarios /Scenarios		Lower Mekong River			Mekong channel			Bassac channel		
		Dry	Rising limb	Receding limb	Dry	Rising limb	Receding limb	Dry	Rising limb	Receding limb
Low fresh water flux year	Contemporary _0.5m SLR	-0.73 (1.09)	-1.62 (0.83)	-1.70 (0.94)	0.18 (0.30)	-0.06 (0.51)	-0.18 (0.63)	0.06 (0.42)	-0.10 (0.52)	-0.25 (0.64)
	Future_ 0.5m SLR	-1.99 (0.82)	-3.49 (0.80)	-3.57 (0.69)	0.08 (0.39)	-0.41 (0.85)	-0.52 (0.97)	-0.06 (0.50)	-0.50 (0.80)	-0.67 (0.96)
	Future_ 1.0m SLR	-1.63 (0.87)	-3.35 (0.79)	-3.36 (0.66)	0.56 (0.40)	0.00 (0.93)	-0.09 (1.02)	0.41 (0.52)	-0.11 (0.89)	-0.25 (1.02)
	Future_ 2.5m SLR	-0.51 (1.07)	-2.89 (0.80)	-2.68 (0.67)	2.01 (0.43)	1.28 (1.13)	1.26 (1.16)	1.86 (0.56)	1.09 (1.16)	1.04 (1.22)
Median fresh water flux year	Contemporary _0.5m SLR	-0.86 (1.07)	-1.61 (0.79)	-1.80 (0.95)	0.18 (0.31)	-0.11 (0.53)	-0.31 (0.71)	0.06 (0.43)	-0.15 (0.54)	-0.38 (0.71)
	Future_ 0.5m SLR	-2.20 (0.84)	-3.45 (0.78)	-3.71 (0.68)	0.06 (0.41)	-0.49 (0.88)	-0.72 (1.09)	-0.09 (0.52)	-0.56 (0.80)	-0.86 (1.05)
	Future_ 1.0m SLR	-1.86 (0.89)	-3.33 (0.77)	-3.51 (0.64)	0.54 (0.43)	-0.09 (0.97)	-0.29 (1.15)	0.39 (0.54)	-0.19 (0.90)	-0.45 (1.12)
	Future_ 2.5m SLR	-0.78 (1.09)	-2.90 (0.76)	-2.86 (0.58)	1.99 (0.47)	1.16 (1.20)	1.03 (1.32)	1.82 (0.60)	0.98 (1.19)	0.81 (1.33)
High fresh water flux year	Contemporary _0.5m SLR	-0.8 (1.08)	-1.54 (0.70)	-1.85 (0.84)	0.17 (0.31)	-0.11 (0.51)	-0.40 (0.73)	0.06 (0.43)	-0.14 (0.52)	-0.44 (0.72)
	Future_ 0.5m SLR	-2.09 (0.82)	-3.37 (0.79)	-3.84 (0.74)	0.07 (0.40)	-0.51 (0.87)	-0.92 (1.19)	-0.08 (0.51)	-0.56 (0.76)	-1.03 (1.09)
	Future_ 1.0m SLR	-1.74 (0.87)	-3.28 (0.78)	-3.69 (0.70)	0.55 (0.41)	-0.12 (0.97)	-0.51 (1.27)	0.40 (0.53)	-0.21 (0.88)	-0.65 (1.18)
	Future_ 2.5m SLR	-0.64 (1.07)	-2.96 (0.77)	-3.20 (0.61)	2.00 (0.45)	1.07 (1.25)	0.74 (1.49)	1.84 (0.58)	0.9 (1.21)	0.53 (1.45)

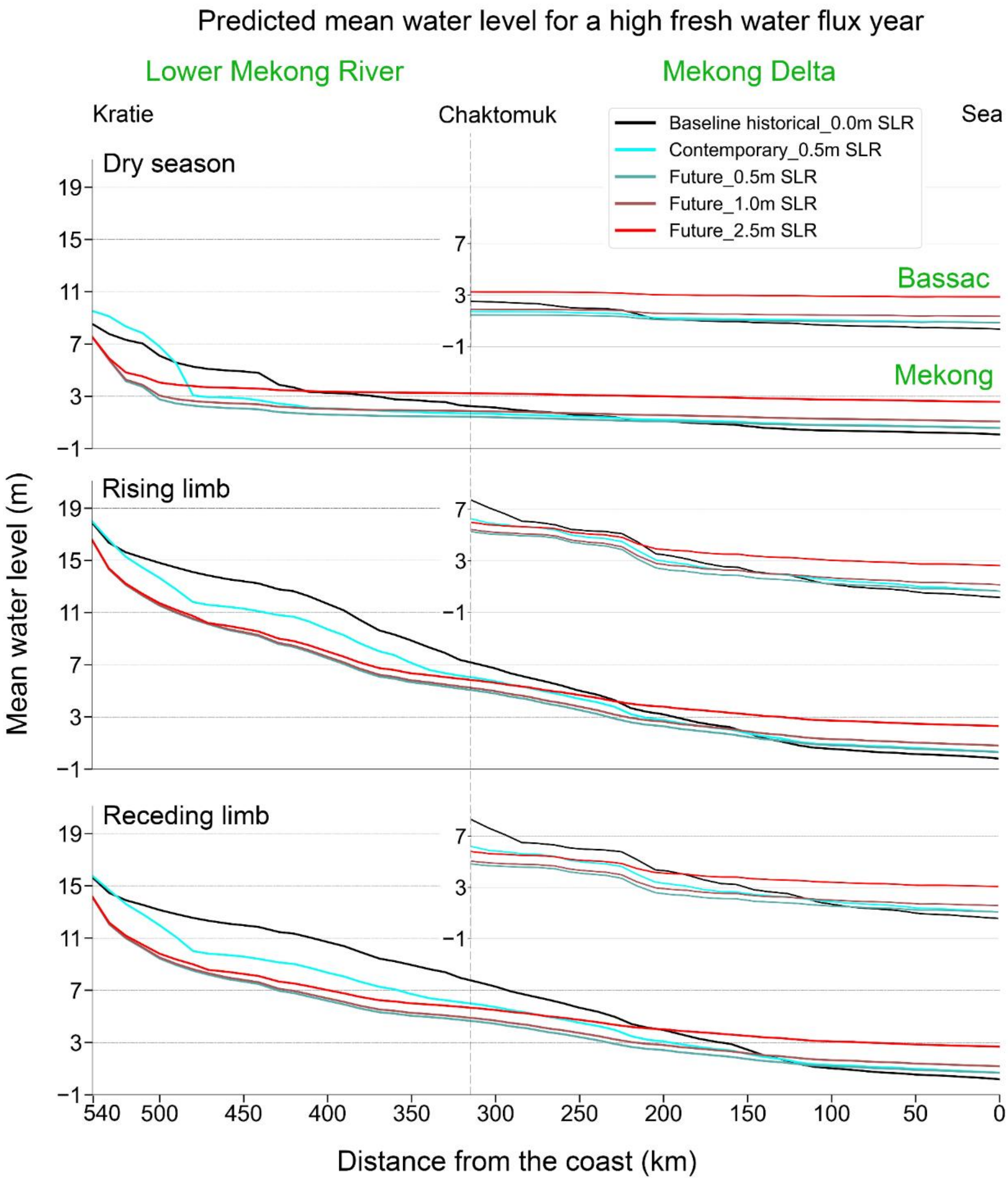

Figure 5-15. The longitudinal profile of mean water level ($\overline{WL}$) along the Lower Mekong River and Mekong and Bassac distributary delta channels for Baseline historical bathymetry with sea level rise of 0 m, Contemporary bathymetric with sea level rise of 0.5 m and Future bathymetric with sea level rise of 0.5 m, 1.0 m and 2.5 m scenarios under high water flux. The main panel focuses on the LMR and Mekong channel, while the insert panel shows the Bassac channel.

5.4.3.2 Future changes in mean tidal range

Aligned with the considerable rise in $\overline{TR}$ driven solely by riverbed lowering, as presented in section 5.4.1.2, and the slight increase in $\overline{TR}$ during both limbs of flood season driven solely by sea level rise, as presented in section 5.4.2.1, Table 5-11 presents the increases in $\overline{TR}$ values are similarly with those influenced solely by riverbed lowering (see section 5.4.1.2 and Table 5-5). However, it is important to note that when combined with future riverbed lowering scenarios, sea level rise tends to reduce the $\overline{TR}$ during the dry season in the seaward parts of the LMB system. For more detail, when compared to the Baseline scenarios, under low fresh water flux year conditions, during the dry season, in the LMR, the $\overline{TR}$ increase an average of 0.16 m (σ = 0.13 m) in the Contemporary scenario. This $\overline{TR}$ increases to 0.42 m (σ = 0.22 m) in both the Future_0.5m SLR and Future_1.0m SLR scenarios, before decreasing slightly to 0.38 m (σ = 0.14 m) in the Future_2.5m SLR scenario. In the Mekong channel, the average increase in $\overline{TR}$ is 0.31 m (σ = 0.11 m) in the Contemporary scenario, 0.56 m (σ = 0.24 m) in the Future_0.5m SLR scenario and 0.54 m (σ = 0.21 m) in the Future_1.0m SLR scenario, before reducing to 0.45 m (σ = 0.13 m) in the Future_2.5m SLR scenario. In the Bassac channel, the average increase in $\overline{TR}$ is 0.23 m (σ = 0.20 m) in the Contemporary scenario, 0.56 m (σ = 0.27 m) in the Future_0.5m SLR scenario and 0.52 m (σ = 0.23 m) in the Future_1.0m SLR scenario, before reducing to 0.36 m (σ = 0.13 m) in the Future_2.5m SLR scenario.

The trend of increasing $\overline{TR}$ due to combined scenarios of riverbed lowering and sea level rise also persists for higher upstream fresh water flux conditions (Table 5-11). Figure 5-16 shows that the combined riverbed lowering and sea level rise scenarios result in a tidal signal expansion and an increase tidal range, similar to that observed with riverbed lowering scenarios alone (see section 5.4.1.2 and Figure 5-10). However, the increased sea level rise when combined with the Future riverbed lowering scenarios tend to reduce the $\overline{TR}$ during the dry season in both Mekong and Bassac channels. For more detail, during the dry season on the Mekong channel, the most notable reduction in $\overline{TR}$ driven by sea level rise occurs when combined with future riverbed lowering scenarios around Tan Chau station (203 km) with $\overline{TR}$ reaches 1.59 m in the Future_0.5m SLR scenario before decreasing to 1.51 m and 1.27 m in the Future_1.0m SLR and Future_2.5m SLR scenarios, respectively. Similarly, on the Bassac channel, the most reduction in $\overline{TR}$ is simulated around 203 km from the coast, with the $\overline{TR}$ reaching 1.55 m in the Future_0.5m SLR scenario and decreasing to 1.41 m and 0.91 m in the Future_1.0m SLR and Future_2.5m SLR scenarios, respectively. (Figure 5-16). The trend of increasing $\overline{TR}$ due to combined scenarios of riverbed lowering and sea level rise also persists for higher upstream water flux conditions (See Table 5-11 and Appendix, Figure 13 and Figure 14).

Table 5-11. The average changes of mean tidal range ($\overline{TR}$) along the LMR, Mekong and Bassac distributary delta channels for Contemporary bathymetric with sea level rise of 0.5 m and Future bathymetric with sea level rise of 0.5 m, 1.0 m and 2.5 m scenarios compared to the Baseline historical scenario with sea level rise of 0m under low water flux. Positive values indicate an increase in water level (m), while negative values indicate a decrease (m). The values in parentheses represent the standard deviation.

Fresh water flux scenarios /Scenarios		Lower Mekong River			Mekong channel			Bassac channel		
		Dry	Rising limb	Receding limb	Dry	Rising limb	Receding limb	Dry	Rising limb	Receding limb
Low water flux year	Contemporary _0.5m SLR	0.16 (0.13)	0.00 (0.00)	0.00 (0.00)	0.31 (0.11)	0.24 (0.14)	0.27 (0.16)	0.23 (0.20)	0.10 (0.14)	0.13 (0.17)
	Future_ 0.5m SLR	0.42 (0.22)	0.03 (0.03)	0.06 (0.05)	0.56 (0.24)	0.52 (0.26)	0.57 (0.30)	0.56 (0.27)	0.42 (0.33)	0.46 (0.35)
	Future_ 1.0m SLR	0.42 (0.20)	0.03 (0.03)	0.06 (0.05)	0.54 (0.21)	0.54 (0.26)	0.58 (0.29)	0.52 (0.23)	0.41 (0.32)	0.44 (0.33)
	Future_ 2.5m SLR	0.38 (0.14)	0.03 (0.03)	0.05 (0.04)	0.45 (0.13)	0.55 (0.27)	0.56 (0.28)	0.36 (0.13)	0.38 (0.29)	0.39 (0.31)
Median fresh water flux year	Contemporary _0.5m SLR	0.12 (0.10)	0.00 (0.00)	0.00 (0.00)	0.28 (0.11)	0.23 (0.13)	0.26 (0.15)	0.22 (0.18)	0.10 (0.13)	0.15 (0.17)
	Future_ 0.5m SLR	0.35 (0.19)	0.02 (0.02)	0.06 (0.05)	0.53 (0.25)	0.46 (0.23)	0.53 (0.26)	0.57 (0.26)	0.43 (0.36)	0.50 (0.38)
	Future_ 1.0m SLR	0.35 (0.18)	0.02 (0.02)	0.06 (0.04)	0.50 (0.22)	0.48 (0.24)	0.54 (0.26)	0.52 (0.22)	0.43 (0.35)	0.49 (0.37)
	Future_ 2.5m SLR	0.31 (0.12)	0.02 (0.02)	0.05 (0.03)	0.42 (0.15)	0.50 (0.26)	0.54 (0.27)	0.36 (0.12)	0.41 (0.35)	0.44 (0.37)
High water flux year	Contemporary _0.5m SLR	0.14 (0.11)	0.00 (0.00)	0.00 (0.00)	0.30 (0.12)	0.22 (0.15)	0.24 (0.18)	0.21 (0.19)	0.08 (0.11)	0.10 (0.12)
	Future_ 0.5m SLR	0.39 (0.20)	0.01 (0.01)	0.02 (0.02)	0.55 (0.24)	0.46 (0.24)	0.50 (0.28)	0.54 (0.26)	0.37 (0.32)	0.40 (0.34)
	Future_ 1.0m SLR	0.38 (0.19)	0.01 (0.01)	0.02 (0.02)	0.52 (0.21)	0.48 (0.26)	0.52 (0.28)	0.50 (0.22)	0.38 (0.32)	0.41 (0.35)
	Future_ 2.5m SLR	0.35 (0.13)	0.01 (0.01)	0.01 (0.01)	0.44 (0.14)	0.53 (0.29)	0.55 (0.32)	0.34 (0.12)	0.39 (0.34)	0.41 (0.37)

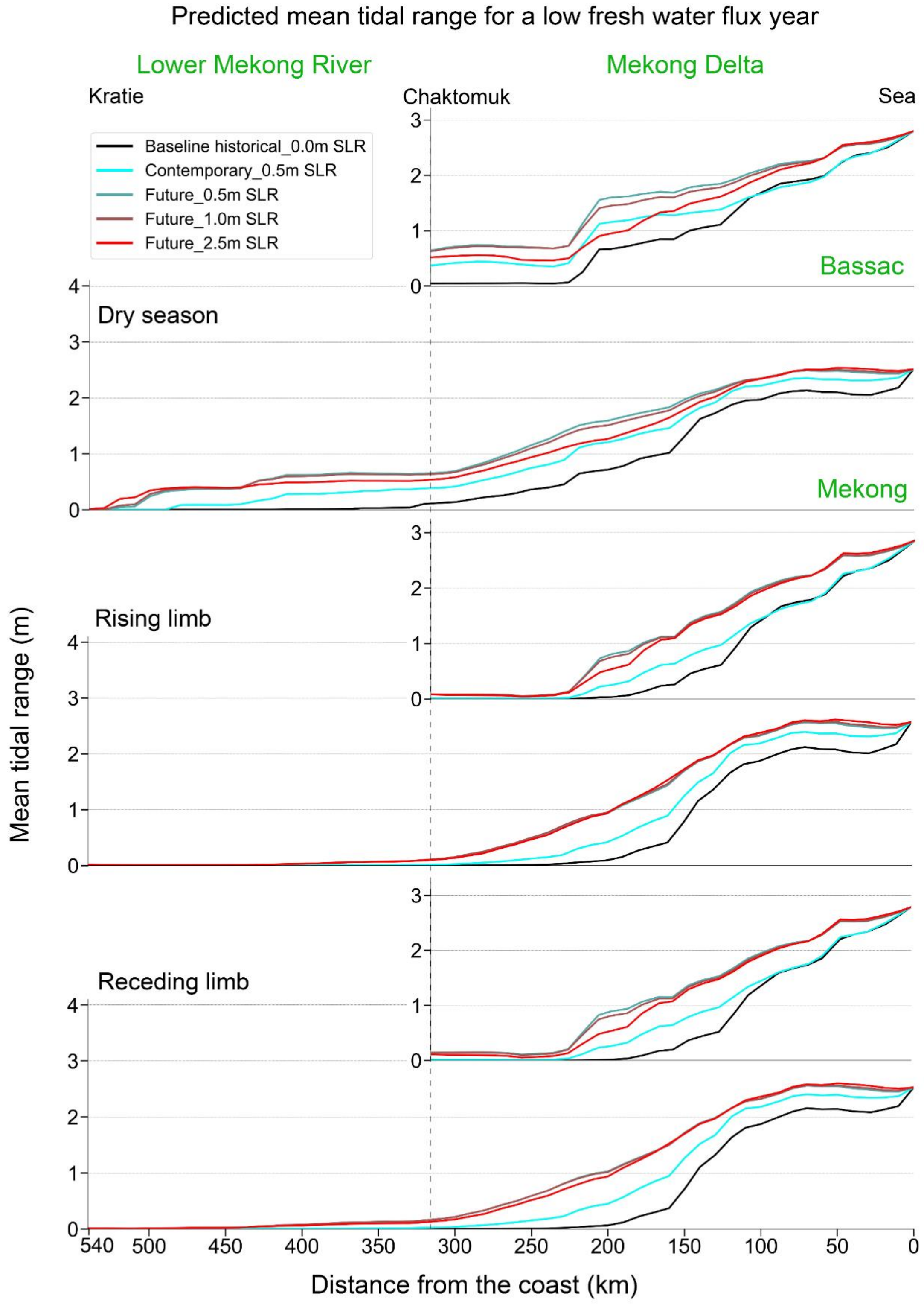

Figure 5-16. The longitudinal profile of mean tidal range ($\overline{TR}$) along the LMR, Mekong and Bassac distributary delta channels for the Baseline historical bathymetry with sea level rise of 0 m, the Contemporary bathymetric with sea level rise of 0.5 m, and the Future bathymetric with sea level rise of 0.5 m, 1 m, and 2.5 m scenarios under low water flux. The main panel focuses on the LMR and Mekong channel, while the insert panel shows the Bassac channel.

5.4.3.3 Future changes in water level extremes

Table 5-12 indicates that for the median fresh water flux condition, compared to the Baseline scenarios, in the LMR, the Contemporary scenario shows a decrease in maximum water levels by an average of 1.49 m (σ = 0.61 m) and minimum water levels by 0.58 m (σ = 1.24 m). These reductions in maximum and minimum water levels become more substantial in the Future_0.5m SLR scenarios, where they decrease by an average of 3.29 m (σ = 0.77 m) and 1.97 m (σ = 0.84 m), respectively. In the Future_1.0m SLR scenario, these reductions are slightly smaller at an average of 3.23 m (σ = 0.77 m) for maximum water levels and 1.59 m (σ = 0.84 m) for minimum water levels. These water levels further decrease in the Future_2.5m SLR scenarios, averaging 2.99 m (σ = 0.76 m) for maximum water levels and 0.32 m (σ = 1.17 m) for minimum water levels. In the Mekong channel, the Contemporary_0.5 m SLR scenario indicates a decrease in maximum water levels by an average of 0.10 m (σ = 0.58 m) and an increase in minimum water levels by 0.12 m (σ = 0.21 m). In the Future_0.5m SLR scenario, both maximum water and minimum water levels decrease by an average of 0.41 m (σ = 0.92 m) and 0.08 m (σ = 0.29 m), respectively. The Future_1.0 m SLR scenario shows a decrease in maximum water levels by an average of 0.03 m (σ = 1.05 m), while increase in minimum water levels by an average of 0.41 m (σ = 0.28 m). In the Future_2.5 m SLR scenario, there is an increase in both maximum water levels and minimum water levels by an average of 1.18 m (σ = 1.37 m) and 1.96 m (σ = 0.24 m), respectively. Similar values can be observed in the Bassac channel akin to those in the Mekong channel, and these trends are consistent across both low and high fresh water flux scenarios (see Table 5-12). Figure 5-17 highlights an increase in both maximum and minimum water levels in the downstream portion, while both maximum and minimum water levels in the landward regions are being reduced. This phenomenon is driven by the impact of reduced water levels due to riverbed lowering, which has a greater impact inland, and the increasing water levels driven by sea level rise, which has a greater impact seaward as presented in section 5.4.1.1 and 5.4.2.1. However, it is noteworthy that the impact of riverbed lowering on reducing water levels is more pronounced for maximum water levels, which occur during high water discharge stages, and has the least impact on minimum water levels, which occur during low water discharge stages. In contrast, the impact of sea level rise on increasing water levels is more pronounced for minimum water levels, which occur during dry season, and has the least impact on maximum water levels, which occur during flood season as presented in the section 5.4.1.3 and 5.4.2.3. As a result, the combination of these influences establishes a boundary where the trend in water levels shifts from increasing to decreasing. This transition boundary extends further inland for minimum water levels, while it extends further seaward for maximum water levels.

For example, under median fresh water flux conditions, in Future_2.5m SLR scenarios, the trend of raising the minimum water level covers entire delta, stretching from the coastal zone to upper Kompong Cham, approximately 440 km from the sea. In contrast, the areas experiencing an increase in the maximum water level extend only to around 250 km from the sea in the same scenarios (Figure 5-17). The most significant reduction in the maximum water level occurs in the upstream part of the study, around 430 km from the sea in LMR for all investigated scenarios with the maximum water level reduction of 2.17 m, 4.15 m, 4.13 m, and 3.94 m for the scenarios of Contemporary, Future_0.5m SLR, Future_1.0m SLR, and Future_2.5m SLR, respectively, compared to Baseline historical scenario. The changes in maximum water level are similar for low and high fresh water flux conditions. Moving downstream in the delta, there is an increasing impact of sea level rise on raising both maximum and minimum water levels, and a diminishing impact of riverbed lowering on reducing maximum and minimum water levels (Figure 5-17).

Table 5-12. The average changes of maximum and minimum water levels along the LMR, Mekong and Bassac distributary delta channels for Contemporary bathymetric with sea level rise of 0.5 m and Future bathymetric with sea level rise of 0.5 m, 1.0 m and 2.5 m scenarios, compared to Baseline historical bathymetry with sea level rise of 0 m under all fresh water flux year conditions. Positive values indicate an increase in water level (m), while negative values indicate a decrease (m). The values in parentheses represent the standard deviation.

Fresh water flux scenarios /Scenarios		Lower Mekong River		Mekong channel		Bassac Channel	
		Maximum water level	Minimum water level	Maximum water level	Minimum water level	Maximum water level	Minimum water level
Low water flux year	Contemporary_ 0.5m SLR	-1.55 (0.71)	-0.44 (1.08)	0.05 (0.52)	0.10 (0.20)	-0.02 (0.48)	0.07 (0.35)
	Future_ 0.5m SLR	-3.41 (0.85)	-1.71 (0.74)	-0.18 (0.88)	-0.14 (0.29)	-0.28 (0.78)	-0.25 (0.39)
	Future_ 1.0m SLR	-3.33 (0.84)	-1.31 (0.81)	0.22 (0.99)	0.36 (0.28)	0.07 (0.90)	0.26 (0.39)
	Future_ 2.5m SLR	-3.03 (0.84)	-0.03 (1.05)	1.46 (1.28)	1.89 (0.25)	1.18 (1.25)	1.83 (0.37)
Median water flux year	Contemporary_ 0.5m SLR	-1.49 (0.61)	-0.58 (1.14)	-0.10 (0.58)	0.12 (0.21)	-0.18 (0.55)	0.07 (0.39)
	Future_ 0.5m SLR	-3.29 (0.77)	-1.97 (0.84)	-0.41 (0.92)	-0.08 (0.29)	-0.46 (0.84)	-0.22 (0.42)
	Future_ 1.0m SLR	-3.23 (0.77)	-1.59 (0.91)	-0.03 (1.05)	0.41 (0.28)	-0.12 (0.97)	0.29 (0.42)
	Future_ 2.5m SLR	-2.99 (0.76)	-0.32 (1.17)	1.18 (1.37)	1.96 (0.24)	0.97 (1.34)	1.87 (0.40)
High water flux year	Contemporary_ 0.5m SLR	-1.33 (0.53)	-0.49 (1.08)	-0.12 (0.61)	0.08 (0.2)	-0.19 (0.55)	0.06 (0.39)
	Future_ 0.5m SLR	-3.11 (0.71)	-1.84 (0.77)	-0.46 (0.99)	-0.16 (0.29)	-0.53 (0.86)	-0.26 (0.41)
	Future_ 1.0m SLR	-3.60 (0.70)	-1.46 (0.83)	-0.09 (1.12)	0.33 (0.28)	-0.20 (0.99)	0.25 (0.41)
	Future_ 2.5m SLR	-2.88 (0.69)	-0.22 (1.07)	1.08 (1.46)	1.87 (0.25)	0.83 (1.38)	1.82 (0.41)

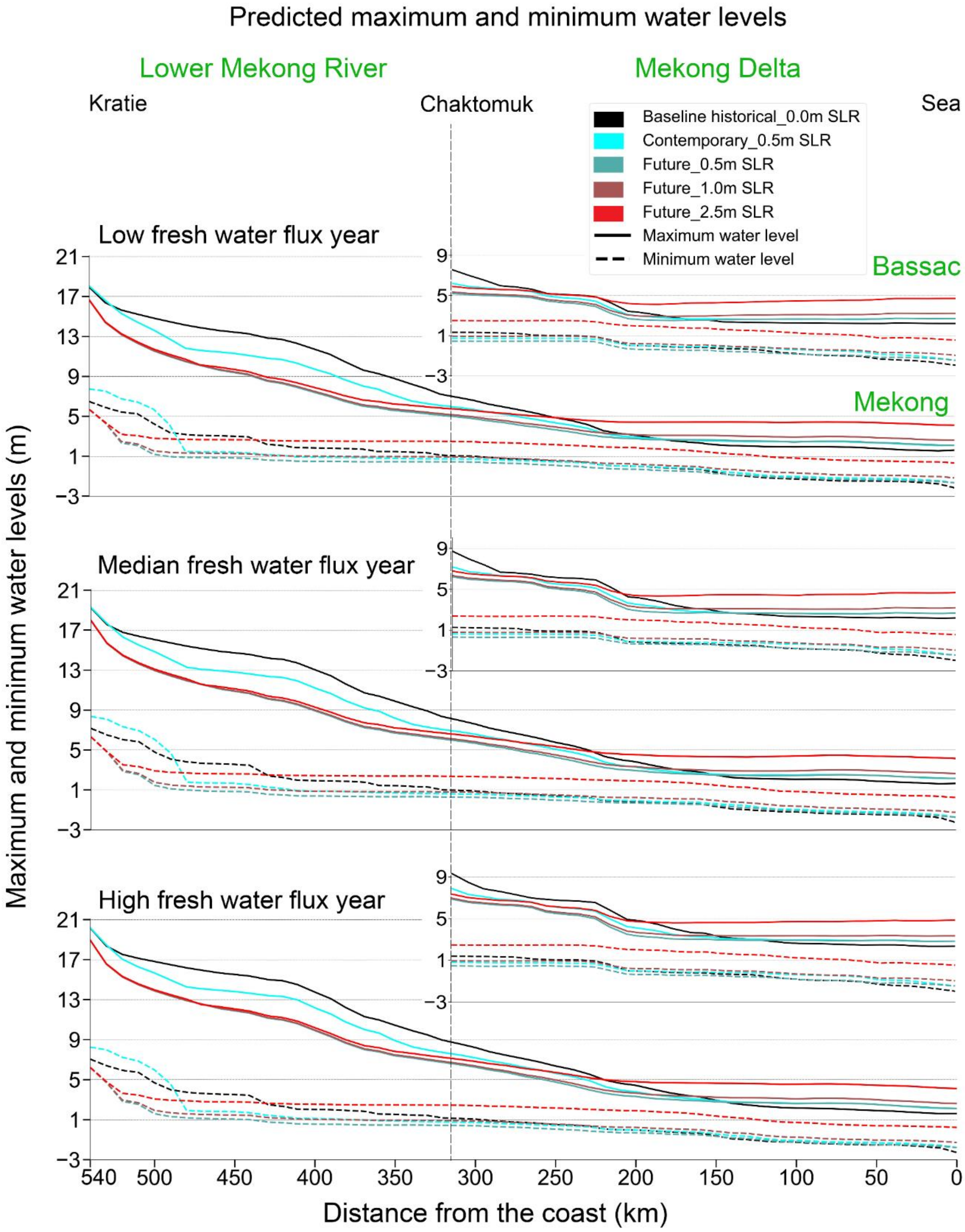

Figure 5-17. The longitudinal profile of changes in maximum and minimum water levels along the LMR, Mekong and Bassac distributary delta channels for Contemporary bathymetric with sea level rise of 0.5 m and Future bathymetric with sea level rise of 0.5 m, 1 m and 2.5 m compared with Baseline historical bathymetry and sea level rise of 0 m conditions, across all fresh water flux scenarios. The main panel focuses on the LMR and Mekong channel, while the insert panel shows the Bassac channel.

5.5 Discussion

The results presented in this Chapter highlight the diverse effects of Contemporary and projected Future riverbed lowering and sea level rise on the hydraulics of the LMR and MD for a range of fresh water flux conditions. Regarding the impact of solely riverbed lowering, consistent with the results presented in Section 4.3.1, Chapter 4, riverbed lowering lead to reductions in water levels (mean, maximum, and minimum) with the decrease being more pronounced in the landward sections and less substantial in the seaward areas. This is because seaward areas are influenced not only by fluvial water flow but also by sea level at the coast. The effect of riverbed lowering on reducing water levels is more noticeable during the flood season compared to the dry season. This is due to the lowering of the riverbed increasing the channel's capacity to carry more water, which had a greater impact during the flood season compared to the dry season. The highest mean water level reduction is observed during the receding limb compared to the rising limb period during the flood season. This is driven by riverbed lowering, which causes a lowering of the water level therefore, consequently results in less water volume flowing into and being stored in the floodplain (detailed presented in in the next section 5.5.1). The reduction of water volume that is stored in the floodplain during the rising limb period, leads to a reduced volume of water flowing back to the mainstream during the receding limb, therefore, lowering the overall mean water levels in the channel (Chua and Lu, 2022).

Riverbed lowering is increasing the tidal range in the entire of LMR and MD for both dry and flood season. These results are driven by the fact that the lowering of the riverbed could (1) increase the capacity to convey tidal water from the river mouth in the mainstream landward, (2) increases the tidal water volume at the river mouth (as the water depth at the river mouth increases), and (3) reduces the water level, consequently decreasing the connectivity of side channels and floodplains, so less tidal water access these side channel, thus tidal flow is propagated further inland.

It is also noted that for the Contemporary scenario in the lower part of delta (<100 km), an increase in $\overline{TR}$ occurs in the Mekong channel, while the $\overline{TR}$ values of the Bassac channel remain almost unchanged (Figure 5-10). A similar phenomenon has been observed in gauged data and has been discussed in Chapter 4 (Section 4.3.2). One potential reason for this result could be the relatively minor reduction in the riverbed elevation at the mouth of the Bassac channel in the Contemporary scenario compared to the Baseline scenario (Figure 5-6, a). This, coupled with the simulated water level changes showing a tendency to remain largely stable in this region for the

Contemporary scenario compared Baseline historical scenarios, leads to minimal alterations in the wet cross-section within this region, which plays a key role in facilitating the propagation of the tidal signal landward. This could explain why the tidal dynamics in the seaward reaches of the Bassac show little change between Baseline historical and Contemporary scenario. The Future scenario bathymetry is lower at this reach which in turn increases the simulated mean $\overline{TR}$ as shown in Figure 5-10.

Regarding the impact of sea level rise alone, the increase in water levels (including mean, maximum, and minimum) is more pronounced in the seaward sections and less so in the landward areas. This is driven by the proximity of the seaward areas to the sea. Additionally, it is worth noting that sea level rise increases water levels more during the dry season than during the flood season. This is because, during the dry season, the fresh water flow is considerably smaller, resulting in lower water levels, which amplifies the impact of sea level rise inland. Conversely, during the flood season, the fresh water flow is high and water levels are higher, which means the greater force of the fluvial input resists the incoming of the sea level rise landward.

Model predictions suggest that sea level rise increases the tidal range during the flood season, but has a negligible impact during the dry season. A possible explanation for this phenomenon is that rising sea levels are causing increased water levels in the main channels, which may enhance connectivity between the mainstream Mekong and Bassac Rivers and their extensive network of side channels and floodplains within the MD delta. This connectivity could contribute to the reduction of tidal range (Eslami et al., 2019). In more detail, without sea level rise, the low water level during the dry season results in limited connectivity between the mainstream channel and its side channels and floodplains. Consequently, the tidal flow at the river mouth propagates further inland. Conversely, during the flood season, the higher water levels increase river-side channels and floodplain connectivity, reducing the inland propagation of tidal flow. However, driven by sea level rise scenarios, the water level in the mainstream increases, with higher values during the dry season and lower values during the flood season (Table 5-7 and Figure 5-12). As a result, the rate of increase in the connectivity between the mainstream and its side channels and floodplains is higher during the dry season than during the flood season. This increased connectivity due to sea level rise will reduce the tidal range and landward tidal flow more during the dry season than during the flood season. In contrast, sea level rise will increase tidal flow at the river mouths of the mainstream due to the greater water depth, affecting both the dry and flood seasons similarly. Therefore, in the mainstream channels, whether the landward tidal propagation and tidal range increase or decrease will depend on the balance between the additional tidal flow caused by sea level rise and the reduction in tidal flow due to the enhanced connectivity of floodplains between channels and the mainstream. This reduction in tidal flow is more pronounced during the dry season.

When considering the combined effects of riverbed lowering and sea level rise, water levels are influenced in opposite ways. Riverbed lowering, which decreases water levels, is more pronounced in landward areas, while sea level rise, which increases water levels, has a greater impact seaward. These opposing forces create a transition zone where the change from increasing to decreasing water levels occurs. For more detail, the transition point for the Contemporary riverbed lowering scenario and the Future riverbed lowering with 0.5 m and 1.0 m SLR scenarios appears to occur around 200 km inland during the dry season and about 150 km during the flood season. However, with an SLR of 2.5 m, the transition point shifts further landward, occurring at approximately 400 km during the dry season and around 200 km during the flood season (Figure 5-15). The changes in the water level regime within the delta, driven by both riverbed lowering and sea level rise, could alter flooding patterns. Specifically, the upstream region of the delta is expected to see a reduction in flooding levels, mainly due to riverbed lowering, with this effect diminishing towards the coast. In contrast, the downstream delta faces potential inundation risks primarily due to a combination of sea level rise and an increased tidal range resulting from riverbed lowering. Implications of the finding's potential lead to potential changes in future flood hazards, which are discussed herein.

5.5.1 Reduction of channel-floodplain connectivity in landward areas

Landward regions of the LMB are expected to experience a reduction in flood levels due to riverbed lowering, and both magnitude and duration of inundation will be affected. In more detail, there is a substantial decrease in the duration that high water levels are sustained for three gauging stations across the LMB region (Figure 5-18). In the median (low; high) fresh water flux year, at the Kompong Cham station (398 km) in LMR, the duration of simulated water levels exceeding 14.1 m (referenced to Hon Dau MSL): the local flood alarm level (HRF, 2022), is approximately 1 (0; 9) days in the Baseline historical scenario, but is not exceeded in the Contemporary and Future riverbed bathymetry scenario (Figure 5-18). At the Chaktomuk station (318 km) in the apex of Mekong delta, the duration during which water levels exceed 9.3 m, the local flood alarm level (HRF, 2022), is 0 (0; 31) days in the Baseline historical scenario and not exceeded in the Contemporary and Future riverbed bathymetry scenario (Figure 5-18). At the Tan Chau station (203 km) in VMD, the period during which water levels surpass 3.5 m, the local flood alarm level, is 68 (0; 107) days in the Baseline historical scenario and is reduced to 0 (0; 37) days in the Contemporary scenario while model predictions show that this level will not be surpassed in the Future scenario under any fresh water flux condition (Figure 5-18).

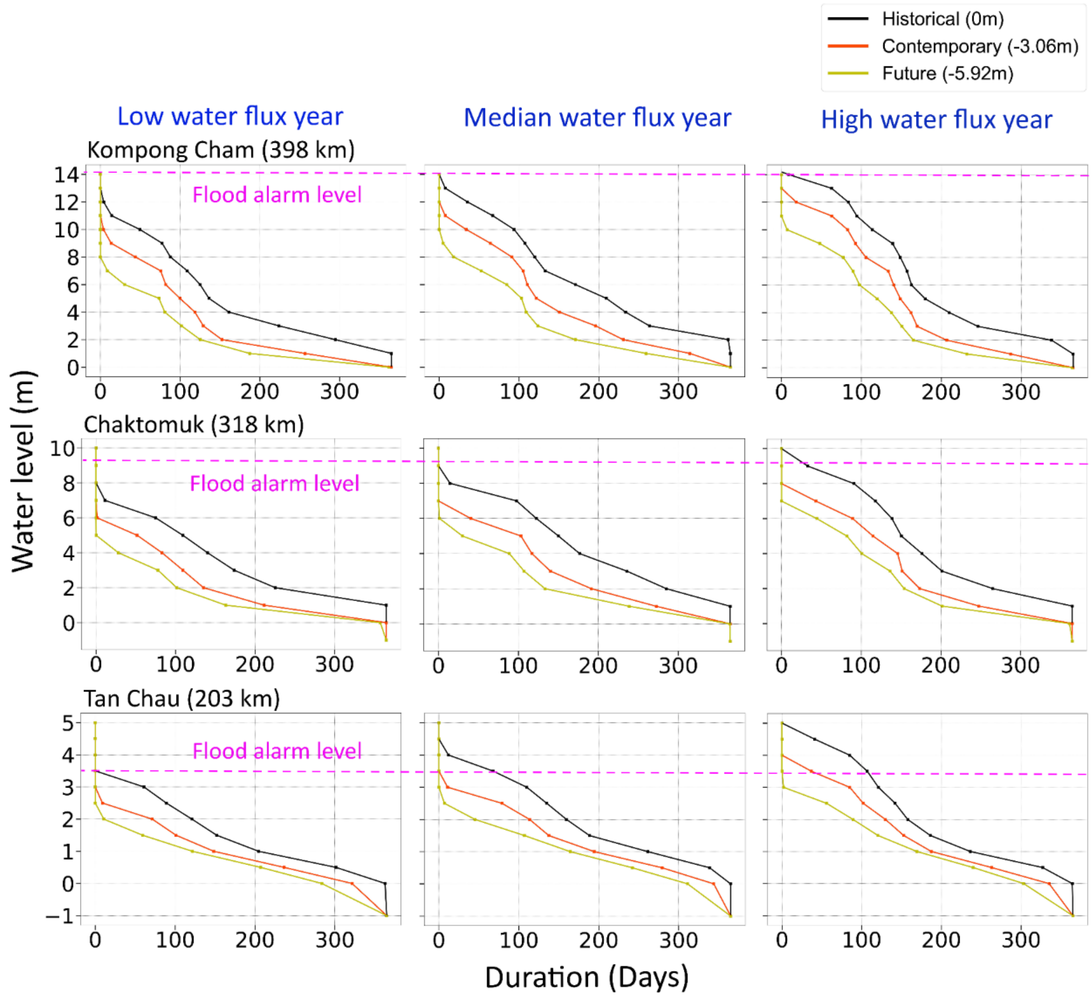

Figure 5-18. The relationships between the water levels and their respective durations are examined at different stations along the Lower Mekong River and Mekong Delta for a range of hydraulic upstream fresh water flux conditions. The figure in the parentheses illustrates the distance (km) from gauges to respective river mouths.

The reduction in the intensity and duration of high-water levels has also led to a disconnection between the river and its floodplain. The floodplains within the Lower Mekong Basin are divided into three zones (Figure 5-19). The first zone, referred to as the Lower Mekong River (LMR) floodplain, encompasses the floodplain area southeast of the Lower Mekong River, extending from Kratie to the Chaktomuk Junction. The second zone, known as the Tonle Sap (TS) floodplain in the southwest region of the Lower Mekong River, adjacent to Tonle Sap Lake (Fujii et al., 2003). The final zone, called the Mekong delta (MD) floodplain, covers the entire floodplain stretching from the Chaktomuk Junction to the coast (Figure 5-19).

Model results indicate a substantial reduction in fresh water flow from the LMR and the Mekong and Bassac channels to floodplains across different riverbed lowering scenarios. Specifically, under median (low; high) fresh water flux conditions, the percentage of the total water volume flowing from the LMR to the LMR floodplain is 10 % (9 %; 14 %) of the total water volume measured at Kratie, which is represented as 100%, in the Baseline historical scenario. However, these percentage decrease to 4 % (3 %; 6 %) when the Contemporary bathymetric scenario is explored and further decrease to approximately 2 % (2 %; 3 %) in the Future bathymetric scenario (see Figure 5-19). This signifies a decrease of 6 % (6 %; 8 %) and 8 % (7 %; 11 %) in the fraction of total water volume from the Mekong River as measured at Kratie overflowing onto the LMR floodplain in the Contemporary and Future scenarios, respectively, compared to the Baseline historical scenario. It is emphasized that there is no indication of water flowing back from the LMR floodplain to the LMR in any of the riverbed lowering scenarios, regardless of upstream fresh water flux conditions (Figure 5-19).

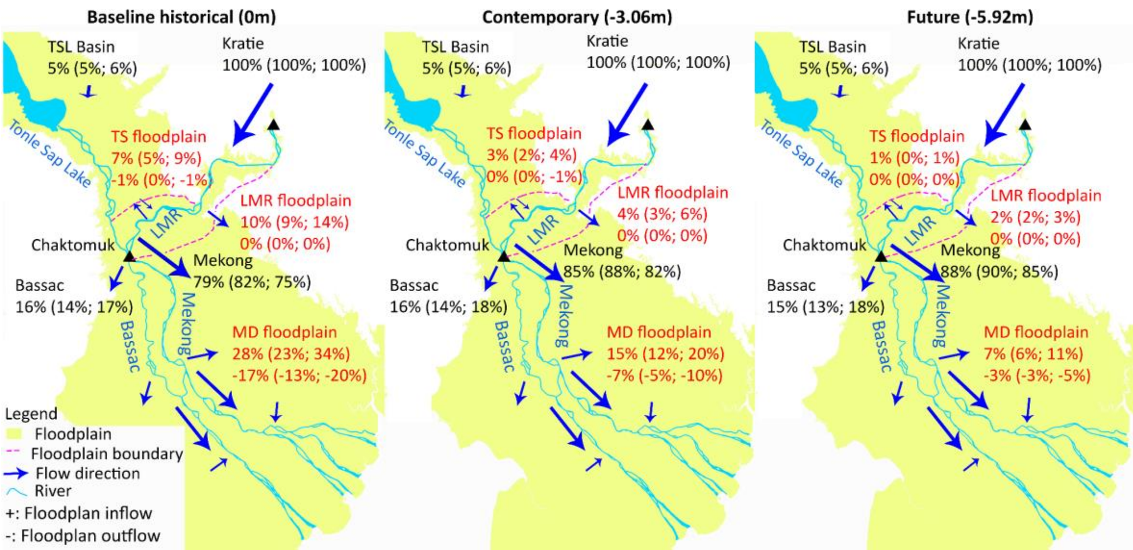

Figure 5-19. Distribution of water volume from the main channels to across different floodplain zones — the Lower Mekong River floodplain (LMR floodplain), the Tonle Sap floodplain (TS floodplain), and the Mekong Delta floodplain (MD floodplain) — for various channel bathymetric scenarios during a median (low, high) freshwater flux year with 0 m sea level rise. The positive percentage values indicate the proportion of total water volume flowing from the river into its respective floodplain, while the negative percentage values represent the proportion of total water volume flowing from the floodplain back into the river

In the TS floodplain, there are 7% (5 %; 9 %) of the total water volume measured at Kratie from the LMR to the TS floodplain, A portion of this water volume flows in the TS floodplain directly into Tonle Sap Lake, while the remainder flows through the Tonle Sap River before eventually reaching the lake (Fujii et al., 2003; MRCS/WUP-FIN, 2007), in the Baseline historical scenario under median (low; high) freshwater flux conditions. However, these percentage decrease to 3 % (2 %; 4 %) in the Contemporary bathymetric scenario and further decrease to approximately 1% (0%; 1 %) in the Future bathymetric scenario (Figure 5-19). This signifies a decrease of 4 % (3 %; 5 %) and 6 % (6 %; 8 %) in the fraction of total water volume from the LMR overflowing onto the Tonle Sap floodplain in the Contemporary and Future scenario, respectively, compared to the Baseline historical scenario. Meanwhile, in the Baseline historical scenario, only 1 % (0 %; 1 %) of the total water volume measured at Kratie returns from the TS floodplain to the LMR. In the contemporary scenarios, this percentage decreases to 0 % (0 %; 1 %), and in the Future scenario, there is no indication of water flowing back from the TS floodplain to the LMR under median (low; high) fresh water flux conditions. (Figure 5-19).

In the MD floodplain, under the Baseline historical scenario, 28 % (23 %; 34 %) of the total water volume measured at Kratie flows from the Mekong and Bassac channels to the MD floodplain, while 17 % (13 %; 20 %) flows back from the MD floodplain to the main Mekong and Bassac channels. In the contemporary scenario, 15 % (12 %; 20 %) of the total water volume at Kratie flows from the Mekong and Bassac channels to the MD floodplain, with 7% (5 %; 10 %) returning to the main channels. This represents a decrease of 13 % (11 %; 14 %) in water flow from the main Mekong and Bassac channels to the MD floodplain and a 10% (8 %; 10 %) reduction in water flowing back from MD floodplain to the main channels compared to the Baseline historical scenario, under median (low; high) fresh water flux conditions (Figure 5-19). In the future scenario, only 7% (6%; 11%) of the total water volume at Kratie flows from the Mekong and Bassac channels to the MD floodplain, with 3% (3%; 5%) returning to the main channels. This reflects a decrease of 21% (15%; 23%) in water flow from the main Mekong and Bassac channels to the MD floodplain and a 14% (10%; 15%) reduction in water flowing back to the main channels compared to the Baseline historical scenario, under median (low; high) fresh water flux conditions (Figure 5-19).

Although, Fluvial flooding imposes significant and severe challenges to the delta for example, large floods can cause loss of human lives, damage to infrastructure and riverbank collapse (Ericson et al., 2006; Chinh et al., 2016; Ward et al., 2018; Ghosh et al,. 2019). Fluvial flooding also brings numerous benefits to the region, including the deposition of sediment layers enriched with nutrients, valuable to agricultural productivity, and also drives delta aggradation counteracting subsidence and sea level rise (Vörösmarty et al., 2009; Hung et al., 2014a; Overeem and Syvitski, 2009; Kondolf et al., 2022). Additionally, fluvial flooding provides fresh water for irrigation and domestic use, increases fishery resources, improves navigation transport, and flushes contaminated and saline water towards the sea (Vörösmarty et al., 2009; Best, 2019).

The findings in this chapter highlight that while riverbed lowering can mitigate flood risk in landward areas, it also results in a reduction in fluvial inundation of the floodplain by disconnecting the channel from its floodplain. If riverbed lowering remains unmitigated, water levels and the water volume entering the floodplain will continue to persistently decrease especially during the flood season, damaging the connection between the channel and its floodplain. The impacts of disconnection include damage to the floodplain ecosystem, such as reduced water depth, shorter durations of high water levels, and decreased water flow to the floodplain, which could reduce the flow of nutrients and organic matter from the river to the floodplain, thereby harming vegetation and aquatic habitats (Sparks, 1995; Tockner and Stanford, 2002), reduce fish populations, diminishing the conditions crucial for riverscape health (Baran, et al., 2007; Wilcox et al., 2013; Arias at al., 2014; Stone et al., 2017; Mauricio et al., 2019). In addition, the reduction of water flow onto the floodplain also contributes to a decrease in the amount of sediment delivered and deposited there (Wohl et al., 2015; Chapman et al., 2016) , which in turn reduces the progresses of delta aggradation and reduces the floodplain's ability to resist land subsidence and sea level rise (Vörösmarty et al., 2009; Syvitski et al., 2009). Finaly, the reduction in the flow of nutrients and organic matter from the river to the floodplain may lead to an increase of synthetic fertilizers use in agriculture. The decrease in average, maximum, and minimum water levels can hinder the effectiveness of irrigation systems, particularly during the dry season when water levels are at their lowest, leading to higher costs for dredging side channels and increased expenses related to pumping systems. Ultimately, these factors contribute to rising food production costs. These results underscore the persistent environmental consequences resulting from sediment deprivation induced by upstream dams and intensive sand mining in the Lower Mekong River and Mekong Delta. This issue is shared by many major river deltas globally undergoing rapid economic development (UNEP, 2019; Best, 2019). As the demand for sand, hydropower, and fresh water supply increases, it becomes critical to establish sustainable policies and practices for managing transnational rivers, agreed upon by the nations that these rivers are running through (Vasilopoulos et al., 2021; Hackney, 2024).

5.5.2 Increased flood risk seaward

The simulated results from section 5.4.2 and 5.4.3 suggest that sea level rise is causing an upward trend in water levels in the downstream delta. This increase in water levels could potentially lead to greater flooding in the downstream delta (Vörösmarty et al., 2009; Syvitski et al., 2009) an area already shrinking due to sediment deficits (Kondolf et al., 2022) and land subsidence from unsustainable groundwater, hydrocarbon, and oil extraction (Erkens et al., 2015; Best and Darby, 2020; Minderhoud et al., 2020). Furthermore, sea level rise results in the submersion of terrestrial land, which facilitates the direct transfer of coastal sediment into the ocean. This process deepens near-shore areas, accelerates coastal erosion, alters the delta's evolutionary trajectory (Nienhuis et al., 2020), and contributes to the loss of wetlands and mangroves (Bucx et al., 2010; EPA, 2016; Syvitski et al., 2022). It also impacts wetland communities and their ecosystem functions (Herbert et al. 2015) and exacerbates saline intrusion (Chang et al., 2011; Herbert et al., 2015; Ensign and Noe, 2018). Additionally, the increase in tidal range near the coast, driven by riverbed lowering and sea level rise, could contribute to tidal inundation in these areas. Combined with the anticipated increase in frequency of tropical storms and typhoons in the region (MONRE, 2016; Wood et al., 2023), this could further heighten the risk of ocean flooding, especially during storm surges.

5.5.3 Recommendations

The aforementioned findings underscore the urgent need for sustainable sediment management to address the degradation of floodplain ecosystems, boost agricultural productivity, preserve biodiversity, and improve flood management, all exacerbated by riverbed lowering due to upstream damming and sand mining. Key recommendations include reducing reliance on natural sand by promoting the use of alternative materials, encouraging sand reuse, and enhancing monitoring systems for sand extraction activities (Bendixen et al., 2019; Hackney, 2024). Additionally, mitigating the effects of upstream dams requires careful assessment of proposed sites, the application of sediment-releasing techniques such as turbidity current venting, and the exploration of cleaner energy sources to reduce dependency on hydropower (Kondolf et al., 2014; Laksitaningtyas et al., 2022; Lai et al., 2024). Optimizing delta infrastructure, including sluice gates and pumping systems, is essential for enhancing sediment transport and addressing the challenges caused by diminished water and sediment flow (Hung, 2011). Urban planning must also incorporate strategies to cope with rising sea levels and tidal surges, in order to mitigate the risk of inundation. While this research primarily focuses on the LMB, the issue of sediment deficit caused by unsustainable sand mining and upstream dams is also prevalent in other major river deltas undergoing rapid economic development (Vörösmarty et al., 2009; Giosan et al., 2014; Best, 2019), including the Pearl River Delta (Lu et al., 2007), Yellow River Delta (Chu, 2014), and Ganges Delta (Daham et al., 2024). Therefore, it is essential to implement enforcement measures to curb the consumption of natural sand, helping to alleviate demand and maintain a balance between fulfilling essential needs and promoting sustainable socio-economic development (Biancamaria et al., 2016; Gleason, et al., 2017; Gleason and Hamdan, 2017; Bendixen, et al., 2019; Best, 2019; Hackney et al., 2021).

5.6 Chapter Summary

In this chapter, a 1D hydrodynamic model for the Mekong, originally developed by Dung (2011), has been adopted and updated. Through calibration and validation, it enables the simulation of hydraulics in the study area, covering the stretch of the Lower Mekong River, the Tonle Sap system, and the Mekong Delta. A series of scenarios involving different level of riverbed lowering, sea level rise and different upstream monsoonal hydrograph conditions have been developed and simulated to study the change of hydraulics and the related water level regime across the LMR and MD. Model results show that the combination of projected channel incision and sea level rise drives a reduction of water level landward, an increase of water level and tidal range seaward and an ingress of the tidal signal landward. This results in reduced connectivity between channels and their floodplains in landward areas while increasing flood risk seaward. These findings map to the second Objective (O2) of the research which aims to understand the evolution of hydraulic regime in the LMR and MD under projected Future riverbed lowering and sea level rise and responds to the specific Research Question (RQ2): How will hydraulics in the Lower Mekong Basin (LMB) change in the future due to projected riverbed lowering and sea-level rise?

These findings provide valuable insights into the critical environmental challenges facing the Lower Mekong Basin, particularly the impacts of riverbed lowering and its cascading effects on ecosystems, agriculture, and flood risks. The research underscores the necessity for innovative sediment management strategies, such as reducing dependence on natural sand, promoting sand reuse, and enhancing delta infrastructure to improve sediment transport and connectivity. Additionally, it highlights the significance of transboundary cooperation in addressing sediment deficits, ensuring ecological sustainability, and enhancing resilience to environmental changes. This study not only addresses immediate challenges but also contributes to long-term socio-economic sustainability in delta regions globally, emphasizing its importance in advancing international efforts for sustainable delta management.

The present Chapter employed a 1D model to simulate the evolution of hydraulic regime in the LMR and MD under different projected scenarios of riverbed lowering and sea level rise. However, the modelling approach has limitations, especially concerning the fragmented spatial and temporal resolution of riverbed bathymetry used to create the riverbed lowering scenarios (see Section 3.3 of Chapter 3) with some assumptions were made in this process (see Section 5.2.1). In addition, the dyke system crosses the VMD is not accounted in the model, however, the existed dyke in VMD could limit the channel floodplain connectivity even further than what model have calculated here. The present Chapter focused on the Lower Mekong River and the Mekong delta. Chapter 6 that follows will extend the research to include the Tonle Sap River and Lake system.

Chapter 6. Human Induced riverbed lowering in the Mekong shrinks the Tonle Sap Lake's critical flood pulse

Chapter 5 has explored the impact of riverbed lowering and sea level rise on the hydraulics of the Lower Mekong River (LMR) and its delta. In this chapter, the focus will be on the effects of riverbed lowering on the flood pulse of Tonle Sap Lake (TSL). This chapter addresses the second objective (O2) of the research, which aims to understand the evolution of the hydraulic regime in the LMR and MD under projected future scenarios of riverbed lowering and sea-level rise, and to answer the specific research question (RQ.3): How will the connection to the Tonle Sap Lake be affected by projected riverbed lowering and sea-level rise? Since the impact of sea level rise on the inland areas of the LMR is minimal, particularly during the flood season (e.g., a 1 m of sea level rise only results in an average increase of 0.04m and 0.08m during the rising and receding limbs, respectively in LMR, see Table 5.7, section 5.4.2, Chapter 5), sea level rise will not be considered here. This chapter is organized as follows: Section 6.1 will present a brief introduction to Tonle Sap Lake, its current critical issues, and an overview of the model scenarios examined. Section 6.2 will outline the results obtained. Section 6.3 will discuss the implications of changes in the Tonle Sap Lake flood pulse on delta function. Finally, Section 6.4 will summarize the chapter's key findings.

6.1 Introduction

TSL is one of the most ecologically diverse lake ecosystems globally (MRC, 2005; Chan et al., 2020) and ranks fourth in fish productivity (Bonheur and Lane, 2002). The lake is encircled by a diverse array of habitats, including flooded forests, scrublands, grasslands, and agricultural areas. The flooded forests, composed of tree species adapted to extended submersion, are critical for maintaining biodiversity and providing essential ecosystem services like carbon sequestration, water regulation, and soil stabilization (Bonheur and Lane, 2002; Campbell et al., 2006; Arias et al., 2013). Recognized as a UNESCO World Heritage Biosphere Reserve since 1997, the lake hosts 885 species, including endangered amphibians, reptiles, mammals, and birds (UNESCO; Bonheur and Lane, 2002; Campbell et al., 2006; Uk et al., 2018) (See Section 2.3.1, Chapter 2 for details).

The TSL is linked to the LMR by the Tonle Sap River (TSR) which joins the LMR at Chaktomuk Junction (Figure 6-1). The hydraulics of Tonle Sap Lake are mainly driven by the Mekong River's monsoonal flood pulse. Specifically, for the majority of the year freshwater in the TSL drains downstream into the MD via the TSR (MRCS/WUP-FIN, 2007). However, during the monsoon flood season (typically June–October), water from the Mekong flows into Tonle Sap Lake (TSL) through two main pathways: (1) water levels in the Mekong at Chaktomuk Junction rise to a level that exceeds the water levels in the lake, creating a hydraulic gradient that causes the flow of the TSR to reverse, driving water from the Mekong River into the TSL (MRCS/WUP-FIN, 2007; Kummu et al., 2014); (2) the Mekong also floods the Tonle Sap floodplain with nearly half of it entering TSL directly and the rest reaching the lake via the TSR (Fujii et al., 2003; MRC, 2005) (See Section 2.3.1, Chapter 2 for details). The flow reversal and the TSL function like a vast water capacitor for the MD, storing a substantial volume of the Mekong's seasonal floodwaters. This storage helps regulate flood season water levels throughout the MD and gradually releases the stored water during the dry season, ensuring a steady flow to the MD precisely when agricultural water demand is highest. Indeed, the TSL outflows could accounts for 20-50 % of the Mekong fluxes at the apex of the delta during the period from October–March (Fujii et al., 2003; Kummu et al., 2014). Therefore, the lake's flood pulse is not only vital for its biological productivity and biodiversity but also essential for maintaining water systems and levels across the MD, home of 23 million people (MRC, 2005; Keskinen et al., 2013; Cochrane et al., 2014; Chan et al., 2020; Morovati et al., 2023) (See Section 2.3.1, Chapter 2 for details).

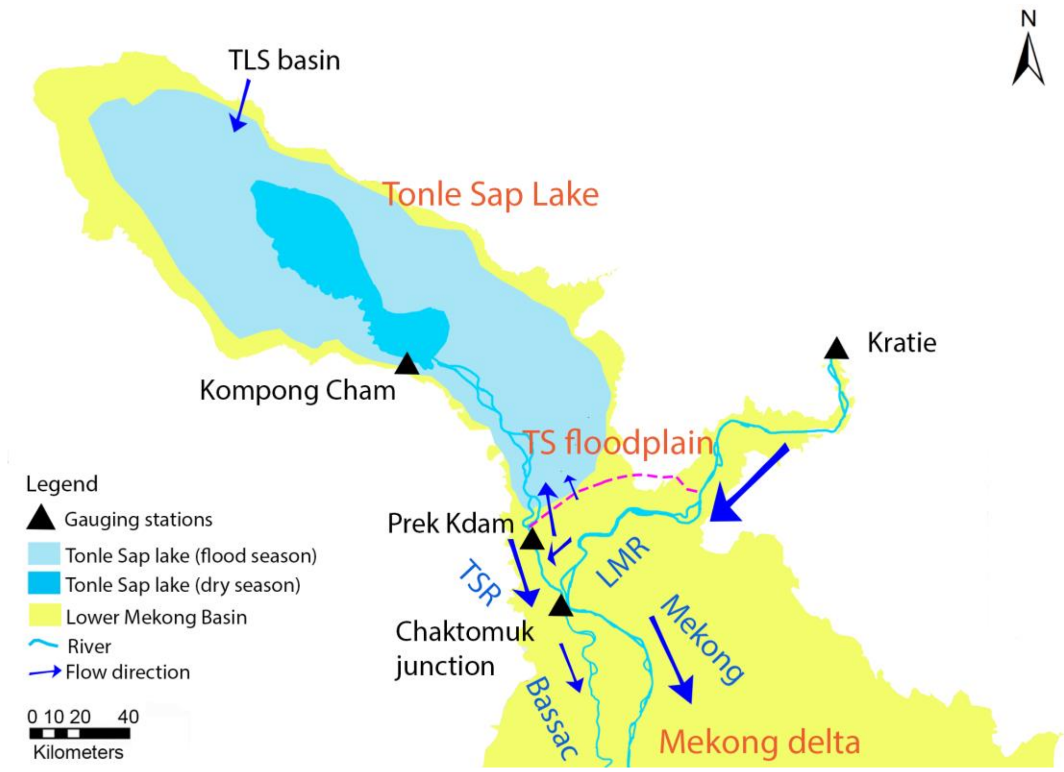

Figure 6-1. The Tonle Sap Lake system, which includes the Tonle Sap Lake (TSL) and the Tonle Sap River (TSR), the Tonle Sap (TS) floodplain, and the Mekong Delta, within the Lower Mekong Basin.

However, recent observations have highlighted changes in the timing and duration of the reverse flow into the TSL, reducing the lake's seasonal inundation extent and raising concerns that the normal functioning of the annual reverse flow pulse is becoming compromised (Cochrane at al., 2014; Wen and Park, 2021; Chua et al., 2022; Dang et al., 2022; Morovati et al., 2023). Specifically, the average annual reverse flow from the LMR to the TSL (at Prek Kdam on the TSR) is estimated to have decreased from 49.7 billion m^3 (during 1962-1972) to 31.7 billion m^3 (2010-2018), a decline of 36.2 % (Chua et al., 2022). Consequently, maximum flood water levels in the TSL (as estimated at Kompong Luong on the lake itself) have decreased by an average of 1.05 m during 2010-2019 compared to 1996-2009 (Chua et al., 2022) and the average maximum annual inundated area of the lake has decreased by 16.4%, from 11,917 km^2 (2001-2009) to 9,967 km^2 (2010-2020) (Morovati et al., 2023).

The causes of the decline in the TSR reverse flow and attendant shrinking of the TSL are unclear. Previous studies have suggested that these declines may variously be attributed to: (i) reductions in flood magnitudes on the Mekong River due to climate change (Ji et al., 2018; Wang et al., 2020; Chen et al., 2021; Morovati et al., 2023), (ii) reductions in flood season water levels on the Mekong River due to flow regulation by upstream dams (Kummu and Sarkkula, 2008; Lauri et al., 2012; Hecht et al., 2019; Dang et al., 2022) and; (iii) urban development (projects for irrigation, flood control, domestic water supply, and navigation) in the Mekong basin (Kummu and Sarkkula, 2008; Cochrane et al., 2014; Cochrane et al., 2014; Morovati et al., 2023) and (iv) infrastructure development in the Tonle Sap floodplain, such as national road construction and road improvements, has obstructed water flow from the LMR to the Tonle Sap floodplain and prevented it from reaching the lake. This has reduced the water flow contribution from around 5 % of the lake's volume (MRC, 2005) to approximately 3 % (Kummu et al., 2014). However, rainfall and flow measurements do not wholly support the first two points. Recorded rainfall in the Cambodian floodplains has remained relatively stable between 1960 and 2019 (Chua et al., 2022) and discharge records from stations on the TSR at Prek Kdam and the Mekong River at Neak Luong, and Chaktomuk stations (Figure 5-1, Chapter 5) indicate that only ~8% of the decreased intensity of the reverse flow can be attributed to upstream hydrograph changes on the Mekong (Chua et al., 2022). This means that the observed decline in the reverse flow into the TSL cannot be explained by hydrological factors as well as infrastructure development in Tonle Sap floodplain alone and may be explained by other factors.

An alternative factor may be the role of riverbed lowering altering the wet season hydraulic gradient between the junction and the TSL and reduces water flow from the LMR to the Tonle

Sap floodplain. In more detail, the results presented in subsection 5.4.1.1, Chapter 5 highlighted how riverbed lowering drives a water level reduction along the LMR as well as a decrease in water volume flowing from the LMR to the Tonle Sap floodplain, which ultimately flows into the TSL (see Figure 5-19, section 5.5.1, Chapter 5). Therefore, it is proposed that the observed reductions in the intensity of the TSR's reverse flow are predominantly driven by riverbed lowering in the LMR and MD, with consequent impacts on the water surface gradients that ultimately drive the TSR reverse flow.

To validate this, the results from a series of riverbed lowering scenarios: Baseline historical (0 m), Contemporary (-3.02 m), and Future (-5.92 m), under different upstream water flux conditions (low, median, and high fresh water flux years) (see more detail in Section 5.2.1 and 5.2.3, Chapter 5) will be analysed. This analysis will quantify changes in the magnitude of the Tonle Sap River flow reversal in response to varying levels of riverbed lowering and assess the significance of these changes for regional provisioning and regulating ecosystem services.

The simulated hourly water level in the lake (at Kompong Luong stations) and water discharge (estimated at Prek Kdam) were extracted and analysed. The simulated hourly water level in the lake (at Kompong Luong stations) and water discharge (estimated at Prek Kdam) was extracted and analysis. The inundation area of the TSL is calculated based on the relationship between the water level at the Kompong Luong station (referenced to the Ha Tien MSL) and the flooded area (A), as described in Eq. 10, adopted from Kummu et al., (2014).

$$A = -5.5701 * WL^3 + 137.4 * WL^2 + 470.29 * WL + 1680.2 \qquad (10)$$

The results of this analysis are presented in the following section.

6.2 Results

The results of riverbed lowering, which drives changes in the Tonle Sap River's flow reversal, will be presented in Section 6.2.1. Changes in water levels and lake inundation will be discussed in Section 6.2.2, while Section 6.3 will cover the changes in water fluxes into the Mekong Delta for both dry and flood seasons.

6.2.1 Changes of the Tonle Sap River flow reversal

Under riverbed lowering scenarios, the total volume of water flowing from the LMR to the TSL (as estimated at Prek Kdam for both TLR and TS floodplain) is reduced compared to Baseline historical scenario (Orange bars; Figure 6-2, a). Notably, for the Baseline historical scenario the total volume of water flowing into the TSL is calculated as 45.1 billion m³ (33.2 billion m³; 61.9

billion m^3) for the median (low; high) fresh water flux years. Of this total volume, about 36.0 billion m^3 (31.1 billion m^3; 48.9 billion m^3) is contributed by the TSR, as measured at Prek Kdam, while 9.1 billion m^3 (2.1 billion m^3; 13.0 billion m^3) comes from the TS floodplain. However, these values decline for all three hydrograph scenarios under the Contemporary scenario, with the total water volumes entering the TSL decreasing to 24.0 billion m^3 (16.7 billion m^3; 37.1 billion m^3) for the median (low; high) water flux years (Figure 6-2, a). Of this total volume, about 21.3 billion m^3 (15.7 billion m^3; 32.9 billion m^3) is contributed by the TSR, while 2.7 billion m^3 (1.0 billion m^3; 4.2 billion m^3) comes from the TS floodplain. This represents a 46.8 % (49.6 %; 40.0 %) decrease in total water volume flowing into the TSL for median (low; high) water flux years compared to the Baseline historical scenario. Finally, for the Future scenario, the total water flux from the Mekong to the TSL is calculated as 13.9 billion m^3 (9.1 billion m^3; 22.4 billion m^3) (Figure 6-2, a) with about 13.2 billion m^3 (8.8 billion m^3; 21.1 billion m^3) is contributed by the TSR, while 0.7 billion m^3 (0.3 billion m^3; 1.3 billion m^3) comes from the TS floodplain. This representing a reduction of 69.3 % (72.6 %; 63.8 %) in inflow volume in total water volume flowing into the TSL for the median (low; high) fresh water flux years compared to Baseline historical scenario (Figure 6-2, a).

A decrease in the duration during which flow is reversed is from the Mekong towards the TSL is also shown by the simulations (Green bars; Figure 6-2, a). In the Baseline historical scenario flow from the Mekong to the TSL occurs for 136 days (128 days; 139 days) for the median (low; high) fresh water flux years. In the Contemporary scenario the duration of flow directed from the Mekong to the TSL is predicted to be 121 days (82 days; 114 days) for the median (low; high) fresh water flux years, a decrease of 11 % (35.9 %; 18 %) compared to Baseline historical scenario. Under the Future scenario, the number of days where flow is directed from the Mekong to the TSL is predicted to decline to 91 days (72 days; 107 days) for the median (low; high) fresh water flux years, a decrease of 33.1 % (43.8 %; 23.0 %) compared to Baseline historical scenario.

The reduction in total water fluxes with increased riverbed lowering is mirrored in a reduction in maximum discharges (as estimated at Prek Kdam for both TLR and floodplain) flowing into the TSL during the flood season (Figure 6-2, b). For the Baseline historical scenario, the peak discharge to the TSL is estimated to be 9,084 m^3s^{-1} (8,147 m^3s^{-1}; 11,539 m^3s^{-1}) for the median (low; high) fresh water flux years. In the Contemporary scenario the estimated peak discharge falls to 5,390 m^3s^{-1} (4,911 m^3s^{-1}; 6,965 m^3s^{-1}) for the median (low; high) fresh water flux years (Figure 6-2, b), a decrease of 40.7 % (39.7 %; 39.6 %) compared to Baseline historical scenario.

For the Future scenario, peak water discharge decreases to approximately 3.675 m^3s^{-1} (3,422 m^3s^{-1}; 4,668 m^3s^{-1}) (Figure 6-2, b), representing a decrease of 59.5 % (58.0 %; 59.5 %) in flow for the median (low; high) fresh water flux years compared to Baseline historical scenario.

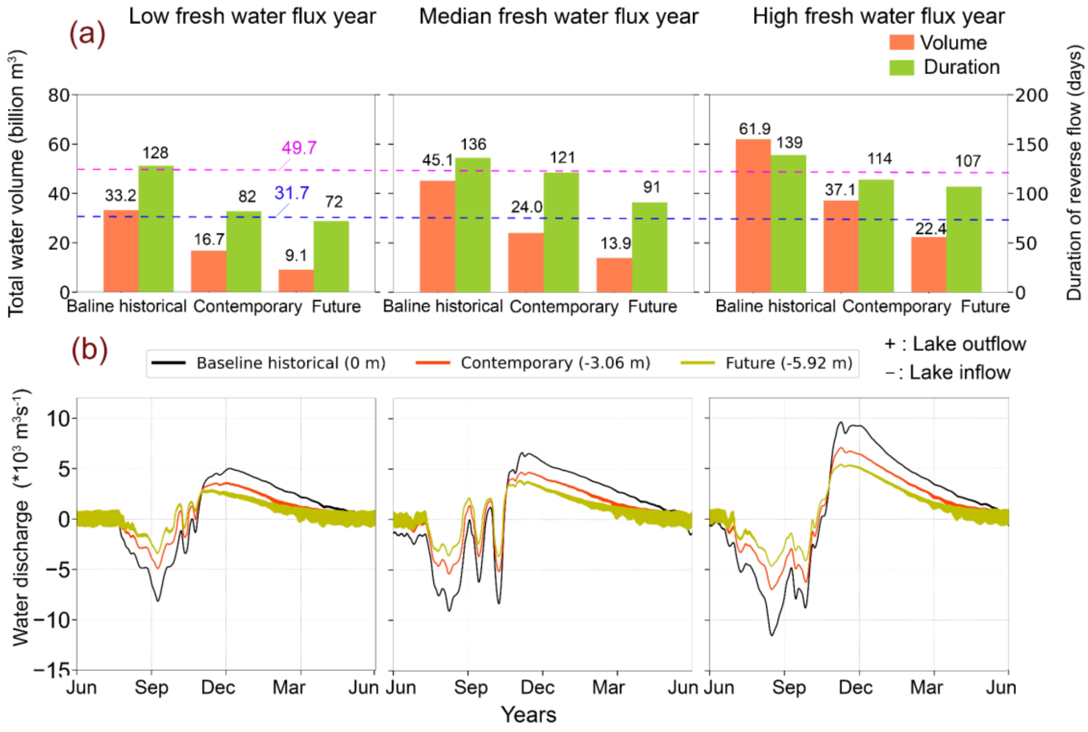

Figure 6-2. (a) Total volume of water flowing from the Mekong River to the TSL and cumulative duration of reverse flow into the TSL for the Baseline historical (0 m), Contemporary (-3.06 m), and projected Future (-5.92 m) river bed level bathymetries under various upstream hydrograph conditions, as simulated at Prek Kdam. The pink dashed line and the blue dashed lines depict the average annual reverse flow volume from the Mekong River to the TSL (as observed at Prek Kdam) during the periods of 1962-1972 and 2010-2019, respectively (Chua et al., 2022). (b) Simulated water discharge between the Mekong River and the TSL (at Prek Kdam) under different scenarios of riverbed lowering and various hydrograph conditions. Negative values indicate lake outflow and positive values indicate lake inflow.

6.2.2 Changes of the Tonle Sap Lake water level and inundation area

As the inflow of water from the Mekong River into the TSL declines with the progressive riverbed lowering, there is a noticeable reduction in both the monsoonal wet season maximum water level in the TSL and the extent and duration of inundation (Figure 6-3, a and b). The maximum water level in the TSL (as simulated at Kompong Luong) decreases from 8.63 m (7.20 m; 9.92 m) from the Baseline historical scenario, to a simulated 6.66 m (5.42 m; 7.96 m) in the Contemporary scenario for medium (low; high) fresh water flux years. The water level reductions further intensify under the Future scenario, reaching just 5.42 m (4.30 m; 6.63 m) for the median (low; high) water flux years (Figure 6-3, a). These simulations indicate an overall reduction in TSL maximum water elevations of 1.97 m (1.78 m; 1.96 m) and 3.21 m (2.90 m; 3.29 m) for the median (low; high) fresh water flux years in the Contemporary and Future scenario, respectively, compared to the Baseline historical scenario.

The reduced lake levels obviously impact both the spatial extents of the TSL inundated area and the durations for which those areas are flooded (Figure 6-3, b). For the Baseline historical scenario, the maximum inundation area of the TSL is simulated to be 12,653 km² (10,375 km²; 14,690 km²) for the median (low; high) fresh water flux years. The maximum area inundated by the lake is predicted to reduce to 9,525 km² (7,621 km²; 11,585 km²) in the Contemporary scenarios, representing a reduction of 24.7 % (26.5 %; 21.1 %) compared to the Baseline historical scenario. Under Future scenario the maximum inundation area of the TSL further reduces to 7,624 km² (6,027 km²; 9,482 km²) for the median (low; high) fresh water flux years, a reduction of 39.7 % (41.9 %; 35.5 %) compared to the Baseline historical scenario.

In addition, this declining trend can also be observed in the simulated duration of specified inundation area levels (Figure 6-3, c). The impacts on the TSL flood extent can be observed by comparing the amount of time the TSL is inundated beyond the long-term mean flooded area value (A_f; 6153 km^2 as calculated for the period 1998 to 2021, was determined using Eq.10). Under the Baseline historical condition, A_f is predicted to be exceeded for 213 days in a year (156 days; 236 days) for medium (low; high) water flux years. However, under the Contemporary scenario A_f decreases to 148 days (86 days; 178 days). For the Future scenario A_f is predicted to decrease further to 99 days (0 days; 141 days) for the medium (low; high) fresh water flux years, highlighting that the maximum inundation area of the lake will not reach the mean flooded area value A_f under low water flux conditions in the Future scenarios. This represents a decrease in A_f values of 65 days (70 days; 58 days) and 114 days (156 days; 95 days) for the medium (low; high) fresh water flux years under the Contemporary and Future scenarios, respectively.

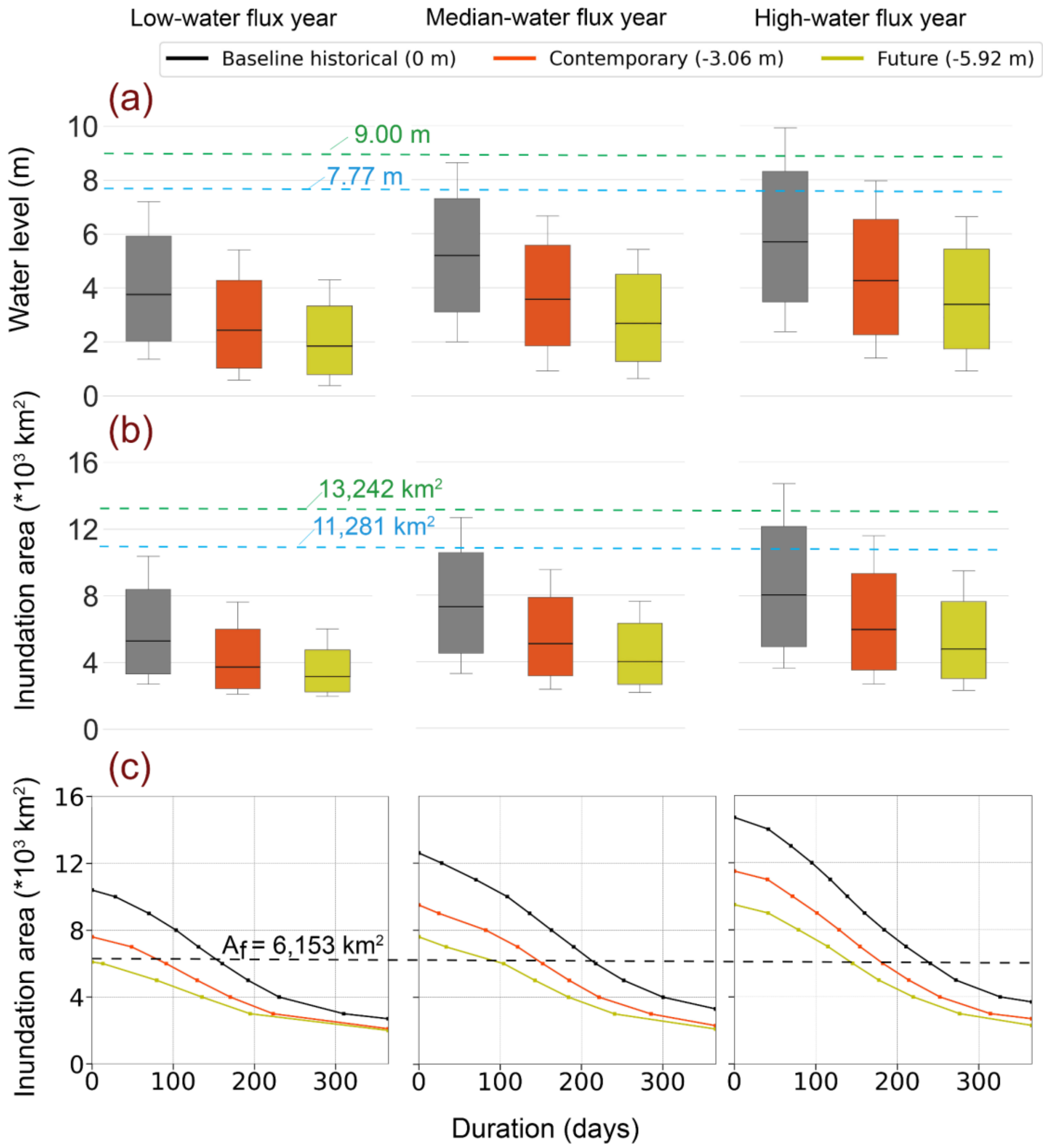

Figure 6-3. (a) Simulated flood season water levels within Tonle Sap Lake (at Kompong Luong gauge) using the Baseline historical, Contemporary and projected Future bathymetries for the three hydrograph flux conditions; with the green dashed line and the deep skyblue dashed lines depicting the observed yearly maximum water levels within the TSL during the periods 1998 -2009 and 2010-2021, respectively. (b) Simulated inundation areas within the TSL under the three bathymetry conditions and hydrograph scenarios with the green dashed line and the deep skyblue dashed lines representing the average yearly maximum inundation within the TSL as calculated from Eq.10 during the periods 1998-2009 and 2010-2021, respectively. (c) The relationship between the magnitudes and the durations of inundation areas within the TSL under the three bathymetry conditions and hydrograph scenarios with the black dashed line represents the long-term mean flooded area as calculated for the period 1998-2021.

6.2.3 Changes of water fluxes into the Mekong delta

The reduction in flow reversal from the LMR to the TSL during the flood season also led to increased water flow into the Mekong delta during this period, especially during times of peak water flow. In more detail, during the flood season of June - November (see Figure 6-4), the total water volume flowing from the LMR (estimated at upstream of the Chaktomuk Junction) to the Chaktomuk Junction (see Figure 6-1) is 281.9 billion m^3 (213.8 billion m^3; 324.0 billion m^3) in the Baseline historical scenario. This total water volume increases to 332.2 billion m^3 (238.7 billion m^3; 394.5 billion m^3) in the Contemporary scenario and 340.1 billion m^3 (247.1 billion m^3; 421.9 billion m^3) in the Future scenario, under median (low; high) freshwater flux years (Figure 6-4). This represents a total water volume increase of 14.7 % (11.6 %; 21.8 %) in the Contemporary scenario and 20.7 % (15.8 %; 30.2 %) in the Future scenario, compared to the Baseline historical scenario. It is note that the increased water flow in the LMR is contributed by the reduced flow from the LMR to the TS floodplain, which ultimately flows into the TSL and the LMR floodplain (see Figure 5-19, Section 5.5.1, Chapter 5).

In the TSL system, the total water volume flowing from the LMR to the TSL (as estimated at Prek Kdam for both TLR and TS floodplain) during flood season is 21.4 billion m^3 (21.2 billion m^3; 33.8 billion m^3) in the Baseline historical scenario. This total water volume decreases to 4.8 billion m^3 (5.4 billion m^3; 14.4 billion m^3) in the Contemporary scenario, and further declines to -4.4 billion m^3 (-1.9 billion m^3; 2.9 billion m^3) in the Future scenario (Figure 6-4), with the negative values indicating that water is flowing back from the TSL to the LMR, highlighting that the TSL no longer receives water from the Mekong River during median and low freshwater flux conditions for the flood season (estimated from June to November). This represents a total water volume reduce of 77.5 % (74.8 %; 57.2 %) in the Contemporary scenario and 120.4 % (109.0 %; 91.4 %) in the Future scenario, compared to the Baseline historical scenario or an additional flood season flow from TSL to the Chaktomuk Junction of 16.6 billion m^3 (15.9 billion m^3; 19.3 billion m^3) in the Contemporary scenario and 25.8 billion m^3 (23.1 billion m^3; 30.9 billion m^3) in the Future scenario compared to the Baseline historical scenario.

The increase in total water volume from the LMR, coupled with the water volume reduced absorption by the TSL, has led to a rise in the total water volume flowing into the MD during the flood season. Specifically, the total water volume flowing from Chaktomuk Junction into the MD (by summing the flows through the Mekong and Bassac channels) is 289.8 billion m^3 (208.0 billion m^3; 341.2 billion m^3) in the Baseline historical scenario, increasing to 328.8 billion m^3 (237.7 billion m^3; 400.4 billion m^3) in the Contemporary scenario and 346.7 billion m^3 (250.5 billion m^3; 424.8 billion m^3) in the Future scenario (Figure 6-4). This represents a total water volume increase of 13.5% (14.3 %; 17.4 %) in the Contemporary scenario and 19.6 % (20.5 %; 24.5 %) in the Future scenario compared to the Baseline historical scenario.

During the dry season (estimated from December-May), the model results indicate a significant reduction in the volume of water flowing from the TSL into the Mekong River at the Chaktomuk Junction during the dry season under various riverbed lowering scenarios, while there is a slight increase in the total volume of water flowing from the LMR to the Chaktomuk Junction (Figure 6-4).

Specifically, in the Baseline historical scenario, the total water volume flowing from the LMR to the Chaktomuk Junction is 64.6 billion m^3 (45.8 billion m^3; 56.6 billion m^3). This volume slightly increases to 67.1 billion m^3 (47.0 billion m^3; 57.6 billion m^3) in the Contemporary scenario and 67.5 billion m^3 (47.1 billion m^3; 57.6 billion m^3) in the Future scenario under median (low; high) fresh water flux years. This represents a total water volume increase of only 3.8 % (2.7 %; 1.8 %) in the Contemporary scenario and 4.4 % (2.8 %; 1.8 %) in the Future scenario compared to the Baseline historical scenario (Figure 6-4). The total volume of water flowing from the TSL to the Chaktomuk Junction during the dry season (estimated at Prekdam) is predicted to be 43.9 billion m^3 (37.7 billion m^3; 61.3 billion m^3) in Baseline historical scenarios. This volume is expected to decrease substantially to 27.3 billion m^3 (21.8 billion m^3; 42.1 billion m^3) in the Contemporary scenario and 18.2 billion m^3 (14.5 billion m^3; 30.5 billion m^3) in the Future scenario, under median (low; high) fresh water flux years. This represents a reduction of 37.8 % (42.1 %; 31.4 %) in the Contemporary scenario and 58.7 % (61.4 %; 50.3 %) in the Future scenario compared to the Baseline historical scenario (Figure 6-4).

These reductions in the water volume supplied from the TSR to the Mekong River lead to modelled decreases in the total dry season water flux flowing downstream from the Chaktomuk Junction into the MD, despite a slight increase in the water volume flow from the LMR to the Chaktomuk Junction. These reductions of dry season flow to the MD are proportionally less than the reductions from the TSR to the Chaktomuk Junction but are nevertheless substantial. Specifically, for the Baseline historical scenario, the total water flux from Chaktomuk Junction to the MD during the dry season is calculated to be 107.8 billion m^3 (82.9 billion m^3; 115.8 billion m^3) for the median (low; high) water flux years. This volume reduces to 92.4 billion m^3 (68.7 billion m^3; 99.2 billion m^3) and 85.6 billion m^3 (61.6 billion m^3; 87.8 billion m^3) in Contemporary and Future scenarios, respectively, for the median (low; high) fresh water flux years. These are total water volume declines of 12.6 % (17.1 %; 14.4 %) and 20.6 % (25.6 %; 24.2 %) in the median (low; high) water flux years for the contemporary and future river bed scenarios, compared to the Baseline historical scenario (Figure 6-4).

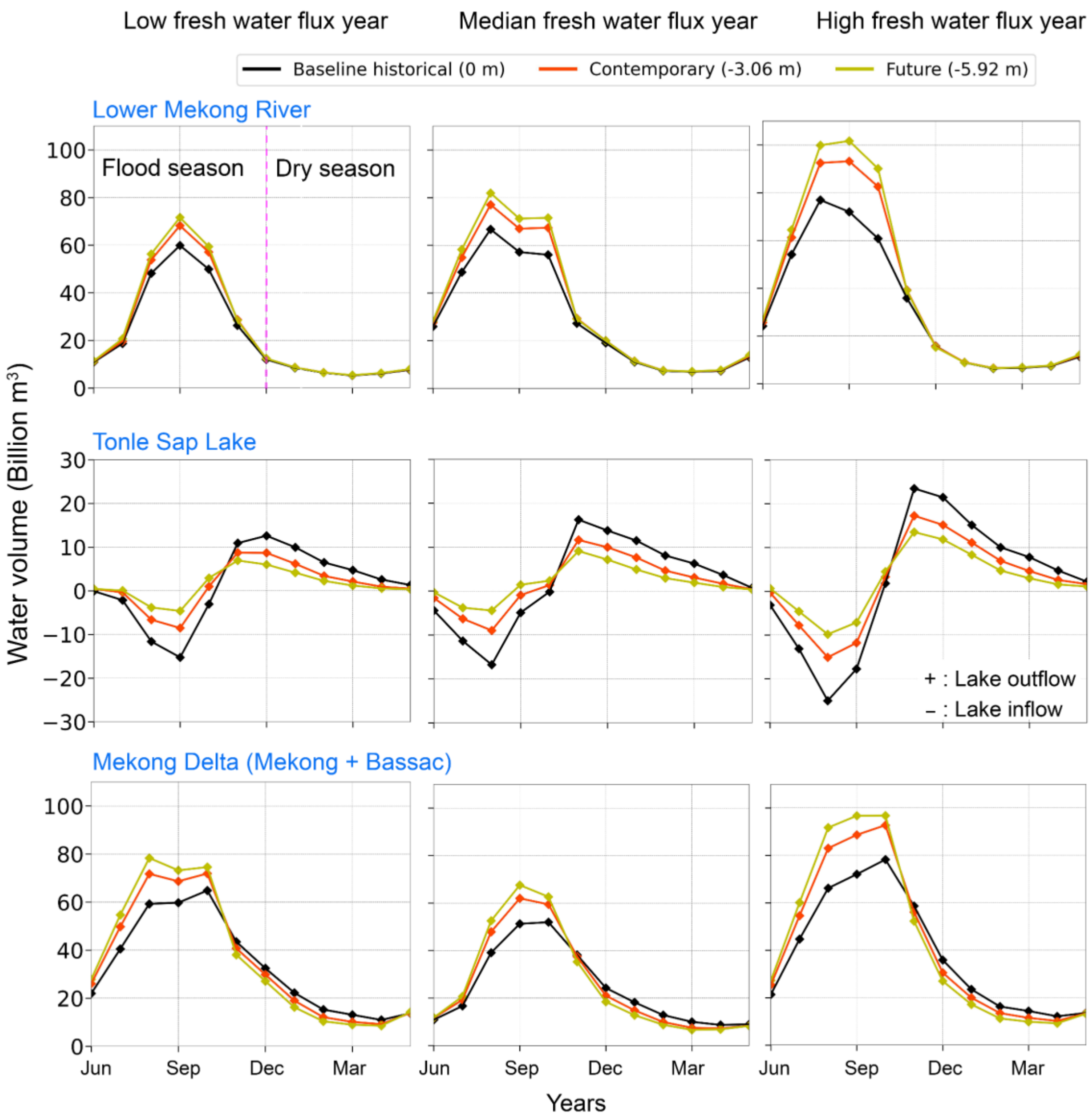

Figure 6-4. The simulated monthly total water volumes flowing from the Lower Mekong River and Tonle Sap Lake to Chaktomuk Junction, and from Chaktomuk Junction to the Mekong delta (via the Mekong and Bassac channels), under different fresh water conditions and riverbed lowering scenarios.

6.3 Discussion

The results from Section 6.2.1 demonstrate how riverbed lowering can reduce water levels at the critical Chaktomuk Junction, decreasing the hydraulic gradient that drives wet season flow reversal into TSL and reducing water flow from the LMR to the Tonle Sap floodplain, which eventually reaches the lake. For instance, under Future riverbed lowering (by 2038) there would be 69.3 % (72.6 %; 63.8 %) reduction in the total volume of water flux to the TSL from the LMR for the median (low; high) fresh water flux years. This would reduce the maximum areal extent of the inundated area of the lake by 39.7 % (41.9 %; 35.5 %) and decreasing the vital return flows to the Mekong River in the dry season by 58.7% (61.4%; 50.3%) with a consequent reduction of around 20.6 % (25.6 %; 24.2 %) in the dry season (from December to May) water flux to the MD. Importantly, the simulated reductions in reverse flow from the Mekong to TSL during the monsoon floods also means that an additional 25.8 billion m^3 (23.1 billion m^3; 30.9 billion m^3) of wet season flow (from June to November) would be transmitted downstream into the MD at a time of already high flood levels, potentially exacerbating flood hazards. Taken together these changes in the dynamics of the TSR flow reversal have profound consequences, not only for the biological productivity of the TSL, but for flow regulation services across the entire delta system, as considered further below.

There are well known and well quantified relationships between the hydraulic regime, the ecosystem services and fish production in the TSL (Fujii et al., 2003; Campbell et al., 2006; Holtgrieve et al., 2013). The projected decline in the reverse flow from the LMR to the TSL has the potential to trigger a variety of damaging socio-ecological impacts, affecting nearly two million residents in Cambodia who depend on the TSL for their livelihoods (Arias et al., 2013). The reduced water volumes entering the TSL will likely lead to a decline in migratory fish populations TSL (MRC 2002; Hogan, 2011; Baran, 2014; Chea et al., 2020; Chevalier et al., 2023), which account for 63% of the overall fisheries catch in the TSL (Zalinge et al., 1998). Recent trends in fish catch have declined by up to 88% over the period 2003-2019 (Chevalier et al. 2023). Additionally, the decrease in both water volume and water discharge from the LMR to TSL will limit the influx of suspended sediment and sediment associated nutrients, thereby impacting the productivity of spawning sites and further impacting agriculture and fish production (Baran, et al., 2007; Arias at al., 2014; Arias et al., 2019; Chan et al., 2020). The projected declines of the lake's inundated areas (Figure 6-3) will also affect the protected flooded forest ecosystems, disrupting plant communities and system biodiversity, notably through onward impacts on the habitats of amphibians, reptiles and birds residing in the flood areas (Campbell et al., 2006; Mauricio at al., 2014; Lohani et al., 2020). The decrease in the volume of water supplied by the TSL to the MD during the dry season (Fig. 4) will give rise to new water-related challenges in the MD. The reduced dry season flows will impact fresh water availability for rice cultivation during the dry season, and reduce the viability of aquaculture activities across the delta, notably through a very significant increase in tidal ingress and saline intrusion (Vasilopoulos et al. 2021; Bricheno etal., 2021), which will result from the reduced discharge in dry season base flows. Additionally, the increased wet season flow from the TSL into the MD during a time of already elevated flood levels could potentially exacerbate flood hazards in the MD.

The only effective mitigation of the trends presented herein involves halting and reversing the process of riverbed lowering driving the disruption of the TSR reverse flow. This could be achieved by establishing positive sediment budgets for the LMB through actions such as restricting or ceasing riverine sand mining (Hackney et al., 2020) and facilitating the release of sediment that is currently trapped behind dams, for example through flushing exercises (Kondolf et al., 2014; Laksitaningtyas et al., 2022; Lai et al., 2024). For example, possible through the "Turbidity Current Venting" method (Kondolf et al., 2014) which utilizes turbidity currents with high sediment concentrations to create a distinct, higher-density current that flows along the bottom of the reservoir toward the dam to flush sediment load during the flood season, has been applied in the Yellow River (IRTCES, 2005; Hu et al., 2012; Kondolf et al., 2014). Applying this method to the existed or projected future dams the Mekong River could amplify the influx of water, sediments, and nutrients into the TSL.

Finally, the case study of the Mekong River presented here demonstrates the significant effects of riverbed lowering, driven by factors such as sand mining and upstream damming, which result in a reduction of water levels and consequently disrupt the connectivity between the river and its floodplain lakes. In contrast, the formation of lakes in the Yangtze River system, where rising water levels, triggered by deglaciation, were combined with upstream sediment input, led to significant bed aggradation (An et al., 2022). This aggradation resulted in the creation of accommodation space, which could not be filled by the tributaries of the Middle-Lower Yangtze. As a consequence, tributary blockage occurred, resulting in the formation of lakes (An et al., 2022). This comparison underscores the contrast between natural processes, such as deglaciation, which can lead to the creation of lakes, and human-induced factors, such as riverbed lowering, which disrupt vital connections between rivers and their lakes. It highlights the potentially devastating impacts of anthropogenic activities on river-lake interactions, emphasizing their critical role in maintaining the ecological health and functionality of these dynamic systems. Human interventions may not only degrade these connections but also hinder the natural processes that contribute to the resilience and sustainability of these complex delta ecosystems.

6.4 Chapter Summary

In the present Chapter, results of a series of scenario simulations involving varying levels of riverbed lowering and different fresh water flux conditions adopted from Chapter 5 have been used to study changes in the wet season flow reversal from the Lower Mekong River into the Tonle Sap Lake. The results highlight a substantial reduction in the wet season flow reversal driven by riverbed lowering, which contributes to decreased Tonle Sap Lake inundation and reduced return flows to the Mekong Delta. The implications of these findings for the biological productivity of the Tonle Sap Lake and the flow regulation services across the entire Lower Mekong River and Delta system are discussed. We acknowledge that Eq. 10 is based on observed data of inundation area and water level collected between 1997 and 2005 (Kummu et al., 2014). Despite its historical basis, the equation remains applicable due to the minimal geomorphological changes in the lake over time (Penny et al., 2005; Kummu et al., 2008). This geomorphological stability ensures that Equation 10 can be effectively utilized for the baseline bathymetry scenario, the contemporary bathymetry scenario, and projected scenarios extending up to 2038. This chapter concludes the study on the large-scale impacts of riverbed lowering across the Lower Mekong Basin. The next chapter will explore various scenarios of local anthropogenic disturbances, including water and sediment flux inputs, and their effects on changes in flow and sediment discharge partitioning at the apex of the delta.

Chapter 7. Water and sand transport capacity through the apex of the Mekong delta under the impact of riverbed lowering

Chapters 4-6 examined the large-scale impacts of riverbed lowering on the hydraulics of the Lower Mekong Basin (LMB) using historical data and 1D modelling, providing valuable insights into broad trends. However, these chapters were limited in capturing the finer, localized dynamics of the region's transformation. In contrast, the current Chapter focuses on more specific, localized scenarios, investigating the effects of anthropogenic perturbations and water and sediment flux inputs on flow patterns and sand discharge partitioning at the delta apex. By integrating both 1D and 2D modelling techniques, this chapter offers a more precise assessment of changes in the delta's sand transport capacity, which is difficult to achieve with 1D modelling alone. While more focused, this chapter considerably contributes to the broader understanding of the delta's evolving dynamics, offering a detailed and nuanced perspective that complements the broader analysis from earlier chapters.

The specific objective (O3) of this chapter is to quantify the changes in the delta's sand transport capacity resulting from riverbed lowering. This objective directly addresses research question (RQ.4) by identifying alterations in the delta's ability to transport sand from the catchment, driven by ongoing changes in channel geometry due to intensified sand mining. The goal is to develop sustainable solutions for future sand extraction practices to inform downstream local governments.

It is highlighted that the influence of sea level rise in this area is nearly negligible, especially during the flood season when sediment transport occurs (see Section 5.4.2, Chapter 5). Consequently, scenarios incorporating sea level rise have been excluded from this modelling work. Additionally, the results in this chapter focus on the sand transport capacity, however, during the model calibration of sediment transport, both suspended sediment transport and sand transport were explored to accurately compare simulated riverbed morphology changes against observed data. Therefore, during the calibration step, the model will include both suspended sediment and sand transport.

The Chapter is organized in the following Sections. Section 7.1 provides a brief introduction to the study area, Section 7.2 provides an overview of the methods employed in the Chapter, Section 7.3 focuses on the development and calibration of 2D hydrodynamic and sediment transport model, Section 7.4 establishes the modelling scenarios that will be investigated while, Section 7.5 presents model predictions. The results of the analysis are discussed in Section 7.6 and Section 7.7 provides a summary of these results.

7.1 Study area

The Chaktomuk Junction, located in Phnom Penh, Cambodia, functions as the apex of the Mekong Delta (Figure 7-1), which connected the Tonle Sap Lake through the Tonle Sap River and two primary distributary channels Mekong and Bassac channels in Mekong delta (MD) (see section 6.1, Chapter 6 for more details). The water discharge partitioning at the delta apex toward the MD is unequal, with the main Mekong channel receiving around five times more water than the Bassac. The unequal flow partition at the delta apex is also evident at the Tan Chau and Chau Doc flow discharge located further seaward in the Vietnamese Mekong Delta (VMD) (see Table 4-1, Chapter 4). The extensive riverine sand mining occurring in the Chaktomuk area (Hackney et al., 2020) along with a significant land reclamation project driven by the rapid expansion of Phnom Penh (Figure 7-1) is consistently altering the configuration of this critical junction.

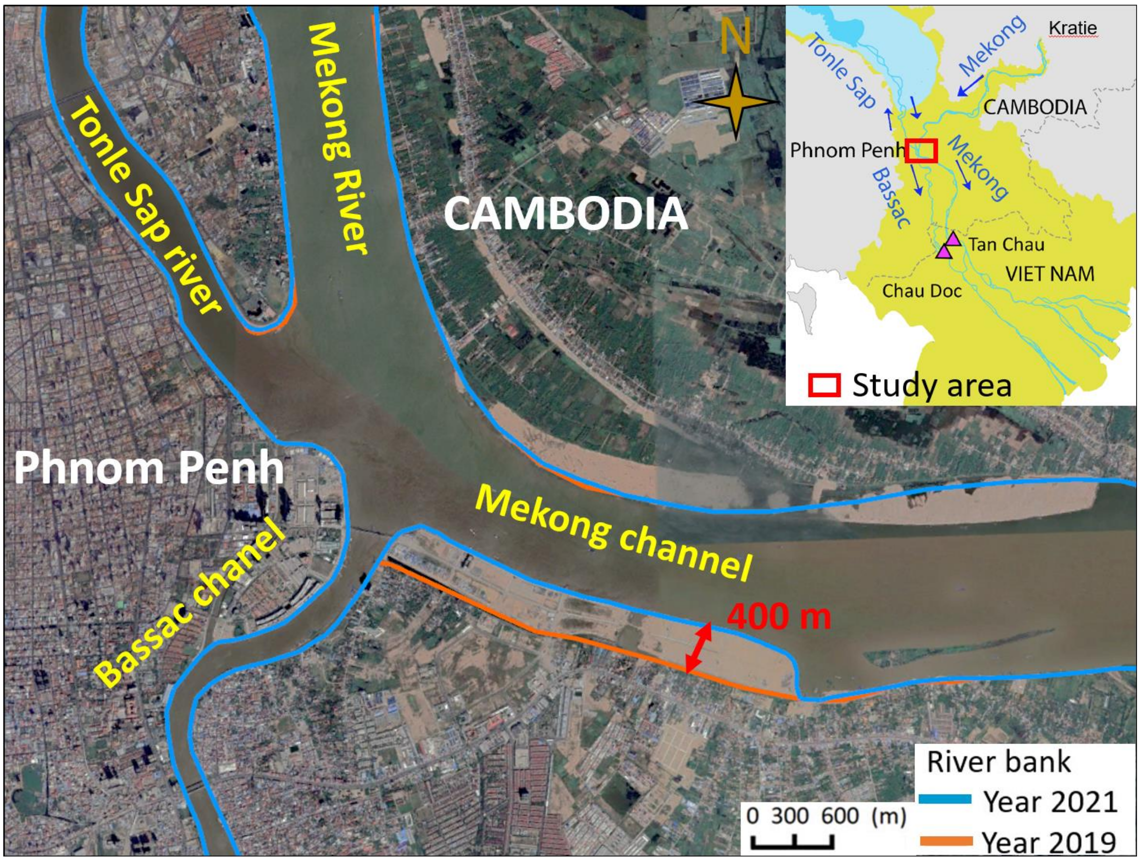

Figure 7-1. The apex of Mekong delta, also known as the Chaktomuk junction, which has experienced rapid urban expansion in recent years, as evidenced by historical imagery from Google Earth.

7.2 Method

To evaluate the changes in the hydraulic regime and sand transport capacity at the Chaktomuk Junction caused by changes in bifurcation geometry, a combination of one-dimensional (1D) and two-dimensional (2D) techniques are employed. This nested modelling approach is driven by the limited coverage of the high-resolution bathymetric data, available only in Chaktomuk junction (see section 3.2, Chapter 3) and the far greater computational resources required in 2D modelling making it currently impractical to be applied to the entire LMR and MD. Additionally, due to the lack of observational hydraulic data necessary for setting up boundary conditions for the 2D model, the predictions from the 1D model at the Chaktomuk Junction are used instead to force the 2D model. The model is using observed bathymetry data from 2013 and 2022 (refer to Section 3.2, Chapter 3 for the availability of high-resolution bathymetry data at this junction) to evaluate the sand transport capacity at this location. The detailed 2D model scenarios will be presented in Section 7.4.1. Simultaneously, 1D hydraulic modelling has been used at a delta-wide scale to assess the hydraulic regime at the delta's apex under scenarios of riverbed lowering across the entire delta. This involves establishing two 1D scenarios for the delta riverbed conditions in 2013 and projecting them forward to 2022, which will presented in section 7.4.1. The selection of years 2013 and 2022 is synchronized with the time frame for 2D modelling. The hydraulic prediction outcomes obtained from 1D modelling of various riverbed scenarios are used as boundary conditions for the 2D model. The detailed introduction of the 1D Mekong modelling is presented in Section 5.1, Chapter 5, while the setup for the 2D modelling will be introduced in the following section.

7.3 Building a two-dimensional (2D) coupled hydrodynamic and sediment transport model for the Chaktomuk Junction

In the present Section, a 2D numerical model for water and sediment transport is developed and calibrated specifically for the Chaktomuk Junction. Subsection 7.3.1 will detail the model setup and calibration procedures for the hydrodynamic solver, whereas subsection 7.3.2 will focus on the integration of the sediment transport solver and its calibration.

7.3.1 Hydrodynamic model solver

7.3.1.1 Model setup

A 2D model for the Chaktomuk Junction was developed using the numerical modelling software MIKE21 FM (DHI, 2014), the model domain covers an area of around 13 km^2 (Figure 7-2, a). The 2013 model bathymetry is constrained using a combination of high-resolution Multibeam Echo Sounder (MBES) datasets adopted from Hackney et al., (2020), which covering 70% of the model domain, and lower-resolution single-beam echo sounder (SBES) datasets adopted from Hackney et al., (2021) covering the remaining outer regions (Figure 7-2, b) (details in section 3.2.2, Chapter 3). The bathymetric data are referenced to the World Geodetic System 1984 coordinates (WGS 84) and the Hon Dau MSL vertical datum. A horizontal flexible mesh approach was employed to represent channel topography, utilizing triangular flexible mesh elements with an average mesh resolution of 13 m (σ = 2.5 m) for the 2D model domain. The upstream model boundaries are defined near Chroy Chang Var on the Lower Mekong River (LMR), using water discharge data ($m^3 s^{-1}$) (Figure 7-2, a). An additional upstream boundary is also forced with water discharge data ($m^3 s^{-1}$) near Phnom Penh Port on the Tonle Sap River (TSR). The downstream boundaries on the Bassac channel are forced with water discharge data ($m^3 s^{-1}$), while the Mekong channel downstream boundary is forced with water level data (m) (Figure 7-1, a). The water discharge is placed at the Bassac channels in 2D model to ensure consistent water discharge distribution between the downstream Mekong and Bassac channels for both 1D and 2D modelling. This is important because the 2D model domain is relatively small, and thus, even minor local changes in topography between the two downstream channels could considerably affect the distribution of water flux between them. However, the distribution of water flow between the two channels is primarily influenced by large-scale factors, such as the topography of the entire downstream channels (Edmonds and Slingerland, 2008) and the connectivity between the floodplain and the downstream channels. These large-scale factors can be accurately captured only through 1D modelling.

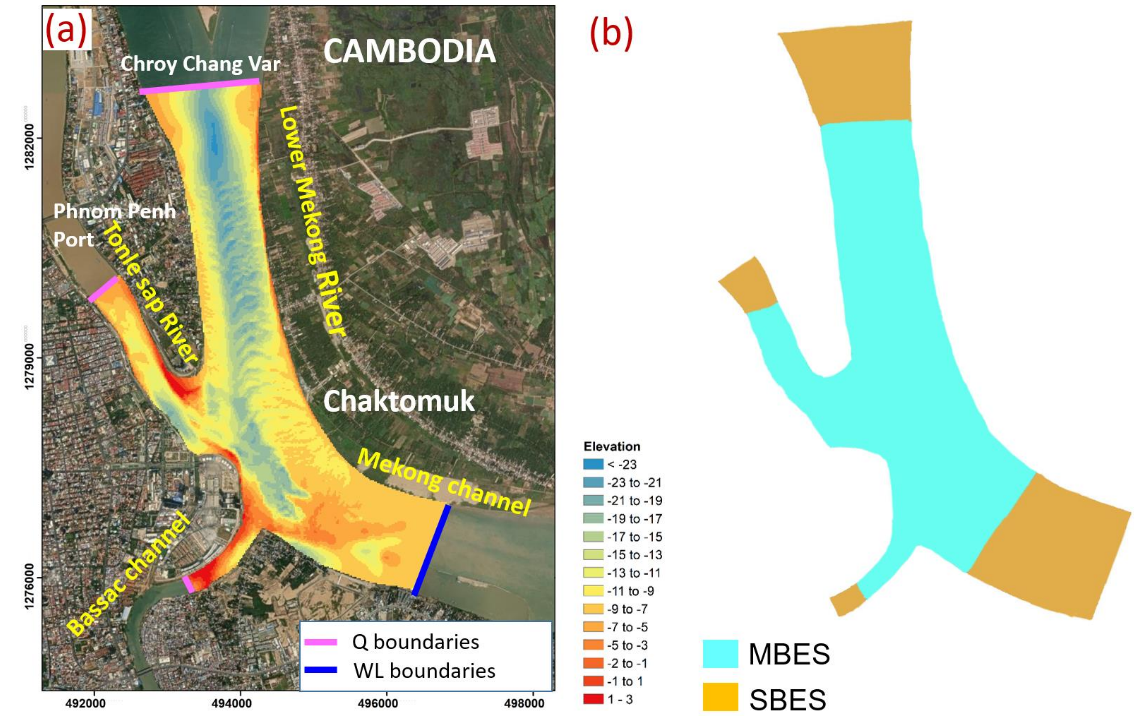

Figure 7-2. (a) 2013 2D model bathymetry, relative to Hon Dau MSL vertical datum. (b) The bathymetric domain of the 2D model formed by merging MBES, covering 70% and SBES bathymetric data covering the remain outer regions observed in Sep 2013.

For the initial model set up, it is assumed that the studied area predominantly consists of a bed material composition comprising of sand with a median grain sand diameter D_{50} of 375 µm, (Hackney et al., 2020) and that the riverbed composition is relatively homogenous across the model domain. It is also assumed that the drag forces exerted by bank roughness are negligible, which, given the much larger channel width (up to 1700 m) in comparison to depth (generally less than 40 m), is reasonable. Therefore, grain roughness is assumed to be constant throughout the model domain and the roughness coefficient is likely to be primarily affected by river depth (Barnes, 1969). In addition, spatial variability in riverbed roughness has been closely linked to bedforms (Milan, 2009). It was shown that zones with higher near-bed velocities are typically associated with deeper channel positions, while areas of shallower flow depth correspond to lower near-bed velocities (Milan, 2009). This relationship indicates that deeper channel positions tend to exhibit smaller riverbed roughness values compared to those in shallower flow depths. This relationship between riverbed roughness and elevation (or river depth) highlights the critical role of spatially distributed roughness in effectively modelling flow dynamics and sediment transport.

In this study, roughness coefficients ($\mathrm{M} = \frac{1}{\mathrm{Manning\ n}}$) were applied using the MIKE21 FM model (DHI, 2014) taking into account spatial variability in the riverbed. It is worth noting that the roughness coefficient (M) as used in MIKE21 FM, is expressed as the inverse of the Manning n coefficient commonly employed in other studies (e.g., Barnes, 1969; Milan, 2009; Ferguson, 2010), where higher M values correspond to smoother riverbed conditions, while lower M values indicate increased roughness. Following Dung et al., (2011), the roughness coefficients (M) for different locations across the LMR and Mekong and Bassac channel in delta are within range of 20 $m^{1/3}$ s^{-1} (Manning n = 0.05 $m^{-1/3}$ s^{1}) and 65 $m^{1/3}$ s^{-1} (Manning n = 0.015 $m^{-1/3}$ s^{1}). These roughness coefficients values vary in accordance with channel bed elevations, which range from +8 m to -40 m, referenced to the Hon Dau MSL.

To account for this spatial variability, a relationship was established between the initial riverbed elevation and the spatially distributed hydraulic roughness ($\mathrm{M0}$) and channel bed elevation given by Eq. (11):

$$M0 = -0.526 \times Riverbed\ elevation + 24.41 \tag{11}$$

Using Eq. (11), a varying roughness coefficient was mapped across the model domain based on riverbed elevation with the roughness coefficient $M0$ conforming to values within the range of 20 and 65 (Figure 7-3, a).

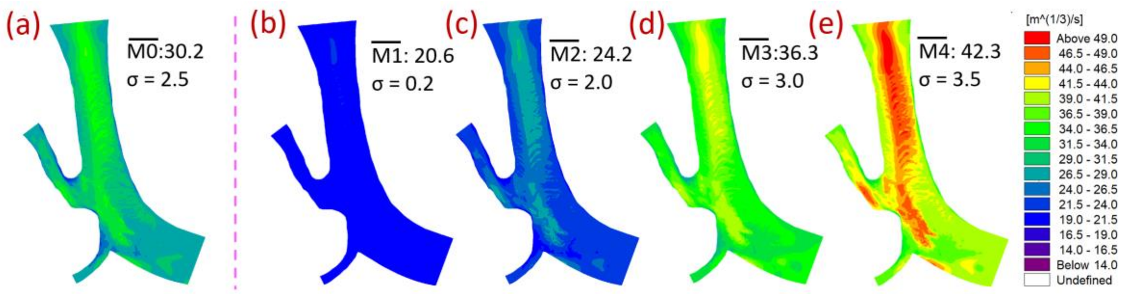

Figure 7-3. (a) The initial hydraulic roughness coefficient dataset for the modelling, (b-e) Various hydraulic roughness coefficient datasets are tested during the calibration step

7.3.1.2 Model hydraulic calibration and validation

The hydrodynamic component of the model underwent calibration and validation using observed flow data, which included velocity fields recorded by an Acoustic Doppler Current Profiler (ADCP) during two field surveys conducted on 12 September 2013, and 27 October 2013, at five cross-sections named 1 to 5 in four channels within Chaktomuk Junction (Figure 7-4) (see more detail in section 3.1.2, Chapter 3). The model is implemented with predetermined constant boundary values, the observed water discharge values at cross-section 1, 5 and 4 and are used to force the model boundaries for the LMR, TSR and Bassac channels respectively. The observed water levels at the Chaktomuk gauge (see section 3.1.1, Chapter 3) during the corresponding survey times used to enforce downstream boundaries in the Mekong channel. Subsequently, the simulated velocity results in the longitude (X) and latitude (Y) directions were extracted at four cross-sections (2, 3, 4, and 5), and the water discharge at cross-section 3 was compared with the observed ADCP data during the calibration and validation steps. The calibration involved analysing data gathered from a survey conducted on 12 September 2013, while the validation step utilized data adopted on 27 October 2013.

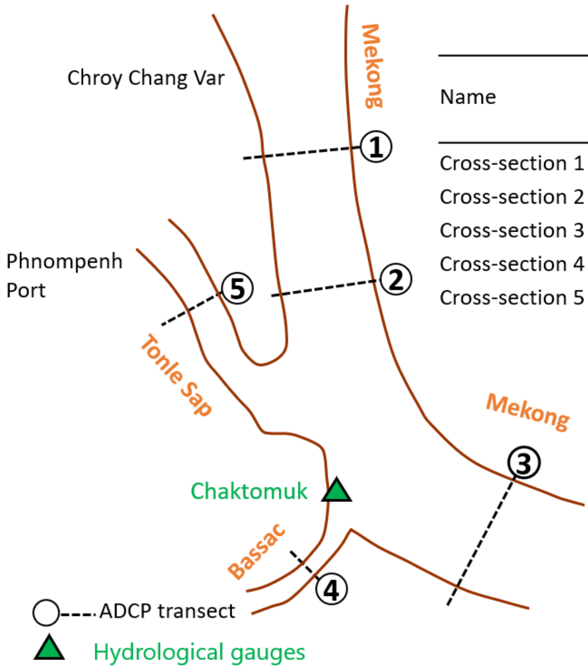

Name	Left bank		Right bank	
	X	Y	X	Y
Cross-section 1	494217	1281507	493239	1281417
Cross-section 2	494577	1279274	493528	1279159
Cross-section 3	495857	1277253	495146	1276216
Cross-section 4	493757	1276047	493637	1276195
Cross-section 5	492822	1279188	492466	1278990

Figure 7-4. Map and the coordinates (WGS 84) of the ADCP cross-sections

a. Hydrodynamic calibration

The hydraulic calibration process entails adjusting the hydraulic roughness parameter until the modelled outcomes closely align with observed data. Here, during the calibration phase, four distinct sets of spatially variable hydraulic roughness covering the model domain, denoted as M1, M2, M3, and M4 scenarios are created. These datasets of roughness coefficient involve variations of 20% (Figure 7-3, b) and 40% (Figure 7-3, c) reductions, as well as 20% (Figure 7-3, d) and 40% (Figure 7-3, e) increases in comparison to the initial data set of hydraulic roughness M0 (Figure 7-3, a). The efficiency coefficients, incorporating deviation values (Dev) as defined in Eq.12 and the Relative Error Vector (REV) (13), are utilized to assess the comparison between model predictions and observed data.

The deviation value: $Dev = \left|\frac{Obs-sim}{Obs}\right| * 100\%$ (12)

where Sim is the simulated value of discharge and Obs is corresponding observed data. The best performant has a Dev of 0.

The relative error vector (REV) defined as:

$$REV = \frac{\sqrt{(U_{x\_obs}-U_{x\_cals})^2+(U_{x\_obs}-U_{y\_cals})^2}}{\left(\sqrt{(U_{x\_obs}+U_{y\_obs})^2}\right)} \quad (13)$$

Where U_{x_cals} and U_{y_cals} are the average simulated flow velocities (m s^{-1}) in longitude (X) and latitude (Y) directions, respectively. U_{x_obs} and U_{y_obs} denote the corresponding average values (m s^{-1}) for the measured flow velocities in in longitude (X) and latitude (Y) (m s^{-1}) (Rijn et al., 2002).

Generally, REV values smaller than 0.2 signify a highly accurate calibration, those below 0.4 correspond to a well-performing calibration, values below 0.7 indicate sufficient results whereas higher values indicate poor model performance (Rijn et al., 2002).

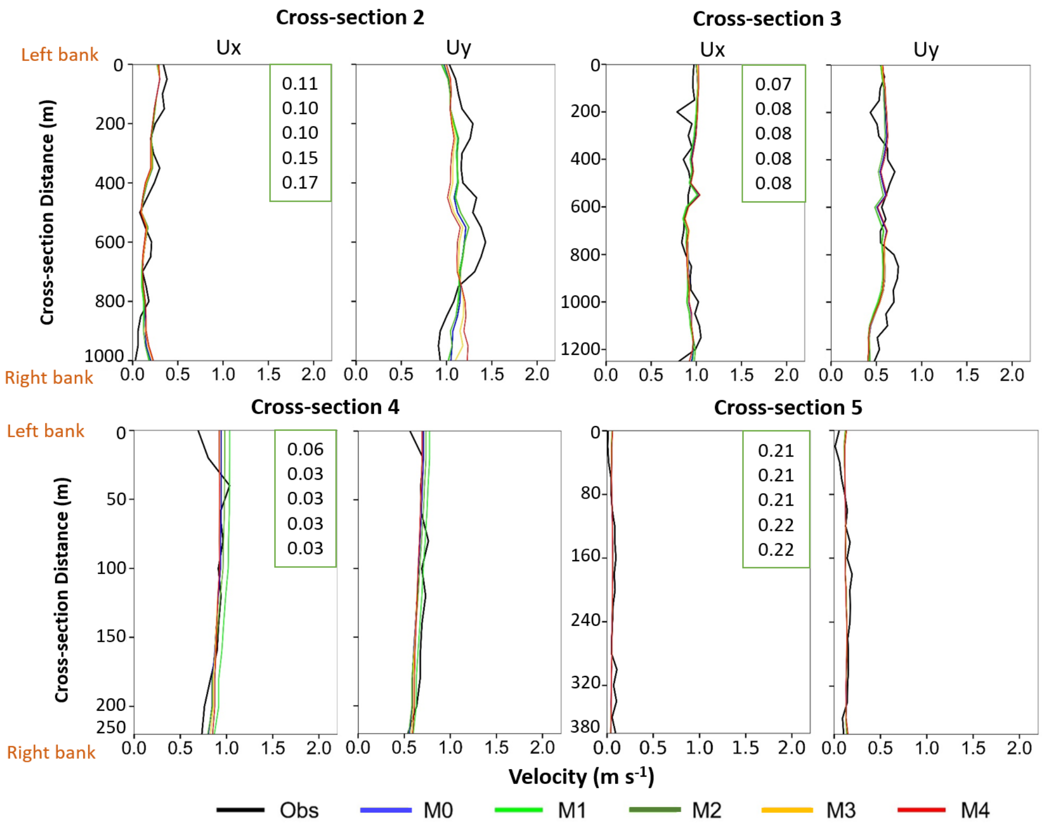

Figure 7-5. Comparison of observed (Obs) and predicted 2D velocity components along four predefined cross-sections for different sets of hydraulic roughness on 12 September 2013. The

table displays the REV values for each scenario of hydraulic roughness, ranging from M0 to M4, listed from top to bottom in the table.

The assessment of simulated and observed velocity values for various hydraulic roughness scenarios indicated a consistent and satisfactory agreement in both longitude and latitude components across all cross-section (Figure 7-5). A disparity was observed particularly in the U_y component within the middle section of cross-section 2, in the LMR. In this area, the maximum simulated velocity reached approximately 1.25 m s^{-1}, while the maximum observed velocity reached 1.5 m s^{-1}. This velocity difference in this area is likely due to the proximity of Cross-Section 2 to the upstream boundary, defined by water discharge forcing. In the 2D model, such boundary conditions result in a more uniform horizontal velocity distribution near the upstream boundary, and the reach length may be insufficient to fully capture complex horizontal velocity variations. In contrast, cross-sections downstream of the Chaktomuk Junction show much closer agreement between simulated and observed velocities, indicating that the model performs well in regions where boundary effects are less influential. Additionally, an exception was noted at cross-section 5, situated on the TSR, where REV values exceeded 0.2, which is still considered acceptable. One potential explanation for the slight increase in REV for cross-section 5 could be attributed to the very low velocity magnitude (less than 0.2 m s^{-1}). Consequently, the deviation between modelled and observed values might be higher compared to other channels during this period (Figure 7-5).

The predicted water discharges at cross-section 3 for the hydraulic roughness scenarios (M0, M1, M2, M3, M4) are 22734, 22570, 22643, 22740, and 22719 (m^3 s^{-1}), respectively, compared to the observed discharge of 22879 (m^3 s^{-1}). These predictions show deviations of 0.6 %, 1.4 %, 1.0 %, 0.6 %, and 0.7 %, respectively, relative to the observed value. The predicted discharge ratio between the two downstream distributary channels, the Mekong and Bassac, at cross-sections 3 and 4 is 0.87 across all hydraulic roughness scenarios (M0, M1, M2, M3, M4). In comparison, the observed discharge ratio is 0.88, demonstrating a high level of accuracy between the predicted and observed values.

The presented results indicate that there are no significant differences among the investigated hydraulic roughness coefficient scenarios. This could be attributed to the model's limited sensitivity to hydraulic roughness, possibly due to the confined extent of the model domain (8 km from upstream to downstream boundary). The outcomes of the M0 hydraulic roughness scenarios exhibit slightly superior performance compared to the other hydraulic roughness scenarios and is chosen for the next steps. This hydraulic roughness selection is supported by the findings of Dung, (2011) and Eslami et al., (2019), which reported average hydraulic roughness values for this area as approximately 34.51 $m^{1/3}$ s^{-1} and 28.5 $m^{1/3}$ s^{-1} respectively. This is compared to the average hydraulic roughness value of 30.2 (σ = 2.5) $m^{1/3}$ s^{-1} in this study. Consequently, in the subsequent validation step, the M0 hydraulic coefficient scenarios will be evaluated under different flow condition.

b. Hydrodynamic validation

The discharge field data from the second survey, undertaken in 27 October 2013 are employed as the model boundary this step. The comparison of observed and simulated results is presented in the Figure 7-6. Figure 7-6 demonstrates good model performance, as the predicted and observed velocities exhibit strong agreement in both X and Y components. Additionally, the REV values consistently remain below 0.2 for all transects across different hydraulic roughness scenarios. The greatest disparity between measured and simulated water velocity values is noted in cross-section 5 along the Y-direction in the TSR with the REV values reach 0.12. The predicted water discharge at cross-section 3 is 24,997 (m^3 s^{-1}), compared to the observed discharge of 25,541 (m^3 s^{-1}), showing a deviation of 2.1%. Similarly, the predicted discharge ratio between the two downstream distributary channels, the Mekong and Bassac, at cross-sections 3 and 4 is 0.87, closely matching the observed ratio of 0.87, indicating a high degree of accuracy in the predictions.

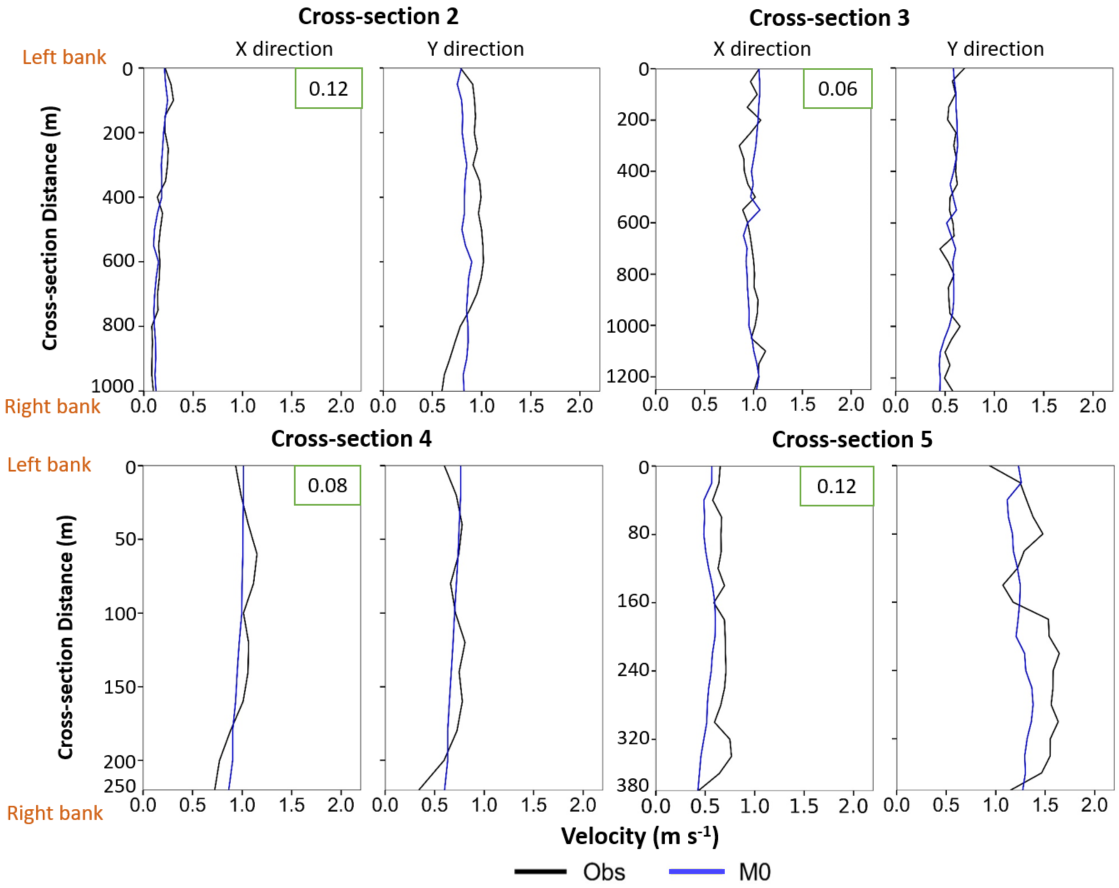

Figure 7-6. The comparison of observed (Obs) and predicted velocities properties on longitude (Y) and latitude (X) components along four predefined cross-sections by hydraulic roughness M0 scenarios and the corresponding coefficient (REV) value on 27 October 2013

In summary, the model exhibits good performance in both the calibration and validation stages. Following the completion of the calibration and validation steps, the model's hydraulic roughness M0 value of 30.2 $m^{1/3}\ s^{-1}$ (σ = 2.5 $m^{1/3}\ s^{-1}$) is used for integration into the subsequent sediment transport module.

7.3.2 Sediment transport solver

The preceding section detailed the configuration of the 2D hydrodynamic model, and the calibration and validation steps verified its robust performance. In this section, the hydrodynamic model is employed to establish and calibrate the sediment transport module. The sediment transport module is separated into two submodules: suspended load transport (Cohesive sediment ≤ 63 µm in diameter and only transported in suspension) and sand transport (bed material ≥ 63 µm in diameter both in suspended load and bedload), described in section 2.4.2, Chapter 2. The sand transport module will be key to the model, as the primary aim of the present Chapter is to quantify sand transport dynamics. However, to accurately compare simulated riverbed morphology changes with observed data, the model will include both suspended sediment and sand transport during the calibration step. Therefore, the calibration of the sediment transport module involves integrating the hydrodynamic model with boundaries for sediment transport (both sediment suspended and sand load), riverbed characteristics, and sediment properties to simulate the riverbed's evolution from September 12, 2013, to October 27, 2013, corresponding with field surveys (see Section 3.2.2, Chapter 3). The specific steps involved in conducting these comparisons will be elaborated upon in the subsequent sections.

7.3.2.1 Sediment transport model setup

a. Model parameters and Sediment properties

For the sand transport module, the studied river region is assumed to feature a sand-bed with a median grain sand diameter D_{50} of 375 µm, and the density for sand is assumed to be 1600 kg m^3 (Hackney et al., 2018; Hackney et al., 2020). The assumption is that the riverbed comprises uniformly erodible sand, with a transport layer up to 20 m in thickness across the whole model domain, which is reasonable for this area (Bravard et al., 2013; Gugliotta et al. 2019; Hackney et al., 2020). 10% of the total sand transport as bed load and 90% as sand suspended load (Hackney et al., 2020). For the suspended load transport module, d_{50} = 35 µm (Hung et al., 2014b), the critical shear stress for erosion τ_{cre} was set at 0.2 N m^{-2} given the conditions prevalent in the study areas, characterized by average water depth around 20 m (Black at al., 2002; Van Rijn, 2020). Conversely, the critical shear stress for deposition τ_{crd} was set at 0.025 N m^{-2} for the suspended sediment in the Mekong delta (Hung et al., 2014b; Manh et al., 2014). The water settling velocity is set to 0.5 x 10^{-4} m s^{-1} (Manh et al., 2014) and the erosion rate was set to 2 x 10^{-5} kg m^{-2} s^{-1} base on the previous studies in the Mekong delta (Tu et al., 2019; Jordan et al., 2020).

b. Sediment transport equations

For sand transport, Three sand transport formulas, including Van Rijn, 1984 (designated as VR); Engelund and Fredsøe, 1976 (EF); Engelund and Hansen, 1967 (EH), are widely used in contemporary modelling and have been applied in the numerical modelling of river deltas globally (Pittaluga at al., 2003; Edmonds and Slingerland 2008; Baar et al., 2018; Jordan et al., 2020) (see section 2.4, Chapter 2). However, these equations are distinct, suggesting variations that may be more suitable in different environments, such as in fluvial or tidal-dominated areas. Hence, all three sand transport equations (VR, EF, EH) are evaluated in this phase to determine the most suitable one for the modelling process. The suspended load transport is calculated by solving the vertically-integrated two-dimensional diffusion-advection equation, where the sediment eddy diffusivities depend on the fluid eddy diffusivities.

c. Sediment transport model boundaries

The sand transport equilibrium condition was applied across all boundaries, meaning the sand transport flux is determined by the modelled hydraulic processes (Edmonds, 2009; Caldwell, 2013) (see section 2.4.2, Chapter 2).

The boundaries for hydraulic conditions and suspended sediment concentration (SSC) are based on existing results from a 1D sediment transport model of the Lower Mekong River and delta, adopted from Manh et al., (2015), which has been calibrated and validated for both hydraulic and suspended sediment transport. To provide further details, the 1D simulated hourly water discharge and SSC time series data are used as boundary conditions for the LMR, TSR, and Bassac Channel. Simultaneously, the simulated hourly water level and SSC time series are applied as boundary conditions for the Mekong channel during the period from 12 September 2013 to 27 October 2013. (Figure 7-7, a).

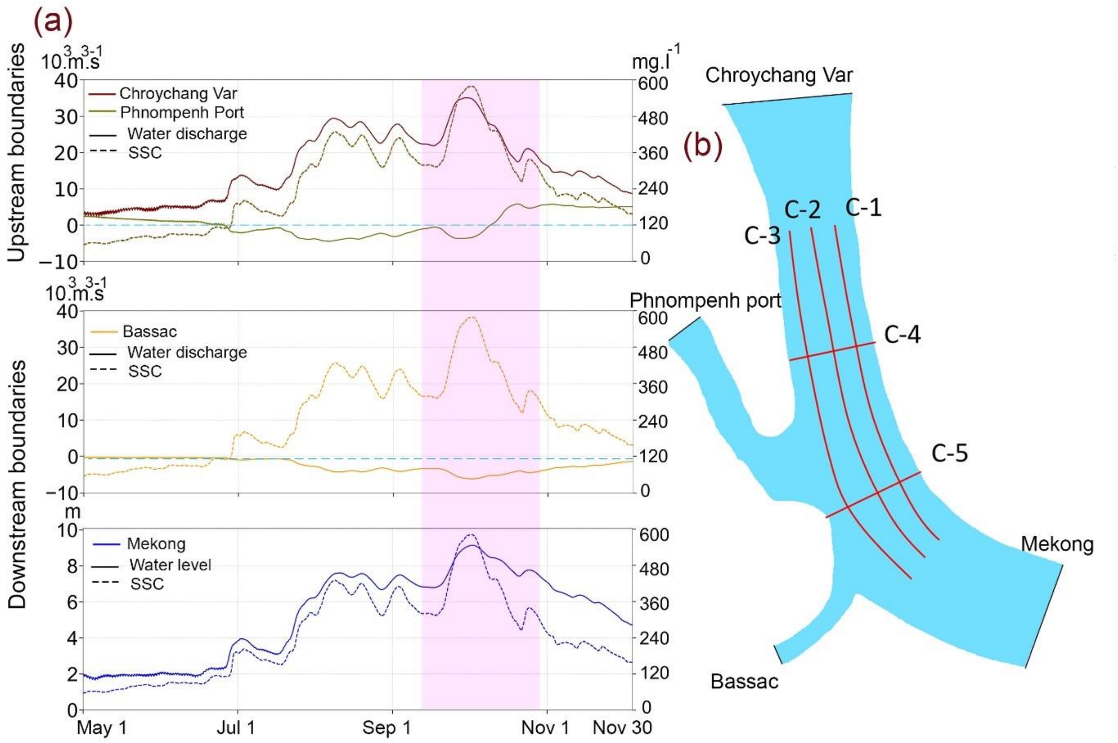

Figure 7-7. (a) The boundaries of the model are defined by the hourly time series of hydraulic and suspended sediment load (SSC) serving as the boundary conditions. Positive discharge values indicate water flow into the model domain, while negative values indicate water flow out of the model domain. This data sets is extracted from 1D sediment transport modelling (Manh et al.,2015), depicts simulated time from Sep 12, 2013, to Oct 27, 2013, represented by a shaded area. (b) The long profiles and cross-sections are employed for the comparison of measured and predicted morphological evolution.

Each scenario simulation was submitted into University of Hull's Viper High Performance Computing system (HPC) using 24 HPC nodes (672 processing cores) for the model calculation. Subsequently, the simulated riverbed and the morphological changes in the riverbed from 12 September 2013, to the final state on 27 October 2013, are extracted. These results will be compared with observed data based on two MBES bathymetries conducted on the same dates (Figure 7-8). Additionally, the evolution of three long profiles named C-1, C-2, and C-3 representing the left bank, middle, and right bank of the longitudinal channel direction, respectively—along with two transverse channel transects, C-4 and C-5, at a resolution of 5 meters, are extracted for comparison with observed data (Figure 7-7, b). These are used to evaluate the riverbed's evolution in both longitudinal and transverse directions, offering a detailed assessment of the morphological changes in the simulation (Figure 7-9).

Table 7-1. The coordinates (WGS 84) of the long profiles (C-1 to C-3) and cross-section (C-4, C-5) examined during the sediment calibration step

Cross name	Start (Upstream)		End (Downstream)	
	X	Y	X	Y
C-1	494009	1281307	495314	1277026
C-2	493735	1281239	495086	1276849
C-3	493455	1281178	494863	1276665
C-4	493287	1281136	494238	1281362
C-5	494335	1280450	493451	1280265

7.3.2.2 Sediment transport model calibration

Initially, the simulation results of the suspended sediment transport module showed minimal impact on river morphology when combined with various scenarios involving sand transport equations (Appendix, Figure. 15). One possible explanation is that high flow velocities keep fine sediment (<63 µm) in suspension throughout the simulation period, causing it to be washed away. Therefore, simulating suspended sediment transport is not crucial for the evolution of the riverbed in this region, which is predominantly influenced by sand transport.

The comparison of the sand transport scenarios with observed data from 12 September 2013 to 27 October 2013 is presented in Figure 7-8 to Figure 7-9 below. Figure 7-8 presents the statistical comparison of datasets comprising observed and predicted model riverbed surface maps for October 27, 2013, considering all sand transport equations scenarios. The results indicate good performance for VR sand transport scenarios compared to the corresponding observed data, with R^2 value is 0.86. However, performance is less satisfactory for scenarios using the EF and EH formulas, with R^2 values standing at approximately 0.67 and 0.57, respectively.

Figure 7-9 presents the comparison of simulated and observed cross-sections in both the longitudinal and transverse directions of the riverbed (C-1 to C-5) on October 27, 2013. The results indicated a close match between the simulated outcomes from VR and the observed riverbed topography, with R^2 values around 0.9 for all cross-sections except for long profile C-3, which had an R^2 value of approximately 0.5 (Figure 7.9). The EF and EH scenarios exhibit overall poorer performance, as the simulated riverbed elevation results align less closely with the observed data. More specifically, the R^2 values for the comparisons between the simulated and observed long profiles are approximately 0.76 and 0.74 for C-1, 0.79 and 0.78 for C-2, and 0.92 for both scenarios in cross-section C-4, respectively. However, these results underperform for long profile C-3 and cross-section C-5, with R^2 values of 0.01 and 0.03 for C-3 and 0.41 and 0.30 for C-5, respectively. However, it is noted that while VR excelled at predicting the overall 'generic' channel topography, it was less effective at capturing finer features (e.g., sand dunes). In contrast, EF and EH made efforts to predict these finer features in the riverbed profiles, but the simulated results from EF and EH formulars still differed significantly from the observed data.

This section has presented the performance of the simulated model of river morphology against the observed river morphology from September 12, 2013, to October 27, 2013, employing different sand transport equations. Although suspended sediment transport is not critical, the riverbed's evolution in this region is primarily driven by sand transport. The Van Rijn (VR) sand transport formula exhibits superior performance compared to the Engelund and Fredsøe, 1976 (EF) and Engelund and Hansen, 1967 (EH) transport formulas. Therefore, the Van Rijn (VR) sand transport equation has been chosen for the subsequent modelling scenarios. However, it is important to note that due to the limited availability of riverbed bathymetry data, the sediment transport model cannot be validated for other periods of hydraulic conditions and riverbed morphology.

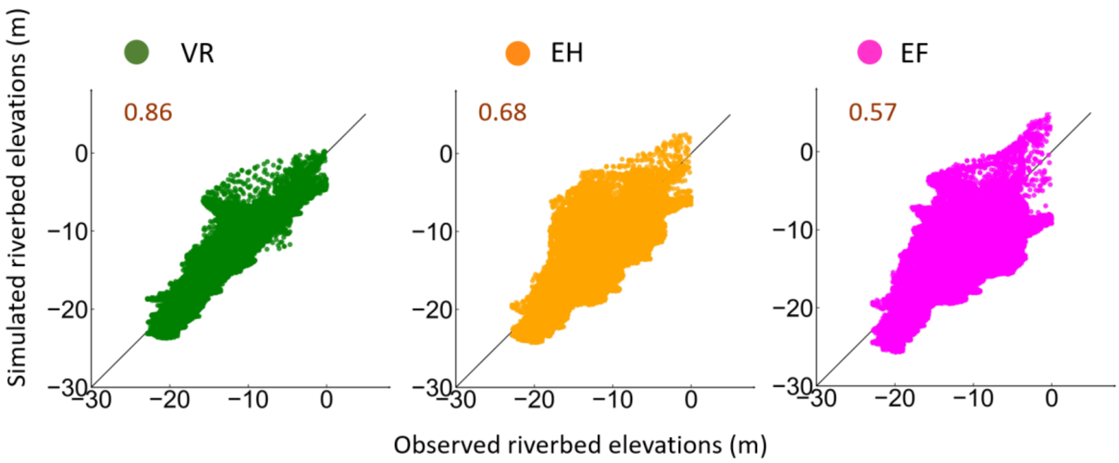

Figure 7-8. The statistical evaluation involved comparing the observed and predicted riverbed elevation surface maps in the study area using various sand transport equations: Van Rijn (VR), Engelund and Fredsøe, 1976 (EF) and Engelund and Hansen, 1967 (EH) on 27 October 2013. The corresponding coefficient of determination (R^2) between them are presented.

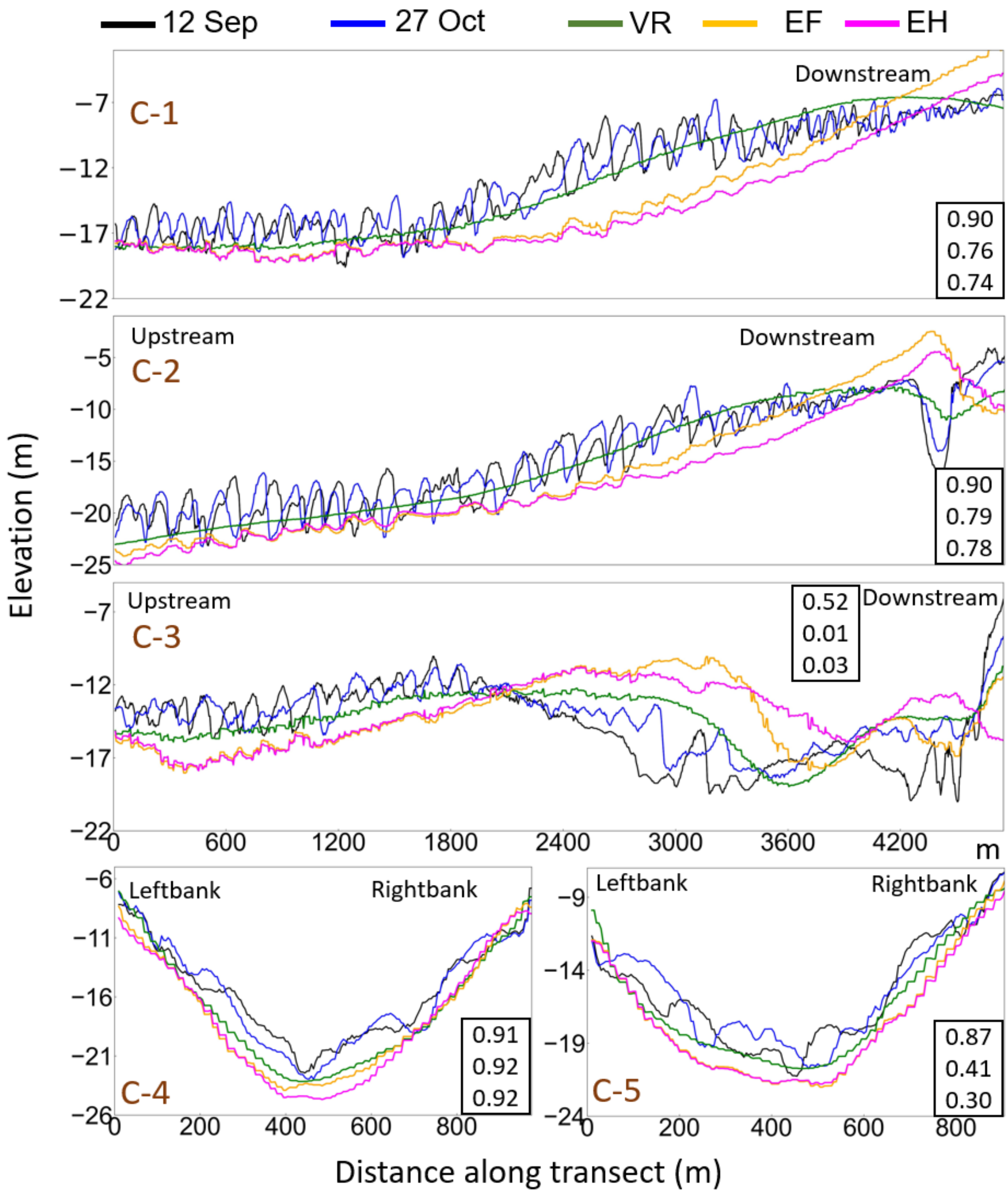

Figure 7-9. The assessments of simulated morphology against the corresponding observed data in long profile C-1, C-2, C-3 and cross-sections C-4, C-5 in various sand transport equations from 12 Sep 2013 to 27 Oct 2013. The table displays the corresponding coefficient of determination (R^2) between the simulated and observed data for each sand transport equation scenario, listed from top to bottom as VR, EF, EH, respectively.

In summary, a 2D numerical hydraulic and sediment transport model, utilizing the DHI MIKE 21 engine, has thus been calibrated for Chaktomuk Junction. The detailed description of the model setup, calibration, and validation steps affirmed that the model performs effectively in representing hydraulic and river morphology processes at the apex of the Mekong delta. It is highlighted that suspended sediment transport is not crucial in this study area, and the evolution of the riverbed is predominantly influenced by sand transport. In the next step of the model scenarios, suspended sediment transport is not included. The analysis of simulated results will focus solely on sand transport.

7.4 Model scenarios

7.4.1 Scenarios of channel bed lowering

In the context of 1D modelling, to evaluate the impact of large-scale riverbed lowering in the model predictions, two bathymetry elevation surface datasets are used. These datasets encompassed the primary river channel and included both bathymetry for the years 2013 and 2022, respectively. These bathymetry datasets result from the integration of bathymetric data from 1998, incorporating spatial observations that illustrate the cumulative riverbed lowering during a 15-year span from 1998 to 2013 and a 24-year period from 1998 to 2022 in entire LMR and MD delta. The cumulative riverbed lowering for the periods from 1998 to 2013 and from 1998 to 2022 was developed through linear extrapolation using observed riverbed lowering data from 1998 to 2018, as detailed in Section 5.2.1, Chapter 5. In more detail, the observed riverbed lowering data from 1998 to 2013 for the LMR from Kratie to Chaktomuk and Mekong channels from Chaktomuk to Neak Luong was adopted from Section 5.2.1, Chapter 5. For the remaining sections of the Mekong channel, from Neak Luong to the coast, and in entire of Bassac channel, where 2013 bathymetry data is unavailable, riverbed lowering was estimated by linear extrapolation using the observed data from 1998 to 2018, adjusted by multiplying a factor of 0.75 (derived from the ratio 15/20, where 15 and 20 represent the years from 1998 to 2013 and 1998 to 2018, respectively).

Similarly, the projected riverbed lowering data for the entire LMR, Mekong, and Bassac channels from 1998 to 2022 was estimated by linear extrapolation using the observed data from 1998 to 2018, adjusted by multiplying a factor of 1.2 (derived from the ratio 24/20, where 24 and 20 represent the years from 1998 to 2022 and 1998 to 2018, respectively). In a small area near Kratie in the Lower Mekong River, the depth differences from 1998 to 2013 show positive values, indicating a shallowing trend in the riverbed from 1998 to 2013 (Figure 7-10). However, for the depth differences from 1998 to the projected 2022, the positive values were set to 0 m, indicating no change in riverbed elevation between 1998 and 2022 in the upper reaches of the LMR, near Kratie (Figure 7-10). The elimination of positive values in the difference in riverbed elevation between 1998 and 2022 in this zone is supported by the anticipation that the riverbed continues to descend from 2013 to 2022, owing to the effects of sand mining and sediment scarcity caused by upstream dams (see Section 5.2.1, Chapter 5 for more details).

The results show an average riverbed lowering of 2.27 m (σ = 1.56 m) from 1998 to 2013 and 3.90 m (σ = 2.05 m) for the 1998 to 2022 scenarios for the combined Lower Mekong River, Mekong and Bassac channels (Figure 7-10). This resulted in a riverbed lowering of 1.63 m (σ = 0.70 m) from 2013 to 2022. However, it is noteworthy that a land reclamation project has been undertaken since 2020 on the right bank of the Mekong channel downstream of the Chaktomuk Junction, resulting in the filling of nearly one third of the river width over a stretch of around 3.8 km (Figure 7-1). This infilling is captured in the 2022 bathymetry and therefore warrants, further consideration given its potential impact on the hydraulic regime and sand transport capacity through the delta apex, as well as the water flow partitioning between two downstream channels. Therefore, to examine the distinct impacts of both the land reclamation project and the riverbed lowering in this area, the 2022 bathymetry DEM is modified by expanding it by 450 m on the right bank at the land reclamation project site (2022 modified scenarios). Combined with the 2022 bathymetry DEMs (2022 scenarios) and the DEMs of 2013 bathymetry (2013 scenarios), three sets of riverbed bathymetry DEMs scenarios have been developed for 1D model.

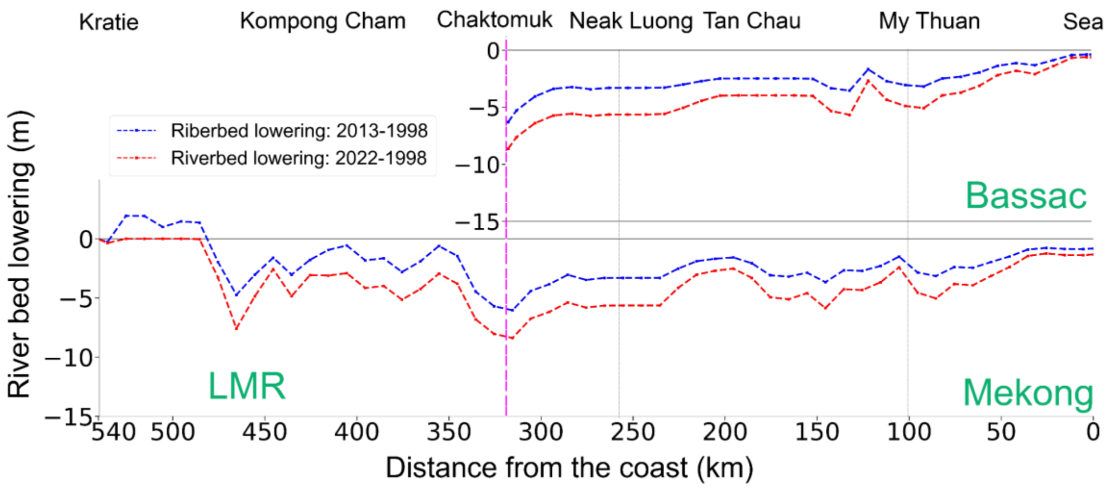

Figure 7-10. Development of two scenarios for the accumulated average riverbed lowering between 1998-2013 and 1998-2022 along the longitudinal axis for the two main Mekong and Bassac channels.

In the context of 2D modelling, the observed MBES 2022 bathymetry have been used to generate model mesh (section 3.2, Chapter 3). However, it is noted that, the 2022 river bathymetric dataset is not covering the entire model domain, so for the remaining areas, an analogous bathymetry for 2022 was created from the SBES riverbed bathymetry of 2013. In more detail, comparison of the DEMs of 2013 and 2022 in the common area reveal that the riverbed has been lowered by 4.2 m (σ = 5.7m) from 2013 to 2022 (Figure 7-11, a). The extent of riverbed lowering in this region surpasses the average reduction of 1.63 m (σ = 0.70 m) observed across the entirety of the LMR and MD delta. This underscores the notable impact of riverbed lowering in this area compared to the rest of the system. For the missing areas of the model domain an analogous topography was generated for 2022 by using the SBES topography data in 2013 and subtracting 4.2m (Figure 7-11, b). This analogue topography was combined with the existing MBES-based dataset to generate the model domain for 2022 (Figure 7-12, b). It is important to note that the 2022 bathymetry includes changes caused by the land reclamation project. Therefore, to analyse the distinct impacts of both the land reclamation project and the riverbed lowering in 2D modelling, a similar adjustment is made by using analogous bathymetry data from 2022 to fill the gap created by the land reclamation project. This process involved incorporating data from 2013 and subtracting it by 4.2 m (2022 modified scenarios) (Figure 7-12, c).

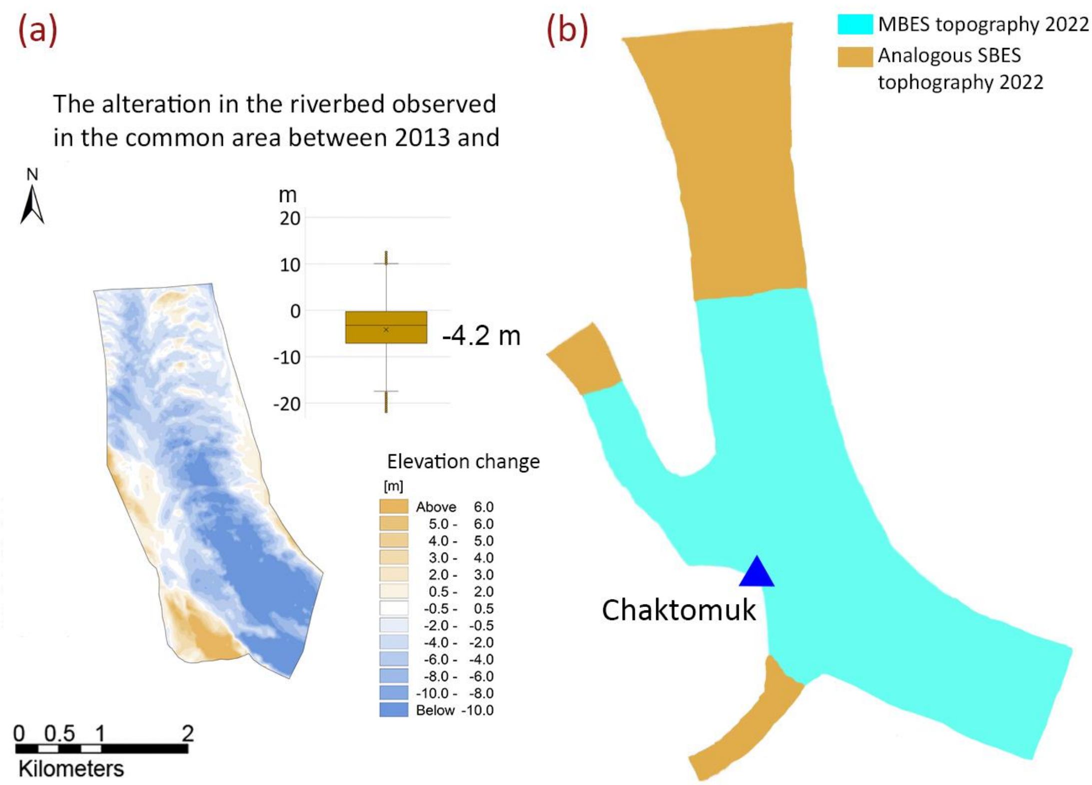

Figure 7-11. (a) The comparison of two 2013 and 2022 DEMs in the overlapping region indicates a riverbed lowering of 4.2 m (σ = 5.7 m) from 2013 to 2022. (b) The bathymetric domain for the 2D model scenarios in 2022 is established by combining MBES data with analogous SBES bathymetric data.

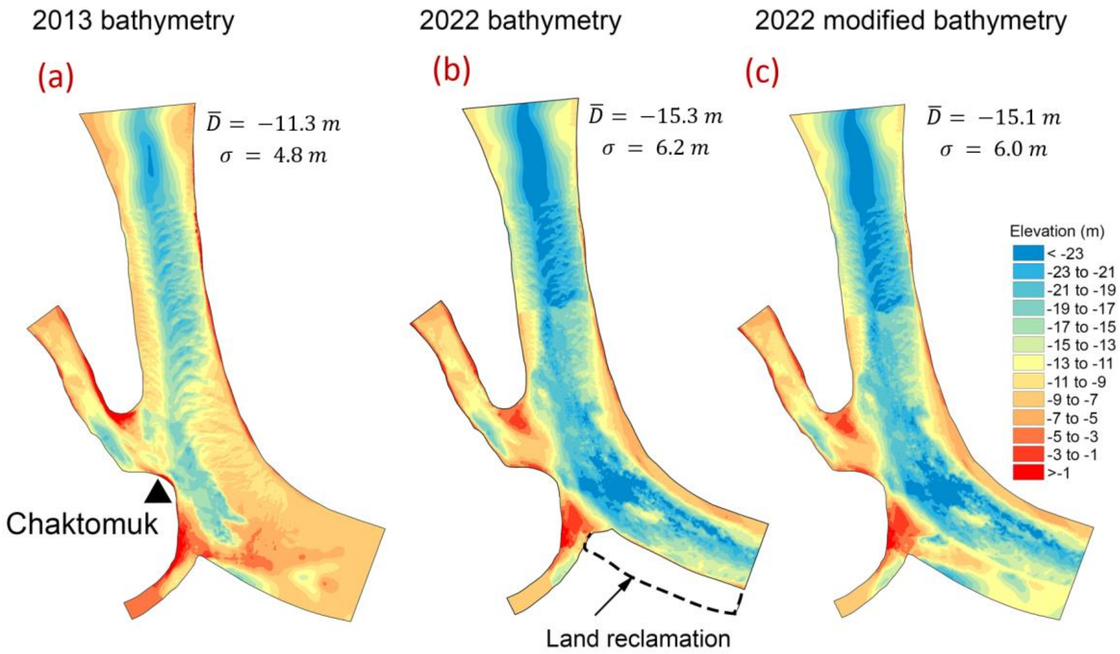

Figure 7-12. Three riverbed bathymetries are employed in the 2D modelling. The numbers in each panel represent the average riverbed elevation and the standard deviation in the model domain for each scenario, referenced to the Hon Dau MSL.

7.4.2 Scenarios of fresh water flux

In the context of 1D modelling, to assess the impact of fresh water flux changes in the model predictions, simulations are performed low (2010), median (2009) and high (2011) fresh water flux years (see section 5.2.3, Chapter 5). The hourly tidal record at a series of gauging stations along the Mekong's coastal area (see section 5.1.1, Chapter 5) from 2013 forced as downstream boundary. These formed the boundary inputs for the 1D model, whilst the outputs from the 1D model simulations are used as forcing datasets for the nested 2D model. The hydraulic scenarios in the 1D model are simulated for the entire year to evaluate the complete hydraulic regime at various water flux stages. Meanwhile, the 2D sediment transport modelling was conducted for a duration of 8 months, from the beginning of May to the end of December. This timeframe was chosen to ensure that the simulation period encompasses the entire flood season each year (approximately June to November) focusing on the movement of sand transport (see Figure 7-16), while maintaining a reasonable computation time for the simulation. Each simulation scenario required an average of 10 hours on University of Hull's Viper High Performance Computing system.

7.5 Results

The results of both 1D and 2D model scenarios are processed to extract data at hourly intervals. The changes in the hydraulic regime at the apex of the Mekong Delta will be evaluated using the results of 1D modelling, as presented in section 7.5.1. Simultaneously, the evolution of sand transport capacity at the delta's apex will be examined using the outcomes of 2D modelling, detailed in section 7.5.2.

7.5.1 Effects on water level and flow discharge

Based on the 1D model results, the land reclamation project on the right bank of the Mekong channel has a minimal impact on the hydraulic regime in this region (Figure 7-13). This encompasses various aspects such as the water discharge flow at LMR, TSR, Mekong and Bassac channels, and the water levels at Chaktomuk Junction. It is elucidated that the hydraulic regime in the delta is predominantly controlled by the large-scale features of the entire delta, rather than being significantly affected by localized perturbations. Consequently, the subsequent hydraulic analysis for this section will compare the 2013 and 2022 bathymetric scenarios, while the '2022_modified' scenario will be used only to calculate the unit stream power for the Mekong channel (see later, Figure 7-15) and sediment transport capacity locally (Figure 7-16). This is because changes in channel width by artificially removing the land reclamation project in this hypothetical scenario are expected to affect the unit stream power calculations.

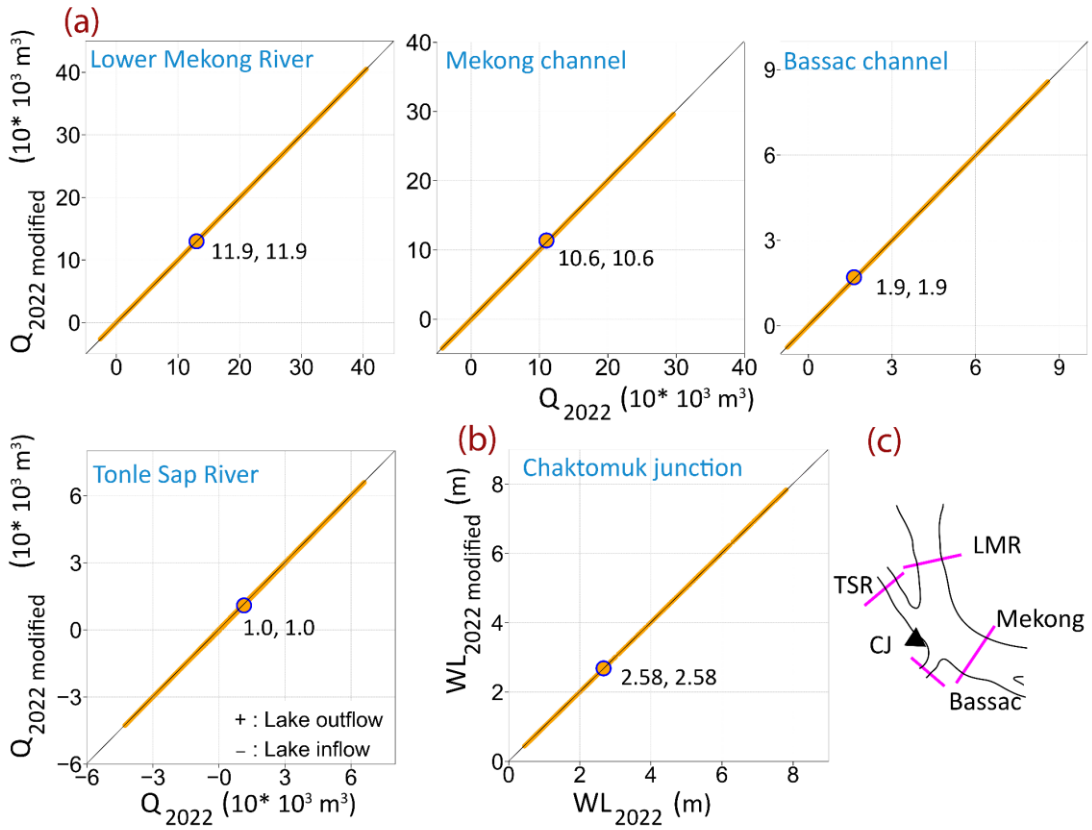

Figure 7-13. The relationship between (a) water discharge (Q) in the Lower Mekong River (LMR), Tonle Sap River (TSR), the Mekong and Bassac channels, Tonle Sap River (TSR) and (b) water level (WL) at the right Chaktomuk junction for two bathymetry scenarios, 2022 and 2022_modified, under combination of three conditions: median (low; high) fresh water flux. In the TSL, a positive value indicates water flowing out of the lake, while a negative value indicates water flowing into the lake. The numbers in each panel represent the average water discharge and average water level for each bathymetry scenarios of 2022 and 2022_modified, respectively. (c) the location where Q and WL are extracted in each reach.

Figure 7-14 illustrates the simulated water discharge at the Chaktomuk Junction, considering the riverbed bathymetry in both 2013 and 2022 scenarios in various fresh water flux conditions. The annual water discharge in the LMR (see Figure 7-13, c for the location) increased from 11.9 (8.9; 13.6) $*10^3$ m^3s^{-1} in the 2013 scenarios to 12.5 (9.2; 14.4) $*10^3$ m^3s^{-1} in the 2022 scenarios for the median (low; high) fresh water flux years, respectively (Figure 7-14, a), representing a 5 % (3 %; 6 %) increase in annual water discharge for the median (low; high) fresh water flux years. In the Mekong channel, the annual water discharge increased from 10.6 (8.3, 11.9) $*10^3$ m^3s^{-1} in the 2013 scenarios to 11.0 (8.4; 12.3) $*10^3$ m^3s^{-1} in the 2022 scenarios (Figure 7-14, a). This presents a 4 % (1 %; 3 %) increase for the median (low; high) fresh water flux years. In the Bassac channel, the annual water discharge remains almost unchanged between the 2022 and 2013 scenarios at 1.9 (1.3; 2.6) $*10^3$ m^3s^{-1} for the median (low; high) fresh water flux years (Figure 7-14, a). In the TSR, the average water discharge lake outflow (indicated by a positive value) at Phnom Penh

Port (see Figure 7-13, c for the location) decreased from 2.6 (1.7; 3.4) $*10^3$ m^3s^{-1} in the 2013 scenarios to 2.1 (1.5; 3.0) $*10^3$ m^3s^{-1} in the 2022 scenarios (Figure 7-14, a), representing a 21% (14%; 11%) decrease for the median (low; high) fresh water flux years. Meanwhile, the average water discharge lake inflow (indicated by a negative value) decreased from 1.7 (1.6; 2.4) $*10^3$ m^3s^{-1} in the 2013 scenarios to 1.5 (1.4; 2.0) $*10^3$ m^3s^{-1} in the 2022 scenarios for the median (low; high) fresh water flux years, representing a 16% (9%; 19%) decrease for the median (low; high) freshwater flux years (Figure 7-14, a). Water levels at Chaktomuk Junction are also impacted by river bed lowering (see section 5.4.1, Chapter 5) with the mean annual water level reduced from 3.3 (2.5; 3.7) m in the 2013 bathymetry scenarios to 2.7 (2.1; 3.1) m in the 2022 bathymetry scenarios for the median (low; high) fresh water flux years.

The increased average water discharge in the LMR, Mekong and Bassac is attributed to the reduced contribution of upstream water flux to the floodplain, resulting in increased water flow within the mainstream, as discussed in Section 5.5, Chapter 5. Similarly, the reduction in water flow into and out of the Tonle Sap Lake, driven by riverbed lowering, is also detailed in Section 6.2.1 of Chapter 6. Additionally, while the annual water discharge in the Bassac channel remains unchanged, there is an increase in the annual water flow in the Mekong channel. This indicates that a greater volume of water is moving towards the downstream Mekong channel. This phenomenon can be attributed to the effect of riverbed lowering in both channels, with the larger Mekong River channel's riverbed lowered more, effectively containing a greater flow compared to the considerable smaller Bassac channel (Figure 7-1). In addition, Figure 7-14 shows that water discharge remains below the one-to-one line during the low water discharge stage in the dry season and above the one-to-one line during the high-water flux stage in the flood season, across different upstream fresh water flux conditions when comparing the 2022 scenarios to the 2013 ones. This could be attributed to the riverbed lowering, which reduce the water volume from the Tonle Sap Lake to MD (Mekong and Bassac channels) during the receding limb and dry season (see section 6.2.3, Chapter 6) as well as an increase the impact of tidal signals during the dry season, which could reduce the lowest water discharge driven by the tidal oscillation (see section 5.4.1, Chapter 5).

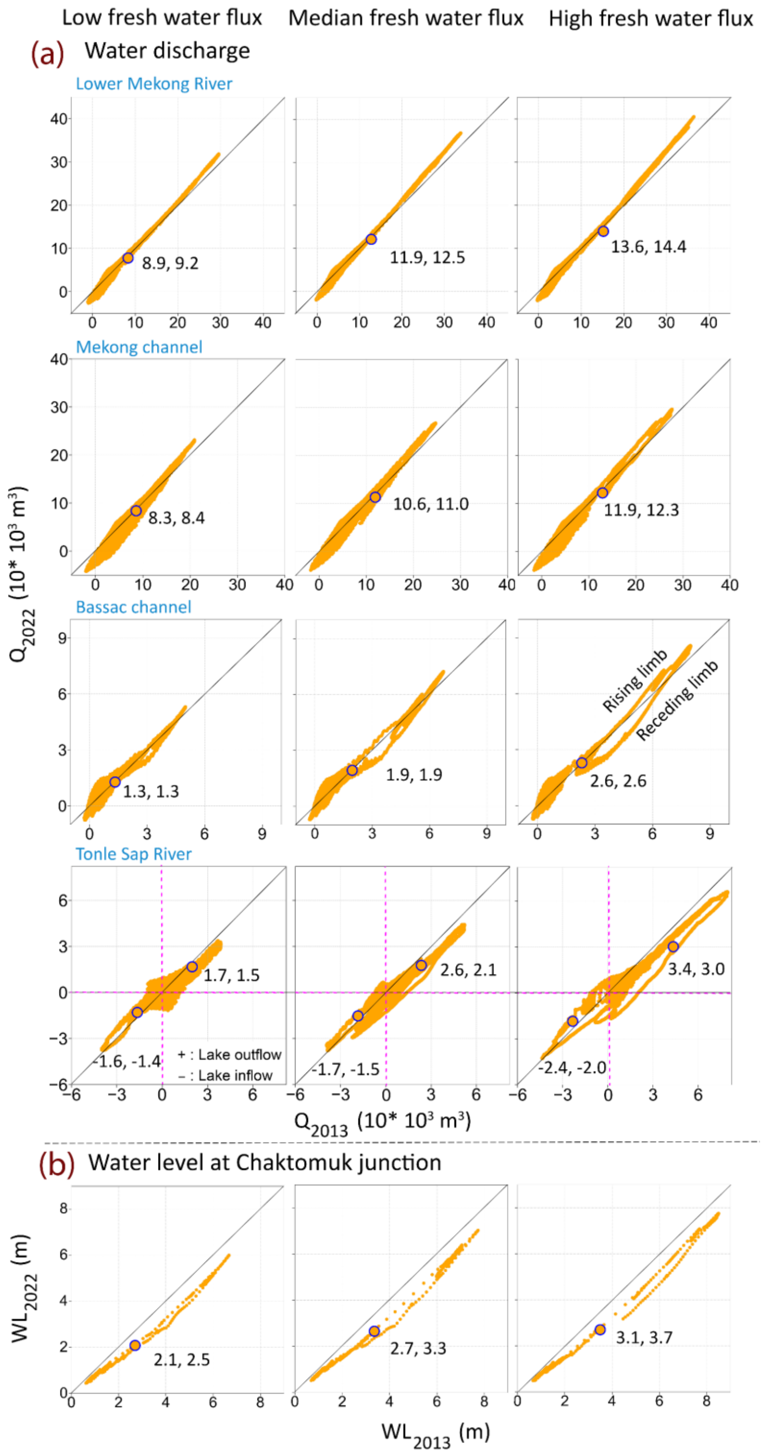

Figure 7-14. (a) The relationship between hourly water discharge through the Chaktomuk junction in Lower Mekong River, Tonle Sap River, Mekong and Bassac channels and (b) water level at Chaktomuk junction for 2013 and 2022 bathymetry scenarios (see Figure 7-13, c for the location) under median (low; high) fresh water flux conditions. The numbers in each panel represent the annual water discharge and water level for 2023 and 2022 scenarios, respectively.

The rise in water discharge in LMR, Mekong and Bassac channels of the Chaktomuk Junction suggests potential implications for an increased capacity to transport sediment. However, the reduction of water level in the river has the potential to reduce water slope, resulting in a smaller capacity for material transport. In order to compare a physically meaningful metric representing the changes in sediment transport capacity, the unit stream power is calculated (Bagnold, 1960) (Eq.14). This metric reflects the amount of energy exerted by the water in a river or stream on its sides and bottom, indicating the river's capacity for material transport (Bagnold, 1980).

The unit stream power:

$$\omega = \frac{\rho g Q S}{W_c} \tag{14}$$

where ρ = 997 (kg m^{-3}) is the water density, g = 9.81 (m s^{-2}) is the gravitational acceleration, Q is the discharge (m^{3}s^{-1}), S is water slope and W_c is the channel width (m).

While the riverbed lowering contributes to an overall increase in water discharge in the channels, it simultaneously reduces the unit stream power in all of reaches in the junction (Figure 7-15). This reduction in unit stream power is more pronounced during the high-water stage, occurring during the flood season. In more detail, in the LMR, the annual unit stream power decreases from 4.4 (2.7; 6.2) watts m^{-1} in the 2013 scenarios to 4.0 (2.3; 5.9) watts m^{-1} in the 2022 scenarios, representing a 9 % (15 %; 5 %) reduction in annual unit stream power for the median (low; high) fresh water flux years (Figure 7-15). In the Mekong channel, the annual unit stream power decreases from 3.8 (2.5; 4.9) watts m^{-1} in the 2013 scenarios to 3.1 (1.9; 4.4) watts m^{-1} in the 2022 scenarios, representing an 18 % (24 %; 10 %) reduction in annual unit stream power for the median (low; high) fresh water flux years (Figure 7-15). However, in the 2022 modified scenarios, the annual unit stream power further decreases to 2.2 (1.4; 3.2) watts m^{-1} representing an 50 % (48 %; 48 %) reduction in annual unit stream power for the median (low; high) fresh water flux years as compared to 2013 scenarios. In the Bassac channel, the annual unit stream power decreases from 1.9 (0.8; 3.7) watts m^{-1} in the 2013 scenarios to 1.0 (0.4; 2.2) watts m^{-1} in the 2022 bathymetry scenarios (Figure 7-15), representing a 47 % (50 %; 41 %) reduction in annual unit stream power for the median (low; high) fresh water flux years. In the TSR, the average unit stream power of lake outflow decreases from 1.0 (0.6; 2.3) watts m^{-1} in the 2013 scenarios to 0.7 (0.4 ; 2.1) watts m^{-1} in the 2022 bathymetry scenarios (Figure 7-15), representing a 28 % (29 %; 9 %) reduction in annual unit stream power for the median (low; high) fresh water flux years. Meanwhile, the average unit stream power of lake inflow decreases from 0.4 (0.4; 0.8) watts m^{-1} in the 2013 scenarios to 0.4 (0.4 ; 0.6) watts m^{-1} in the 2022 bathymetry scenarios (Figure 7-15), representing a 0 % (0 %; 25 %) reduction in annual unit stream power for the median (low; high) fresh water flux years. These decreasing unit stream power results suggest that riverbed lowering in the LMR and Delta could reduce the capacity to transport material seaward through the Chaktomuk Junction. The next section will quantify the sand transport capacity through the junction based on 2D modelling results.

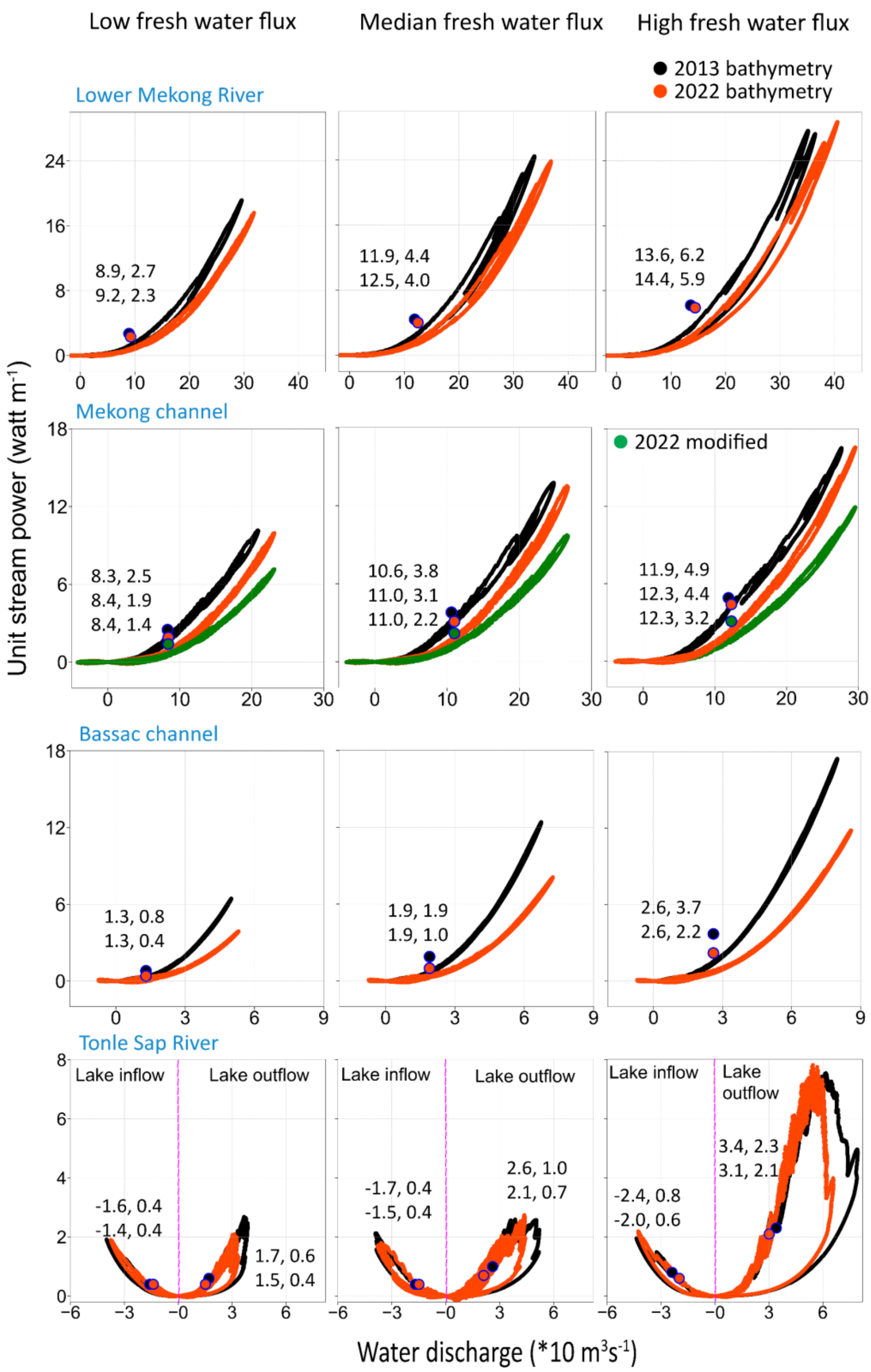

Figure 7-15. The relationship between water discharge and unit stream power through the Chaktomuk Junction in the LMR, TSR, Mekong and Bassac channels. The analysis considers the 2013, 2022 and 2022 modified riverbed bathymetry scenarios under median (low; high) fresh water flux conditions. The numbers in each panel represent the annual water discharge and annual unit stream power, respectively.

7.5.2 Effects on sand transport capacity

The results from 2D modelling indicated that during periods of low water discharge in the dry season (highlighted by the shaded blue area in each panel of Figure 7-16, sand transport is negligible in the LMR, Mekong and Bassac channels. However, during the flood season, there is a significant increase in sand transport observed across LMR, Mekong and Bassac channels under all water flux condition scenarios (Figure 7-16).

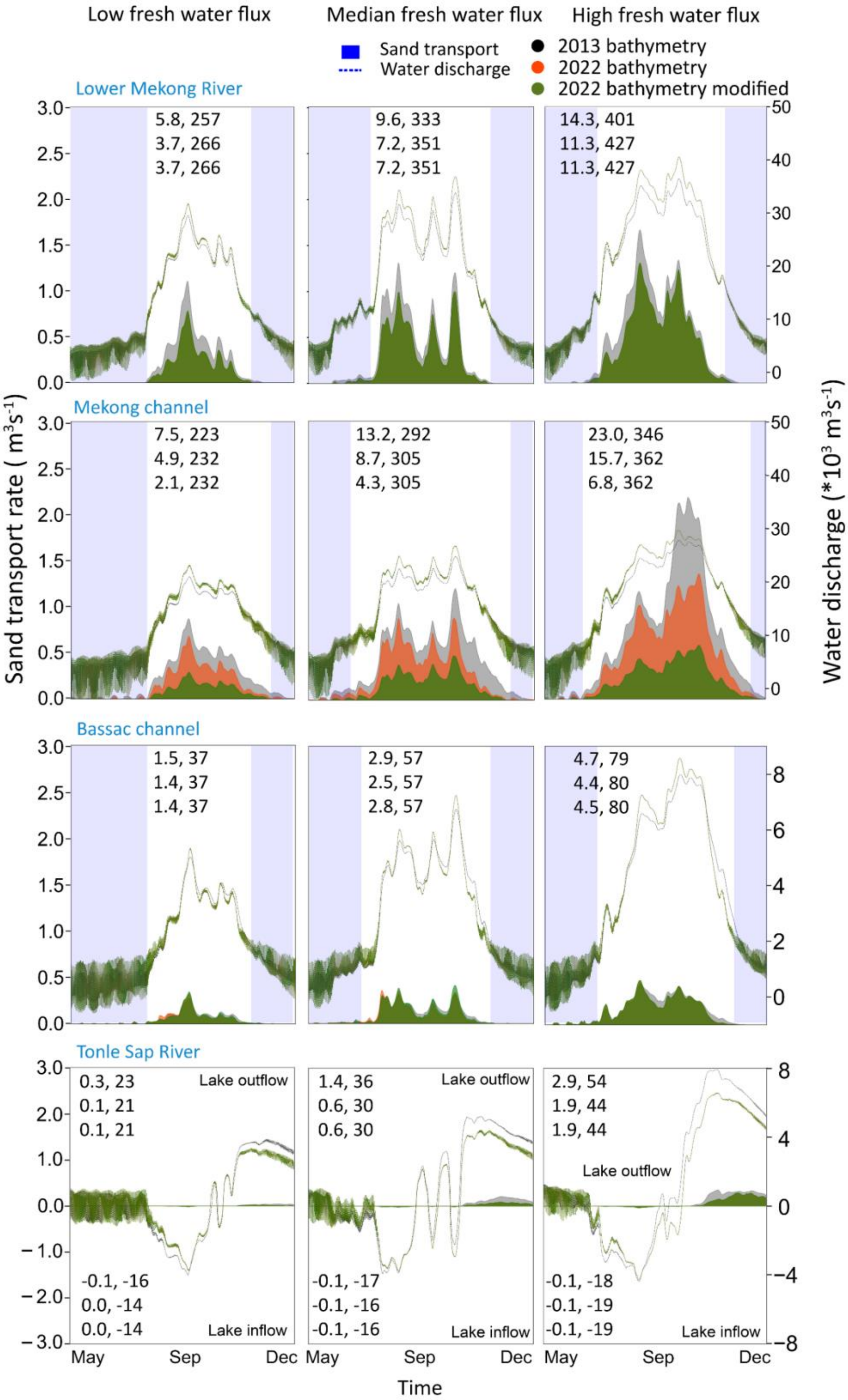

Figure 7-16. The sand transport through the Chaktomuk Junction in the Lower Mekong River, Mekong and Bassac channels, is analysed for different upstream fresh water flux scenarios. The numbers in each panel represent the total amount of sand transport and the total water volume over the 8-month simulation period from May to December, respectively.

In more detail, despite the increase in water flow in the main stream driven by riverbed lowering in LMR, Mekong and Bassac channels, as presented in the previous section, there are a decrease in sand transport capacity in LMR, Mekong and Bassac channels. Specifically, in the LMR, the sand transport capacity decreases from 9.6 (5.8; 14.3) million tons (Mt) in the 2013 bathymetry scenario to 7.2 (3.7; 11.3) Mt in both the 2022 and the 2022 modified bathymetry scenarios for median (low; high) fresh water flux years, representing a 25 % (36 %; 21 %) reduction in total sand transport for the median (low; high) fresh water flux years. In the Mekong channel, the sand transport capacity decreased from 13.2 (7.5, 23.0) Mt in the 2013 scenarios to 8.7 (4.9; 15.7) Mt in the 2022 scenario and 4.3 (2.1; 6.8) Mt in the 2022 modified scenario for median (low; high) fresh water flux years. This corresponds to a 34 % (35 %; 32 %) reduction in total sand transport in the 2022 scenarios and a 67% (72%; 71%) reduction in the 2022 modified scenarios compared to the 2013 scenarios for median (low; high) fresh water flux years in the Mekong channel. In the Bassac channel, the sand transport capacity decreased from 2.9 (1.5; 4.7) Mt in the 2013 scenarios to 2.5 (1.4; 4.4) Mt in the 2022 scenario and 2.8 (1.4; 4.5) Mt in the 2022 modified scenario for median (low; high) fresh water flux years. This corresponds to a 12% (9 %; 7 %) reduction in total sand transport in the 2022 scenarios and a 3 % (6 %; 4 %) reduction in the 2022 modified scenarios compared to the 2013 bathymetry scenarios for median (low; high) fresh water flux years in the Bassac channel.

In the TSR, sand transport capacity of lake outflow decreased from 1.4 (0.3; 2.9) Mt in the 2013 scenarios to 0.6 (0.1; 1.9) Mt in both the 2022 and the 2022 modified bathymetry scenarios for median (low; high) fresh water flux years. This corresponds to a 57 % (67 %; 34 %) reduction in total sand transport in the 2022 scenarios and the 2022 modified scenarios compared to the 2013 bathymetry scenarios for median (low; high) fresh water flux years. Meanwhile, the sand transport capacity of the lake inflow is almost negligible, remaining equal to or below 0.1 Mt across all riverbed lowering scenarios and fresh water flux conditions.

Along with the reduction in total sand transport across all reaches of the junction, there is a decrease in the maximum sand transport rate due to riverbed lowering. Specifically, in the LMR, the maximum sand transport rate decreases from 1.3 (1.1; 1.7) m^3s^{-1} in the 2013 bathymetry scenarios to 1.0 (0.8; 1.3) m^3s^{-1} in both the 2022 and 2022 modified bathymetry scenarios, representing a 24 % (29 %; 22 %) reduction in the maximum sand transport rate for median (low; high) fresh water flux years. In the Mekong channel, the maximum sand transport rate decreases from 1.2 (0.9; 2.2) m^3s^{-1} in the 2013 scenarios to 0.9 (0.7; 1.4) m^3s^{-1} in the 2022 and 0.5 (0.3; 0.6) m^3s^{-1} in the 2022 modified scenarios. This corresponds to a 27 % (22 %; 38 %) and 60 % (67 %;

73 %) reduction in maximum sand transport rate in the 2022 and 2022 modified scenarios compared to the 2013 scenarios, respectively, for median (low; high) fresh water flux years. In the Bassac channel, the maximum sand transport rate shows negligible change, being 0.4 (0.3; 0.4) m^3s^{-1} in the 2013 scenarios and 0.4 (0.3; 0.5) m^3s^{-1} in both 2022 and 2022 modified scenarios, respectively, for median (low; high) fresh water flux years (Figure 7-16). In the TSR, the maximum sand transport rate of lake outflow decreased from 0.2 (<0.1; 0.4) m^3s^{-1} in the 2013 scenarios to 0.1 (<0.1; 0.3) m^3s^{-1} in both the 2022 and the 2022 modified bathymetry scenarios for median (low; high) fresh water flux years (Figure 7-16). This corresponds to a 50 % (50 %; 25 %) reduction in maximum sand transport rate in the 2022 scenarios and the 2022 modified scenarios compared to the 2013 bathymetry scenarios for median (low; high) fresh water flux years. Meanwhile, the maximum sand transport rate of the lake inflow is almost negligible, remaining below 0.1 m^3s^{-1} across all riverbed lowering scenarios and fresh water flux conditions (Figure 7-16).

Figure 7-16 also highlights that the increase in sand transport is not linear with increases in water transport, and sand transport is notably higher during periods of high-water discharge. For example, in the 2013 bathymetry scenarios, the water volume passing through the LMR over the 8-month simulation period during high fresh water flux years is 401 billion m^3, about 1.5 times that of low fresh water flux years, which is 257 billion m^3. However, sand transport in high fresh water flux scenarios is approximately 14.3 Mt, roughly 2.5 times higher compared to low fresh water flux scenarios, which record 5.8 Mt (Figure 7-16). This trend is also evident in the Mekong River and Bassac channels, where during high fresh water flux years, the water volume over the 8-month simulation period is 1.5 to 2.1 times greater than in low fresh water flux year respectively, while the sand transport capacity is roughly 3 times higher in high water flux conditions compared to low water flux conditions for both channels (Figure 7-16).

The findings indicate that the land reclamation project in the Mekong channels, which reduced the width of the channels by nearly one-third (around 400 m, Figure 7-1), increased the sand transport capacity by 51% (57%; 57%) in the 2022 bathymetry scenarios compared to the 2022 bathymetry modified scenarios for median (low; high) fresh water flux years. However, the land reclamation project has a negligible effect on sand transport capacity in the LMR and TSR, showing similar sand transport capacities in both the 2022 and 2022 modified scenarios. The project has only a minor impact on the Bassac channel, with a slight reduction of 12% (0%; 2%) in the 2022 scenarios compared to the 2022 modified scenario for median (low; high) fresh water flux years.

7.6 Discussion

Riverbed lowering reduces the unit stream power and the capacity of flow to transport sand through the delta apex (see section 7.5.1). The reduced rates of sediment transport may help sand accumulate at this location and function as a self-regulating natural mechanism acting to mitigate the lowering of riverbed levels in the Chaktomuk Junction. In more detail, if the volume of supplied sediment exceeds the sediment carrying capacity of the river, a portion of the sediment will be deposited. This sediment accumulation could lead to increased local stream power as local riverbeds will aggrade, enhancing transport capacity and causing sediment to be redistributed further downstream (Gilbert 1877; Orford and Knight, 2015). This progression would persist downstream and could gradually transform the riverbed to a more natural state, characterized by smoother surfaces, natural sand ripples, and the absence of sand mining pits, as it was before the riverbed lowering perturbation. However, if the sediment supply is smaller than the sediment carrying capacity of the river, it may lead to erosion of the riverbed or riverbanks (Hackney et al., 2020) to meet the required sediment capacity (Orford and Knight, 2015), causing further lowering of the riverbed. This ongoing process, involving the sediment transportation, erosion and deposition of sediment for river healing, signifies the river's inherent effort to restore its natural state before human-induced disturbances in riverbed lowering occurred with the trend will happened in the upstream section first. The time it takes for the river to self-heal could depends on the rate of upstream sediment supply to the delta and the rate of sediment extraction from the delta.

The findings also highlighted that under the 2022 bathymetry scenario, the sand transport capacity at the apex of the delta is 7.2 million tons (ranging from 3.7 million to 11.3 million tons) in the Lower Mekong River and 11.2 million tons (ranging from 6.3 million to 20.1 million tons) for the combined Mekong and Bassac channels, during upstream fresh water flux years with a 41% flood exceedance probability (ranging from 87% to 7%) over the 22-year period from 2000 to 2021. This sand transport rate is considerably smaller than the estimated volume of sand extracted from this reach of Lower Mekong River and its delta. In 2020 alone, sand extraction in Cambodia was estimated at approximately 59 million tons (Hackney et al., 2021), while Gruel et al., (2022) suggested a volume of 67.2 million tons yr^{-1} (42 million cubic meters yr^{-1}) for sand mining in the Vietnam Mekong Delta from 2015 to 2020. As a result, the sand transport at the apex of the delta, given a sufficient upstream supply, seems to be less than 10 times that of current sand extraction in entire of Lower Mekong River and its delta. Critically, the results presented in this Chapter indicate that the excessive sand extraction, which is outpacing the natural sand supply and diminishing the river's ability to recover from riverbed lowering, could exacerbate the impacts of sediment deficit in the delta, leading to increased delta sinking (Syvitski et al., 2009; Kondolf et al., 2022), It could also increase riverbank instability (Hackney et al., 2020), thereby compromising nearby riverine structures (Kondolf 1994; Best 2019) and threatening communities along riverbanks (Bendixen et al., 2019). Additionally, it contributes to coastal land loss (Anthony et al., 2015), exacerbates tidal ingress landward (Vasilopoulos et al., 2021), increasing the disconnection between the river and its floodplain, as well as the risk of tidal flooding in the downstream delta, as discussed in Section 5.5, Chapter 5, and promotes saline intrusion (Eslami et al., 2021).

Moreover, the sediment deficits and lowered riverbed elevations can reduce the likelihood of delta avulsion (Slingerland and Smith, 2004). Avulsions play a vital role in redistributing sediments across the delta plain, helping to sustain deltaic landforms and counteracting local subsidence (Mackey and Bridge, 1995; Slingerland and Smith, 2004; Reitz and Jerolmack, 2012). A reduction in avulsion frequency diminishes the natural processes that replenish and maintain delta ecosystems, further threatening the long-term stability and resilience of deltas under human and climate-induced pressures.

The presented results have far-reaching implications. Beyond the Mekong, riverbed lowering is causing similar issues in many other large sand-bedded rivers (Dunn et al., 2019), such as the Pearl River Delta (Lu et al., 2007), Yellow River Delta (Chu, 2014), and the Ganges Delta (Daham et al., 2024). This underscores the importance of implementing appropriate measures to mitigate sand extraction for the long-term stability of the delta.

In addition, the unit stream power as well as sand transport capacity is elevated during high-water discharge stages, particularly at flood peaks. This underscores the importance of high-water discharge events, such as tropical-cyclone activity (Darby et al., 2016), as they have the potential to transport large quantities of sand to the downstream deltas. Although anthropogenic climate change is projected to increase runoff in the Mekong River during the flood season under all Representative Concentration Pathways, such as a 9±8 % increase over 100 years under RCP2.6 (Wang et al., 2024), the extent of hydrological changes due to hydropower development and irrigation expansion somewhat mitigates the effects of future climate change (Horton et al. 2022). Upstream dams have the potential to decrease water flow during the flood season while increasing it during the dry season (Hecht et al., 2019; Dang et al., 2022). For instance, Lauri et al. (2012) indicated that changes in discharge due to planned reservoir operations in the Mekong basin are likely to be significantly larger than those resulting from climate change by around 2050, with 5–24 % lower flood peaks in Kratie (Cambodia). Furthermore, hydropower projects will continue to capture and store sediment in their reservoirs, potentially reducing sediment loads by up to 96% (Kondolf et al., 2014). Consequently, this could lead to decreased sediment supply and diminished sediment transport capacity in the downstream region, as well as extended recovery times for the river system.

It should be noted that the hydraulics of the TSR differ from those of the LMR, Mekong, and Bassac channels. In the TSR, flow into the lake begins to increase around June, peaks in around August, and then reverses to flow out of the lake around October (see Section 6.1, Chapter 6 for more details). However, in this analysis, the limited of simulation duration covers only 8 months, from May to the end of December, which does not fully capture the entire sand transport simulation in the TSR. The unit stream power and sand transport capacity for lake outflow are considerable higher than those for lake inflow. This is due to the fact that, in addition to receiving water from the Mekong River, the lake also has other sources from the TSL basin (approximately 30% of the total water received, as detailed in Section 2.3.1, Chapter 2), which increases the lake's water outflow. This heightened outflow boosts both the unit stream power and sand transport capacity, potentially enhancing the capacity to discharge sediment from the lake to the Mekong River. However, riverbed lowering reduced the water discharge for both lake inflow and outflow, as well as reduced the unit stream power and sand transport capacity, which could potentially decrease sediment exchange between the lake and the Mekong River.

Riverbed lowering alters the distribution of water between the two downstream channels at the delta apex, directing more flow to the Mekong channel (see section 7.5.1). The modifications of the partitioning of the flow discharge can exacerbate riverbank erosion processes (Kleinhans et al., 2008), leading to bank collapses that pose risks to infrastructure and human lives in riparian communities, and contributing to increased land loss in the downstream delta.

Finally, the results also show that the land reclamation project downstream of the Chaktomuk Junction in the right bank of Mekong channel has a negligible impact on water discharge and water levels across all reaches of the Mekong delta apex (see section 7.5.1). This indicates that the hydraulic regime is primarily influenced by the large-scale features of the entire delta, rather than being significantly affected by localized disturbances. However, by narrowing the channels, the land reclamation project increases the sand transport capacity in the Mekong channel at the site. This may trigger erosion of the riverbed and the opposite channel banks at the project location, potentially causing long-term changes to the morphology of the Mekong channel and affecting the downstream Mekong channel in the delta.

7.7 Chapter Summary

In this chapter, 2D modelling for the apex of the Mekong delta, Chaktomuk Junction, has been developed and calibrated. This 2D model, along with 1D modelling for the entire Lower Mekong River and delta system, has been employed to simulate changes in the hydraulic regime and sand transport capacity across all reaches of the junction under scenarios of riverbed lowering and varying upstream monsoonal hydrograph conditions. The findings suggest that riverbed lowering leads to increased water discharge in the LMR, Mekong, and Bassac channels, reduces both inflow and outflow to the lake, and decreases unit stream power and sand transport capacity throughout the junction. Additionally, riverbed lowering alters the water distribution between the two downstream channels of the junction, directing more water flow into the larger channel (Mekong). While local land reclamation projects in the Mekong channels have a negligible impact on the hydraulic regime, they increase sand transport capacity in the Mekong channel at the site, potentially triggering erosion of the riverbed and opposite channel banks, and causing long-term changes in the morphology of the Mekong channel. The implications of these results for the long-term evolution of the delta are discussed.

However, limitations are noted regarding the 2022 bathymetric and 2022 modified scenarios. The irregular transitions observed between the single-beam echo sounder (SBES) and multibeam echo sounder (MBES) data arise from the combination of these datasets (Figure 7-12). These transitions are limited to relatively small mesh areas. Although this issue affects only certain mesh areas at the transition zones, it has been incorporated into the riverbed lowering scenarios, which account for an average riverbed lowering of 4.2 m observed across the entire model domain between the 2013 and 2022 scenarios.

Chapter 8. Conclusions and Recommendations

8.1 Summary

8.1.1 Introduction

River deltas sustain around 4.5% (339 million) of the world's population (Edmonds et al., 2020) and support vital ecosystem services crucial for livelihoods and well-being (Stanley and Warne, 1997; Ericson et al., 2006; Best and Darby, 2020). These low-lying areas face significant vulnerability to the effects of climate change and sea level rise, with additional pressures exerted by local resource exploitation (Vörösmarty et al., 2009; Overeem and Syvitski, 2009; Bendixen et al., 2019). Understanding how deltas evolve is crucial for making informed decisions and implementing management practices that can reduce the negative impacts of climate change, sea level rise and local resource exploitation.

In the last century, the demand for sand from river deltas and their adjacent regions has surged dramatically owing to population expansion, urbanization, and economic progress (Torres et al., 2017; Bendixen et al., 2019). Furthermore, the establishment of upstream hydropower dams has played a role in depriving sediment in numerous delta systems (Lehner et al., 2011; Xu et al., 2023). These combined effects, resulting in riverbed lowering (Huang et al., 2014; Arróspide et al., 2018; Koehnken et al., 2020, Vasilopoulos et al., 2021; Zhang et al., 2022), alongside alterations to hydrological conditions and sea level rise at the delta front, can alter delta functions and impact delta future sustainability (Vörösmarty et al., 2009; Syvitski et al., 2009; Best, 2019).

Despite numerous studies addressing delta-related issues caused by riverbed lowering, such as destabilizing riverbanks (Kondolf 1994; Hackney et al., 2020), increasing coastal erosion (Anthony et al., 2015), intensifying scouring processes that undermine embankments and other riverine infrastructure (Kondolf 1994; Best 2019), lowering of the water table (Chevallier, 2014; Best, 2019), exacerbating tidal ingress landward (Vasilopoulos et al., 2021), promoting saline intrusion (Eslami et al., 2021), degrading water quality and the health of fluvial and riparian ecosystems (Sreebha and Padmalal, 2011; Saviour, 2012; Venson et al., 2017; Torres et al. 2017). There is a substantial knowledge gap regarding the interplay of changes to water level, discharge and sediment transport capacity due to human-induced riverbed lowering and projected climate change. Understanding and predicting changes in these dynamics are essential for anticipating unforeseen hazards, including the implementation of flood protection measures (Alphen, 2016;

Oppenheimer et al., 2019; Binh et al., 2020), efficiently utilizing water for irrigation in agriculture (Hoang et al., 2016; Salem et al., 2021), maintaining navigation in delta channels (Paarlberg et al., 2015; Yang et al., 2017), salinity intrusion (Eslami et al., 2019), and ensuring the stability of river and coastal banks (Anthony et al., 2015, Hackney et al., 2020).

The present Thesis explores the effects of riverbed lowering resulting mainly from sand mining and sediment deprivation due to upstream damming on the hydraulic regime and sediment transport within the Lower Mekong Basin (LMB: Lower Mekong River (LMR) from Kratie to Chaktomuk, Tonle Sap Lake system (TSL) and Mekong delta (MD) stretch from Chaktomuk to the coastal zone (see Figure 3.1, Chapter 3). This study area serves as a prominent illustration of a delta system confronting a convergence of anthropogenic pressures. The overarching aim of this study is to quantify the relationship between riverbed lowering and the associated hydraulic patterns and the sediment transport capacity at the delta apex under various upstream water flux conditions and projected sea level rise. The main objectives of the study, and how they have been addressed, are summarised in Sections 8.1.2-8.1.4 below.

8.1.2 Impact of riverbed lowering on the hydraulic regime and sand transport capacity in a delta

8.1.2.1 Reduction in water levels

The reduction in water level driven by riverbed lowering is presented in two sections. Section 4.3.1, Chapter 4, involved quantifying the relationship between the observed mean water level and the corresponding mean water discharge during the 25-hour tidal oscillation within the VMD for each consecutive year from 2000 to 2021. Additionally, the "specific-gage" method (Blench, 1969) was used, which involves choosing a reference flow discharge and tracking the corresponding mean water level trend over time in the VMD from 2000 to 2021. Section 5.4.1.1 and Section 5.4.1.3, Chapter 5, uses 1D modelling to present changes in water level (mean, maximum, minimum) under various riverbed lowering scenarios for the entire LMB. The riverbed lowering scenarios include a Baseline historical scenario assuming zero riverbed lowering based on bathymetric data from 1998 (see Section 5.2.1, Chapter 5); a Contemporary scenario where channel bed levels have reduced by 3.06 m (σ = 2.03 m) based on observed differences between 1998 and 2018 bathymetries (see Section 5.2.1, Chapter 5); a Future scenario where channel bathymetry has reduced by an average of 5.92 m (σ = 2.84 m) based on projecting observed annual lowering rates from 1998-2018 bathymetries to the year 2038 (see Section 5.2.1, Chapter 5).

Observed and predicted results (see more detail in Section 4.3.1, Chapter 4 and section 5.4.1.1, section 5.4.1.3, Chapter 5 respectively) highlighted that there is a decreasing trend in mean water level driven by riverbed lowering across all periods throughout a year. The decrease in mean water level becomes more pronounced with greater riverbed lowering and distance inland, with the most significant decline occurring during the flood season compared to dry season, and the most notable rate of water level decrease occurs during the receding limb phase in flood season (see Figure 4-2 and Table 4-3, Chapter 4, and Figure 5-9 and Table 5-4, Chapter 5). The effect of riverbed lowering on extreme water levels (maximum and minimum) is similar to its impact on the mean water level. However, the decrease in maximum water levels is the highest compared to mean water levels, while the reduction in minimum water levels is the smallest (see details in Table 5-4 and Table 5-6, Chapter 5). It is noteworthy that seaward areas of both the Mekong and Bassac channels, extending from the coast up to approximately 100 km inland, show minimal reductions in mean, maximum and minimum water level (<0.2 m) under all of riverbed lowering scenarios (see Figure 5-9, Chapter 5). For instance, in the projected 2038 future scenario, the mean water level could decrease by up to 3.96 m (σ = 0.77 m) in the LMR, 1.31 m (σ = 1.10 m) in the Mekong channel, and 1.39 m (σ = 0.99 m) in the Bassac channel compared to the Baseline historical scenario from 1998 (see Table 5-4, Chapter 5 for more details).

These findings suggest both positive and negative implications for the future LMB system under anticipated decreases in water levels. On the positive side, lower water levels during the flood season are predicted to reduce flood risk in landward areas (located more than 100 km from the coast) (see Figure 5-9 and Figure 5-11, Chapter 5). This reduction can help alleviate extensive flooding caused by high fluvial discharge events, such as those during tropical storms and typhoons, which are expected to become more frequent in the future (IPCC, 2023; Wood et al., 2023). However, lowering water level presents also negative impacts for the LMB. Decreasing the connectivity between the river and its floodplain (see more detail in section 5.5.1, Chapter 5) may reduce the volume of water and sediment reaching secondary channels and the floodplain (Wohl et al., 2015) hindering the delta's ability to counteract subsidence and sea level rise (Milliman and Syvitski, 1992; Syvitski et al., 2009; Kondolf et al., 2022). It can negatively impact the floodplain ecosystem by harming vegetation, aquatic habitats, and other species, disrupting the delicate balance of riparian and floodplain flora, leading to a decline in plant biodiversity and the degradation of habitats essential for the survival of both terrestrial and aquatic species (Baran, et al., 2007; Wilcox et al., 2013; Arias at al., 2014; Stone et al., 2017; Mauricio et al., 2019). The reduction in water levels could potentially hinder the efficiency of irrigation systems (Hoang et al., 2016; Salem et al., 2021) and humper navigation in delta channels (Paarlberg et al., 2015; Yang et al., 2017). All of these impacts may ultimately drive a decrease in agricultural yields while increasing the costs associated with food production.

8.1.2.2 Expansion of tidal range

The increase in tidal range driven by riverbed lowering is presented in two sections: Section 4.3.2, Chapter 4, which involves quantifying the relationship between the observed tidal range and the corresponding mean water discharge during the 25-hour tidal oscillation within the VMD for each consecutive year from 2000 to 2021, using the observational record. And in section 5.2.1, Chapter 5, which uses the 1D model. These observed and predicted results highlight that riverbed lowering causes a propagation of the tidal signal further landward while the tidal range increases throughout a year. The increase in tidal range and tidal progression is more pronounced with increased riverbed lowering. For instance, in the Future scenario, the average tidal range is projected to increase by up to 0.41 m (σ = 0.23 m) in the LMR, 0.58 m (σ = 0.27 m) in the Mekong channel, and 0.59 m (σ = 0.29 m) in the Bassac channel compared to the baseline historical scenario (see section 5.4.1.2, Chapter 5 for more details). Tidal influences on river discharge play a significant role in modulating sediment supply rates to the coastal ocean, serving as a critical factor in delta formation and evolution (Galloway, 1975; Orton and Reading, 1993). An increasing tidal signal within the delta indicates a shift toward a tide-affected delta system, which refers to the increasing dominance of tidal forces in shaping the delta's hydrodynamics and sedimentary processes. Specifically, as tidal influences intensify, they alter sediment distribution and transport within the delta, promoting a more even deposition across its channel distributaries (Frings and Kleinhans, 2008; Sassi et al., 2011; Leonardi et al., 2013; Hoitink et al., 2017; Iwantoro et al., 2020). Tidal motion can counteract the reduced sediment transport capacity of the river, pushing sediment deposition seaward and potentially extending the delta's progradation into the coastal ocean (Hoitink and Jay, 2016). Furthermore, stronger tidal dynamics enhance the stability of delta bifurcations, reducing the likelihood of avulsions and channel migrations, and contributing to a more stable delta network (Frings and Kleinhans, 2008; Reitz et al., 2010; Sassi et al., 2011; Hoitink et al., 2017). However, as a low-lying area, the increasing tidal range could contribute to tidal flooding and storm surges in the delta, especially seaward (Chen and Liu, 2014; Araújo et al., 2021; Wood et al., 2023). Additionally, the increased tidal range could enhance backwater effects, leading to the expansion of salinity intrusion (Eslami, Hoekstra, Trung, et al. 2019), which impacts water management and agriculture in the downstream delta (Eslami et al., 2021; Thach et al., 2023). Moreover, the increased water level variation during the tidal cycle could drive riverbank instability (Gasparotto et al. 2023).

8.1.2.3 Reduction in Tonle Sap Lake's Flood Pulse

In recent times, there has been a notable shrinking of the TSL, largely linked to a reduction in water discharge from the Mekong River into the lake (Cochrane at al., 2014; Wen and Park, 2021; Chua et al., 2022; Morovati et al., 2023). The modelling findings here underscore the critical importance of riverbed lowering within the LMR and MD. For instance, for median water flux years, under Future scenario compared to Baseline historical scenario, the total volume of water flux to the TSL from Mekong River could decrease by up to 69 %. This would lead to a reduction of around 40 % in the maximum inundated area of the lake and a 59 % decrease in essential return flows to the Mekong River during the dry season. Consequently, there would be 21 % reduction in the dry season (December to May) water flux to the MD, and an additional to 26 billion m^3 of wet season flow (June to November) would be directed downstream into the MD during already high flood conditions (see more detail in section 6.2, Chapter 6).

Given the interplay between the hydraulic regime, ecosystem dynamics, and fish production in the TSL, the reduction in reverse flow from the main Mekong River to the lake has the potential to unleash a variety of detrimental socio-ecological repercussions, impacting millions of residents in Cambodia who rely on the TSL for their livelihoods. For instance, the decreased water volume from the Mekong River entering the TSL could precipitate a decline in the migratory fish population journeying from the main Mekong River to the TSL and vice-versa (MRC 2002; Baran et al., 2007; Chea et al., 2020; Chevalier et al., 2023), potentially restricting the influx of suspended sediment, nutrients, aquatic organisms, flora, and fauna from the main river to the TSL, thereby impacting the economic value of the surrounding areas crucial for agriculture and fish production (Baran, et al., 2007; Arias at al., 2014; Arias et al., 2019; Chan et al., 2020). The reduction in water level and inundation areas in the TSL in both magnitude and timing result in a loss of biodiversity, adversely affecting the habitats of amphibians, reptiles, fishes, birds, and mammals residing in the flood areas (Campbell et al., 2006; Mauricio at al., 2014; Lohani et al., 2020). The reduction in the volume of water supplied by the TSL to the delta during the dry season will create new water-related challenges in the MD. The decreased dry season flows will affect fresh water availability for rice cultivation and diminish the feasibility of aquaculture activities throughout the delta. This will be notably exacerbated by a significant increase in tidal ingress and saline intrusion (Vasilopoulos et al., 2021; Bricheno etal., 2021). Additionally, the increased wet season flow from the TSL into the MD during a time of already elevated flood levels could potentially exacerbate flood hazards in the MD.

8.1.2.4 Reduction in sediment transport capacity

The 1D modelling results indicate that the average observed riverbed lowered by 1.7 m (σ = 1.52 m) in the LMB between 2013 and 2022, leads to a reduction in the unit stream power and diminishes the river's sediment transport capacity across all reaches of the delta apex. In more detail, the 2022 bathymetry scenarios show that annual unit stream power decreases by up to 15 %, 24 %, 50 % and 29 % in the LMR, Mekong, Bassac channels, and Tonle Sap Rivers, respectively, compared to the 2013 bathymetry scenarios (see more detail in Figure 7-15, Chapter 7). Given sediment flux from the upstream Mekong River has already decreased significantly due to damming, and this trend is expected to persist, further limiting sediment availability and making the remaining sediment volumes increasingly vital (Kondolf, et al., 2014; Bussi et al., 2021). However, the reduced sediment transport capacity caused by riverbed lowering may allow sediment to accumulate locally, acting as a self-regulating mechanism to mitigate further riverbed lowering. This local accumulation, however, reduces the amount of sediment transported downstream, exacerbating the sediment deficit in the downstream delta. As a consequence, the reduced sediment supply further limits the delta's natural ability to recover from the ongoing riverbed lowering (for more details, see Section 7.6, Chapter 7).

In addition, the 2D simulation results highlighted that under the 2022 bathymetry scenario, the sand transport capacity at the apex of the delta is 7.2 million tons (ranging from 3.7 million to 11.3 million tons) in the Lower Mekong River and 11.2 million tons (ranging from 6.3 million to 20.1 million tons) for the combined Mekong and Bassac channels during fresh water flux years with a 37 % (ranging from 88 % to 7 %) flood exceedance probability over the period from 2000 to 2021. This sand transport range is considerably smaller than the estimated volume of sand extracted from this reach of the Lower Mekong River and its delta. In 2020 alone, sand extraction in Cambodia was estimated at approximately 59 million tons (Hackney et al., 2021), while Gruel et al., (2022) suggested a volume of 67.2 million tons yr^{-1} for sand mining in the VMD from 2015 to 2020. Consequently, the sand transport at the apex of the delta, assuming a sufficient upstream supply, appears to be less than one-tenth of the current sand extraction in the entire Lower Mekong River and its delta.

This excessive sand extraction, which surpasses the natural sand supply and reduces the river's capacity to recover from riverbed lowering, could worsen the sediment deficit in the delta. This may lead to increased delta subsidence (Syvitski et al., 2009; Kondolf et al., 2022), increases the disconnection between the river and its floodplain, heightens the risk of tidal flooding in the downstream delta, and riverbank instability (Hackney et al., 2020), potentially compromising nearby riverine structures (Kondolf 1994; Best 2019) and endangering communities along the riverbanks (Bendixen et al., 2019). Additionally, it contributes to coastal land loss (Anthony et al. 2015), exacerbates landward tidal ingress (Vasilopoulos et al., 2021) and promotes saline intrusion (Eslami et al., 2019).

Finally, sediment deficits and lowered riverbed elevations can decrease the likelihood of delta avulsions (Slingerland and Smith, 2004). Avulsions are crucial for redistributing sediments across the delta plain, supporting the maintenance of deltaic landforms and mitigating local subsidence (Mackey and Bridge, 1995; Slingerland and Smith, 2004; Reitz and Jerolmack, 2012). A decline in avulsion frequency disrupts the natural processes that replenish and sustain delta ecosystems, further jeopardizing the long-term stability and resilience of deltas under the combined pressures of human activity and climate change.

The effects of riverbed lowering on the hydraulic regime and sediment transport capacity in the Mekong Delta are summarized in Figure 8-1 below.

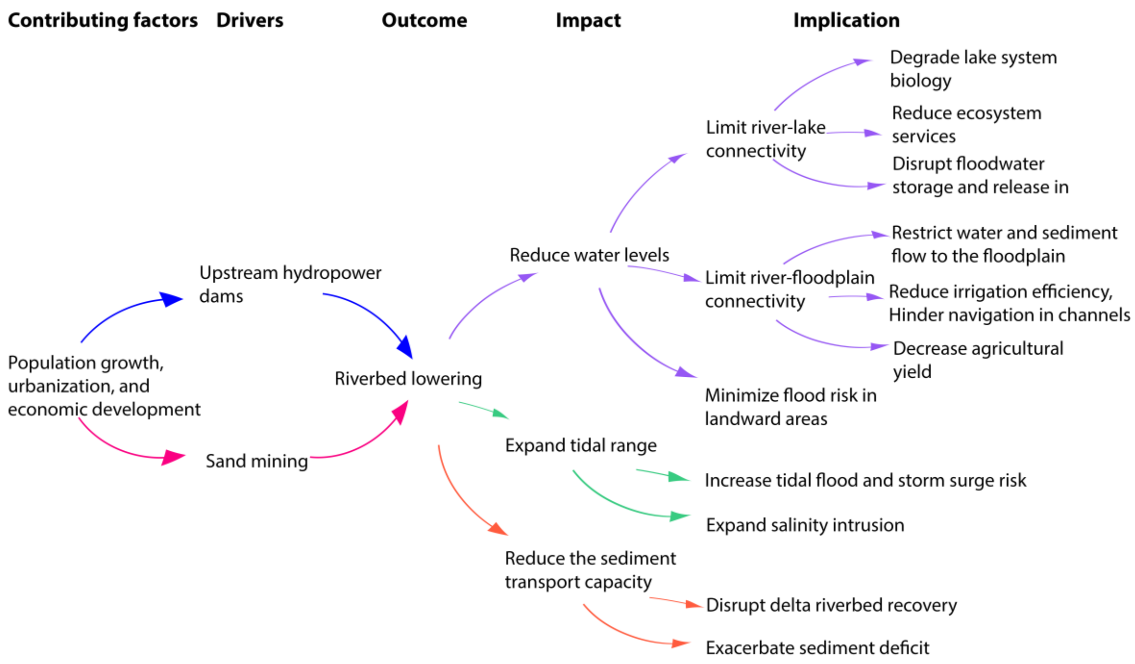

Figure 8-1. The conceptual figure illustrates the key drivers of riverbed lowering, their impacts on the hydraulic regime and sediment transport capacity, and their broader implications

8.1.3 Impact of sea level rise in the water level regime (water level and tidal range)

The 1D modelling results indicate that sea level rise leads to an increasing trend in water levels (mean, maximum, and minimum) in the LMB. This upward trend gradually diminishes inland, with the most increases occurring during the dry season compared to the flood season (see more details in Section 5.4.2.1 and Section 5.4.2.3, Chapter 5). The increase in minimum water levels is higher compared to the mean water levels, while the reduction in maximum water levels is the smallest. For instance, in the 1.0 m SLR scenarios, the mean water level rises by up to 0.27 m (σ = 0.18 m), 0.85 m (σ = 0.13 m), and 0.80 m (σ = 0.17 m) in the LMR, Mekong, and Bassac channels, respectively, compared to the 0 m SLR scenario (See more detail in table 5-7, Chapter 5). Sea level rise also caused small increase in tidal range (< 0.35 m; in 2.5 m SLR scenarios) and tidal expansion (< 318 km; in 2.5 m SLR scenarios) in LMR and Mekong delta. The slight rise in tidal range in the LMB system driven by sea level rise enhances connectivity between the main Mekong and Bassac channels and their side channel network and floodplains within the delta, which play a role in absorbing a part of the tidal energy (Eslami et al., 2019) (see more detail in section 5.5, Chapter 5).

The increase in water level could potentially increase flooding in the delta (Vörösmarty et al., 2009; Kondolf et al., 2022), which areas are shrinking due to sediment deficits (Kondolf et al., 2022) and land subsidence driven by unsustainable groundwater, hydrocarbon, and oil extraction in the delta (Erkens et al., 2015; Best and Darby, 2020; Minderhoud et al. 2020). Additionally, sea level rise causes the submersion of terrestrial land, leading to the direct transfer of coastal sediment into the ocean. This process deepens near-shore areas, intensifies coastal erosion, and contributes to the depletion of wetlands and mangroves (Bucx et al., 2010; EPA, 2016; Syvitski et al., 2022), as well as altering wetland communities and their ecosystem functions (Herbert et al., 2015).

8.1.4 Riverbed lowering combined with Sea-level rise alters the water level and tidal expansion in MD

Under the combined influence of projected future riverbed lowering and sea level rise, water levels are expected to be higher in seaward reaches and lower in landward areas (Figure 8-2). The specific location (km point) where this transition from an increase to a decrease occurs varies between scenarios of riverbed lowering and sea level rise, as well as across different parts of the hydrograph (see more details in Section 5.4.3, Chapter 5). Higher levels of riverbed lowering result in this transition occurring further seaward, while increasing sea levels tend to shift the transition point further landward. For further detail, the transition point for the

Contemporary scenario and the Future 0.5 m and 1.0 m SLR scenarios appears to occur at approximately 200 km during the dry season and around 150 km during the flood season. However, an SLR of 2.5 m seems to shift the transition point further landward, occurring at about 400 km during the dry season and around 200 km during both phases of the flood season (Figure 8-2, see more detail in Section 5.4.3, Chapter 5). The changes in the water level regime within the delta, caused by both riverbed lowering and sea level rise, have the potential to alter the flooding patterns in the delta. Specifically, the upstream region of the delta is anticipated to witness a decrease in flooding levels predominantly due to riverbed lowering. This reduction in water level becomes less pronounced towards the seaward direction. Conversely, the downstream delta is confronted with potential inundation risks primarily driven by a combination of sea level rise and an increase in tidal range caused by riverbed lowering. Understanding the future dynamics of flooding is crucial for decision-making for flood management and to minimize its societal impacts. These insights are highly significant for spatial planning and local authorities, offering guidance on implementing measures to mitigate flood damage and ensuring the long-term stability and development of the delta.

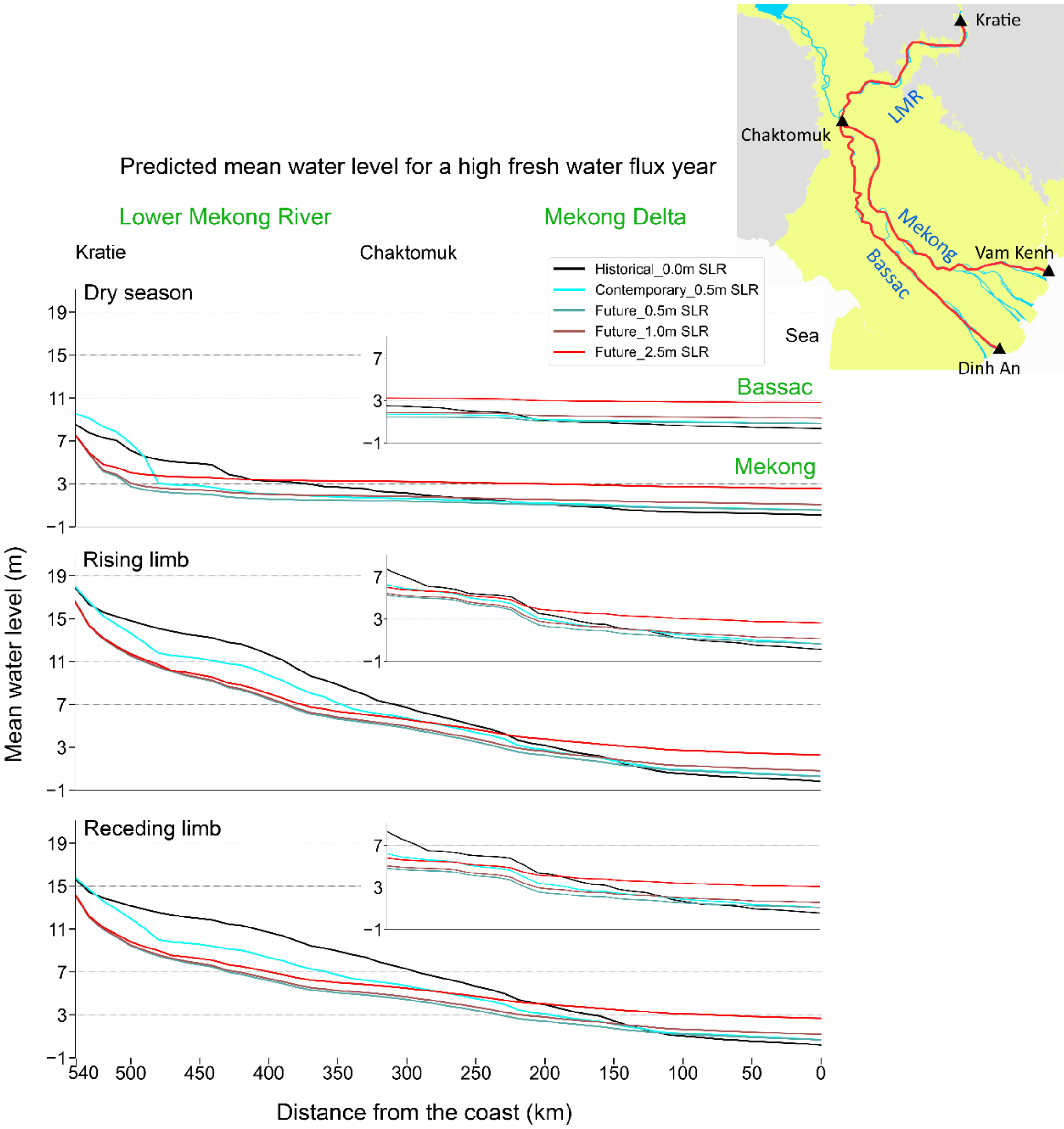

Figure 8-2. The longitudinal profile of mean water level along the LMR, Mekong and Bassac distributary delta channels under various future projected scenarios of riverbed lowering and sea level rise adopted from Figure 5-5, Chapter 5. These scenarios inducing for Baseline historical bathymetry with sea level rise of 0 m, Contemporary bathymetric with sea level rise of 0.5 m and Future bathymetric with sea level rise of 0.5 m, 1.0 m and 2.5 m scenarios under high water flux. The main panel focuses on the LMR and Mekong channel, while the insert panel shows the Bassac channel. All water levels are referenced to Hon Dau MSL.

8.2 Limitations

The present study employed 1D and 2D modelling to assess the effects of riverbed lowering and sea level rise on the hydraulic and sand transport capacity of the delta system. While the robustness of the modelling approach is crucial to this analysis, there are limitations exist in model setup, calibration, validation and model scenarios due to the various data used.

Regarding the riverbed bathymetry used for the 1D modelling, the DEM generated from the SBES dataset using Kriging interpolation may introduce uncertainties in elevation. These uncertainties arise from both the interpolation process and the natural variability in riverbed morphology, such as scour and fill features (Heritage et al., 2009; Milan et al., 2011; Glenn et al., 2016). In addition, while the 1998 bathymetric dataset offers the broadest coverage, the other datasets for channel bed elevations, although extensive, are fragmented both spatially and temporally, being sourced from various origins. This fragmentation complicates the quantification of temporal changes in riverbed morphology due to anthropogenic activities, leading to some necessary assumptions. For the 2D model, the high-resolution riverbed bathymetry data obtained via MBES covers only a limited area around the Chaktomuk Junction. Additionally, converting MBES bathymetry data from the EGM 2008 geoid to the Hon Dau MSL vertical datum may introduce minor inaccuracies, with a range of approximately 0.10 m (σ = 0.05 m). Furthermore, using boundary data extracted from the 1D model for the 2D model could increase uncertainties in the results.

The hydrological data, including flow discharge, flow velocity, and water level recordings, provide valuable insights but also pose research limitations. The water level archive covers the entire area of interest and spans many decades, but Cambodia data is limited to daily and twice-daily measurements. Similarly, although flow discharge records for the VMD are available at an hourly resolution, long-term discharge data for Cambodia is only measured at Kratie and recorded daily. The daily water discharge at Kratie is derived from a rating curve (stage-discharge relationship) based on daily water level data, which introduces uncertainties into the discharge calculations. The velocity data is collected at Chaktomuk Junction only twice, which may limit the calibration and validation efficiency of the 2D modelling.

Additionally, while the impact of changing monsoon intensity and frequency driven by climate change, particularly with regard to extremely high-water discharge and storm surges, is not included in this work, it is recognized as a factor that could influence the results

8.3 Recommendations and Future works

The study has highlighted challenges in the Lower Mekong Basin caused by anthropogenic-driven riverbed lowering, resulting from a combination of factors, including the interplay of sand mining and sediment starvation due to upstream damming as well as sea level rise.

However, regulating and enforcing international laws on sand mining is challenging in large river basins like the Mekong, which extends across multiple countries (Bendixen et al., 2019; Hackney, 2024). Despite efforts to address unsustainable sand mining, including the Vietnamese government's ban on the export of river sand since 2000 and Cambodia's claim to have regulated or "banned" sand exports in 2009 (Bravard et al., 2013), these efforts focus on international exports, but neglect the ever increasing national demand for sand driving increased extraction. Moreover, with the challenges posed by population growth, anticipated urbanization, and expanding industries, the demand for increased sand mining output is expected to persist (WWF, 2018; United Nations, 2018; UNEP 2019, Bendixen et al., 2019). Consequently, it is necessary to take enforcement measures to reduce natural sand consumption through a variety of methods to alleviate the demand for natural sand, ensuring a balance between meeting essential requirements and sustaining socio-economic development. A number of measures to address sustainable sand mining, such as utilizing of construction materials as substitutes for sand, exploration and utilization of artificial sand, tapping into passive sand sources (deposits in floodplain sediments and sand trapped behind dams), encouraging the reuse of sand, implementing monitoring systems for sand mines (Bendixen et al., 2019), and promoting education about the impacts of sand mining (Shrestha, 2013; Koehnken et al., 2020). Additionally, a sustainable approach to sand mining is deemed essential, emphasizing the need to consider not only local but also large basin-scale impacts (Hackney et al., 2021).

To mitigate the impact of upstream damming on delta in terms of environmental and social consequences, it is crucial to evaluate proposed dam sites within the framework of sustaining a range of ecosystem services and biodiversity conservation. This assessment should be based on a comprehensive analysis of multiple factors, including hydrology, sediment dynamics, ecosystem productivity, biodiversity, fisheries, and the impact on rural livelihoods throughout watersheds. (IHA, 2010; Finer and Jenkins, 2012; Winemiller et al., 2016). Additionally, there is a need to explore cleaner forms of energy that have less environmental impact to alleviate the pressure on hydroelectric energy. Furthermore, it is necessary to implement cutting-edge technologies like remote sensing techniques, which could effectively monitor hydrological, sediment parameters in the river, such as, monitoring water discharge (Gleason, et al., 2017), water levels (Biancamaria et al., 2016), suspended sediment dynamics (Park and Latrubesse 2014), as well as mapping and monitoring sand mining activities (Hackney et al., 2021). Providing comprehensive measures across vast spatial and temporal scales, allowing public access for informed decision-making (Best, 2019). This strategy is especially beneficial in regions with limited resources or in international river basins where watersheds and watercourses traverse political boundaries, often becoming areas of significant political tension and conflict on a global scale (Gleason and Hamdan, 2017). Finally, the creation of regulatory frameworks in transboundary regions is crucial to tackling these challenges. This can be accomplished by establishing transboundary river commissions aimed at sharing and efficiently utilizing water resources, while collaboratively working to protect this vital resource (Hackney, 2024).

In addition to the aforementioned methods, effectively mitigating and reversing the riverbed lowering that disrupts the TSR reverse flow could involve facilitating the release of sediment currently trapped behind dams. This can be achieved through techniques like flushing exercises (Kondolf et al., 2014; Laksitaningtyas et al., 2022; Lai et al., 2024). One example is the "Turbidity Current Venting" method (Kondolf et al., 2014), which uses high-sediment turbidity currents to create a denser current that moves along the reservoir bottom towards the dam, flushing out sediment during the flood season. This method has been used in the Yellow River (IRTCES, 2005; Hu et al., 2012; Kondolf et al., 2014). Applying this method to existing or future dams on the Mekong River could increase the influx of water, sediments, and nutrients into the TSL.

For future decision-making, it is essential to consider developing infrastructure within the delta, such as channels, dykes, sluice gates, and pumping stations. These should support agricultural development while minimizing environmental impacts and improving sediment trapping for soil fertilization. For instance, sluices could be opened at optimal times during the flood season to maximize sediment flow to the floodplain (Hung, 2011). This is particularly important given the potential reduction in water and sediment flow to the delta floodplain due to riverbed lowering. Furthermore, the standards design of these structures (including culvert, pump, canal bottoms, and dike crests) should account for water level reductions caused by riverbed lowering to prevent waste and maximize efficiency.

To mitigate the impact of future tidal and storm surge inundation resulting from rising sea levels and increased tidal range due to riverbed lowering in the downstream delta, it's vital considering standards design to build and upgrade roads, dyke and tidal barrier systems, taking into account these escalating inundation factors in the region. This is particularly critical in the Vietnamese Mekong Delta, where major cities are situated along the main channels, including Can Tho, Dai Ngai (50 km downstream from Can Tho) in the Basac channels, Vinh Long (My Thuan), My Tho, and Ben Tre (60 km downstream from Vinh Long) in the Mekong channels.

Although the research herein has focused on the LMB, the issue of sediment deficit primarily by unsustainable sand mining and upstream dams, is similar to other major river deltas experiencing swift economic development (Vörösmarty et al., 2009; Giosan et al., 2014; Best, 2019), such as the Pearl River Delta (Lu et al., 2007), Yellow River Delta (Chu, 2014), and the

Ganges Delta (Daham et al., 2024). The implications of these trends are significantly in terms of the delta's future sustainability and its ability to adapt to ongoing and future changes in river bed levels, upstream water flux variation and sea level rise, which include a potential reduction in the level of flooding in landward parts of the delta system but very significant consequences associated with tidal flood hazard seaward, an elevated risk of storm surge hazards as well as associated impacts such as the disconnection of channels from floodplains, decreased efficiency of infrastructure and irrigation works, shortage of water supply during the dry season as well as the increased likelihood of riverbank instability and water salinization. Therefore, It is necessary to take enforcement measures to reduce natural sand consumption to alleviate the demand for natural sand, ensuring a balance between meeting essential requirements and sustaining socio-economic development (Biancamaria et al., 2016; Gleason, et al., 2017; Gleason and Hamdan, 2017; Bendixen, et al., 2019; Best, 2019; Hackney et al. 2021).

Building on this study, several aspects that require further investigation can be undertaken here.

- ✓ Riverbed lowering could drive tidal expansion within the delta system, making the delta more dominated by tidal influences. This could potentially change the sediment transport regime, including the deposition and erosion patterns. Additionally, sea level rise, by increasing the downstream water level, could potentially reduce the water slope, thereby altering sediment transport in the delta. Therefore, a comprehensive study of sediment transport, encompassing both suspended sediment and sand in the delta system, is essential. This study should aim to understand sediment transport under various anthropogenic impacts, including upstream changes due to climate change and damming, local sand mining, and sea level rise. Understanding these sediment transport dynamics is crucial for local governments to make informed decisions regarding long-term delta sustainability, water management, and the protection of river and coastal banks.
- ✓ The potential reduction in flood hazards upstream in the delta system due to riverbed lowering, along with the potential increase in flood hazards downstream due to sea level rise, have been highlighted. However, the impact of climate change-driven changes in monsoon intensity and frequency, particularly concerning extremely high-water discharge and storm surges, is not included in this study. A comprehensive evaluation of the full range of flood risk changes—covering hazard, vulnerability, and exposure (such as through flood hazard mapping)—should be addressed in future work. Such an assessment is essential for local governments to make informed decisions regarding flood protection.

✓ Additionally, changes in water partitioning at the delta apex due to riverbed lowering resulting in increased flow towards the greater channel, combined with the effects of sea level rise, could alter the distribution of water and sediment as well as affect the stability of delta bifurcations. Since these bifurcations are crucial to the long-term morphology of the delta, a comprehensive study to evaluate the future stability of the bifurcation system is recommended.

Reference List

Ackers, P., and W. R. White. 1973. “Sediment Transport: New Approach and Analysis.” *Journal of the Hydraulics Division*. doi: https://doi.org/10.1061/JYCEAJ.0003791.

Adams, K. 2017. “Hydropower Status Report.” *International Hydropower Association*.

Alabyan, A. M., and S. V. Lebedeva. 2018. “Flow Dynamics in Large Tidal Delta of the Northern Dvina River: 2D Simulation.” *Journal of Hydroinformatics* 20:798–814. doi: 10.2166/hydro.2018.051.

Alphen, V. J. 2016. “The Delta Programme and Updated Flood Risk Management Policies in the Netherlands.” *Journal of Flood Risk Management* 310–19. doi: 10.1111/jfr3.12183.

Alvarado-Aguilar, D., J. A. Jiménez, and R. J. Nicholls. 2012. “Flood Hazard and Damage Assessment in the Ebro Delta (NW Mediterranean) to Relative Sea Level Rise.” *Natural Hazards* 62:1301–21. doi: 10.1007/s11069-012-0149-x.

An, Chenge, Hongwei Fang, Li Zhang, Xinyue Su, Xudong Fu, He Qing Huang, Gary Parker, Marwan A. Hassan, Nooreen A. Meghani, Alison M. Anders, and Guangqian Wang. 2022. “Poyang and Dongting Lakes, Yangtze River: Tributary Lakes Blocked by Main-Stem Aggradation.” *Proceedings of the National Academy of Sciences* 119(30):1–7. doi: 10.1073/pnas.2101384119.

Anthony, E. J., G. Brunier, M. Besset, M. Goichot, P. Dussouillez, and V. L. Nguyen. 2015. “Linking Rapid Erosion of the Mekong River Delta to Human Activities.” *Scientific Reports* 5. doi: 10.1038/srep14745.

Araújo, P. V. N., V. E. Amaro, L. S. Aguiar, C. C. Lima, and A. B. Lopes. 2021. “Tidal Flood Area Mapping in the Face of Climate Change Scenarios: Case Study in a Tropical Estuary in the Brazilian Semi-Arid Region.” *Natural Hazards and Earth System Sciences* 21(11):3353–66. doi: 10.5194/nhess-21-3353-2021.

Arias, M. E., T. Cochrane, and V. Elliott. 2013. “Modelling Future Changes of Habitat and Fauna of the Tonle Sap Wetland of the Mekong.” *Environmental Conservation*. doi: 10.1017/S0376892913000283.

Arias, M. E., G. W. Holtgrieve, P. B. Ngor, T. D. Dang, and T. Piman. 2019. “Maintaining Perspective of Ongoing Environmental Change in the Mekong Floodplains.” *Current Opinion in Environmental Sustainability* 37:1–7. doi: 10.1016/j.cosust.2019.01.002.

Arias, M. E., T. Piman, H. Lauri, T. A. Cochrane, and M. Kummu. 2014. “Dams on Mekong Tributaries as Significant Contributors of Hydrological Alterations to the Tonle Sap Floodplain in Cambodia.” *Hydrology and Earth System Sciences* 5303–15. doi: 10.5194/hess-18-5303-2014.

Arnell, N. W., and S. N. Gosling. 2016. “The Impacts of Climate Change on River Flood Risk at the Global Scale.” *Climatic Change* 134:387–401. doi: 10.1007/s10584-014-1084-5.

Arns, A., S. Dangendorf, J. Jensen, S. Talke, J. Bender, and C. Pattiaratchi. 2017. “Sea-Level Rise Induced Amplification of Coastal Protection Design Heights.” *Scientific Reports* 7:1–9. doi: 10.1038/srep40171.

Arróspide, F., L. Mao, and C. Escauriaza. 2018. "Morphological Evolution of the Maipo River in Central Chile : Influence of Instream Gravel Mining." *Geomorphology* 306:182–97. doi: 10.1016/j.geomorph.2018.01.019.

Ashton, A. D., and L. Giosan. 2011. "Wave - Angle Control of Delta Evolution." *Geophysical Research Letters* 38:1–6. doi: 10.1029/2011GL047630.

Asselman, N. E. M., H. Middelkoop, and P. M. V. Dujk. 2003. "The Impact of Changes in Climate and Land Use on Soil Erosion, Transport and Deposition of Suspended Sediment in the River Rhine." *Hydrological Processes* 17:3225–44. doi: 10.1002/hyp.1384.

Baar, A. W., D. J. Smit, W. S. J. Uijttewaal, and M. G. Kleinhans. 2018. "Sediment Transport of Fine Sand to Fine Gravel on Transverse Bed Slopes in Rotating Annular Flume Experiments." *Water Resources Research* 54:19–45. doi: 10.1002/2017WR020604.

Bagnold, R. A. 1960. "Sediment Discharge and Stream Power." *Geological Survey Circular 421*.

Bagnold, R. A. 1980. "Empirical Correlation of Bedload Transport Rates in Flumes and Natural Rivers." *Proceedings of The Royal Society of London* 372:453–73.

Balica, S., Q. Dinh, I. Popescu, T. Q. Vo, and D. Q. Pham. 2014. "Flood Impact in the Mekong Delta, Vietnam." *Journal of Maps* 10:257–68. doi: 10.1080/17445647.2013.859636.

Bao, Shiyu, Wei Zhang, Jie Qin, Jinhai Zheng, Hui Lv, Xi Feng, Yanwen Xu, and A. J. F. Hoitink. 2022. "Peak Water Level Response to Channel Deepening Depends on Interaction Between Tides and the River Flow." *Journal of Geophysical Research: Oceans* 127(4). doi: 10.1029/2021JC017625.

Baran, E. 2010. *Fisheries Sections in the Strategic Environmental Assessment of Mekong Mainstream Dams*.

Baran, E., P. Starr, and Y. Kura. 2007. "Influence of Built Structures on Tonle Sap Fisheries." *Cambodia National Mekong Committee and the WorldFish Center. Phnom Penh, Cambodia*.

Barnes, H. H. 1969. "Roughness Characteristics of Natural Channels." *US Geological Survey* 7(3):354.

Becker, M., F. Papa, M. Karpytchev, C. Delebecque, Y. Krien, J. U. Khan, V. Ballu, F. Durand, G. L. Cozannet, A. K. M. S. Islam, S. Calmant, and C. K. Shum. 2020. "Water Level Changes, Subsidence, and Sea Level Rise in the Ganges-Brahmaputra-Meghna Delta." *Proceedings of the National Academy of Sciences of the United States of America* 117(4):1867–76. doi: 10.1073/pnas.1912921117.

Bendixen, M., J. L. Best, C. Hackney, and L. L. Iversen. 2019. "Time Is Running out for Sand." *Nature* 571(July):29–31. doi: 10.1038/d41586-019-02042-4.

Benjankar, R. 2009. "Quantification of Reservoir Operation-Based Losses to Floodplain Physical Processes and Impact on the Floodplain Vegetation at Kootenai River, USA."

Benjankar, R., D. Tonina, and J. Mckean. 2014. "One-Dimensional and Two-Dimensional Hydrodynamic Modeling Derived Flow Properties: Impacts on Aquatic Habitat Quality Predictions." *Earth Surface Processes and Landforms*. doi: 10.1002/esp.3637.

Bertoldi, W., and M. Tubino. 2007. "River Bifurcations: Experimental Observations on Equilibrium Configurations." *Water Resources Research* 43(10):1–10. doi: 10.1029/2007WR005907.

Best, J. 2019. "Anthropogenic Stresses on the World's Big Rivers." *Nature Geoscience* 12:7–21. doi: 10.1038/s41561-018-0262-x.

Best, J., and S. E. Darby. 2020. "The Pace of Human-Induced Change in Large Rivers: Stresses, Resilience, and Vulnerability to Extreme Events." *One Earth* 2(6):510–14. doi: 10.1016/j.oneear.2020.05.021.

Betsholtz, Alexander. 2017. "Potentials and Limitations of 1D, 2D and Coupled 1D-2D Flood Modelling in HEC-RAS."

Bhattacharya, J. P., and L. Giosan. 2003. "Wave-Influenced Deltas : Geomorphological Implications for Facies Reconstruction." *Sedimentology* 50:187–210. doi: 10.1046/j.1365-3091.2003.00545.x.

Biancamaria, S., D. P. Lettenmaier, and T. M. Pavelsky. 2016. "The SWOT Mission and Its Capabilities for Land Hydrology." *Surveys in Geophysics* 37:307–37. doi: 10.1007/s10712-015-9346-y.

Binh, D. V., S. A. Kantoush, M. Saber, N. P. Mai, S. Maskey, D. T. Phong, and T. Sumi. 2020. "Long-Term Alterations of Flow Regimes of the Mekong River and Adaptation Strategies for the Vietnamese Mekong Delta." *Journal of Hydrology: Regional Studies* 32. doi: 10.1016/j.ejrh.2020.100742.

Binh, D. V., S. A. Kantoush, T. Sumi, N. P. Mai, T. A. Ngoc, L. V. Trung, and T. D. An. 2021. "Effects of Riverbed Incision on the Hydrology of the Vietnamese Mekong Delta." *Hydrological Processes* 35:1–21. doi: 10.1002/hyp.14030.

Black, K., T. J. Tolhurst, D. M. Paterson, and S. E. Hagerthey. 2002. "Working with Natural Cohesive Sediments Working with Natural Cohesive Sediments." *Journal of Hydraulic Engineering*. doi: 10.1061/(ASCE)0733-9429(2002)128:1(2).

Blench, T. 1969. *Mobile-Bed Fluviology: A Regime Theory Treatment of Canals and Rivers for Engineers and Hydrologists*. University.

Bonheur, N., and D. B. Lane. 2002. "Natural Resources Management for Human Security in Cambodia's Tonle Sap Biosphere Reserve." *Environmental Science and Policy* 5:33–41. doi: S1462-9011(02)00024-2.

Boretti, A. 2020. "Implications on Food Production of the Changing Water Cycle in the Vietnamese Mekong Delta." *Global Ecology and Conservation* 22. doi: https://doi.org/10.1016/j.gecco.2020.e00989.

Brauer, J. E. 2009. "The Limitations of Using Specific Gage Analysis to Analyze the Effect of Navigation Structures on Flood Heights in the Middle Mississippi River." *Smart River' 21* (August):1–14.

Bravard, J. P., M. Goichot, and S. Gaillot. 2013. "Geography of Sand and Gravel Mining in the Lower Mekong River." *EchoGéo* 0–20. doi: 10.4000/echogeo.13659.

Bricheno, L. M., J. Wolf, and Y. Sun. 2021. “Saline Intrusion in the Ganges-Brahmaputra-Meghna Megadelta.” *Estuarine, Coastal and Shelf Science* 252. doi: 10.1016/j.ecss.2021.107246.

Bridge, J. S., and J. L. Best. 1988. “Flow , Sediment Transport and Bedform Dynamics over the Transition from Dunes to Upper-Stage Plane Beds : Implications for the Formation of Planar Laminae.” *Sedimentology* 753–63.

Brozović, N., D. W. Burbank, and A. J. Meigs. 1997. “Climatic Limits on Landscape Development in the Northwestern Himalaya.” *Science* 276:571–74. doi: 10.1126/science.276.5312.571.

Brunier, G., E. J. Anthony, M. Goichot, M. Provansal, and P. Dussouillez. 2014. “Recent Morphological Changes in the Mekong and Bassac River Channels, Mekong Delta: The Marked Impact of River-Bed Mining and Implications for Delta Destabilisation.” *Geomorphology* 224:177–91. doi: 10.1016/j.geomorph.2014.07.009.

Bryant, M., P. Falk, and C. Paola. 1995. “Experimental Study of Avulsion Frequency and Rate of Deposition.” *Geology* 23(4):365–68. doi: 10.1130/0091-7613(1995)023<0365:ESOAFA>2.3.CO;2.

Bucx, T., M. Marchand, B. Makaske, and C. V. .. Guchte. 2010. *Comparative Assessment of the Vulnerability and Resilience of 10 Deltas– Synthesis Report*.

Buschman, F. A., A. J. F. Hoitink, M. Van Der Vegt, and P. Hoekstra. 2010. “Subtidal Flow Division at a Shallow Tidal Junction.” *Water Resources Research* 46:1–12. doi: 10.1029/2010WR009266.

Bussi, G., S. E. Darby, P. G. Whitehead, L. Jin, S. J. Dadson, H. E. Voepel, G. Vasilopoulos, C. R. Hackney, C. Hutton, T. Berchoux, D. R. Parsons, and A. Nicholas. 2021. “Impact of Dams and Climate Change on Suspended Sediment Flux to the Mekong Delta.” *Science of the Total Environment* 755. doi: 10.1016/j.scitotenv.2020.142468.

Cabezas, A., M. Angulo-Martínez, M. Gonzalez-Sanchís, J. J. Jimenez, and F. A. Comín. 2010. “Spatial Variability in Floodplain Sedimentation: The Use of Generalized Linear Mixed-Effects Models.” *Hydrology and Earth System Sciences* (7):1655–68. doi: 10.5194/hess-14-1655-2010.

Caldwell, L. R. 2013. “The Effect of Grain Size on River Delta Process and Morphology.”

Caldwell, R. L., and D. A. Edmonds. 2014. “The Effects of Sediment Properties on Deltaic Processes and Morphologies: A Numerical Modeling Study.” *Journal of Geophysical Research : Earth Surface* 961–82. doi: 10.1002/2013JF002965.

Cambodia. 2013. *Census of Agriculture of the Kingdom of Cambodia 2013*.

Campbell, I. C., C. Poole, W. Giesen, and J. Valbo-jorgensen. 2006. “Species Diversity and Ecology of Tonle Sap Great Lake , Cambodia.” *Aquatic Sciences* 68:355–73. doi: 10.1007/s00027-006-0855-0.

Canestrelli, A., W. Nardin, D. Edmonds, S. Fagherazzi, and R. Slingerland. 2014. “Importance of Frictional Effects and Jet Instability on the Morphodynamics of River Mouth Bars and Levees.” *Journal of Geographical Sciences: Oceans* 119:1–14. doi: 10.1002/2013JC009312.

Cardinale, B. J., J. E. Duffy, A. Gonzalez, D. U. Hooper, C. Perrings, P. Venail, A. Narwani, G. .. Mace, D. Tilman, D. A. Wardle, A. P. Kinzig, G. C. Daily, M. Loreau, J. B. Grace, A. Larigauderie, Srivastava. D, and S. Naeem. 2012. “Biodiversity Loss and Its Impact on Humanity Bradley.” *Nature* 486:59–67. doi: http://dx.doi.org/doi:10.1038/nature11148.

Carter, T. R., M. Hulme, J. F. Crossley, S. Malyshev, M. G. New, M. E. Schlesinger, and H. Tuomenvirta. 2000. *Climate Change in the 21st Century - Interim Characterizations Based on the New IPCC Emissions Scenarios*.

CEIC. 2010. “Cambodia Aquaculture Production Indicators.”

Chadwick, A. J., S. Steele, J. Silvestre, and Lamb.M.P. 2022. “Effect of Sea-Level Change on River Avulsions and Stratigraphy for an Experimental Lowland Delta.” *JGR Earth Surface* 1–27. doi: https://doi. org/10.1029/2021JF006422.

Chan, B., S. Brosse, Z. S. Hogan, P. B. Ngor, and S. Lek. 2020. “Influence of Local Habitat and Climatic Factors on the Distribution of Fish Species in the Tonle Sap Lake.” *Water* 12(3). doi: 10.3390/w12030786.

Chang, K. C., A. A. Ghani, R. Abdullah, and N. A. Zakaria. 2008. “Sediment Transport Modeling for Kulim River – A Case Study.” *Journal of Hydro-Environment Research* 47–59. doi: 10.1016/j.jher.2008.04.002.

Chang, S. W., T. P. Clement, M. J. Simpson, and K. K. Lee. 2011. “Does Sea-Level Rise Have an Impact on Saltwater Intrusion?” *Advances in Water Resources* 34:1283–91. doi: 10.1016/j.advwatres.2011.06.006.

Chapman, A. D., S. E. Darby, H. M. Hồng, E. L. Tompkins, and T. P. D. Van. 2016. “Adaptation and Development Trade-Offs: Fluvial Sediment Deposition and the Sustainability of Rice-Cropping in An Giang Province, Mekong Delta.” *Climatic Change* 137(3–4):593–608. doi: 10.1007/s10584-016-1684-3.

Chea, R., T. K. Pool, M. Chevalier, P. Ngor, N. So, K. O. Winemiller, S. Lek, and G. Grenouillet. 2020. “Impact of Seasonal Hydrological Variation on Tropical Fish Assemblages: Abrupt Shift Following an Extreme Flood Event.” *Ecosphere* 11. doi: 10.1002/ecs2.3303.

Chen, A., J. Liu, M. Kummu, O. Varis, Q. Tang, G. Mao, J. Wang, and D. Chen. 2021. “Multidecadal Variability of the Tonle Sap Lake Flood Pulse Regime.” *Hydrological Processes*. doi: 10.1002/hyp.14327.

Chen, W. B., and W. C. Liu. 2014. “Modeling Flood Inundation Induced by River Flow and Storm Surges over a River Basin.” *Water* 6:3182–99. doi: 10.3390/w6103182.

Chevalier, M., P. B. Ngor, K. Pin, B. Touch, S. Lek, G. Grenouillet, and Z. Hogan. 2023. “Long-Term Data Show Alarming Decline of Majority of Fish Species in a Lower Mekong Basin Fishery.” *Science of the Total Environment*. doi: 10.1016/j.scitotenv.2023.164624.

Chinh, D. T., P. Bubeck, N. V. Dung, and H. Kreibich. 2016. “The 2011 Flood Event in the Mekong Delta: Preparedness, Response, Damage and Recovery of Private Households and Small Businesses.” *Disasters* 40(4):753–78. doi: 10.1111/disa.12171.

Chow, VT. 1959. “Open Channel Hydraulics.” doi: 07-010776-9.

Chu, Z. 2014. “The Dramatic Changes and Anthropogenic Causes of Erosion and Deposition in the Lower Yellow (Huanghe) River since 1952.” *Geomorphology* 216:171–79. doi: 10.1016/j.geomorph.2014.04.009.

Chua, S. D. .., and X. X. Lu. 2022. “What Can Stage Curves Tell Us about Water Level Changes? Case Study of the Lower Mekong Basin.” *Catena* 216(February). doi: 10.1016/j.catena.2022.106385.

Chua, S. D. X., X. X. Lu, C. Oeurng, T. Sok, and C. Grundy-Warr. 2022. “Drastic Decline of Flood Pulse in the Cambodian Floodplains (Mekong River and Tonle Sap System).” *Hydrology and Earth System Sciences* 26:609–25. doi: 10.5194/hess-26-609-2022.

Church, M. 2006. “Bed Material Transport and the Morphology of Alluvial River Channels.” *The Annual Review of Earth and Planetary Science* 325–54. doi: 10.1146/annurev.earth.33.092203.122721.

Clark, M. P., R. M. Vogel, J. R. Lamontagne, N. Mizukami, W. J. M. Knoben, G. Tang, S. Gharari, J. E. Freer, P. H. Whitfield, K. R. Shook, and S. M. Papalexiou. 2021. “The Abuse of Popular Performance Metrics in Hydrologic Modeling.” *Water Resources Research* 57:1–16. doi: 10.1029/2020WR029001.

Cochrane, T. A., M. E. Arias, and T. Piman. 2014. “Historical Impact of Water Infrastructure on Water Levels of the Mekong River and the Tonle Sap System.” *Hydrology and Earth System Sciences* 4529–41. doi: 10.5194/hess-18-4529-2014.

Colby, R. B. 1964. “Discharge of Sands and Mean-Velocity Relationships in Sand-Bed Streams.” *Geological Survey Professional Paper*.

Coleman, J. M., and L. D. Wright. 1971. “Analysis of Major River Systems and Their Deltas: Procedures and Rationale, With Two Examples.” *Technical Report - Coastal Studies Institute, Louisiana State University*.

Correggiari, A., A. Cattaneo, and F. Trincardi. 2005. “Depositional Patterns in the Late Holocene Po Delta System.” *Society for Sedimentary Geology* (83):365–92. doi: 10.2110/pec.05.83.0365.

Cox, J. R., Y. Huismans, S. M. Knaake, J. R. F. W. Leuven, N. E. Vellinga, M. V. D. Vegt, A. J. F. Hoitink, and M. G. Kleinhans. 2021. “Anthropogenic Effects on the Contemporary Sediment Budget of the Lower Rhine-Meuse Delta Network.” *Earth’s Future* 1–22. doi: 10.1029/2020EF001869.

Croke, J., K. Fryirs, and C. Thompson. 2013. “Channel-Floodplain Connectivity during an Extreme Flood Event: Implications for Sediment Erosion, Deposition, and Delivery.” *Earth Surface Processes and Landforms* 38:1444–56. doi: 10.1002/esp.3430.

Dade, W. B., and P. F. Friend. 1998. “Grain-Size, Sediment-Transport Regime, and Channel Slope in Alluvial Rivers.” *Journal of Geology* 106:661–75. doi: 10.1086/516052.

Dadson, S. J., N. Hovius, H. Chen, B. W. Dade, M. L. Hsieh, S. D. Willett, J. C. Hu, M. J. Horng, M. C. Chen, C. P. Stark, D. Lague, and J. C. Lin. 2003. “Links between Erosion, Runoff Variability and Seismicity in the Taiwan Orogen.” *Nature* 426(11):648–51. doi: 10.1038/nature02150.

Daham, A., G. H. S. Smith, A. P. Nicholas, A. Gasparotto, and J. Clark. 2024. “Sand Mining across the Ganges – Brahmaputra – Meghna Catchment ; Assessment of Activity and Implications for Sediment Delivery.” *Environmental Research Letters* 19. doi: https://doi.org/10.1088/1748-9326/ad6016.

Dang, H., Y. Pokhrel, S. Shin, J. Stelly, D. Ahlquist, and D. D. Bui. 2022. “Hydrologic Balance and Inundation Dynamics of Southeast Asia ’ s Largest Inland Lake Altered by Hydropower Dams in the Mekong River Basin.” *Science of the Total Environment* 831. doi: 10.1016/j.scitotenv.2022.154833.

Dang, T. D., T. A. Cochrane, M. E. Arias, P. D. T. Van, and T. T. .. Vries. 2016. “Hydrological Alterations from Water Infrastructure Development in the Mekong Floodplains.” *Hydrological Processes* 30(21):3824–38. doi: 10.1002/hyp.10894.

Darby, S. E., C. R. Hackney, J. Leyland, M. Kummu, H. Lauri, D. R. Parsons, J. L. Best, A. P. Nicholas, and R. Aalto. 2016. “Fluvial Sediment Supply to a Mega-Delta Reduced by Shifting Tropical-Cyclone Activity.” *Nature* 539:276–79. doi: 10.1038/nature19809.

Day, J. W., J. Agboola, Z. Chen, C. D’Elia, D. L. Forbes, L. Giosan, P. Kemp, C. Kuenzer, R. R. Lane, R. Ramachandran, J. Syvitski, and A. Yañez-Arancibia. 2016. “Approaches to Defining Deltaic Sustainability in the 21st Century.” *Estuarine, Coastal and Shelf Science* 183:275–91. doi: 10.1016/j.ecss.2016.06.018.

Day, J.W., D. F. Boesch, E. J. Clairain, G. P. Kemp, S. D. Laska, W. J. Mitsch, K. Orth, H. Mashriqui, D. J. Reed, L. Shabman, C. A. Simenstad, B. J. Streever, R. R. Twilley, C. C. Watson, J. T. Wells, and D. F. Whigham. 2007. “Restoration of the Mississippi Delta: Lessons from Hurricanes Katrina and Rita.” *Science* 315:1679–84. doi: 10.1126/science.1137030.

Day, J. W., H. C. Clark, C. Chang, R. Hunter, and C. R. Norman. 2020. “Life Cycle of Oil and Gas Fields in the Mississippi River Delta: A Review.” *Water* 12(5):1–29. doi: 10.3390/w12051492.

Day, John W., Joel D. Gunn, William J. Folan, Alejandro Yáñez-Arancibia, and Benjamin P. Horton. 2007. “Emergence of Complex Societies after Sea Level Stabilized.” *Eos* 88(15):169–70. doi: 10.1029/2007EO150001.

Delgado, J. M., H. Apel, and B. Merz. 2010. “Hydrology and Earth System Sciences Flood Trends and Variability in the Mekong River.” *Hydrol. Earth Syst. Sci* 14:407–18.

Delgado, J. M., B. Merz, and H. Apel. 2012. “A Climate-Flood Link for the Lower Mekong River.” *Hydrology and Earth System Sciences* 16(5):1533–41. doi: 10.5194/hess-16-1533-2012.

DHI. 2012. “MIKE_11.”

DHI. 2014. “MIKE 21 & MIKE 3 Flow Model FM Sand, Transport Module.”

Dokka, R. K. 2006. “Modern-Day Tectonic Subsidence in Coastal Louisiana.” *Geology* 34:281–84. doi: 10.1130/G22264.1.

Duc, L., and Y. Sawada. 2023. “A Signal-Processing-Based Interpretation of the Nash-Sutcliffe Efficiency.” *Hydrology and Earth System Sciences* 27:1827–39. doi: 10.5194/hess-27-1827-2023.

Dudgeon, D., A. H. Arthington, M. O. Gessner, Z. I. Kawabata, D. J. Knowler, C. Lévêque, R. J. Naiman, A. H. Prieur-Richard, D. Soto, M. L. J. Stiassny, and C. A. Sullivan. 2006. “Freshwater Biodiversity: Importance, Threats, Status and Conservation Challenges.” *Freshwater Biodiversity* 81:163–82. doi: 10.1017/S1464793105006950.

Dung, N. V. 2011. “Multi-Objective Automatic Calibration of Hydrodynamic Models – Development of the Concept and an Application in the Mekong Delta.” *PhD Thesis* (978-3-942036-11–5):133.

Dung, N. V., B. Merz, A. Bárdossy, T. D. Thang, and H. Apel. 2011. “Multi-Objective Automatic Calibration of Hydrodynamic Models Utilizing Inundation Maps and Gauge Data.” *Hydrology and Earth System Sciences* 15:1339–54. doi: 10.5194/hess-15-1339-2011.

Dunn, F. E. 2017. “Multidecadal Fluvial Sediment Fluxes to Major Deltas under Environmental Change Scenarios: Projections and Their Implications.”

Dunn, F. E., S. E. Darby, R. J. Nicholls, S. Cohen, C. Zarfl, and B. M. Fekete. 2019. “Projections of Declining Fluvial Sediment Delivery to Major Deltas Worldwide in Response to Climate Change and Anthropogenic Stress.” *Environmental Research Letters* 14. doi: 10.1088/1748-9326/ab304e.

Eco-Business. 2017. “Cambodia Dismisses Claims of Illicit Sand Exports despite Ban.” accessed 7.12.2023.

Edmonds, D. A. 2009. “The Growth and Evolution of River-Dominated Deltas and Their Distributary Networks.” *PhD Thesis*.

Edmonds, D. A., R. L. Caldwell, E. S. Brondizio, and S. M. O. Siani. 2020. “Coastal Flooding Will Disproportionately Impact People on River Deltas.” *Nature Communications* 11:1–8. doi: 10.1038/s41467-020-18531-4.

Edmonds, D. A., and R. L. Slingerland. 2007. “Mechanics of River Mouth Bar Formation: Implications for the Morphodynamics of Delta Distributary Networks.” *Journal of Geophysical Research: Earth Surface* 112(2):1–14. doi: 10.1029/2006JF000574.

Edmonds, D. A., and R. L. Slingerland. 2010. “Significant Effect of Sediment Cohesion on Delta Morphology.” *Nature Geoscience* (July). doi: 10.1038/ngeo730.

Edmonds, D., R. Slingerland, J. Best, D. Parsons, and N. Smith. 2010. “Response of River-Dominated Delta Channel Networks to Permanent Changes in River Discharge.” *Geophysical Research Letters* 37:1–5. doi: 10.1029/2010GL043269.

Edmonds, D., and R. L. Slingerland. 2008. “Stability of Delta Distributary Networks and Their Bifurcations.” *Water Resources Research* 44:1–13. doi: 10.1029/2008WR006992.

Einstein, H. A. 1950. “The Bed-Load Function for Sediment Transportation in Open Channel Flow.” *Technical Bulletin* No. 1026,:U.S. Dep. of Agriculture, Washington, D.C.

Engelund, F., and J. Fredsoe. 1976. “A Sediment Transport Model for Straight Alluvial Channels.” *Nordic Hydrology* 7:293–306.

Engelund, F., and E. Hansen. 1967. “A Monograph on Sediment Transport Inn Alluvial Streams.”

Technical University of Denmark.

Ensign, S. H., and G. B. Noe. 2018. "Tidal Extension and Sea- Level Rise: Recommendations for a Research Agenda." *Frontiers in Ecology and the Environment* 16:37–43. doi: 10.1002/fee.1745.

EPA. 2016. "What Climate Change Means for Mississippi." *The National Climate Assessments*.

Erban, L. E., S. M. Gorelick, and H. A. Zebker. 2014. "Groundwater Extraction, Land Subsidence, and Sea-Level Rise in the Mekong Delta, Vietnam." *Environmental Research Letters* 9. doi: 10.1088/1748-9326/9/8/084010.

Ericson, J. P., C. J. Vörösmarty, S. L. Dingman, L. G. Ward, and M. Meybeck. 2006. "Effective Sea-Level Rise and Deltas: Causes of Change and Human Dimension Implications." *Global and Planetary Change* 50:63–82. doi: 10.1016/j.gloplacha.2005.07.004.

Erkens, G., T. Bucx, R. Dam, G. De Lange, and J. Lambert. 2015. "Sinking Coastal Cities." *Proceedings of the International Association of Hydrological Sciences* 372:189–98. doi: 10.5194/piahs-372-189-2015.

Eslami, S., P. Hoekstra, H. Kernkamp, N. N. Trung, D. D. Duc, T. T. Quang, M. Februarianto, A. V. Dam, and M. V. D. Vegt. 2019. "Flow Division Dynamics in the Mekong Delta: Application of a 1D-2D Coupled Model." *Water* 11:1–25. doi: 10.3390/w11040837.

Eslami, S., P. Hoekstra, P. S. J. Minderhoud, N. N. Trung, J. M. Hoch, E. H. Sutanudjaja, D. D. Dung, T. Q. Tho, H. E. Voepel, M. N. Woillez, and M. V. D. Vegt. 2021. "Projections of Salt Intrusion in a Mega-Delta under Climatic and Anthropogenic Stressors." *Communications Earth and Environment* 2:1–11. doi: 10.1038/s43247-021-00208-5.

Eslami, S., P. Hoekstra, N. N. Trung, S. A. Kantoush, D. V. Binh, D. D. Dung, T. T. Quang, and M. V. .. Vegt. 2019. "Tidal Amplification and Salt Intrusion in the Mekong Delta Driven by Anthropogenic Sediment Starvation." *Scientific Reports* 9:1–10. doi: 10.1038/s41598-019-55018-9.

Eslami, Sepehr, Piet Hoekstra, Herman W. J. Kernkamp, Nam Nguyen Trung, and Dung Do Duc. 2021. "Dynamics of Salt Intrusion in the Mekong Delta : Results of Field Observations and Integrated Coastal – Inland Modelling." 953–76. doi: https://doi.org/10.5194/esurf-9-953-2021.

Evans, G. 2012. "Review Paper Deltas : The Fertile Dustbins of the Continents." *Proceedings of the Geologists' Association* 123:397–418. doi: 10.1016/j.pgeola.2011.11.001.

Fagherazzi, S., D. A. Edmonds, W. Nardin, N. Leonardi, and A. Canestrelli. 2015. "Dynamics of River Mouth Deposits." *Reviews of Geophysics* 642–72. doi: 10.1002/2014RG000451.Received.

Falcini, F., and D. J. Jerolmack. 2010. "A Potential Vorticity Theory for the Formation of Elongate Channels in River Deltas and Lakes." *Journal of Geophysical Research* 115:1–18. doi: 10.1029/2010JF001802.

Fan, H., D. He, and H. Wang. 2015. "Environmental Consequences of Damming the Mainstream Lancang-Mekong River: A Review." *Earth-Science Reviews* 146:77–91. doi:

10.1016/j.earscirev.2015.03.007.

FAO. 2011. *The State of the World's Land and Water Resources for Food and Agriculture*. The Food and Agriculture Organization of the United Nations.

FAO. 2016. "Global Soil Partnership Endorses Guidelines on Sustainable Soil Management." Retrieved May 12, 2024 (https://www.fao.org/global-soil-partnership/resources/highlights/detail/en/c/416516/).

Fattah, A. S., A. Amin, and L. C. .. Rijn. 2004. "Sand Transport in Nile River, Egypt." *Journal of Hydraulic Engineering* 130(6). doi: 10.1061/(ASCE)0733- 9429(2004)130:6(488).

Federici, B., and C. Paola. 2003. "Dynamics of Channel Bifurcations in Noncohesive Sediments." *Water Resources Management* 39(6). doi: 10.1029/2002WR001434.

Ferguson, R. 2010. "Time to Abandon the Manning Equation ?" *Earth Surface Processes and Landforms* 1876:1873–76. doi: 10.1002/esp.2091.

Filho, W. L., J. Hunt, A. Lingos, J. Platje, L. W. Vieira, M. Will, and M. D. Gavriletea. 2021. "The Unsustainable Use of Sand: Reporting on a Global Problem." *Sustainability (Switzerland)* 13:1–16. doi: 10.3390/su13063356.

Finer, M., and C. N. Jenkins. 2012. "Proliferation of Hydroelectric Dams in the Andean Amazon and Implications for Andes-Amazon Connectivity." *PLoS ONE* 7(4):1–9. doi: 10.1371/journal.pone.0035126.

Fisher, W. L., and J. H. McGowen. 1967. *Depositional Systems in the Wilcox Group of Texas and Their Relationship to Occurrence of Oil and Gas*. The University of Texas at Austin.

Frings, R. M., and M. G. Kleinhans. 2008. "Complex Variations in Sediment Transport at Three Large River Bifurcations during Discharge Waves in the River Rhine." *Sedimentology* 1145–71. doi: 10.1111/j.1365-3091.2007.00940.x.

Fujihara, Y., K. Hoshikawa, H. Fujii, A. Kotera, T. Nagano, and S. Yokoyama. 2016. "Analysis and Attribution of Trends in Water Levels in the Vietnamese Mekong Delta." *Hydrological Processes* 30:835–45. doi: 10.1002/hyp.10642.

Fujii, H., H. Garsdal, P. Ward, M. Ishii, K. Morishita, and T. Boivin. 2003. "Hydrological Roles of the Cambodian Floodplain of the Mekong River." *International Journal of River Basin Management* 1:253–66. doi: 10.1080/15715124.2003.9635211.

Galloway, D. L., and T. J. Burbey. 2011. "Review: Regional Land Subsidence Accompanying Groundwater Extraction." *Hydrogeology Journal* 19:1459–86. doi: 10.1007/s10040-011-0775-5.

Galloway, W. E. 1975. "Process Framework for Describing the Morphologic and Stratigraphic Evolution of Deltaic Depositional System." *Deltas: Models for Exploration* 87-98.

Ganti, V., A. J. Chadwick, H. J. Hassenruck-Gudipati, and M. P. Lamb. 2016. "Avulsion Cycles and Their Stratigraphic Signature on an Experimental Backwater-Controlled Delta." *Journal of Geophysical Research : Earth Surface* 1651–1675. doi: 10.1002/ 2016JF003915.

Gasparotto, A., S. E. Darby, J. Leyland, and P. A. Carling. 2023. "Water Level Fluctuations Drive

Bank Instability in a Hypertidal Estuary." *Earth Surface Dynamics* 11:343–61. doi: 10.5194/esurf-11-343-2023.

Gelfenbaum, G., A. Stevens, E. Elias, and J. Warrick. 2009. "Modeling Sediment Transport and Delta Morphology on the Dammed Elwha River, Washington State, USA." *Coastal Dynamics* 1–15. doi: 10.1142/9789814282475_0109.

Gerald, D. M. F., I. Buynevich, and B. Argow. 2006. "Model of Tidal Inlet and Barrier Island Dynamics in a Regime of Accelerated Sea Level Rise." *Journal of Coastal Research* (39):789–95. doi: ISSN 0749-0208.

Ghosh, A., S. Das, T. Ghosh, and S. Hazra. 2019. "Risk of Extreme Events in Delta Environment: A Case Study of the Mahanadi Delta." *Science of the Total Environment* 664:713–23. doi: 10.1016/j.scitotenv.2019.01.390.

Gilbert, G. K. 1877. *Report on the Geology of the Henry Mountains*. Department of the Interior, U. S. Geographical and Geol. Surv. of Mountain Region.

Giosan, L., J. Syvitski, S. Constantinescu, and J. W. Day. 2014. "Climate Change: Protect the World's Deltas." *Nature* 516:31–33. doi: 10.1038/516031a.

Gleason, C. J., P. A. Garambois, and M. T. Durand. 2017. "Tracking River Flows from Space." *Eos*. doi: 10.1029/2017eo078085.

Gleason, C. J., and A. N. Hamdan. 2017. "Crossing the (Watershed) Divide: Satellite Data and the Changing Politics of International River Basins." *Geographical Journal* 183:2–15. doi: 10.1111/geoj.12155.

Glenn, Jill, Daniele Tonina, Mark D. Morehead, Fritz Fiedler, and Rohan Benjankar. 2016. "Effect of Transect Location, Transect Spacing and Interpolation Methods on River Bathymetry Accuracy." *Earth Surface Processes and Landforms* 41(9):1185–98. doi: 10.1002/esp.3891.

Gomez, Basil, and Michael Church. 1989. "An Assessment of Bed Load Sediment Transport Formulae for Gravel Bed Rivers." *Water Resources Research* 25:1161–86. doi: https://doi.org/10.1029/WR025i006p01161.

Grill, G., B. Lehner, M. Thieme, B. Geenen, D. Tickner, F. Antonelli, S. Babu, P. Borrelli, L. Cheng, H. Crochetiere, H. Ehalt Macedo, R. Filgueiras, M. Goichot, J. Higgins, Z. Hogan, B. Lip, M. E. McClain, J. Meng, M. Mulligan, C. Nilsson, J. D. Olden, J. J. Opperman, P. Petry, C. R. Liermann, L. Sáenz, S. Salinas-Rodríguez, P. Schelle, R. J. P. Schmitt, J. Snider, F. Tan, K. Tockner, P. H. Valdujo, A. .. Soesbergen, and C. Zarfl. 2019. "Mapping the World's Free-Flowing Rivers." *Nature* 569:215–21. doi: 10.1038/s41586-019-1111-9.

Gruel, C. R., E. Park, A. D. Switzer, S. Kumar, H. H. Loc, Kantoush.S., D. V. Binh, and L. Feng. 2022. "New Systematically Measured Sand Mining Budget for the Mekong Delta Reveals Rising Trends and Significant Volume Underestimations." *International Journal of Applied Earth Observation and Geoinformation* 108. doi: 10.1016/j.jag.2022.102736.

GSOV. 2024. "General Statistics Office of Vietnam." Retrieved June 12, 2024 (https://www.gso.gov.vn/en/homepage/).

Gu, C., L. Hu, X. Zhang, X. Wang, and J. Guo. 2011. "Climate Change and Urbanization in the

Yangtze River Delta." *Habitat International* 35:544–52. doi: 10.1016/j.habitatint.2011.03.002.

Gugliotta, M., Y. Saito, V. L. Nguyen, T. K. O. Ta, R. Nakashima, T. Tamura, K. Uehara, K. Katsuki, and S. Yamamoto. 2017. "Process Regime, Salinity, Morphological, and Sedimentary Trends along the Fluvial to Marine Transition Zone of the Mixed-Energy Mekong River Delta, Vietnam." *Continental Shelf Research* 147:7–26. doi: 10.1016/j.csr.2017.03.001.

Gugliotta, M., Y. Saito, V. L. Nguyen, T. K. O. Ta, and T. Tamura. 2019. "Sediment Distribution and Depositional Processes along the Fluvial to Marine Transition Zone of the Mekong River Delta, Vietnam." *Sedimentology* 66:146–64.

Gupta, H. V., H. Kling, K. K. Yilmaz, and G. F. Martinez. 2009. "Decomposition of the Mean Squared Error and NSE Performance Criteria: Implications for Improving Hydrological Modelling." *Journal of Hydrology* 377:80–91. doi: 10.1016/j.jhydrol.2009.08.003.

Habibi, M. 1994. "Sediment Transport Estimation Methods in River Systems." University of Wollongong.

Hackney, C. R. 2024. "Migrating Sands: Refocusing Transboundary Flows from Water to Sediment." *Area* 1–10. doi: 10.1111/area.12954.

Hackney, C. R., S. E. Darby, D. R. Parsons, J. Leyland, R. Aalto, A. P. Nicholas, and J. L. Best. 2018. "The Influence of Flow Discharge Variations on the Morphodynamics of a Diffluence–Confluence Unit on a Large River." *Earth Surface Processes and Landforms* 43:349–62. doi: 10.1002/esp.4204.

Hackney, C. R., S. E. Darby, D. R. Parsons, J. Leyland, J. L. Best, R. Aalto, A. P. Nicholas, and R. C. Houseago. 2020. "River Bank Instability from Unsustainable Sand Mining in the Lower Mekong River." *Nature Sustainability* 3(March):217–25. doi: 10.1038/s41893-019-0455-3.

Hackney, C. R., G. Vasilopoulos, S. Heng, V. Darbari, S. Walker, and D. R. Parsons. 2021. "Sand Mining Far Outpaces Natural Supply in a Large Alluvial River." *Earth Surface Dynamics* (May):1–20. doi: https://doi.org/10.5194/esurf-2021-39.

Haddadchi, A., M. H. Omid, and A. A. Dehghani. 2013. "Bedload Equation Analysis Using Bed Load-Material Grain Size Bedload Equation Analysis Using Bed Load-Material Grain Size." *Journal of Hydrology and Hydromechanics* 241–49. doi: 10.2478/johh-2013-0031.

Hagenlocher, M., F. G. Renaud, S. Haas, and Z. Sebesvari. 2018. "Vulnerability and Risk of Deltaic Social-Ecological Systems Exposed to Multiple Hazards." *Science of the Total Environment* 631–632:71–80. doi: 10.1016/j.scitotenv.2018.03.013.

Hak, D., K. Nadaoka, P. B. Lawrence, L. P. Vo, N. H. Quan, Q. T. To, H. T. Nguyen, V. N. Duong, and P. V. D. Van. 2016. "Spatio-Temporal Variations of Sea Level around the Mekong Delta: Their Causes and Consequences on the Coastal Environment." *Hydrological Research Letters* 10:60–66. doi: 10.3178/hrl.10.60.

Hall, J. A., C. P. Weaver, J. Obeysekera, M. Crowell, R. M. Horton, R. E. Kopp, J. Marburger, D. C. Marcy, A. Parris, W. V. Sweet, C. Veatch, and K. D. White. 2019. "Rising Sea Levels : Helping Decision-Makers Confront the Inevitable." *Coastal Management* 47:127–50. doi: 10.1080/08920753.2019.1551012.

Harvey, A. M. 2012. “The Coupling Status of Alluvial Fans and Debris Cones: A Review and Synthesis.” *Earth Surface Processes and Landforms* 37:64–76. doi: 10.1002/esp.2213.

Hecht, J. .., G. Lacombe, M. E. Arias, T. D. Dang, and T. Piman. 2019. “Hydropower Dams of the Mekong River Basin: A Review of Their Hydrological Impacts.” *Journal of Hydrology* 285–300.

Heller, P. L., and C. Paola. 1996. “Downstream Changes in Alluvial Architecture: An Exploration of Controls on Channel-Stacking Patterns.” *Journal of Sedimentary Research* 66:297–306. doi: 10.1306/d4268333-2b26-11d7-8648000102c1865d.

Herbert, E. R., P. Boon, A. J. Burgin, S. C. Neubauer, R. B. Franklin, M. Ardon, K. N. Hopfensperger, L. P. M. Lamers, P. Gell, and J. A. Langley. 2015. “A Global Perspective on Wetland Salinization: Ecological Consequences of a Growing Threat to Freshwater Wetlands.” *Ecosphere* 6:1–43. doi: 10.1890/ES14-00534.1.

Heritage, George L., David J. Milan, Andrew R. G. Large, and Ian C. Fuller. 2009. “Influence of Survey Strategy and Interpolation Model on DEM Quality.” *Geomorphology* 112(3–4):334–44. doi: 10.1016/j.geomorph.2009.06.024.

Hoang, L. P., H. Lauri, M. Kummu, J. Koponen, M. T. H. V. Vliet, I. Supit, R. Leemans, P. Kabat, and F. Ludwig. 2016. “Mekong River Flow and Hydrological Extremes under Climate Change.” *Hydrology and Earth System Sciences* 20:3027–41. doi: 10.5194/hess-20-3027-2016.

Hoang, L. P., M. T. H. van Vliet, M. Kummu, H. Lauri, Jo. Koponen, I. Supit, R. Leemans, P. Kabat, and F. Ludwig. 2019. “The Mekong’s Future Flows under Multiple Drivers: How Climate Change, Hydropower Developments and Irrigation Expansions Drive Hydrological Changes.” *Science of the Total Environment* 649:601–9. doi: 10.1016/j.scitotenv.2018.08.160.

Hock, R., P. Jansson, and L. N. Braun. 2005. “Modelling the Response of Mountain Glacier Discharge to Climate Warming.” *Global Change and Mountain Regions* (Ipcc 2001):243–52. doi: 10.1007/1-4020-3508-x_25.

Hogan, Zeb. 2011. “Imperiled Giant Fish and Mainstream Dams in the Lower Mekong Basin: Assessment of Current Status, Threats, and Mitigation.”

Hogeboom, R. J., L. Knook, and A. Y. Hoekstra. 2018. “The Blue Water Footprint of the World’s Artificial Reservoirs for Hydroelectricity, Irrigation, Residential and Industrial Water Supply, Flood Protection, Fishing and Recreation.” *Advances in Water Resources* 113:285–94. doi: 10.1016/j.advwatres.2018.01.028.

Hoitink, A. J. F., and D. A. Jay. 2016. “Tidal River Dynamics: Implications for Deltas.” *Reviews of Geophysics* 54:240–72. doi: 10.1002/2015RG000507.

Hoitink, A. J. F., Z. Wang, B. Vermeulen, Y. Huismans, and K. Kästner. 2017. “Tidal Controls on River Delta Morphology.” *Nature Geoscience* 10:637–45. doi: 10.1038/NGEO3000.

Holtgrieve, G. W., M. E. Arias, K. N. Irvine, D. Lamberts, E. J. Ward, M. Kummu, J. Koponen, J. Sarkkula, and J. E. Richey. 2013. “Patterns of Ecosystem Metabolism in the Tonle Sap Lake , Cambodia with Links to Capture Fisheries.” *PLoS ONE* 8(8). doi: 10.1371/journal.pone.0071395.

Hooijer, A., and R. Vernimmen. 2020. “Global LiDAR Land Elevation Data Reveal Greatest Sea-Level Rise Vulnerability in the Tropics.” *Nature Communications* (2021):1–7. doi: 10.1038/s41467-021-23810-9.

Hori, K., and Y. Saito. 2007. “Classifi Cation , Architecture , and Evolution of Large-River Deltas.” *Large Rivers: Geomorphology and Management* 75–96.

Horritt, M. S., and P. D. Bates. 2002. “Evaluation of 1D and 2D Numerical Models for Predicting River Flood Inundation.” *Journal of Hydrology* 268:87–99.

Horton, A. J., N. V. K. Triet, L. P. Hoang, S. Heng, P. Hok, S. Chung, J. Koponen, and M. Kummu. 2022. “The Cambodian Mekong Floodplain under Future Development Plans and Climate Change.” *Natural Hazards and Earth System Sciences* 22:967–83. doi: https://doi.org/10.5194/nhess-22-967-2022.

Hossain, M. M., and M. L. Rahman. 1998. “Sediment Transport Functions and Their Evaluation Using Data from Large Alluvial Rivers of Bangladesh.” *Modelling Soil Erosion, Sediment Transport and Closely Related Hydrological Processes* (249):375–82.

Houghton, R. A. 1990. “The Global Effects of Tropical Deforestation.” *Environmental Science and Technology* 24:414–22. doi: 0013-936X190/0924-0414$02.50/0.

HRF. 2022. *Situation Report No . 1 – Floods in Cambodia*.

Hu, P., Z. Cao, G. Pender, and G. Tan. 2012. “Numerical Modelling of Turbidity Currents in the Xiaolangdi Reservoir, Yellow River, China.” *Journal of Hydrology* 464–465:41–53. doi: 10.1016/j.jhydrol.2012.06.032.

Huang, M. W., J. J. Liao, Y. W. Pan, and M. H. Cheng. 2014. “Rapid Channelization and Incision into Soft Bedrock Induced by Human Activity - Implications from the Bachang River in Taiwan.” *Engineering Geology* 177:10–24. doi: 10.1016/j.enggeo.2014.05.002.

Huang, W. P. 2017. “Modelling the Effects of Typhoons on Morphological Changes in the Estuary of Beinan, Taiwan.” *Continental Shelf Research* 135:1–13. doi: 10.1016/j.csr.2017.01.011.

Hung, N. N. 2011. *Sediment Dynamics in the Floodplain of the Mekong Delta, Vietnam*. Heft 208.

Hung, N. N., J. M. Delgado, A. Güntner, B. Merz, A. Bárdossy, and H. Apel. 2014a. “Sedimentation in the Fl Oodplains of the Mekong Delta , Vietnam . Part I : Suspended Sediment Dynamics.” 3144:3132–44. doi: 10.1002/hyp.9856.

Hung, N. N., J. M. Delgado, A. Güntner, B. Merz, A. Bárdossy, and H. Apel. 2014b. “Sedimentation in the Fl Oodplains of the Mekong Delta , Vietnam Part II : Deposition and Erosion.” 3160:3145–60. doi: 10.1002/hyp.9855.

Hunter, N. M., P. D. Bates, M. S. Horritt, and M. D. Wilson. 2007. “Simple Spatially-Distributed Models for Predicting Flood Inundation: A Review.” *Geomorphology* 90:208–25. doi: 10.1016/j.geomorph.2006.10.021.

Ibáñez, C., J. W. Day, and E. Reyes. 2014. “The Response of Deltas to Sea-Level Rise: Natural Mechanisms and Management Options to Adapt to High-End Scenarios.” *Ecological Engineering* 65:122–30. doi: 10.1016/j.ecoleng.2013.08.002.

IHA. 2010. *Hydropower Sustainability Assessment Protocol*. International Hydropower Association.

IPCC. 2007. "Climate Change 2007: Impacts, Adaptation and Vulnerability. Contribution of Working Group II to the Fourth Assessment Report of the Intergovernmental Panel on Climate Change." *M.L. Parry, O.F. Canziani, J.P. Palutikof, P.J. van Der Linden and C.E. Hanson, Eds., Cambridge University Press, Cambridge, UK, 976pp. Editorial* (Cambridge University Press,Cambridge, UK, 976pp).

IPCC. 2014. "Climate Change 2014 Synthesis Report." *Contribution of Working Groups I, II and III to the Fifth Assessment Report of the Intergovernmental Panel on Climate Change [Core Writing Team, R.K. Pachauri and L.A. Meyer (Eds.)]. IPCC, Geneva, Switzerland*.

IPCC. 2023. "Climate Change2023 Synthesis Report, Summary for Policymakers." *Contribution of Working Groups I, II and III to the Sixth Assessment Report of the Intergovernmental Panel on Climate Change*. doi: 10.59327/IPCC/AR6-9789291691647.001.

IRTCES. 2005. "Case Study on the Yellow River Sedimentation." *International Research and Training Centre on Erosion and Sedimentation*.

Iwantoro, A. P., M. V. .. Vegt, and M. G. Kleinhans. 2020. "Morphological Evolution of Bifurcations in Tide-Influenced Deltas." *Earth Surface Dynamics* 8:413–29.

Iwantoro, A. P., M. V. D. Vegt, and M. G. Kleinhans. 2021. "Effects of Sediment Grain Size and Channel Slope on the Stability of River Bifurcations." *Earth Surface Processes and Landforms* 46:2004–18. doi: 10.1002/esp.5141.

Iwantoro, A. P., M. V. D. Vegt, and M. G. Kleinhans. 2022. "Stability and Asymmetry of Tide-Influenced River Bifurcations." *JGR Earth Surface* 127. doi: https://doi.org/10.1029/2021JF006282.

Jansen, P. P., L. V. Bendegom, J. V.D. Berg, M. D. Vries, and A. Zanen. 1979. "Principles of River Engineering."

Jansson, P., R. Hock, and T. Schneider. 2003. "The Concept of Glacier Storage: A Review." *Journal of Hydrology* 282:116–29. doi: 10.1016/S0022-1694(03)00258-0.

Jerolmack, D. J. 2009. "Conceptual Framework for Assessing the Response of Delta Channel Networks to Holocene Sea Level Rise." *Quaternary Science Reviews* 28:1786–1800. doi: 10.1016/j.quascirev.2009.02.015.

Jerolmack, D. J., and D. Mohrig. 2007. "Conditions for Branching in Depositional Rives." *Geology* 35:463–66. doi: 10.1130/G23308A.1.

Jerolmack, DJ., and C. Paola. 2007. "Complexity in a Cellular Model of River Avulsion." *Geomorphology* 91:259–70. doi: 10.1016/j.geomorph.2007.04.022.

Ji, X., and Y. Li. 2018. "Changes in the Lake Area of Tonle Sap : Possible Linkage to Runoff Alterations in the Lancang River ?" *Remote Sensing* 10(866). doi: 10.3390/rs10060866.

Jia, Liangwen, Zhangren Luo, Qingshu Yang, Shuying Ou, and Yaping Lei. 2007. "Impacts of the Large Amount of Sand Mining on Riverbed Morphology and Tidal Dynamics in Lower

Reaches and Delta of the Dongjiang River." *Journal of Geographical Sciences* 17(2):197–211. doi: 10.1007/s11442-007-0000-0.

Jordan, C., J. Visscher, N. V. Dung, H. Apel, and T. Schlurmann. 2020. "Impacts of Human Activity and Global Changes on Future Morphodynamics within the Tien River, Vietnamese Mekong Delta." *Water* 12(8). doi: 10.3390/w12082204.

Käkönen, M. 2008. "Mekong Delta at the Crossroads: More Control or Adaptation?" *Ambio* 37(3):205–12.

Keskinen, Marko, M. Kummu, A. Salmivaara, P. Someth, H. Lauri, H. D. Moel, P. W. Pech, and Sokhem. 2013. *Tonle Sap Now and in the Future ?*

Kim, W., A. Dai, T. Muto, and G. Parker. 2009. "Delta Progradation Driven by an Advancing Sediment Source : Coupled Theory and Experiment Describing the Evolution of Elongated Deltas." *Water Resources Research* 45:1–16. doi: 10.1029/2008WR007382.

Kingston, D. G., J. R. Thompson, and G. Kite. 2011. "Uncertainty in Climate Change Projections of Discharge for the Mekong River Basin." *Hydrology and Earth System Sciences* 15:1459–71. doi: 10.5194/hess-15-1459-2011.

Kleinhans, M. G., R. I. Ferguson, S. N. Lane, and R. J. Hardy. 2013. "Splitting Rivers at Their Seams: Bifurcations and Avulsion." *Earth Surface Processes and Landforms* 38(1):47–61. doi: 10.1002/esp.3268.

Kleinhans, M. G., H. R. A. Jagers, E. Mosselman, and C. J. Sloff. 2008. "Bifurcation Dynamics and Avulsion Duration in Meandering Rivers by One-Dimensional and Three-Dimensional Models." *Water Resources Research* 44(8):1–31. doi: 10.1029/2007WR005912.

Kleinhans, M. G., H. .. .. T. Weerts, and K. M. Cohen. 2010. "Avulsion in Action : Reconstruction and Modelling Sedimentation Pace and Upstream Fl Ood Water Levels Following a Medieval Tidal-River Diversion Catastrophe (Biesbosch, The Netherlands, 1421–1750 AD)." *Geomorphology* 118(1–2):65–79. doi: 10.1016/j.geomorph.2009.12.009.

Knoben, W. J. M., J. E. Freer, and R. A. Woods. 2019. "Technical Note: Inherent Benchmark or Not? Comparing Nash-Sutcliffe and Kling-Gupta Efficiency Scores." *Hydrology and Earth System Sciences* 23:4323–31. doi: 10.5194/hess-23-4323-2019.

Koehnken, L., M. S. Rintoul, M. Goichot, D. Tickner, A. C. Loftus, and M. C. Acreman. 2020. "Impacts of Riverine Sand Mining on Freshwater Ecosystems: A Review of the Scientific Evidence and Guidance for Future Research." *River Research and Applications* 36:362–70. doi: 10.1002/rra.3586.

Kondolf, G. M. 1994. "Geomorphic and Environmental Effects of Instream Gravel Mining." *Landscape and Urban Planning* 28(93):225–43.

Kondolf, G.M., Y. Gao, G. W. Annandale, G. L. Morris, E. Jiang, J. Zhang, Y. Cao, P. Carling, K. Fu, Q. Guo, R. Hotchkiss, C. Peteuil, T. Sumi, H. W. Wang, Z. Wang, and Z. Wei. 2014. "Sustainable Sediment Management in Reservoirs and Regulated Rivers : Experiences from Five Continents." *Earth's Future* 256–80. doi: 10.1002/2013EF000184.of.

Kondolf, G. M., Z. K. Rubin, and J. T. Minear. 2014. "Dams on the Mekong: Cumulative Sediment

Starvation." *Water Resources Research* 50:5158–69. doi: 10.1002/2013WR014651.

Kondolf, G. M., R. J. P. Schmitt, P. A. Carling, M. Goichot, M. Keskinen, M. E. Arias, S. Bizzi, A. Castelletti, T. A. Cochrane, S. E. Darby, M. Kummu, P. S. J. Minderhoud, D. Nguyen, T. H. Nguyen, N. T. Nguyen, C. Oeurng, J. Opperman, Z. Rubin, D. C. San, S. Schmeier, and T. Wild. 2022. "Save the Mekong Delta from Drowning." *Science* 376(6593):583–86. doi: 10.1126/science.abm5176.

Kondolf, G. Mathias, Rafael J. P. Schmitt, Paul Carling, Steve Darby, Mauricio Arias, Simone Bizzi, Andrea Castelletti, Thomas A. Cochrane, Stanford Gibson, Matti Kummu, Chantha Oeurng, Zan Rubin, and Thomas Wild. 2018. "Changing Sediment Budget of the Mekong: Cumulative Threats and Management Strategies for a Large River Basin." *Science of the Total Environment* 625:114–34. doi: 10.1016/j.scitotenv.2017.11.361.

Kostaschuk, R. A., and J. L. Luternauer. 1989. "The Role of the Salt-Wedge in Sediment Resuspension and Deposition : Fraser River Estuary , Canada." *Journal of Coastal Research* 5(1):93–101.

Krausmann, F., D. Wiedenhofer, C. Lauk, W. Haas, H. Tanikawa, T. Fishman, Al. Miatto, H. Schandl, and H. Haberl. 2017. "Global Socioeconomic Material Stocks Rise 23-Fold over the 20th Century and Require Half of Annual Resource Use." *PNAS* 114(8):1880–85. doi: 10.1073/pnas.1613773114.

Kummu, M., D. Penny, J. Sarkkula, and J. Koponen. 2008. "Sediment: Curse or Blessing for Tonle Sap Lake?" *Ambio* 37(3):158–63.

Kummu, M., and J. Sarkkula. 2008. "Impact of the Mekong River Flow Alteration on the Tonle Sap Flood Pulse." *Ambio* 37(3):185–92.

Kummu, M., S. Tes, S. Yin, P. Adamson, J. Józsa, J. Koponen, J. Richey, and J. Sarkkula. 2014. "Water Balance Analysis for the Tonle Sap Lake – Floodplain System." *Hydrological Processes* 1722–33. doi: 10.1002/hyp.9718.

Kundzewicz, Z. W., L. J. Mata, N. W. Arnell, P. Döll, P. Kabat, B. Jiménez, K. A. Miller, T. Oki, Z. Sen, and I. A. Shiklomanov. 2007. "Global Water Resources and Their Management." *Climate Change 2007: Impacts, Adaptation and Vulnerability. Contribution OfWorking Group II to the Fourth Assessment Report of the Intergovernmental Panel on Climate Change* 1(2):173–210. doi: 10.1016/j.cosust.2009.10.001.

Lai, Y. G., J. Huang, and B. P. Greimann. 2024. "Hydraulic Flushing of Sediment in Reservoirs : Best Practices of Numerical Modeling." *Fluids* 1–30. doi: https://doi.org/10.3390/fluids9020038.

Laksitaningtyas, A. P., D. Legono, Istiarto, and R. Jayadi. 2022. "Preliminary Experiment on Reservoir Sediment Flushing." *IOP Conference Series: Earth and Environmental Science* 1105. doi: 10.1088/1755-1315/1105/1/012031.

Lane, S. N. 1998. "Hydraulic Modelling in Hydrology and Geomoprhology: A Review of High Resolution Approaches." *Hydrological Processes* 12:1131–50.

Latrubesse, E. M., M. L. Amsler, R. P. de Morais, and S. Aquino. 2009. "The Geomorphologic Response of a Large Pristine Alluvial River to Tremendous Deforestation in the South

American Tropics: The Case of the Araguaia River." *Geomorphology* 113:239–52. doi: 10.1016/j.geomorph.2009.03.014.

Lauri, H., H. De Moel, P. J. Ward, T. A. Räsänen, M. Keskinen, and M. Kummu. 2012. "Future Changes in Mekong River Hydrology: Impact of Climate Change and Reservoir Operation on Discharge." *Hydrology and Earth System Sciences* 16:4603–19. doi: 10.5194/hess-16-4603-2012.

Legates, D. R., and G. J. McCabe. 1999. "Evaluating the Use of Goodness-of-fit Measures in Hydrologic and Hydroclimatic Model Validation." *Water Resources Research* 35:233–241.

Lehner, B., C. R. Liermann, C. Revenga, C. Vörösmarty, B. Fekete, P. Crouzet, P. Döll, M. Endejan, K. Frenken, J. Magome, C. Nilsson, J. C. Robertson, R. Rödel, N. Sindorf, and D. Wisser. 2011. "High-resolution Mapping of the World s Reservoirs and Dams for Sustainable River-Flow Management." *Frontiers in Ecology and the Environment* 9:494–502. doi: 10.1890/100125.

Leonardi, N., A. Canestrelli, T. Sun, and S. Fagherazzi. 2013. "Effect of Tides on Mouth Bar Morphology and Hydrodynamics." 118:4169–83. doi: 10.1002/jgrc.20302.

Lin, W., Y. Sun, S. Nijhuis, and Z. Wang. 2020. "Scenario-Based Flood Risk Assessment for Urbanizing Deltas Using Future Land-Use Simulation (FLUS): Guangzhou Metropolitan Area as a Case Study." *Science of the Total Environment* 739. doi: 10.1016/j.scitotenv.2020.139899.

Lohani, S., T. E. Dilts, P. J. Weisberg, S. E. Null, and Z. S. Hogan. 2020. "Rapidly Accelerating Deforestation in Cambodia's Mekong River Basin: A Comparative Analysis of Spatial Patterns and Drivers." *Water* 12. doi: 10.3390/W12082191.

Lu, X.X., M. Kummu, and C. Oeurng. 2014. "Reappraisal of Sediment Dynamics in the Lower Mekong River, Cambodia." *Earth Surface Processes and Landforms* 39:1855–65. doi: 10.1002/esp.3573.

Lu, X. X., S. Li, M. Kummu, R. Padawangi, and J. J. Wang. 2014. "Observed Changes in the Water Flow at Chiang Saen in the Lower Mekong: Impacts of Chinese Dams?" *Quaternary International* 336:145–57. doi: 10.1016/j.quaint.2014.02.006.

Lu, X. X., S. R. Zhang, S. P. Xie, and P. K. Ma. 2007. "Rapid Channel Incision of the Lower Pearl River (China) since the 1990s as a Consequence of Sediment Depletion." *Hydrology and Earth System Sciences* 11:1897–1906.

Lyddon, C., N. Chien, G. Vasilopoulos, M. Ridgill, S. Moradian, and A. Olbert. 2024. "Thresholds for Estuarine Compound Flooding Using a Combined Hydrodynamic – Statistical Modelling Approach." *Natural Hazards and Earth System Sciences* 973–97. doi: https://doi.org/10.5194/nhess-24-973-2024.

Macedo, H. D. .., J. C. Stevaux, M. L. Assine, A. Silva, F. D. .. Pupim, E. R. Merino, and E. Lo. 2017. "Calculating Bedload Transport in Rivers: Concepts, Calculus Routines and Application." *Revista Brasileira de Geomorfologia* 4. doi: ttp://dx.doi.org/10.20502/rbg.v18i4.1227.

Mackey, S. D., and J. S. Bridge. 1995. "Three-Dimensional Model of Alluvial Stratigraphy: Theory and Application." *Journal of Sedimentary Research* 7–31.

Manh, N. V., N. V. Dung, N. N. Hung, M. Kummu, B. Merz, and H. Apel. 2015. "Future Sediment Dynamics in the Mekong Delta Floodplains: Impacts of Hydropower Development, Climate Change and Sea Level Rise." *Global and Planetary Change* 127:22–33. doi: 10.1016/j.gloplacha.2015.01.001.

Manh, N. V., N. V. Dung, N. N. Hung, B. Merz, and H. Apel. 2014. "Large-Scale Suspended Sediment Transport and Sediment Deposition in the Mekong Delta." *Hydrology and Earth System Sciences* 18(8):3033–53. doi: 10.5194/hess-18-3033-2014.

Marchesiello, P., N. M. Nguyen, N. Gratiot, H. Loisel, E. J. Anthony, C. S. Dinh, T. Nguyen, R. Almar, and E. Kestenare. 2019. "Erosion of the Coastal Mekong Delta: Assessing Natural against Man Induced Processes." *Continental Shelf Research* 181:72–89. doi: 10.1016/j.csr.2019.05.004.

Martin, Y., and D. Ham. 2005. "Testing Bedload Transport Formulae Using Morphologic Transport Estimates and Field Data : Lower Fraser River , British Columbia." *Earth Surface Processes and Landforms* 1282:1265–82. doi: 10.1002/esp.1200.

Meckel, T. A., U. S. Ten Brink, and S. J. Williams. 2007. "Sediment Compaction Rates and Subsidence in Deltaic Plains: Numerical Constraints and Stratigraphic Influences." *Basin Research* 19:19–31. doi: 10.1111/j.1365-2117.2006.00310.x.

Meyer-Peter, E. and Müller, R. 1948. "Formulas for Bed Load Transport." *IAHSR 2nd Meeting, Stockholm, Appendix 2. IAHR* 2. doi: 10.1002/esp.3715.

Michener, W. K., E. R. Blood, K. L. Bildstein, M. M. Brinson, and L. R. Gardner. 1997. "Climate Change, Hurricanes and Tropical Storms, and Rising Sea Level in Coastal Wetlands." *Ecological Applications* 7(3):770–801.

Milan, David J. 2009. "Terrestrial Laser Scan-Derived Topographic and Roughness Data for Hydraulic Modelling of Gravel-Bed Rivers." *Laser Scanning for the Environmental Sciences* (December):133–46. doi: 10.1002/9781444311952.ch9.

Milan, David J., George L. Heritage, Andrew R. G. Large, and Ian C. Fuller. 2011. "Filtering Spatial Error from DEMs: Implications for Morphological Change Estimation." *Geomorphology* 125(1):160–71. doi: 10.1016/j.geomorph.2010.09.012.

Milliman, J. D., and S. J. Kao. 2005. "Hyperpycnal Discharge of Fluvial Sediment to the Ocean: Impact of Super-Typhoon Herb (1996) on Taiwanese Rivers." *Journal of Geology* 113:503–16.

Milliman, J. D., and R. H. Meade. 1983. "World-Wide Delivery of River Sediment to the Oceans." *The Journal of Geology* 91(1):1–23.

Milliman, J. D., and J. P. M. Syvitski. 1992. "Geomorphic / Tectonic Control of Sediment Discharge to the Ocean : The Importance of Small Mountainous Rivers." *Journal of Geology* 100(5):525–44.

Minderhoud, P. S. J., L. Coumou, G. Erkens, H. Middelkoop, and E. Stouthamer. 2019. "Mekong Delta Much Lower than Previously Assumed in Sea-Level Rise Impact Assessments." *Nature Communications* 1–13. doi: 10.1038/s41467-019-11602-1.

Minderhoud, P. S. J., G. Erkens, V. H. Pham, V. T. Bui, L. Erban, H. Kooi, and E. Stouthamer. 2017. "Impacts of 25 Years of Groundwater Extraction on Subsidence in the Mekong Delta, Vietnam." *Environmental Research Letters* 12. doi: 10.1088/1748-9326/aa7146.

Minderhoud, P. S. J., H. Middelkoop, G. Erkens, and E. Stouthamer. 2020. "Groundwater Extraction May Drown Mega-Delta : Projections of Extraction-Induced Subsidence and Elevation of the Mekong Delta for the 21st Century." *Environmental Research Letters*. doi: https://doi.org/10.1088/2515-7620/ab5e21.

Miori, S., R. Repetto, and M. Tubino. 2006. "A One-Dimensional Model of Bifurcations in Gravel Bed Channels with Erodible Banks." *Water Resources Research* 42:1–12.

Molnar, P. 2001. "Climate Change, Flooding in Arid Environments, and Erosion Rates." *Geology* 29(12):1071–74.

Morehead, M. D., J. P. Syvitski, E. W. H. Hutton, and S. D. Peckham. 2003. "Modeling the Temporal Variability in the Flux of Sediment from Ungauged River Basins." *Global and Planetary Change* 39:95–110. doi: 10.1016/S0921-8181(03)00019-5.

Moriasi, D. N., J. G. Arnold, M. W. V. Liew, R. L. Bingner, R. D. Harmel, and T. L. Veith. 2007. "Model Evaluation Guidelines for Systematic Quantification of Accuracy in Watershed Simulations." *American Society of Agricultural and Biological Engineers* 50:885−900.

Moriasi, D. N., M. W. Gitau, N. Pai, and P. Daggupati. 2015. "Hydrologic and Water Quality Models: Performance Measures and Evaluation Criteria." *American Society of Agricultural and Biological Engineers* 58:1763–85. doi: 10.13031/trans.58.10715.

Morita, A. 2016. "Infrastructuring Amphibious Space: The Interplay of Aquatic and Terrestrial Infrastructures in the Chao Phraya Delta in Thailand." *Science as Culture* 25(1):117–40. doi: 10.1080/09505431.2015.1081502.

Morovati, K., F. Tian, M. Kummu, L. Shi, M. Tudaji, P. Nakhaei, and M. Alberto. 2023. "Contributions from Climate Variation and Human Activities to Flow Regime Change of Tonle Sap Lake from 2001 to 2020." *Journal of Hydrology* 616. doi: 10.1016/j.jhydrol.2022.128800.

Morton, R. A., J. C. Bernier, and J. A. Barras. 2006. "Evidence of Regional Subsidence and Associated Interior Wetland Loss Induced by Hydrocarbon Production, Gulf Coast Region, USA." *Environmental Geology* 50:261–74. doi: 10.1007/s00254-006-0207-3.

MRC. 2002. *Fish Migrations of the Lower Mekong River Basin: Implications for Development, Planning and Environmental Management*.

MRC. 2004. "Hydro-Meteorological Monitoring for Water Quantity Rules in Mekong River Basin."

MRC. 2005. "Overview of the Hydrology of the Mekong Basin." (November).

MRC. 2009. "The Flow of the Mekong, Mekong River Commmission."

MRC. 2010. *State of the Basin Report 2010*.

MRC. 2011. "Flood Situation Report 2011." (36).

MRC. 2023. “Mekong Bulletin_Zero Gauge above M.S.L.”

MRCS/WUP-FIN. 2007. “Final Report – Part 2: Research Findings and Recommendations. WUP-FIN Phase 2 – Hydrological, Environmental and Socio- Economic Modelling Tools for the Lower Mekong Basin Impact Assessment.”

Najafpour, N. 2016. “Estimation of Sediment Transport Rate of Karun River (Iran).” *Journal of Hydraulic Structures* 74–84. doi: 10.22055/jhs.2016.12874.

Nakato, By Tatsuaki. 1990. “Tests of Selected Sediment-Transport Formulas.” (3):362–79.

Nardin, W., and S. Fagherazzi. 2012. “The Effect of Wind Waves on the Development of River Mouth Bars.” *Geophysical Research Letters* 39:1–6. doi: 10.1029/2012GL051788.

Nardin, W., G. Mariotti, D. A. Edmonds, R. Guercio, and S. Fagherazzi. 2013. “Growth of River Mouth Bars in Sheltered Bays in the Presence of Frontal Waves.” *Journal of Geophysical Research: Earth Surface* 118:872–86. doi: 10.1002/jgrf.20057.

NASA. 2021. “Sea Level Projection Tool, IPCC 6th Assessment Report Sea Level Projections.” Retrieved May 12, 2024 (https://sealevel.nasa.gov/ipcc-ar6-sea-level-projection-tool).

NASA. 2022. “How Long Have Sea Levels Been Rising? How Does Recent Sea Level Rise Compare to That over the Previous Centuries?” Retrieved July 15, 2024 (https://sealevel.nasa.gov/faq/13/how-long-have-sea-levels-been-rising-how-does-recent-sea-level-rise-compare-to-that-over-the-previous/).

Nash, J. E., and J. V. Sutcliffe. 1970. “River Flow Forecasting through Conceptual Models Part I - A Discussion of Principles.” *Journal of Hydrology* 10:pp: 282-290.

Nations, United. 2014. *World Urbanization Prospects: The 2014 Revision, Highlights*. Vol. 12.

Nations, United. 2018. *World Urbanization Prospects 20188—World’s Largest Cities*.

NG, W. X., and E. Park. 2021. “Shrinking Tonlé Sap and the Recent Intensification of Sand Mining in the Cambodian Mekong River.” *Science of the Total Environment* 777. doi: 10.1016/j.scitotenv.2021.146180.

Nguyen, L. V., T. K. O. Ta, and M. Tateishi. 2000. “Late Holocene Depositional Environments and Coastal Evolution of the Mekong River Delta, Southern Vietnam.” *Journal of Asian Earth Sciences* 18:427–39. doi: 10.1016/S1367-9120(99)00076-0.

Nguyen, T. C., K. Schwarzer, and K. Ricklefs. 2023. “Water-Level Changes and Subsidence Rates along the Saigon-Dong Nai River Estuary and the East Sea Coastline of the Mekong Delta.” *Estuarine, Coastal and Shelf Science* 283. doi: 10.1016/j.ecss.2023.108259.

Nicholas, A. P. 2013. “Modelling the Continuum of River Channel Patterns.” *Earth Surface Processes and Landforms* 1187–96. doi: 10.1002/esp.3431.

Nicholas, A. P., S. D. Sandbach, P. J. Ashworth, M. L. Amsler, J. L. Best, R. J. Hardy, S. N. Lane, O. Orfeo, D. R. Parsons, A. J. H. Reesink, G. H. Sambrook, and Ricardo N. Szupiany. 2012. “Geomorphology Modelling Hydrodynamics in the Rio Paraná , Argentina : An Evaluation and Inter-Comparison of Reduced-Complexity and Physics Based Models Applied to a Large Sand-Bed River.” *Geomorphology* 169–170:192–211. doi:

10.1016/j.geomorph.2012.05.014.

Nienhuis, J. H., A. D. Ashton, D. A. Edmonds, A. J. F. Hoitink, A. J. Kettner, J. C. Rowland, and T. E. Törnqvist. 2020. "Global-Scale Human Impact on Delta Morphology Has Led to Net Land Area Gain." *Nature* 577:514–18. doi: 10.1038/s41586-019-1905-9.

Nienhuis, J. H., and R. S. W. V. D. Wal. 2021. "Projections of Global Delta Land Loss From Sea-Level Rise in the 21st Century." *Research Letter* (48). doi: https://doi.org/10.1029/2021GL093368.

Nilsson, C., C. A. Reidy, M. Dynesius, and C. Revenga. 2005. "Fragmentation and Flow Regulation of the World's Large River Systems." *Science* 308:405–8.

NOAA. 2024. "Is Sea Level Rising?" Retrieved July 15, 2024 (https://oceanservice.noaa.gov/facts/sealevel.html).

Novak, P., Vi. Guinot, A. Jeffrey, and D. E. Reeve. 2010. *Hydraulic Modelling – an Introduction*.

Olaniyan, O., and A. Adegbola. 2018. "Comparison of Sediment Transport Models on River Omi, South-Western Nigeria." *Biodiversity International Journal*. doi: 10.15406/bij.2018.02.00042.

Olaniyan, O. S., A. A. Adegbola, K. S. Adejumo, and A. T. Adeyokunu. 2020. "Estimation of Bed Load Transport in River Osun, South-Western of Nigeria Using Grain Size Distribution Data." *Journal of Engineering and Environmental Sciences* 2. doi: 10.36108/ujees/0202.20.0240.

Olsen, Nils Reidar B. 2012. *Numerical Modelling and Hydraulics*.

Omorede, C. K. 2014. "Assessment of the Impact of Oil and Gas Resource Exploration on the Environment of Selected Communities in Delta State, Nigeria." *International Journal of Management, Economics and Social Sciences* 3(2):79–99.

Oppenheimer, Michael, Bruce Glavovic, Jochen Hinkel, Roderik van de Wal, Alexandre K. Magnan, Amro Abd-Elgawad, Rongshuo Cai, Miguel Cifuentes-Jara, Robert M. DeConto, Tuhin Ghosh, John Hay, Federico Isla, Ben Marzeion, Benoit Meyssignac, and Zita Sebesvari. 2019. "Sea Level Rise and Implications for Low Lying Islands, Coasts and Communities." *IPCC Special Report on the Ocean and Cryosphere in a Changing Climate* 355(6321):126–29.

Orford, J. D., and P. G. Knight. 2015. "Reviews of Geophysics The Concept of Transport Capacity in Geomorphology." *Reviews of Geophysics* 53:1155–1202. doi: 10.1002/2014RG000474.

Orton, G. J., and H. G. Reading. 1993. "Variability of Deltaic Processes in Terms of Sediment Supply, with Particular Emphasis on Grain Size." *Sedimentology* 40:475–512.

Overeem, I., and J. P. M. Syvitski. 2009. "Dynamics and Vulnerability of Delta Systems." *Global Water System Project* (35):LOICZ Reports & Studies No. 35. GKSS Research Cent.

Overeem, I., J. P. M. Syvitski, and E. W. H. Hutton. 2005. "Three-Dimensional Numerical Modeling of Deltas." *River Deltas-Concepts, Models, and Examples* 13–30.

Overeem, I., G. J. Weltje, C. Bishop-Kay, and S. B. Kroonenberg. 2001. "The Late Cenozoic

Eridanos Delta System in the Southern North Sea Basin: A Climate Signal in Sediment Supply?” *Basin Research* 13:293–312.

Paarlberg, A. J., M. Guerrero, F. Huthoff, and M. Re. 2015. “Optimizing Dredge-and-Dump Activities for River Navigability Using a Hydro-Morphodynamic Model.” *Water* 7:3943–62. doi: 10.3390/w7073943.

Park, E., and E. M. Latrubesse. 2014. “Modeling Suspended Sediment Distribution Patterns of the Amazon River Using MODIS Data.” *Remote Sensing of Environment* 147:232–42. doi: 10.1016/j.rse.2014.03.013.

Parsons, D. R., P. R. Jackson, J. A. Czuba, F. L. Engel, B. L. Rhoads, K. A. Oberg, J. L. Best, D. S. Mueller, K. K. Johnson, and J. D. Riley. 2013. “Velocity Mapping Toolbox (VMT): A Processing and Visualization Suite for Moving-Vessel ADCP Measurements.” *Earth Surface Processes and Landforms* 38(11):1244–60. doi: 10.1002/esp.3367.

Patro, S., C. Chatterjee, R. Singh, and N. S. Raghuwanshi. 2009. “Hydrodynamic Modelling of a Large Flood-Prone River System in India with Limited Data Shivananda.” *Hydrological Processes* 23:2774–2791. doi: 10.1002/hyp.7375.

Penny, D., G. Cook, and S. I. Sok. 2005. “Long-Term Rates of Sediment Accumulation in the Tonle Sap, Cambodia: A Threat to Ecosystem Health?” *Journal of Paleolimnology* 33:95–103.

Petts, Geoffrey E. 1984. “Sedimentation within a Regulated River.” *Earth Surface Processes and Landforms* 9(2):125–34. doi: 10.1002/esp.3290090204.

Piégay, H., C. R. Hupp, A. Citterio, S. Dufour, B. Moulin, and D. E. Walling. 2008. “Spatial and Temporal Variability in Sedimentation Rates Associated with Cutoff Channel Infill Deposits: Ain River, France.” *Water Resources Research* 44:1–18. doi: 10.1029/2006WR005260.

Pin, K., S. Nut, Z. S. Hogan, S. Chandra, S. Saray, B. Touch, P. Chheng, and P. B. Ngor. 2020. “Cambodian Freshwater Fish Assemblage Structure and Distribution Patterns: Using a Large-Scale Monitoring Network to Understand the Dynamics and Management Implications of Species Clusters in a Global Biodiversity Hotspot.” *Water* 12(9). doi: 10.3390/w12092506.

Pinter, N., and R. A. Heine. 2005. “Hydrodynamic and Morphodynamic Response to River Engineering Documented by Fixed-Discharge Analysis, Lower Missouri River, USA.” *Journal of Hydrology* 302:70–91. doi: 10.1016/j.jhydrol.2004.06.039.

Pittaluga, M. B., G. Coco, and M. G. Kleinhans. 2015. “A Unified Framework for Stability of Channel Bifurcations in Gravel and Sand Fluvial Systems.” *Geophysical Research Letters* 42:7521–36. doi: 10.1002/2015GL065175.

Pittaluga, M. B., R. Repetto, and M. Tubino. 2003. “Channel Bifurcation in Braided Rivers: Equilibrium Configurations and Stability.” *Water Resources Research* 39(3):1–13. doi: 10.1029/2001WR001112.

Pizzuto, J. E. 1987. “Sediment Diffusion during Overbank Flows.” *Sedimentology* 301–17.

Planning, National Institute of Statistics Ministry of. 2019. *General Population Census of the Kingdom of Cambodia 2019*.

Pont, D., J. W. Day, P. Hensel, E. Franquet, F. Torre, P. Rioual, C. Ibànez, and E. Coulet. 2002. "Response Scenarios for the Deltaic Plain of the Rhône in the Face of an Acceleration in the Rate of Sea-Level Rise with Special Attention to Salicornia-Type Environments." *Estuaries* 25(3):337–58.

Prajapati, H. N., S. M. Shah, S. I. Waikhom, and S. M. Yadav. 2016. "Evaluation of Sediment Transport Function Using Different Fall Velocity Equations." *GRD Journals* 00039(March):564–68.

Pringle, C. 2003. "What Is Hydrologic Connectivity and Why Is It Ecologically Important?" *Hydrological Processes* 17:2685–89.

Qian, H., Z. Cao, H. Liu, and G. Pender. 2016. "Numerical Modelling of Alternate Bar Formation, Development and Sediment Sorting in Straight Channels." *Earth Surface Processes and Landforms*. doi: https://doi.org/10.1002/esp.3988.

Ragno, Ni., N. Tambroni, and M. B. Pittaluga. 2020. "Effect of Small Tidal Fluctuations on the Stability and Equilibrium Con Fi Gurations of Bifurcations." *JGR Earth Surface* 1–20. doi: 10.1029/2020JF005584.

Rai, P. K., C. T. Dhanya, and B. R. Chahar. 2018. "Coupling of 1D Models (SWAT and SWMM) with 2D Model (IRIC) for Mapping Inundation in Brahmani and Baitarani River Delta." *Natural Hazards* 92:1821–40. doi: 10.1007/s11069-018-3281-4.

Räsänen, T. A., P. Someth, H. Lauri, J. Koponen, J. Sarkkula, and M. Kummu. 2017. "Observed River Discharge Changes Due to Hydropower Operations in the Upper Mekong Basin." *Journal of Hydrology* 545:28–41. doi: 10.1016/j.jhydrol.2016.12.023.

Redolfi, M., G. Zolezzi, and M. Tubino. 2016. "Free Instability of Channel Bifurcations and Morphodynamic Influence." *Journal of Fluid Mechanics* 799:476–504.

Reitz, M. D., and D. J. Jerolmack. 2012. "Experimental Alluvial Fan Evolution: Channel Dynamics, Slope Controls, and Shoreline Growth." *Journal of Geophysical Research: Earth Surface* 117:1–19. doi: 10.1029/2011JF002261.

Reitz, M. D., D. J. Jerolmack, and J. B. Swenson. 2010. "Flooding and Flow Path Selection on Alluvial Fans and Deltas." *Geophysical Research Letters* 37. doi: 10.1029/2009GL041985.

Rempel, A. W., J. A. Marshall, and J. J. Roering. 2016. "Modeling Relative Frost Weathering Rates at Geomorphic Scales." *Earth and Planetary Science Letters* 453:87–95. doi: 10.1016/j.epsl.2016.08.019.

Revenga, C., J. Brunner, N. Henninger, K. Kassem, and R. Payne. 2000. "Pilot Ananlysis of Globle Ecosystems: Freshwater Systems." *World Resources Institute*.

Rijn, L. C. V. 1984a. "Sediment Transport, Part I: Bed Load Transport." *Journal of Hydraulic Engineering* 110(10):1431–56.

Rijn, L. C. V. 1984b. "Sediment Transport, Part II: Suspended Load Transport." *Journal of Hydraulic Engineering* Vol. 110.

Rijn, L. C. V. 2013. "Simple General Formulae for Sand Transport in Rivers." 1–16.

Rijn, L. C. V. 2020. “Critical Bed-Shear Stress for Mud-Sand Beds.”

Rijn, L. C. V., D. J. R. Walstra, B. T. Grasmeijer, J. Sutherland, S. Pan, and J. P. Sierra. 2002. “Simulation of Nearshore Hydrodynamics and Morphodynamics on the Time Scale of Storms and Seasons Using Process-Based Profile Models.” *In Coast3D—Egmond: The Behaviour of a Straight Sandy Coast on the Time Scale of Storms and Seasons: Process Knowledge and Guidelines for Coastal Management: End Document, March*.

Ritter, A., and R. Muñoz-carpena. 2013. “Performance Evaluation of Hydrological Models : Statistical Significance for Reducing Subjectivity in Goodness-of-Fit Assessments.” *Journal of Hydrology* 480:33–45. doi: 10.1016/j.jhydrol.2012.12.004.

Romy Chevallier. 2014. “Illegal Sand Mining in South Africa.” *Governance of Africa’s Resources Programme*.

Rossi, V. M., W. Kim, J. L. López, D. Edmonds, N. Geleynse, C. Olariu, R. J. Steel, M. Hiatt, and P. Passalacqua. 2016. “Impact of Tidal Currents on Delta-Channel Deepening, Stratigraphic Architecture, and Sediment Bypass beyond the Shoreline.” *Geology* 44(11):927–30. doi: 10.1130/G38334.1.

Routschek, A., J. Schmidt, W. Enke, and Th. Deutschlaender. 2014. “Future Soil Erosion Risk - Results of GIS-Based Model Simulations for a Catchment in Saxony/Germany.” *Geomorphology* 206:299–306. doi: 10.1016/j.geomorph.2013.09.033.

Rowland, J. C., W. E. Dietrich, and M. T. Stacey. 2010. “Morphodynamics of Subaqueous Levee Formation : Insights into River Mouth Morphologies Arising from Experiments.” 115:1–20. doi: 10.1029/2010JF001684.

Salem, M. G., N. M. Eshra, and N. M. Shafiq. 2021. “Impact of Nile Levels Decline on Irrigation Pump Stations in Delta Region; Technical and Economical.” *Energy Reports* 7:380–94. doi: 10.1016/j.egyr.2021.07.112.

Salter, G., C. Paola, and V. R. Voller. 2018. “Control of Delta Avulsion by Downstream Sediment Sinks.” *Journal of Geophysical Research : Earth Surface* 123:142–66. doi: 10.1002/2017JF004350.

Samantaray, D., C. Chatterjee, R. Singh, P. K. Gupta, and S. Panigrahy. 2015. “Flood Risk Modeling for Optimal Rice Planning for Delta Region of Mahanadi River Basin in India.” *Natural Hazards* 76(1):347–72. doi: 10.1007/s11069-014-1493-9.

Sassi, M. G., A. J. F. Hoitink, B. D. Brye, B. Vermeulen, and E. Deleersnijder. 2011. “Tidal Impact on the Division of River Discharge over Distributary Channels in the Mahakam Delta.” *Ocean Dynamics* 61(12):2211–28. doi: 10.1007/s10236-011-0473-9.

Saviour, M. N. 2012. “Environmental Impact of Soil and Sand Mining: A Review.” *International Journal of Science, Environment* 1(3):125–34.

Schandl, H., M. Fischer-Kowalski, J. West, S. Giljum, M. Dittrich, N. Eisenmenger, A. Geschke, M. Lieber, H. Wieland, A. Schaffartzik, F. Krausmann, S. Gierlinger, K. Hosking, M. Lenzen, H. Tanikawa, A. Miatto, and T. Fishman. 2016. *Global Material Flows and Resource Productivity. An Assessment Study of the UNEP International Resource Panel*.

Scown, M. W., F. E. Dunn, S. C. Dekker, D. P. van Vuuren, S. Karabil, E. H. Sutanudjaja, M. J. Santos, P. S. J. Minderhoud, A. S. Garmestani, and H. Middelkoop. 2023. "Global Change Scenarios in Coastal River Deltas and Their Sustainable Development Implications." *Global Environmental Change* 82. doi: 10.1016/j.gloenvcha.2023.102736.

Scudder, Thayer Ted. 2012. *The Future of Large Dams*.

Shen, H. W. 1970. *An Engineering Approach to Total Bed-Material Load by Regression Analysis*. Colorado State University.

Shi, X., R. Fang, J. Wu, H. Xu, Y. Y. Sun, and J. Yu. 2012. "Sustainable Development and Utilization of Groundwater Resources Considering Land Subsidence in Suzhou, China." *Engineering Geology* 124:77–89. doi: 10.1016/j.enggeo.2011.10.005.

Shrestha, H. K. 2013. "Sand Mining as a Flood Hazard Mitigation Measure in Nepal." *International Journal of Landslide and Environment* 1:87–88.

Shukla, G. 2012. *Global Perspectives on Sustainable Forest Management*.

Siev, S., V. Ann, T. Nakamura, H. Fujii, and C. Yoshimura. 2020. "Flood Mapping under an Extreme Event in a Large Shallow Lake Influenced by Flood Pulse in Southeast Asia." *Web of Conferences* 4:3–6. doi: https://doi.org/10.1051/e3sconf/202014806004.

Simm, D. J., and D. E. Walling. 1998. "Lateral Variability of Overbank Sedimentation on a Devon Flood Plain." *Hydrological Sciences Journal* 43:715–32. doi: 10.1080/02626669809492168.

Siqueira, V. A., R. C. D. Paiva, A. S. Fleischmann, F. M. Fan, A. L. Ruhoff, P. R. M. Pontes, A. Paris, S. Calmant, and W. Collischonn. 2018. "Toward Continental Hydrologic-Hydrodynamic Modeling in South America." *Hydrology and Earth System Sciences* 22:4815–42. doi: 10.5194/hess-22-4815-2018.

Skinner, C. J., T. J. Coulthard, D. R. Parsons, J. A. Ramirez, L. Mullen, and S. Manson. 2015. "Estuarine , Coastal and Shelf Science Simulating Tidal and Storm Surge Hydraulics with a Simple 2D Inertia Based Model , in the Humber Estuary , U . K." *Estuarine, Coastal and Shelf Science* 155:126–36. doi: 10.1016/j.ecss.2015.01.019.

Slater, L. J. 2014. "Trends in Alluvial Channel Geometry and Streamflow: An Investigation of Patterns and Controls."

Slingerland, R., and N. D. Smith. 2004. "River Avulsions and Their Deposits." *Annual Review of Earth and Planetary Sciences* 32:257–85.

Smith, N. D., T. A. Cross, J. P. Dufficy, and S. R. Clough. 1989. "Anatomy of an Avulsion." *Sedimentology* 36(1):1–23.

Sparks, R. E. 1995. "Need for Ecosystem Management of Large Rivers and Their Floodplains." *BioScience* 45(3):168–82.

Sreebha, S., and D. Padmalal. 2011. "Environmental Impact Assessment of Sand Mining from the Small Catchment Rivers in the Southwestern Coast of India: A Case Study." *Environmental Management* 47:130–40. doi: 10.1007/s00267-010-9571-6.

Stanley, D. J., and A. G. Warne. 1994. "Worldwide Initiation of Holocene Marine Deltas by

Deceleration of Sea-Level Rise.” *Science* 265:228–31.

Stanley, D. J., and A. G. Warne. 1997. “Holocene Sea-Level Change and Early Human Utilization of Deltas.” *Gsa Today* 1–7.

Stevens, H. H., and C. T. Yang. 1989. *Summary and Use of Selected Fluvial Sediment-Discharge Formulas*.

Stone, M. C., C. F. Byrne, and R. R. Morrison. 2017. “Evaluating the Impacts of Hydrologic and Geomorphic Alterations on Floodplain Connectivity.” *Ecohydrology* 10(5):1–11. doi: 10.1002/eco.1833.

Strick, R. J. P. 2016. “Floodplain Geomorphology and Topography in Large Rivers.”

Sulaiman, S. Ol., N. Al-ansari, A. Shahadha, and S. Mohammad. 2021. “Evaluation of Sediment Transport Empirical Equations : Case Study of the Euphrates River West Iraq.” *Arabian Jounrnal of Geosciences*. doi: https://doi.org/10.1007/s12517-021-07177-1https://doi.org/10.1007/s12517-021-07177-1.

Swart, H. E. D., and J. T. F. Zimmerman. 2009. “Morphodynamics of Tidal Inlet Systems.” *Annual Review of Fluid Mechanics*. doi: 0066-4189/09/0115-0203.

Sweet, W. V., R. E. Kopp, C. P. Weaver, J. Obeysekera, R. M. Horton, E. R. Thieler, and C. Zervas. 2017. “Global and Regional Sea Level Rise Scenarios for the United States.” *NOAA Technical Report NOS CO-OPS 083*.

Syvitski, J. P. M. 2002. “Sediment Discharge Variability in Arctic Rivers: Implications for a Warmer Future.” *Polar Research* 21:323–30.

Syvitski, J. P. M. 2003. “Supply and Flux of Sediment along Hydrological Pathways: Research for the 21st Century.” *Global and Planetary Change* 39:1–11. doi: 10.1016/S0921-8181(03)00008-0.

Syvitski, J. P. M., J. R. Ángel, Y. Saito, I. Overeem, C. J. Vörösmarty, H. Wang, and D. Olago. 2022. “Earth’s Sediment Cycle during the Anthropocene.” *Nature Reviews*. doi: 10.1038/s43017-021-00253-w.

Syvitski, J. P. M., S. Cohen, A. Miara, and J. Best. 2019. “River Temperature and the Thermal-Dynamic Transport of Sediment.” *Global and Planetary Change* 178:168–83. doi: 10.1016/j.gloplacha.2019.04.011.

Syvitski, J.P. M., N. Harvey, E. Wolanski, W. C. Burnett, G. M. E. Perillo, and V. Gornitz. 2005. “Dynamics of the Coastal Zone.” *Coastal Fluxes in the Anthropocene*.

Syvitski, J.P.M., A. J. Kettner, A. Correggiari, and B. W. Nelson. 2005. “Distributary Channels and Their Impact on Sediment Dispersal.” *Marine Geology* 222–223:75–94. doi: 10.1016/j.margeo.2005.06.030.

Syvitski, J. P. M., A. J. Kettner, I. Overeem, E. W. H. Hutton, M. T. Hannon, G. R. Brakenridge, J. Day, C. Vörösmarty, Y. Saito, L. Giosan, and R. J. Nicholls. 2009. “Sinking Deltas Due to Human Activities.” *Nature Geoscience* 2:681–86. doi: 10.1038/ngeo629.

Syvitski, J. P. M., and J. D. Milliman. 2007. “Geology, Geography, and Humans Battle for

Dominance over the Delivery of Fluvial Sediment to the Coastal Ocean.” *Journal of Geology* 115:1–19.

Syvitski, J. P. M., and Y. Saito. 2007. “Morphodynamics of Deltas under the Influence of Humans.” *Global and Planetary Change* 57:261–82. doi: 10.1016/j.gloplacha.2006.12.001.

Szupiany, R. N., M. L. Amsler, J. L. Best, and D. R. Parsons. 2007. “Comparison of Fixed- and Moving-Vessel Flow Measurements with an ADp in a Large River.” *Journal of Hydraulic Engineering* 133:1299–1309. doi: 10.1061/(asce)0733-9429(2007)133:12(1299).

Takagi, H., T. V. Ty, N. D. Thao, and M. Esteban. 2015. “Ocean Tides and the Influence of Sea-Level Rise on Floods in Urban Areas of the Mekong Delta.” *Journal of Flood Risk Management* 8(4):292–300. doi: 10.1111/jfr3.12094.

Talke, S. A., R. Familkhalili, and D. A. Jay. 2021. “The Influence of Channel Deepening on Tides, River Discharge Effects, and Storm Surge.” *Journal of Geophysical Research: Oceans* 126(5):1–24. doi: 10.1029/2020JC016328.

TCVN_8478:2010. 2010. “TCVN 8478:2010_Hydraulic Work - Demand for Element and Volume of the Topographic Survey in Design Stages.”

Tessler, Z. D., C. J. Vörösmarty, I. Overeem, and J. P. M. Syvitski. 2018. “A Model of Water and Sediment Balance as Determinants of Relative Sea Level Rise in Contemporary and Future Deltas.” *Geomorphology* 305:209–20. doi: 10.1016/j.geomorph.2017.09.040.

Thach, K. S. R., J. Y. Lee, M. T. Ha, M. T. Cao, R. M. Nayga, and J. E. Yang. 2023. “Effect of Saline Intrusion on Rice Production in the Mekong River Delta.” *Heliyon* 9(10). doi: 10.1016/j.heliyon.2023.e20367.

Thomsen, T. 1982. “A Modified Sediment Transport Model for Natural Streams.” *Nordic Hydrology* 79–92.

Tockner, K., and J. A. Stanford. 2002. “Riverine Flood Plains: Present State and Future Trends.” *Environmental Conservation* 29(3):308–30. doi: 10.1017/S037689290200022X.

Toombes, L., and H. Chanson. 2011. “Numerical Limitations of Hydraulic Models.” *Hydrology and Water Resources Symposium* 2322–29.

Törnqvist, T. E., and J. S. Bridge. 2002. “Spatial Variation of Overbank Aggradation Rate and Its Influence on Avulsion Frequency.” *Sedimentology* 49:891–905.

Törnqvist, T. E., D. J. Wallace, J. E. A. Storms, J. Wallinga, R. L. Van Dam, M. Blaauw, M. S. Derksen, C. J. W. Klerks, C. Meijneken, and E. M. A. Snijders. 2008. “Mississippi Delta Subsidence Primarily Caused by Compaction of Holocene Strata.” *Nature Geoscience* 1:173–76. doi: 10.1038/ngeo129.

Torres, A., J. Brandt, K. Lear, and J. Liu. 2017. “A Looming Tragedy of the Sand Commons.” *Science* 357(6355):970–71. doi: 10.1126/science.aao0503.

Towner, J., H. L. Cloke, E. Zsoter, Z. Flamig, J. M. Hoch, J. Bazo, E. C. .. Perez, and E. M. Stephens. 2019. “Assessing the Performance of Global Hydrological Models for Capturing Peak River Flows in the Amazon Basin.” *Hydrology and Earth System Sciences* 23:3057–80. doi:

10.5194/hess-23-3057-2019.

Tran, T., VT Nguyen, TLH Huynh, VK Mai, XH Nguyen, and Doan HP. 2016. *Kịch Bản Biến Đổi Khí Hậu và Nước Biển Dâng Cho Việt Nam (Climate Change and Sea Level Rise Scenarios for Vietnam)*. Nhà xuất bản Tài Nguyên Môi Trường và Bản Đồ Việt Nam, Bộ Tài Nguyên và Môi Trường, Hà Nội, p 188 [Publishing House of Natural Resources, Enviroment and Cartography, Ministry of Natural Resources and Environment, Ha Noi, p 188].

Triet, N. V. K., N. V. Dung, H. Fujii, M. Kummu, B. Merz, and H. Apel. 2017. "Has Dyke Development in the Vietnamese Mekong Delta Shifted Flood Hazard Downstream?" *Hydrology and Earth System Sciences Discussions* 3991–4010. doi: https://doi.org/10.5194/hess-21-3991-2017.

Tsukawaki, S. 1997. "Lithological Features of Cored Sediments from the Northern Part of Lake Tonle Sap, Cambodia." *The International Conference on Stratigraphy and Tectonic Evolution of Southeast Asia and the South Pacific* 232–39.

Tu, L. X., V. Q. Thanh, J. Reyns, S. P. Van, D. T. Anh, T. D. Dang, and D. Roelvink. 2019. "Sediment Transport and Morphodynamical Modeling on the Estuaries and Coastal Zone of the Vietnamese Mekong Delta." *Continental Shelf Research* 64–76. doi: 10.1016/j.csr.2019.07.015.

Uhlemann, Sebastian, Oliver Kuras, Laura A. Richards, Emma Naden, and David A. Polya. 2017. "Electrical Resistivity Tomography Determines the Spatial Distribution of Clay Layer Thickness and Aquifer Vulnerability, Kandal Province, Cambodia." *Journal of Asian Earth Sciences* 147(March):402–14. doi: 10.1016/j.jseaes.2017.07.043.

Uk, S., C. Yoshimura, S. Siev, S. Try, H. Yang, O. Chantha, S. Li, and S. Hul. 2018. "Tonle Sap Lake : Current Status and Important Research Directions for Environmental Management." *Lakes & Reservoirs: Science, Policy and Management for Sustainable Use* 177–89. doi: 10.1111/lre.12222.

UNEP. 2019. *Sand and Sustainability: Finding New Solutions for Environmental Governance of Global Sand Resources*.

UNESCO. n.d. "Tonle Sap Biosphere Reserve." Retrieved May 14, 2024 (https://www.unesco.org/en/articles/promoting-environmental-conservation-tonle-sap-biosphere-reserve).

Vasilopoulos, G., Q. L. Quan, D. R. Parsons, S. E. Darby, V. P. D. Tri, N. N. Hung, I. D. Haigh, H. E. Voepel, A. P. Nicholas, and R. Aalto. 2021. "Establishing Sustainable Sediment Budgets Is Critical for Climate-Resilient Mega-Deltas." *Environmental Research Letters* 16. doi: 10.1088/1748-9326/ac06fc.

Vellinga, N. E., A. J. F. Hoitink, M. van der Vegt, W. Zhang, and P. Hoekstra. 2014. "Human Impacts on Tides Overwhelm the Effect of Sea Level Rise on Extreme Water Levels in the Rhine-Meuse Delta." *Coastal Engineering* 90:40–50. doi: 10.1016/j.coastaleng.2014.04.005.

Venson, G. R., R. C. Marenzi, and T. C. M. Almeida. 2017. "Restoration of Areas Degraded by Alluvial Sand Mining : Use of Soil Microbiological Activity and Plant Biomass Growth to Assess Evolution of Restored Riparian Vegetation." *Environ Monit Assess* 189. doi:

10.1007/s10661-017-5852-3.

Vörösmarty, C. J., M. Meybeck, B. Fekete, K. Sharma, P. Green, and J. P. M. Syvitski. 2003. “Anthropogenic Sediment Retention: Major Global Impact from Registered River Impoundments.” *Global and Planetary Change* 39:169–90. doi: 10.1016/S0921-8181(03)00023-7.

Vörösmarty, C. J., J. P. M. Syvitski, D. A. Y. John, A. D. Sherbinin, L. Giosan, and C. Paola. 2009. “Battling to Save the World’s River Deltas.” *Bulletin of the Atomic Scientists* 65:31–43.

Vrieling, A., J. C. B. Hoedjes, and M. V. D. Velde. 2014. “Towards Large-Scale Monitoring of Soil Erosion in Africa : Accounting for the Dynamics of Rainfall Erosivity.” *Global and Planetary Change* 115:33–43. doi: 10.1016/j.gloplacha.2014.01.009.

Walling, D. E. 2006. “Human Impact on Land-Ocean Sediment Transfer by the World’s Rivers.” *Geomorphology* 79:192–216. doi: 10.1016/j.geomorph.2006.06.019.

Walling, D. E., and Q. He. 1998. “The Spatial Variability of Overbank Sedimentation on River Floodplains.” *Geomorphology* 24(2–3):209–23. doi: 10.1016/S0169-555X(98)00017-8.

Wang, C., S. Leisz, L. Li, X. Shi, J. Mao, Y. Zheng, and A. Chen. 2024. “Historical and Projected Future Runoff over the Mekong River Basin.” *Earth System Dynamic* 15:75–90. doi: https://doi.org/10.5194/esd-15-75-2024.

Wang, J., A. Chu, Z. Dai, and J. Nienhuis. 2024. “Delft3D Model-Based Estuarine Suspended Sediment Budget with Morphodynamic Changes of the Channel-Shoal Complex in a Mega Fluvial-Tidal Delta.” *Engineering Applications of Computational Fluid Mechanics* 18(1). doi: 10.1080/19942060.2023.2300763.

Wang, Ye., L. Feng, J. Liu, X. Hou, and D. Chen. 2020. “Changes of Inundation Area and Water Turbidity of Tonle Sap Lake : Responses to Climate Changes or Upstream Dam Construction ?” *Environmental Research Letters* 15. doi: https://doi.org/10.1088/1748-9326/abac79.

Wang, Z. B., M. De Vries, R. J. Fokkink, and A. Langerak. 1995. “Stability of River Bifurcations in ID Morphodynamic Models.” *Journal of Hydraulic Research* 33:739–50. doi: 10.1080/00221689509498549.

Ward, P. J., A. Couasnon, D. Eilander, I. D. Haigh, A. Hendry, S. Muis, T. I. E. Veldkamp, H. C. Winsemius, and T. Wahl. 2018. “Dependence between High Sea-Level and High River Discharge Increases Flood Hazard in Global Deltas and Estuaries.” *Environmental Research Letters* 13. doi: 10.1088/1748-9326/aad400.

Watson, R. J., A. Y. Sidorchuk, D. E. Walling, C. Vörösmarty, H. Oeschger, S. Leroy, J. Knox, E. Zangger, E. Weigandt, S. Kempe, W. Froehlich, F. Oldfield, and K. Fröhlic. 1996. “Land Use and Climate Impacts on Fluvial Systems during the Period of Agriculture: Recommendations for a Research Project and Its Implementation.”

Wester, Sjoerd J., Rafael Grimson, Priscilla G. Minotti, Martijn J. Booij, and Marcela Brugnach. 2018. “Hydrodynamic Modelling of a Tidal Delta Wetland Using an Enhanced Quasi-2D Model.” *Journal of Hydrology* 559:315–26. doi: 10.1016/j.jhydrol.2018.02.014.

White, W. R., H. Milli, and A. D. Crabbe. 1973. “Sediment Transport: An Appraisal of Available Methods.”

Wilcox, A. C., and Patrick B. S. 2013. “Coupled Hydrogeomorphic and Woody-seedling Responses to Controlled Flood.” *Water Resources Research* 49:2843–2860. doi: doi:10.1002/wrcr.20256.

Wilson, L. 1973. “Variations in Mean Annual Sediment Yield as a Function of Mean Annual Precipitation.” *American Journal of Science* 273:335–49.

Winemiller, K. O., P. B. McIntyre, L. Castello, E. Fluet-Chouinard, T. Giarrizzo, S. Nam, I. G. Baird, W. Darwall, N. K. Lujan, I. Harrison, M. L. J. Stiassny, R. A. M. Silvano, D. B. Fitzgerald, F. M. Pelicice, A. A. Agostinho, L. C. Gomes, J. S. Albert, E. Baran, M. Petrere, C. Zarfl, M. Mulligan, J. P. Sullivan, C. C. Arantes, L. M. Sousa, A. A. Koning, D. J. Hoeinghaus, M. Sabaj, J. G. Lundberg, J. Armbruster, M. L. Thieme, P. Petry, J. Zuanon, G. Torrente Vilara, J. Snoeks, C. Ou, W. Rainboth, C. S. Pavanelli, A. Akama, A. Van Soesbergen, and L. Sáenz. 2016. “Balancing Hydropower and Biodiversity in the Amazon, Congo, and Mekong.” *Science* 351(6269):128–29. doi: 10.1126/science.aac7082.

WLE Greater Mekong. 2016. “Dams in the Mekong River Basin: Commissioned, Under Construction and Planned Dams in April 2016. Vientiane, CGIAR Research Program on Water, Land and Ecosystems - Greater Mekong.”

Wohl, E., B. P. Bledsoe, R. B. Jacobson, N. L. Poff, S. L. Rathburn, D. M. Walters, and A. C. Wilcox. 2015. “The Natural Sediment Regime in Rivers: Broadening the Foundation for Ecosystem Management.” *BioScience* 65:358–71. doi: 10.1093/biosci/biv002.

Wood, M., I. .. Haigh, Q. Q. Le, H. N. Nguyen, H. B. Tran, S. E. Darby, R. Marsh, N. Skliris, J. J. Hirschi, R. .. Nicholls, and N. Bloemendaal. 2023. “Climate-Induced Storminess Forces Major Increases in Future Storm Surge Hazard in the South China Sea Region.” *Natural Hazards and Earth System Sciences* 23:2475–2504. doi: https://doi.org/10.5194/nhess-23-2475-2023.

Wright, L. D. 1977. “Sediment Transport and Deposition at River Mouths : A Synthesis.” *Geological Society of America Bulletin* (70614).

Wright, L. D., and J. M. Coleman. 1972. “River Delta Morphology: Wave Climate and the Role of the Subaqueous Proffile.” *Science* 176:282–284.

WWF. 2018. “Impacts of Sand Mining on Ecosystem Structure, Process and Biodiversity in Rivers.”

Xiqing, C., Z. Qiaoju, and Z. Erfeng. 2006. “In-Channel Sand Extraction from the Mid-Lower Yangtze Channels and Its Management: Problems and Challenges.” *Journal of Environmental Planning and Management* 49:309–20. doi: 10.1080/09640560500508247.

Xu, R., Z. Zeng, M. Pan, A. D. Ziegler, J. Holden, D. V. Spracklen, L. E. Brown, X. He, D. Chen, B. Ye, Haiwei Xu, Sonia Jerez, Chunmiao Zheng, Junguo Liu, Peirong Lin, Yuan Yang, Junyu Zou, Dashan Wang, Mingyi Gu, Zongliang Yang, Dongfeng Li, Junling Huang, Venkataraman, Lakshmi, and Eric. F. Wood. 2023. “A Global-Scale Framework for Hydropower Development Incorporating Strict Environmental Constraints.” *Nature Water*. doi: https://doi.org/10.1038/s44221-022-00004-1.

Yalin, M. S. 1963. "An Expression for Bed-Load Transportation." *Journal of the Hydraulics Division* 89:221–50.

Yang, C. T. 1984. "Unit Stream Power Equation for Gravel." *Journal of Hydraulic Engineering* 110:1783–97.

Yang, Y., M. Zhang, L. Zhu, W. Liu, J. Han, and Y. Yang. 2017. "Influence of Large Reservoir Operation on Water-Levels and Flows in Reaches below Dam: Case Study of the Three Gorges Reservoir." *Scientific Reports* 7:1–15. doi: 10.1038/s41598-017-15677-y.

Yao, Jing, Dan Zhang, Yunliang Li, Qi Zhang, and Junfeng Gao. 2019. "Quantifying the Hydrodynamic Impacts of Cumulative Sand Mining on a Large River-Connected Floodplain Lake: Poyang Lake." *Journal of Hydrology* 579(June):124156. doi: 10.1016/j.jhydrol.2019.124156.

Ysebaert, T., D. J. V. D. Hoek, R. Wortelboer, J. W. M. Wijsman, M. Tangelder, and A. Nolte. 2016. "Management Options for Restoring Estuarine Dynamics and Implications for Ecosystems: A Quantitative Approach for the Southwest Delta in the Netherlands." *Ocean and Coastal Management* 121:33–48. doi: 10.1016/j.ocecoaman.2015.11.005.

Zalinge, N., T. Nao, and S. T. Touch. 1998. "Where There Is Water, There Is Fish? Fisheries Issues in the Lower Mekong Basin from a Cambodian Perspective." *Mekong River Commission/Dof/Danida* 14.

Zarfl, C., A. E. Lumsdon, J. Berlekamp, L. Tydecks, and K. Tockner. 2015. "A Global Boom in Hydropower Dam Construction." *Aquatic Sciences* 77:161–70. doi: 10.1007/s00027-014-0377-0.

Zhang, C. B., L. H. Chen, and J. Jiang. 2014. "Why Fine Tree Roots Are Stronger than Thicker Roots: The Role of Cellulose and Lignin in Relation to Slope Stability." *Geomorphology* 206:196–202. doi: 10.1016/j.geomorph.2013.09.024.

Zhang, M., X. Feng, T. Yan, and X. Wang. 2022. "Human Impacts on Riverbed Morphology and Hydrology in the Lower Reaches of the West River, China." *River Research and Applications* 38(5):952–64. doi: 10.1002/rra.3960.

Zhang, M., I. Townend, H. Cai, J. He, and X. Mei. 2018. "The Influence of Seasonal Climate on the Morphology of the Mouth-Bar in the Yangtze Estuary, China." *Continental Shelf Research* 153:30–49. doi: 10.1016/j.csr.2017.12.004.

Zhu, L., Q. He, J. Shen, and Y. Wang. 2016. "The Influence of Human Activities on Morphodynamics and Alteration of Sediment Source and Sink in the Changjiang Estuary." *Geomorphology* 273:52–62. doi: 10.1016/j.geomorph.2016.07.025.

Zhu, Q., Y. P. Wang, S. Gao, J. Zhang, M. Li, Y. Yang, and J. Gao. 2017. "Modeling Morphological Change in Anthropogenically Controlled Estuaries." *Anthropocene* 17:70–83. doi: 10.1016/j.ancene.2017.03.001.

Appendix

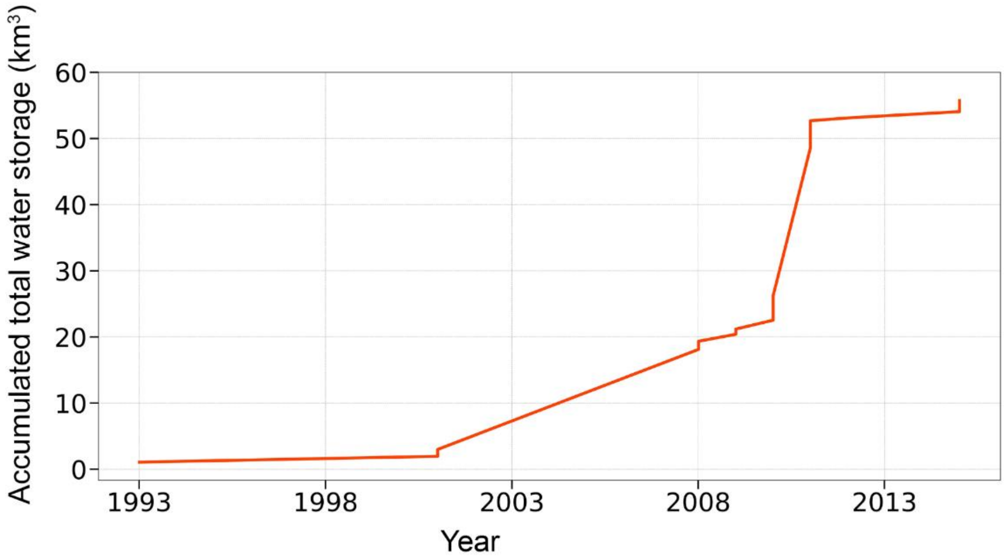

Figure 1. The cumulative total water storage of significant commissioned dams in the Mekong basin, spanning from the first major dam in 1993 to 2015, is based on data compiled from Binh et al., (2021)

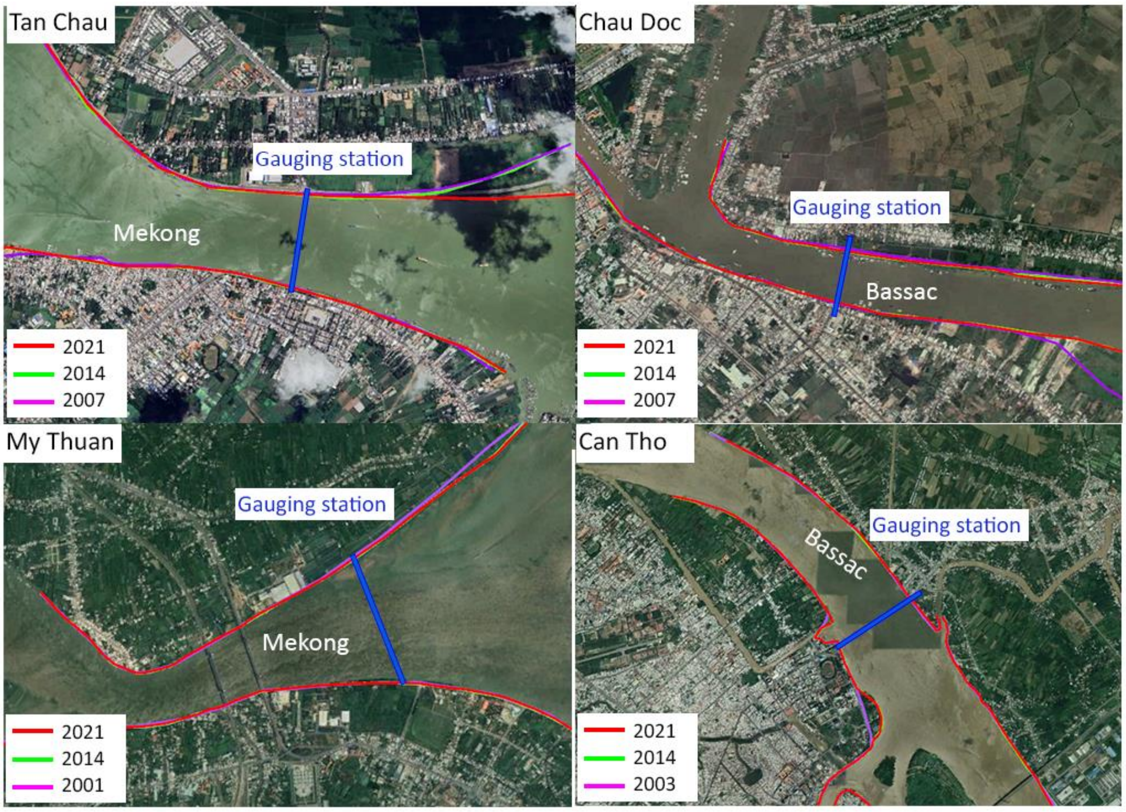

Figure 2. The temporal change of river bank lines at Tan Chau, My Thuan stations in Mekong channel and Chau Doc, Can Tho stations in Bassac channel base on the available historical Google Earth satellite images

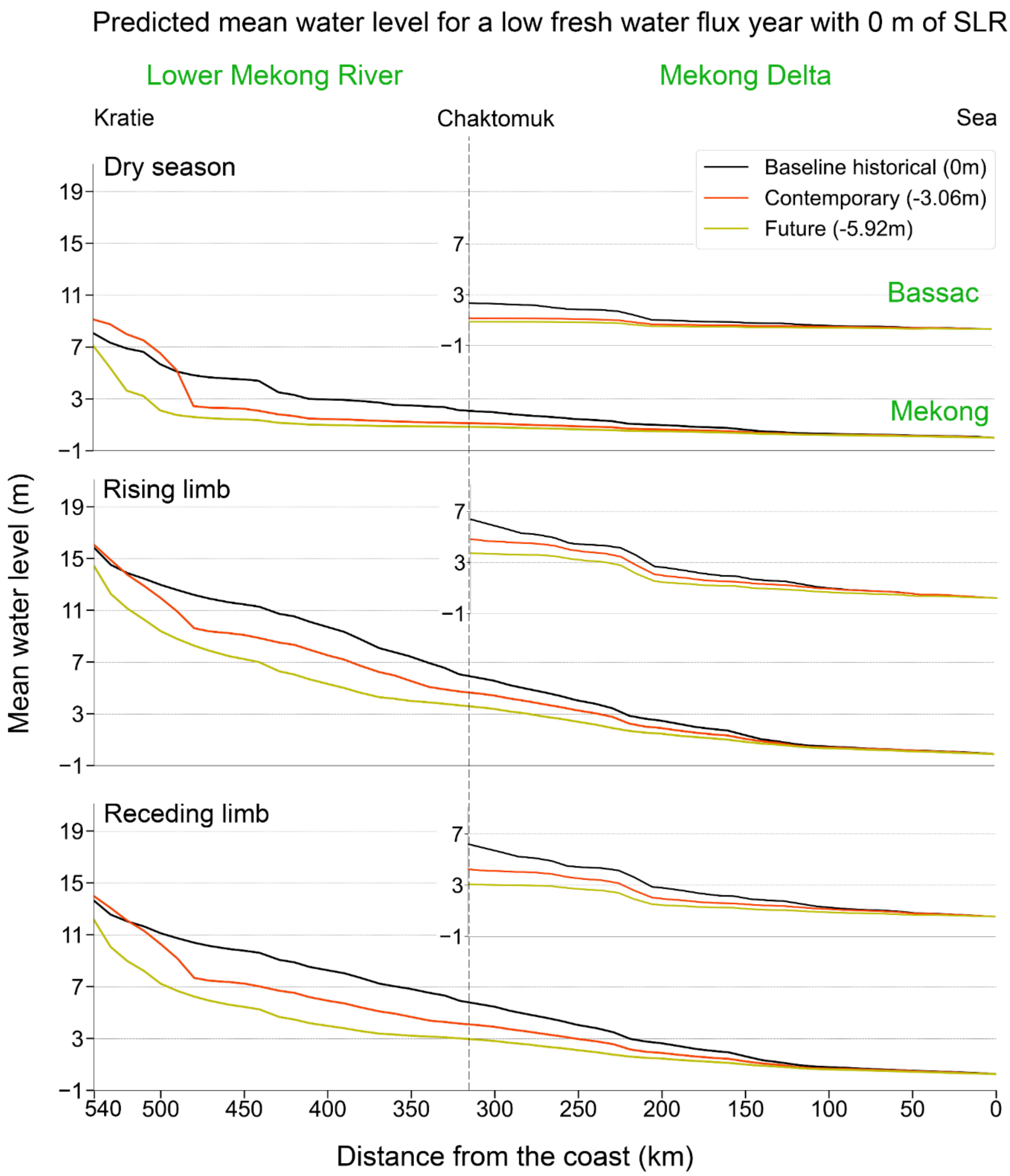

Figure 3. The longitudinal profile of mean water level ($\overline{WL}$) along the LMR, Mekong and Bassac distributary delta channels for the bathymetric scenarios investigated under low fresh water flux condition and 0 m sea level rise. The main panel focuses on the LMR and Mekong channel, while the insert panel shows the Bassac channel. All water levels are referenced to Hon Dau Mean Sea Level (MSL).

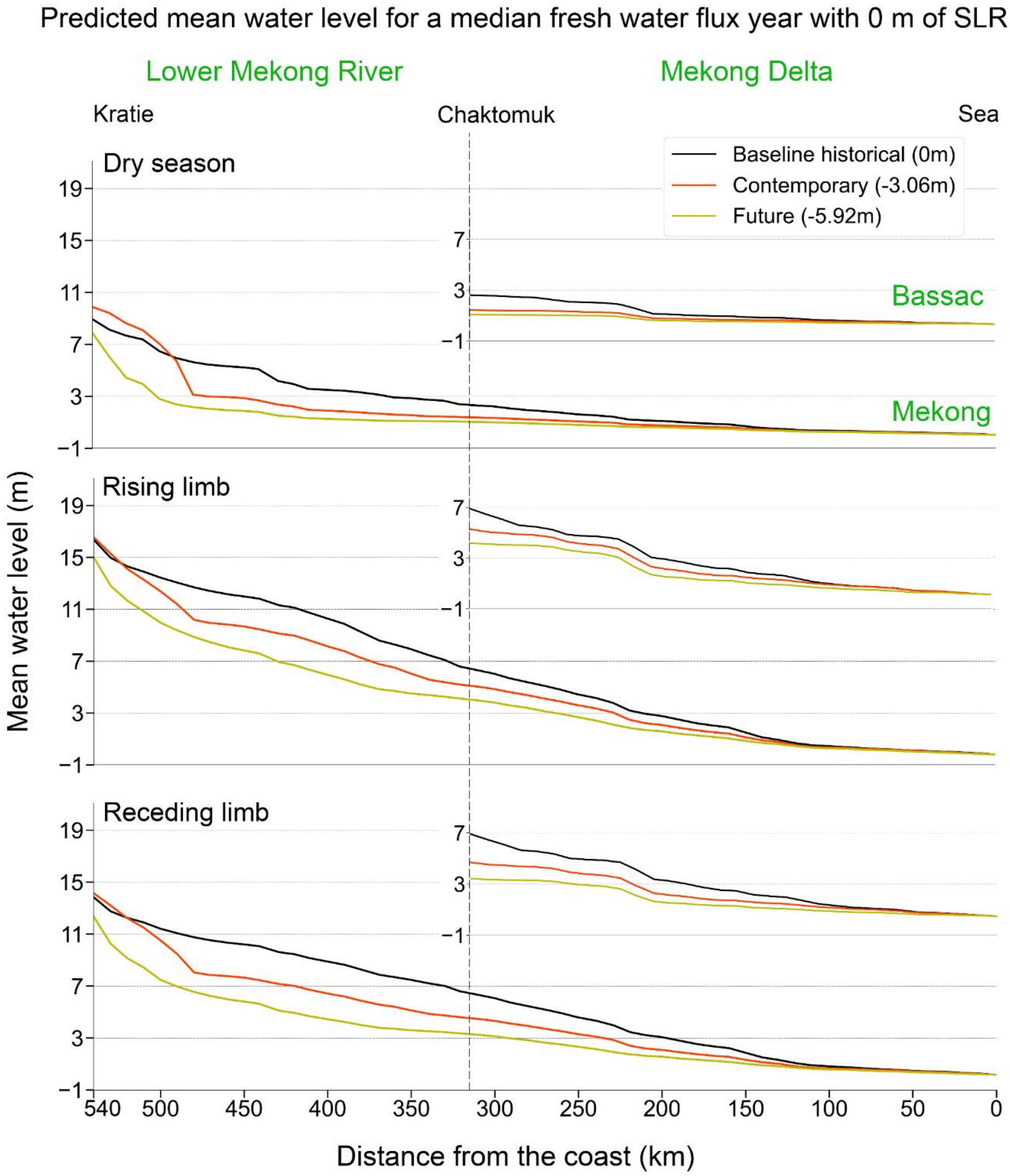

Figure 4. The longitudinal profile of mean water level ($\overline{WL}$) along the LMR, Mekong and Bassac distributary delta channels for the bathymetric scenarios investigated under median fresh water flux condition and 0 m sea level rise. The main panel focuses on the LMR and Mekong channel, while the insert panel shows the Bassac channel. All water levels are referenced to Hon Dau Mean Sea Level (MSL).

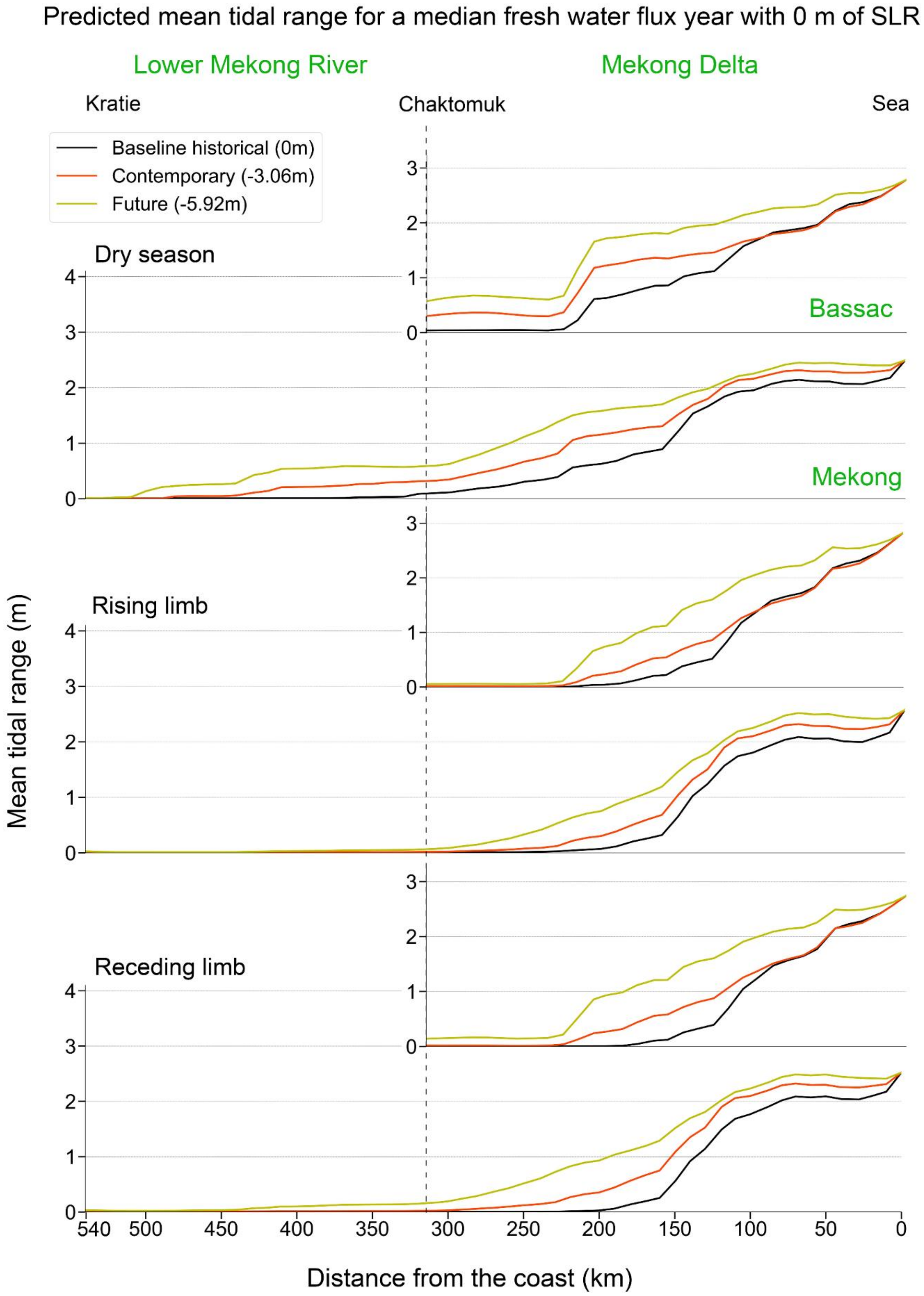

Figure 5. The longitudinal profile of mean tidal range ($\overline{TR}$) along the LMR, Mekong and Bassac distributary delta channels for the bathymetric scenarios investigated under median fresh water flux year and 0 m sea level rise. The main panel focuses on the LMR and Mekong channel, while the insert panel shows the Bassac channel.

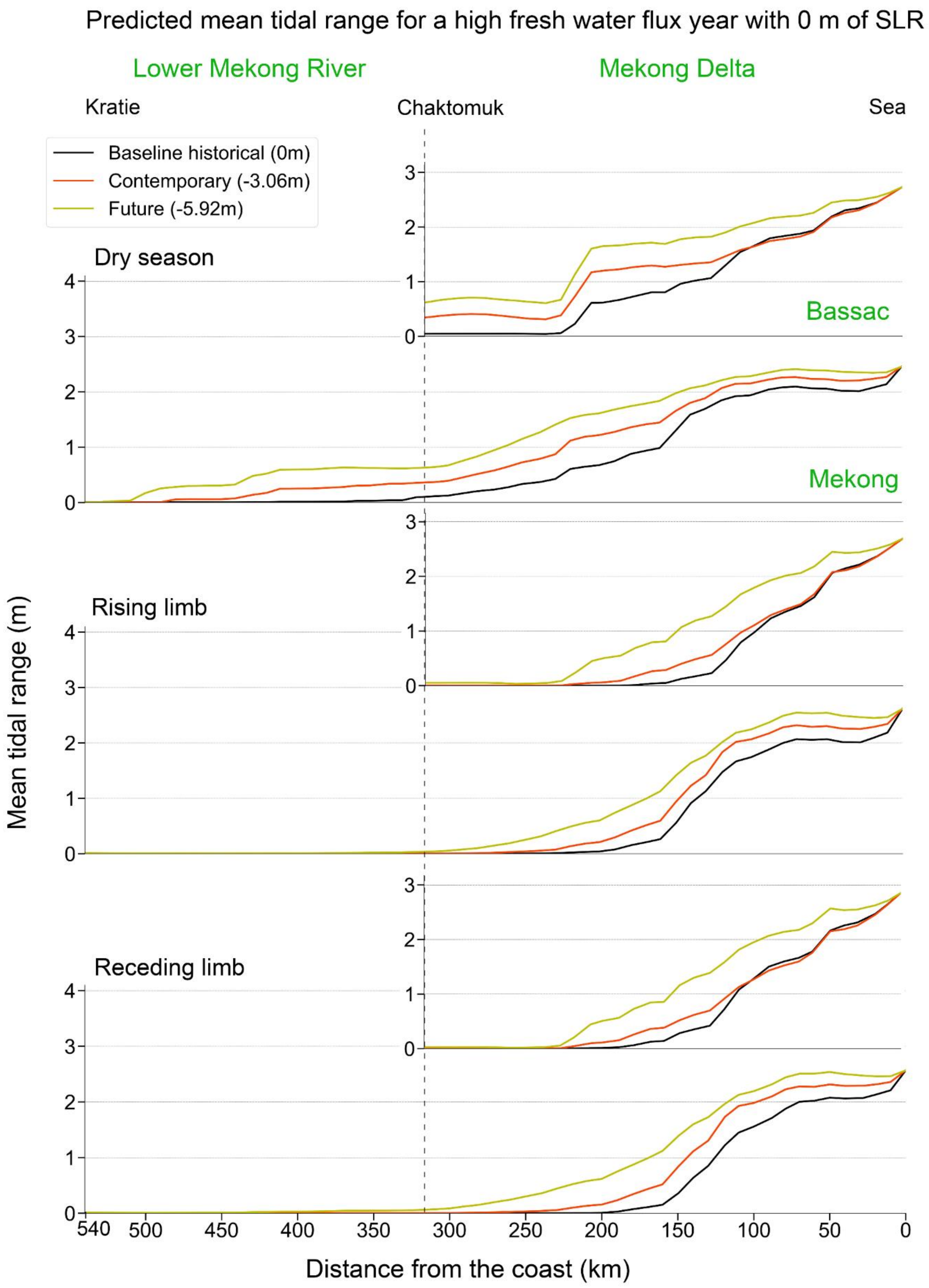

Figure 6. The longitudinal profile of mean tidal range ($\overline{TR}$) along the LMR, Mekong and Bassac distributary delta channels for the bathymetric scenarios investigated under high fresh water flux year and 0 m sea level rise. The main panel focuses on the LMR and Mekong channel, while the insert panel shows the Bassac channel.

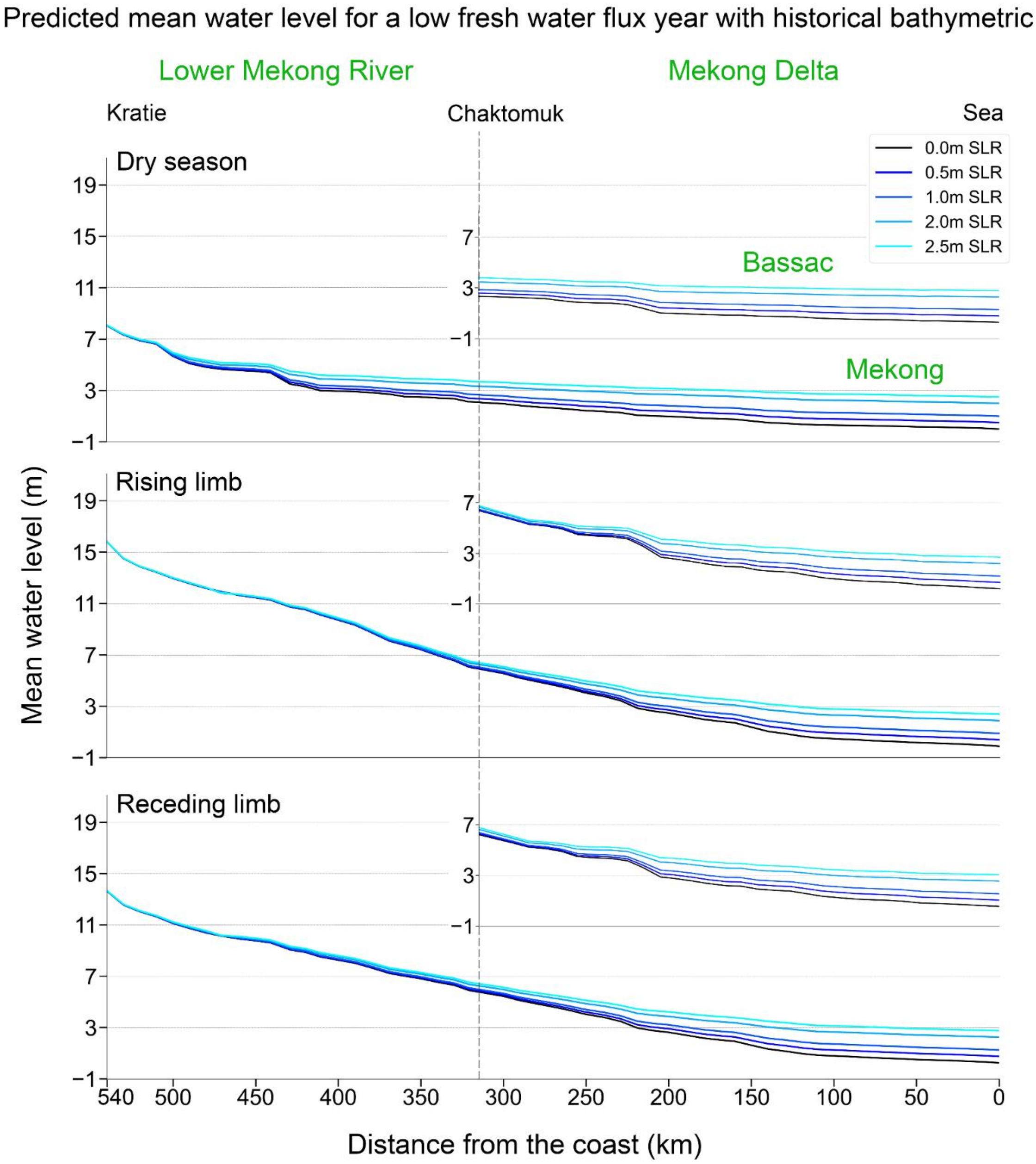

Figure 7. The longitudinal profile of mean water level $\overline{WL}$ along the LMR, Mekong and Bassac distributary delta channels for the sea level rise scenarios investigated under low fresh water flux and Historical bathymetric scenarios. The main panel focuses on the LMR and Mekong channel, while the insert panel shows the Bassac channel. All water levels are referenced to Hon Dau Mean Sea Level (MSL).

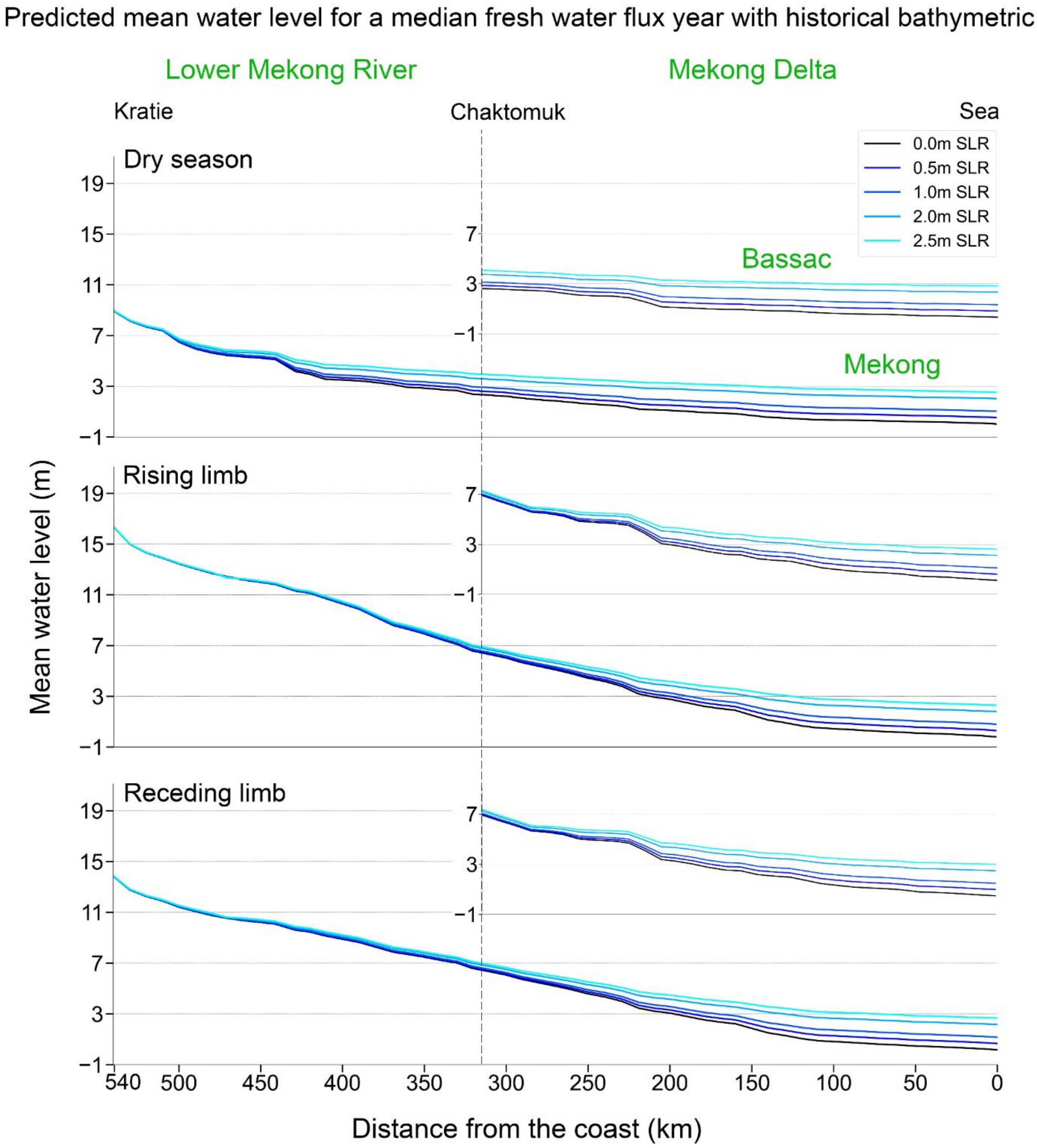

Figure 8. The longitudinal profile of mean water level $\overline{WL}$ along the LMR, Mekong and Bassac distributary delta channels for the sea level rise scenarios investigated under median fresh water flux and Historical bathymetric scenarios. The main panel focuses on the LMR and Mekong channel, while the insert panel shows the Bassac channel. All water levels are referenced to Hon Dau Mean Sea Level (MSL).

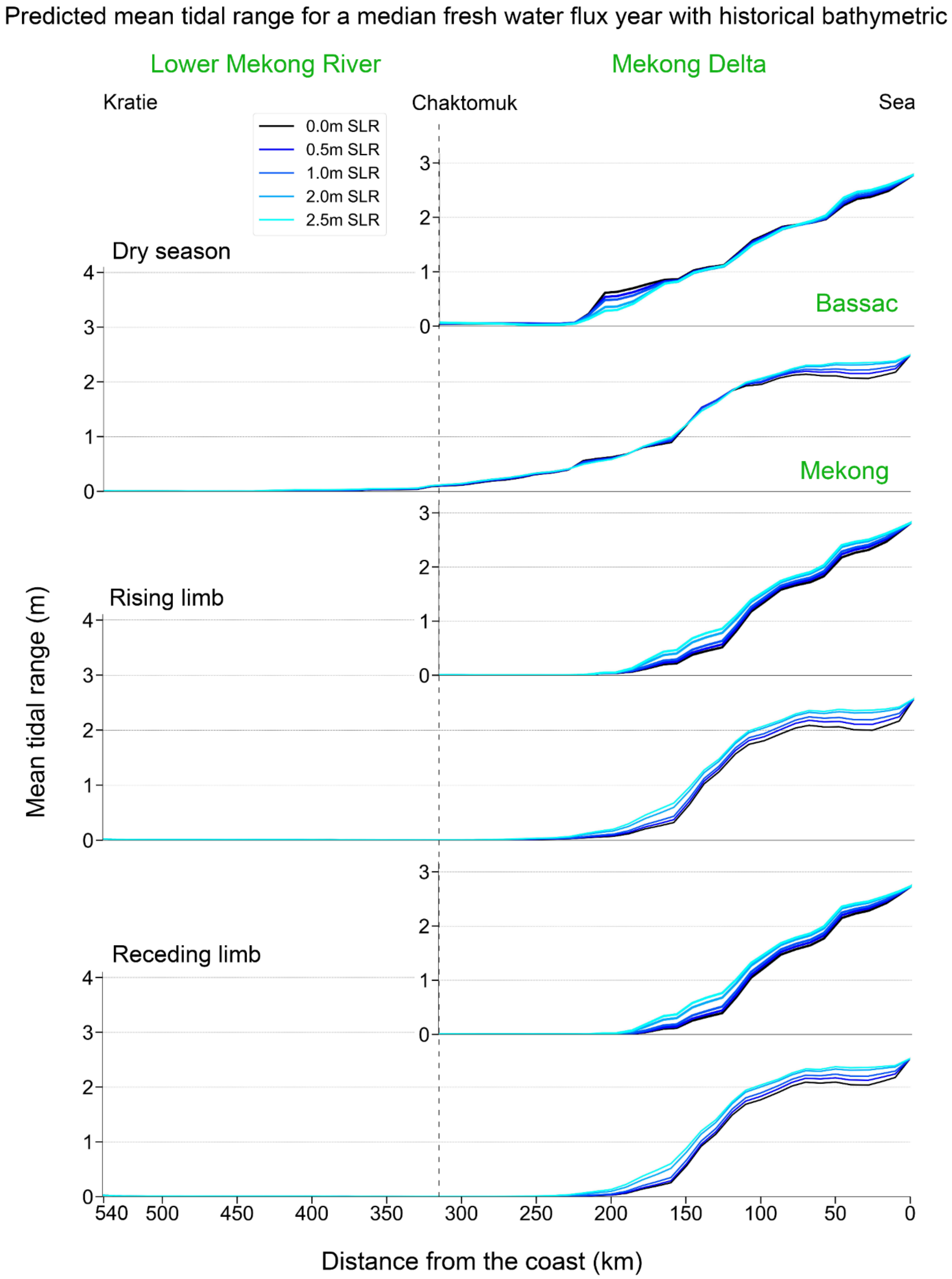

Figure 9. The longitudinal profile of mean tidal range ($\overline{TR}$) along the LMR, Mekong and Bassac distributary delta channels for sea level rise scenarios investigated under median fresh water flux and Historical bathymetric scenarios. The main panel focuses on the LMR and Mekong channel, while the insert panel shows the Bassac channel.

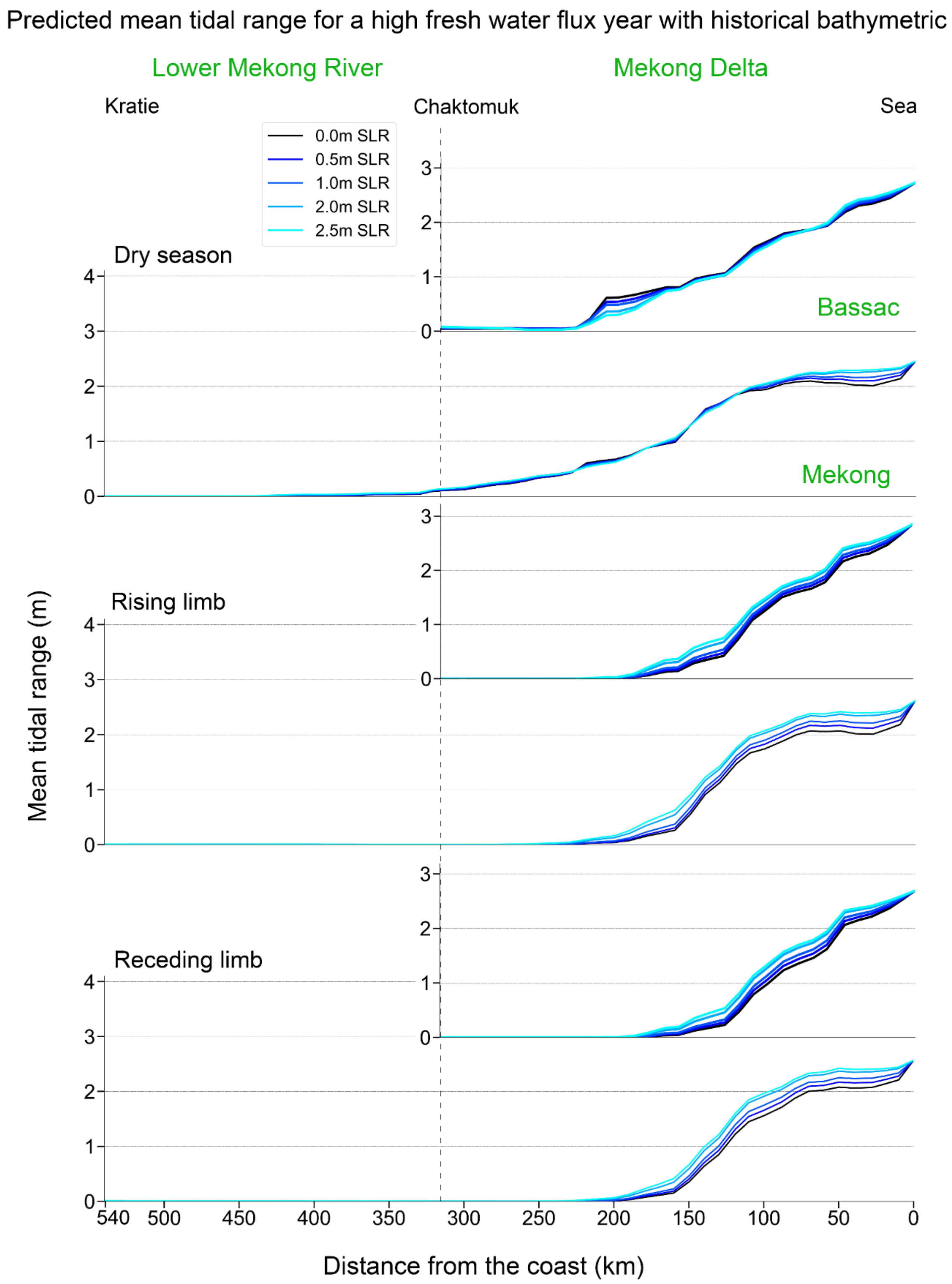

Figure 10. The longitudinal profile of mean tidal range ($\overline{TR}$) along the LMR, Mekong and Mekong and Bassac distributary delta channels for sea level rise scenarios investigated under high fresh water flux and Historical bathymetric scenarios. The main panel focuses on the LMR and Mekong channel, while the insert panel shows the Bassac channel.

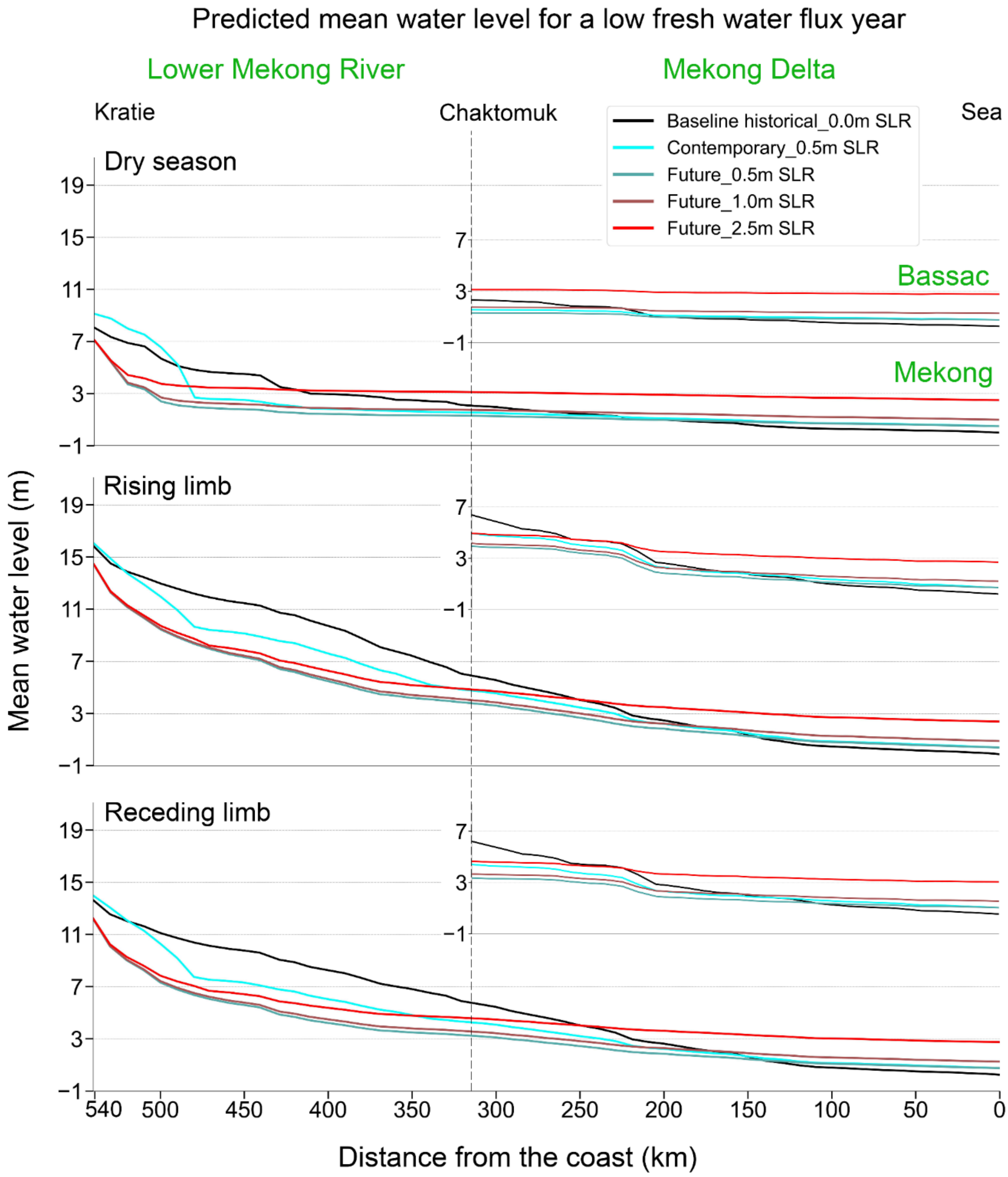

Figure 11. The longitudinal profile of mean water level ($\overline{WL}$) along the LMR, Mekong and Bassac distributary delta channels for Baseline historical bathymetry with a SLR of 0 m, Contemporary bathymetric scenario is combined with an SLR of 0.5 m and Future bathymetric scenario is combined with SLR scenarios of 0.5, 1 and 2.5 m under low water flux. The main panel focuses on the LMR and Mekong channel, while the insert panel shows the Bassac channel. All water levels are referenced to Hon Dau Mean Sea Level (MSL).

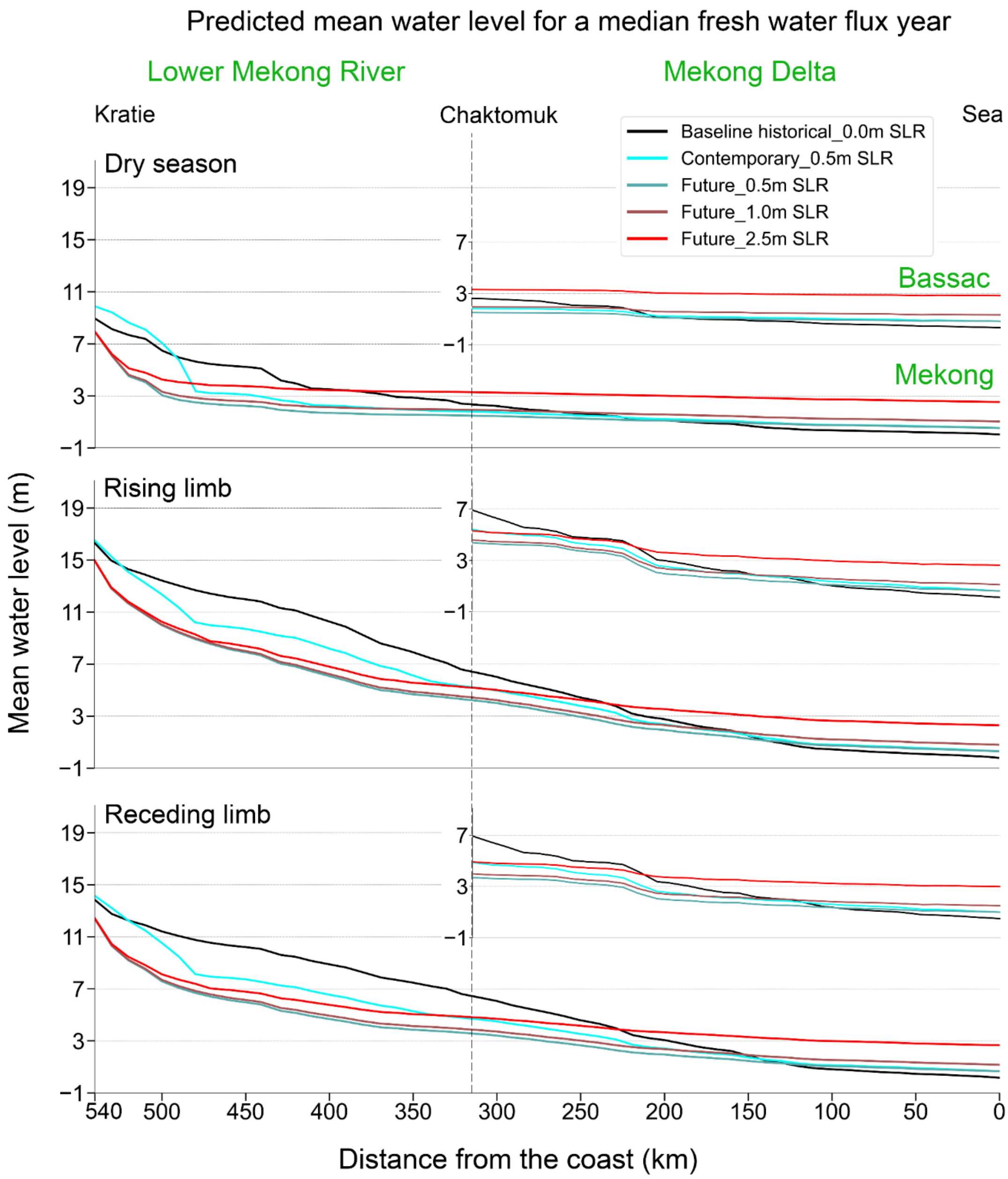

Figure 12. The longitudinal profile of mean water level ($\overline{WL}$) along the LMR, Mekong and Bassac distributary delta channels for Baseline historical bathymetry with a SLR of 0 m, Contemporary bathymetric scenario is combined with an SLR of 0.5 m and Future bathymetric scenario is combined with SLR scenarios of 0.5, 1 and 2.5 m under median water flux. The main panel focuses on the LMR and Mekong channel, while the insert panel shows the Bassac channel. All water levels are referenced to Hon Dau Mean Sea Level (MSL).

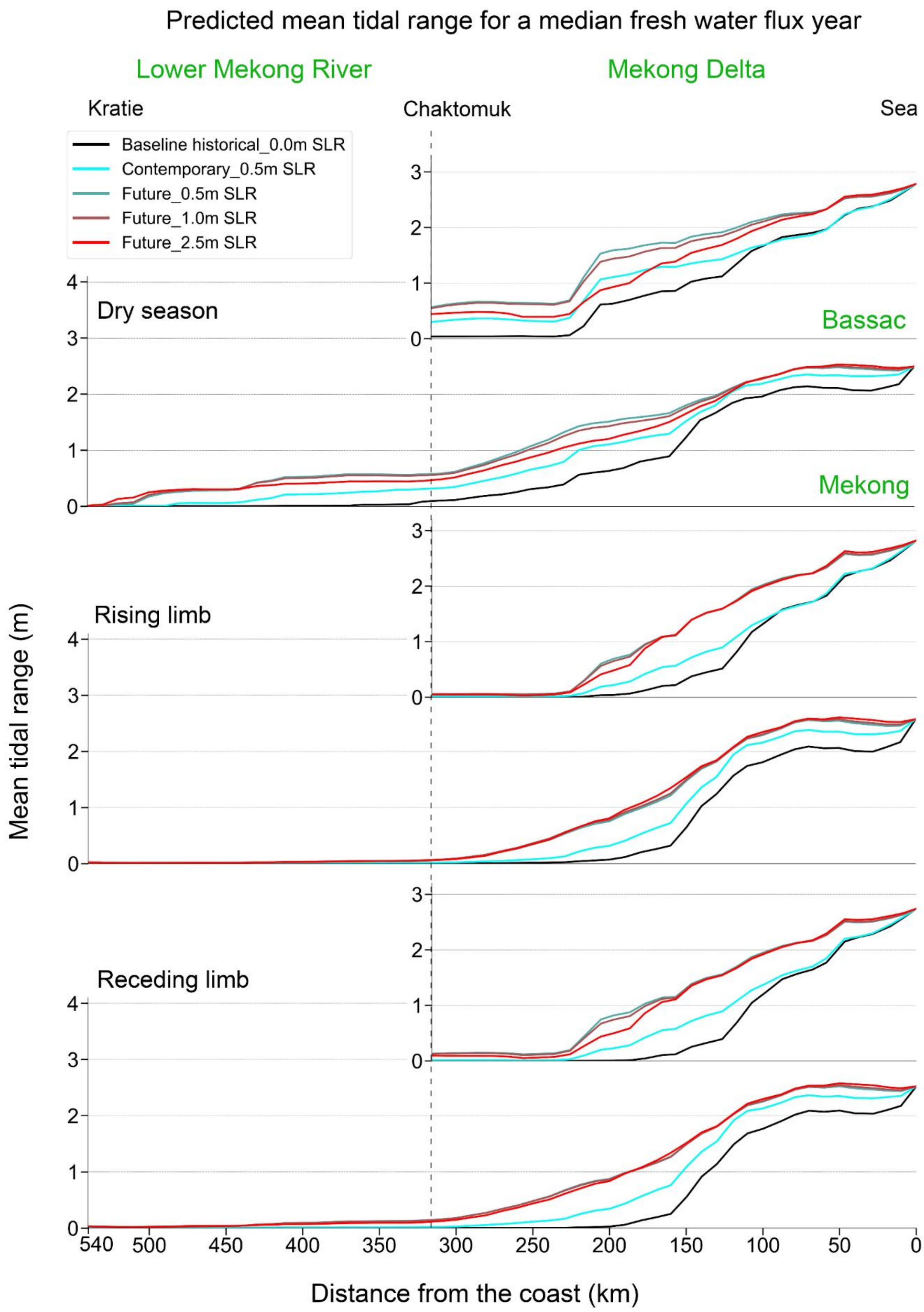

Figure 13. The longitudinal profile of mean tidal range ($\overline{TR}$) along the LMR, Mekong and Bassac distributary delta channels for the baseline historical bathymetry with a sea-level rise (SLR) of 0 m, the Contemporary bathymetric scenario combined with an SLR of 0.5 m, and the future bathymetric scenario combined with SLR scenarios of 0.5 m, 1 m, and 2.5 m under median fresh water flux. The main panel focuses on the LMR and Mekong channel, while the insert panel shows the Bassac channel.

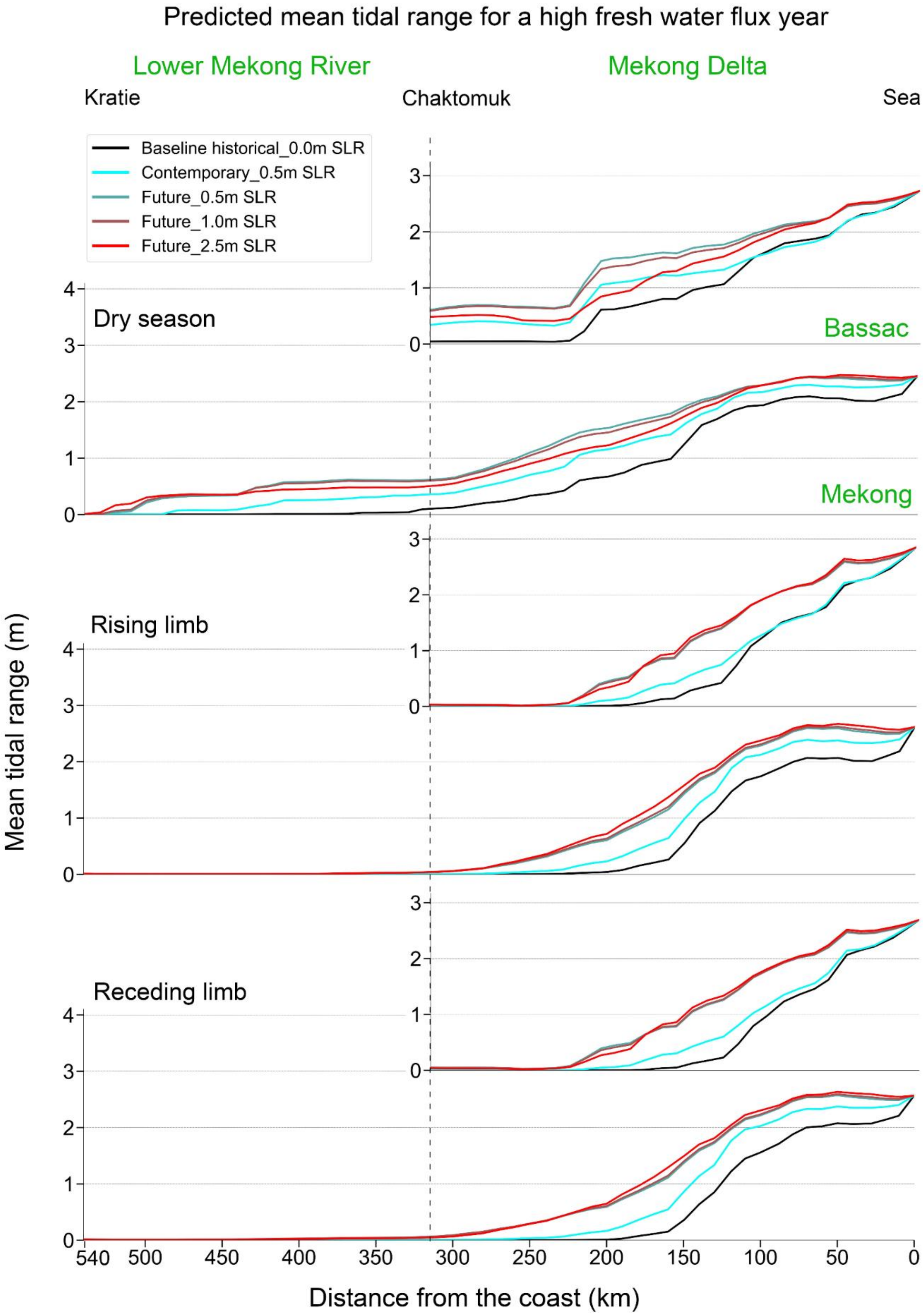

Figure 14. The longitudinal profile of mean tidal range ($\overline{TR}$) along the LMR, Mekong and Bassac distributary delta channels for the historical bathymetry with a sea-level rise (SLR) of 0 m, the Contemporary bathymetric scenario combined with an SLR of 0.5 m, and the future bathymetric scenario combined with SLR scenarios of 0.5 m, 1 m, and 2.5 m under high water flux. The main panel focuses on the LMR and Mekong channel, while the insert panel shows the Bassac channel.

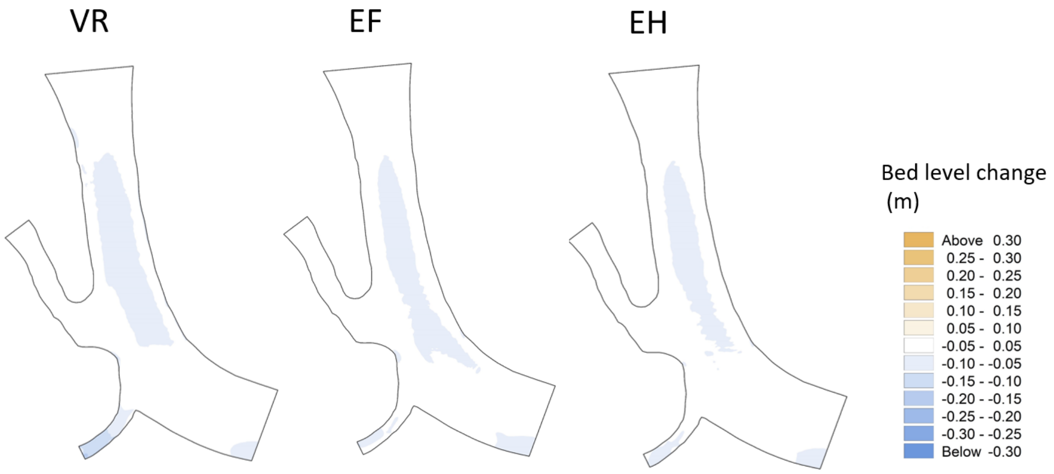

Figure 15. The simulated evolution in riverbed elevation is forecasted exclusively for the suspended sediment transport module, considering different scenarios of sand transport equations spanning from 12 September 2013 to 27 October 2013. The labels positioned at the top of each panel indicate the specific sand transport equations utilized in the respective scenarios.

Table 1. The offset between the local vertical datum at Cambodian measuring gauges and the Ha Tien MSL (m)

No.	Gauges (code)	Zero gauge above Ha Tien M.S.L (m)	No.	Gauges (code)	Zero gauge above Ha Tien M.S.L (m)
1	Kraite (KH_014901)	-1.08	5	Prek Kdam (KH_020102)	0.08
2	Kompong Cham (KH_019802)	-0.93	6	Kompong Luong (KH_020106)	0.64
3	Chroy Chang Var (KH_019801)	-1.08	7	Neak Luong (KH_019806)	-0.33
4	Chaktomuk (KH_033401)	-1.02	8	Koh Khel (KH_033402)	-1.00

Table 2. The linear regression analysis of the mean water level and mean water discharge at four gauging stations in the VMD covers the period from 2000 to 2021 during the dry season.

	Tan Chau				My Thuan				Chau Doc				Can Tho			
Year	Slope	Intercept	R^2	P-	Slope	Intercept	R^2	P-	Slope	Intercept	R^2	P-	Slope	Intercept	R^2	P-
2000	1.78E-04	0.28	0.81	<0.01	3.06E-05	0.25	0.06	<0.01	4.63E-04	0.33	0.76	<0.01	4.26E-05	0.12	0.11	<0.01
2001	1.61E-04	0.32	0.79	<0.01	3.23E-05	0.23	0.05	<0.01	4.59E-04	0.36	0.75	<0.01	4.99E-05	0.09	0.16	<0.01
2002	1.57E-04	0.37	0.84	<0.01	5.75E-05	0.16	0.16	<0.01	5.42E-04	0.31	0.79	<0.01	5.16E-05	0.10	0.17	<0.01
2003	1.45E-04	0.33	0.82	<0.01	3.80E-05	0.17	0.07	<0.01	5.04E-04	0.27	0.77	<0.01	6.06E-05	0.06	0.15	<0.01
2004	1.20E-04	0.41	0.75	<0.01	3.48E-05	0.17	0.07	<0.01	4.44E-04	0.32	0.69	<0.01	2.78E-05	0.12	0.06	<0.01
2005	1.34E-04	0.32	0.69	<0.01	3.92E-05	0.10	0.10	<0.01	5.74E-04	0.22	0.79	<0.01	4.26E-05	0.10	0.14	<0.01
2006	1.45E-04	0.27	0.73	<0.01	6.87E-05	0.07	0.14	<0.01	5.18E-04	0.27	0.70	<0.01	6.59E-05	0.11	0.20	<0.01
2007	1.35E-04	0.34	0.76	<0.01	3.26E-05	0.14	0.08	<0.01	3.89E-04	0.37	0.69	<0.01	2.67E-05	0.18	0.05	<0.01
2008	1.05E-04	0.50	0.69	<0.01	1.57E-05	0.24	0.02	0.10	3.01E-04	0.48	0.62	<0.01	6.07E-06	0.22	0.00	0.46
2009	9.15E-05	0.55	0.59	<0.01	-1.07E-05	0.28	0.01	0.22	3.62E-04	0.40	0.57	<0.01	3.63E-05	0.21	0.06	<0.01
2010	1.13E-04	0.40	0.71	<0.01	4.57E-05	0.13	0.11	<0.01	4.32E-04	0.32	0.68	<0.01	4.88E-05	0.15	0.16	<0.01
2011	9.18E-05	0.56	0.50	<0.01	-1.80E-05	0.34	0.02	0.08	2.85E-04	0.53	0.39	<0.01	1.44E-05	0.30	0.01	0.13
2012	1.24E-04	0.33	0.64	<0.01	1.05E-05	0.18	0.00	0.40	3.91E-04	0.36	0.52	<0.01	1.48E-05	0.25	0.01	0.17
2013	8.38E-05	0.54	0.52	<0.01	2.05E-05	0.23	0.02	0.03	3.36E-04	0.48	0.45	<0.01	3.26E-05	0.26	0.06	<0.01
2014	1.12E-04	0.35	0.55	<0.01	5.72E-05	0.03	0.14	0.00	4.28E-04	0.38	0.63	<0.01	6.07E-05	0.16	0.15	<0.01
2015	1.01E-04	0.36	0.49	<0.01	2.83E-05	0.12	0.02	0.02	3.68E-04	0.40	0.53	<0.01	7.15E-05	0.12	0.22	<0.01
2016	1.08E-04	0.40	0.50	<0.01	-1.42E-05	0.29	0.01	0.15	3.27E-04	0.47	0.57	<0.01	3.33E-05	0.25	0.05	<0.01
2017	8.24E-05	0.52	0.44	<0.01	-8.83E-06	0.35	0.00	0.41	2.79E-04	0.58	0.43	<0.01	3.03E-05	0.31	0.06	<0.01
2018	7.74E-05	0.53	0.36	<0.01	-2.26E-05	0.36	0.02	0.06	2.62E-04	0.59	0.35	<0.01	-9.46E-06	0.41	0.01	0.28
2019	8.36E-05	0.41	0.29	<0.01	2.80E-05	0.14	0.02	0.02	3.49E-04	0.48	0.38	<0.01	4.42E-05	0.23	0.06	<0.01
2020	6.66E-05	0.48	0.35	<0.01	-1.79E-06	0.25	0.00	0.81	3.95E-04	0.43	0.54	<0.01	4.44E-05	0.28	0.11	<0.01
2021	5.55E-05	0.55	0.31	<0.01	-2.40E-05	0.34	0.05	<0.01	2.91E-04	0.55	0.52	<0.01	2.69E-05	0.34	0.03	0.01

Table 3. The linear regression analysis of the mean water level and mean water discharge at four gauging stations in the VMD covers the period from 2000 to 2021 during the rising limb period.

	Tan Chau				My Thuan				Chau Doc				Can Tho			
Year	Slope	Intercept	R^2	P-	Slope	Intercept	R^2	P-	Slope	Intercept	R^2	P-	Slope	Intercept	R^2	P-
2000	2.45E-04	-1.33	0.76	<0.01	7.82E-05	-0.29	0.51	<0.01	7.03E-04	-0.73	0.99	<0.01	3.86E-05	0.09	0.38	<0.01
2001	2.48E-04	-1.03	0.95	<0.01	7.38E-05	-0.24	0.70	<0.01	7.03E-04	-0.63	0.99	<0.01	5.19E-05	-0.09	0.54	<0.01
2002	2.10E-04	-0.55	0.99	<0.01	8.15E-05	-0.37	0.71	<0.01	6.93E-04	-0.58	0.97	<0.01	4.87E-05	-0.04	0.60	<0.01
2003	2.00E-04	-0.43	0.99	<0.01	8.45E-05	-0.30	0.58	<0.01	5.37E-04	0.15	0.97	<0.01	6.56E-05	-0.18	0.43	<0.01
2004	2.81E-04	-1.76	0.90	<0.01	8.23E-05	-0.39	0.47	<0.01	6.97E-04	-0.68	0.99	<0.01	5.08E-05	-0.07	0.40	<0.01
2005	2.57E-04	-1.22	0.94	<0.01	9.34E-05	-0.66	0.59	<0.01	5.96E-04	-0.18	0.98	<0.01	7.33E-05	-0.35	0.40	<0.01
2006	2.55E-04	-1.42	0.97	<0.01	7.91E-05	-0.40	0.64	<0.01	6.16E-04	-0.39	0.96	<0.01	4.85E-05	-0.05	0.53	<0.01
2007	2.37E-04	-1.10	0.97	<0.01	9.95E-05	-0.70	0.65	<0.01	5.95E-04	-0.47	0.98	<0.01	5.90E-05	-0.06	0.27	<0.01
2008	2.67E-04	-1.61	0.93	<0.01	6.44E-05	-0.30	0.61	<0.01	5.89E-04	-0.39	0.98	<0.01	6.77E-05	-0.29	0.65	<0.01
2009	2.89E-04	-2.18	0.87	<0.01	8.09E-05	-0.49	0.54	<0.01	5.83E-04	-0.49	0.96	<0.01	5.59E-05	-0.05	0.28	<0.01
2010	2.21E-04	-1.01	0.97	<0.01	4.77E-05	0.00	0.26	<0.01	4.82E-04	-0.08	0.95	<0.01	4.15E-05	0.20	0.23	<0.01
2011	2.76E-04	-2.01	0.95	<0.01	5.17E-05	-0.19	0.68	<0.01	5.62E-04	-0.45	0.99	<0.01	5.34E-05	-0.03	0.60	<0.01
2012	1.98E-04	-0.83	0.96	<0.01	6.87E-05	-0.36	0.44	<0.01	4.31E-04	0.09	0.93	<0.01	6.83E-05	-0.14	0.57	<0.01

	Tan Chau				My Thuan				Chau Doc				Can Tho			
Year	Slope	Intercept	R^2	P-	Slope	Intercept	R^2	P-	Slope	Intercept	R^2	P-	Slope	Intercept	R^2	P-
2013	2.37E-04	-1.64	0.90	<0.01	5.74E-05	-0.29	0.58	<0.01	4.99E-04	-0.21	0.93	<0.01	5.56E-05	-0.02	0.44	<0.01
2014	2.04E-04	-1.12	0.96	<0.01	4.61E-05	-0.16	0.37	<0.01	4.90E-04	-0.17	0.96	<0.01	5.48E-05	-0.04	0.48	<0.01
2015	1.96E-04	-1.06	0.89	<0.01	3.02E-05	0.00	0.06	<0.01	2.57E-04	0.59	0.34	<0.01	2.41E-05	0.28	0.05	0.11
2016	1.96E-04	-0.92	0.93	<0.01	6.18E-05	-0.32	0.37	<0.01	5.93E-04	-0.54	0.99	<0.01	7.08E-05	-0.13	0.53	<0.01
2017	2.10E-04	-1.13	0.95	<0.01	4.32E-05	-0.15	0.47	<0.01	5.09E-04	-0.17	0.92	<0.01	5.44E-05	0.08	0.33	<0.01
2018	2.02E-04	-1.17	0.97	<0.01	4.41E-05	-0.27	0.76	<0.01	5.24E-04	-0.22	0.96	<0.01	3.71E-05	0.21	0.30	<0.01
2019	1.93E-04	-1.40	0.90	<0.01	4.24E-05	-0.24	0.71	<0.01	4.53E-04	0.06	0.95	<0.01	5.78E-05	-0.02	0.68	<0.01
2020	1.49E-04	-0.72	0.90	<0.01	7.66E-05	-0.37	0.32	<0.01	4.78E-04	0.07	0.75	<0.01	8.01E-05	0.00	0.52	<0.01
2021	1.14E-04	-0.09	0.89	<0.01	6.10E-05	-0.29	0.38	<0.01	3.89E-04	0.33	0.86	<0.01	7.03E-05	-0.01	0.43	<0.01

Table 4. The linear regression analysis of the mean water level and mean water discharge at four gauging stations in the VMD covers the period from 2000 to 2021 during the receding limb period.

	Tan Chau				My Thuan				Chau Doc				Can Tho			
Year	Slope	Intercept	R^2	P-	Slope	Intercept	R^2	P-	Slope	Intercept	R^2	P-	Slope	Intercept	R^2	P-
2000	2.07E-04	0.64	0.91	<0.01	5.74E-05	0.40	0.59	<0.01	6.87E-04	0.27	0.96	<0.01	3.13E-05	0.49	0.29	<0.01
2001	2.73E-04	-1.01	0.98	<0.01	5.16E-05	0.42	0.59	<0.01	6.62E-04	-0.10	0.99	<0.01	3.88E-05	0.41	0.33	<0.01
2002	2.40E-04	-0.44	0.98	<0.01	4.77E-05	0.43	0.53	<0.01	6.62E-04	-0.09	0.99	<0.01	2.80E-05	0.52	0.31	<0.01
2003	2.06E-04	-0.08	0.96	<0.01	5.27E-05	0.32	0.44	<0.01	5.77E-04	0.21	1.00	<0.01	1.16E-05	0.68	0.05	0.11
2004	2.75E-04	-1.08	0.99	<0.01	4.70E-05	0.40	0.51	<0.01	6.22E-04	0.07	0.99	<0.01	3.80E-05	0.44	0.43	<0.01
2005	2.22E-04	-0.16	0.95	<0.01	3.02E-05	0.51	0.30	<0.01	5.63E-04	0.22	0.99	<0.01	2.84E-05	0.52	0.24	<0.01
2006	2.64E-04	-1.06	0.98	<0.01	6.04E-05	0.13	0.50	<0.01	5.92E-04	0.01	0.99	<0.01	2.02E-05	0.59	0.12	<0.01
2007	2.68E-04	-1.23	0.97	<0.01	5.11E-05	0.23	0.59	<0.01	5.41E-04	0.09	0.99	<0.01	4.91E-05	0.37	0.44	<0.01
2008	2.53E-04	-1.01	0.97	<0.01	1.33E-05	0.65	0.06	0.02	4.96E-04	0.25	0.98	<0.01	4.97E-05	0.35	0.61	<0.01
2009	2.60E-04	-1.18	0.97	<0.01	1.88E-05	0.60	0.09	0.04	5.35E-04	0.01	0.97	<0.01	2.39E-05	0.57	0.16	<0.01
2010	2.04E-04	-0.44	0.97	<0.01	4.02E-05	0.31	0.24	<0.01	3.98E-04	0.56	0.97	<0.01	2.44E-05	0.60	0.13	0.01
2011	2.47E-04	-0.93	0.98	<0.01	3.07E-05	0.47	0.50	<0.01	5.08E-04	0.17	0.99	<0.01	3.36E-05	0.55	0.51	<0.01
2012	1.96E-04	-0.44	0.98	<0.01	1.59E-05	0.54	0.08	0.04	4.21E-04	0.46	0.95	<0.01	3.39E-05	0.50	0.21	<0.01
2013	2.24E-04	-0.82	0.98	<0.01	3.61E-05	0.38	0.42	<0.01	4.87E-04	0.26	0.98	<0.01	3.95E-05	0.50	0.48	<0.01
2014	1.83E-04	-0.38	0.96	<0.01	1.80E-05	0.51	0.09	0.02	4.01E-04	0.41	0.96	<0.01	2.20E-05	0.62	0.06	0.03
2015	1.14E-04	0.47	0.86	<0.01	-1.45E-05	0.74	0.01	0.60	1.35E-04	1.28	0.16	<0.01	-2.48E-06	0.74	<0.01	0.85
2016	1.67E-04	-0.20	0.96	<0.01	-4.91E-07	0.67	<0.01	0.95	4.20E-04	0.41	0.91	<0.01	1.15E-05	0.70	0.02	0.21
2017	1.95E-04	-0.63	0.95	<0.01	9.30E-06	0.63	0.04	0.08	4.21E-04	0.63	0.84	<0.01	2.66E-05	0.67	0.20	<0.01
2018	1.97E-04	-0.80	0.98	<0.01	2.15E-05	0.46	0.20	<0.01	4.94E-04	0.28	0.97	<0.01	3.68E-05	0.53	0.41	<0.01
2019	1.53E-04	-0.29	0.95	<0.01	1.27E-05	0.53	0.07	0.11	4.65E-04	0.25	0.97	<0.01	3.26E-05	0.55	0.29	<0.01
2020	1.06E-04	0.36	0.94	<0.01	1.46E-05	0.56	0.07	0.07	4.59E-04	0.09	0.85	<0.01	3.29E-05	0.61	0.18	0.01
2021	1.00E-04	0.40	0.92	<0.01	-9.91E-06	0.84	0.04	0.18	3.17E-04	0.77	0.92	<0.01	-2.91E-09	0.89	<0.01	0.77

Table 5. The linear regression analysis of the tidal range and mean water discharge at four gauging stations in the VMD covers the period from 2000 to 2021 during the dry season.

	Tan Chau				My Thuan				Chau Doc				Can Tho			
Year	Slope	Intercept	R^2	P-	Slope	Intercept	R^2	P-	Slope	Intercept	R^2	P-	Slope	Intercept	R^2	P-
2000	-8.16E-05	1.05	0.78	<0.01	-9.34E-06	1.56	0.01	0.26	-2.67E-04	1.03	0.99	<0.01	-2.25E-05	1.84	0.03	0.04
2001	-7.12E-05	1.02	0.87	<0.01	-1.99E-05	1.62	0.03	0.04	-2.69E-04	1.01	0.99	<0.01	-5.40E-05	1.96	0.14	<0.01
2002	-6.47E-05	1.02	0.79	<0.01	-2.22E-05	1.63	0.04	0.01	-2.91E-04	1.05	0.97	<0.01	-4.62E-05	1.99	0.11	<0.01
2003	-6.94E-05	1.05	0.83	<0.01	-2.19E-05	1.67	0.04	<0.01	-2.86E-04	1.08	0.97	<0.01	-4.06E-05	1.96	0.07	<0.01
2004	-5.60E-05	1.03	0.80	<0.01	-1.35E-05	1.69	0.02	0.03	-2.61E-04	1.12	0.99	<0.01	-3.22E-05	1.93	0.07	<0.01
2005	-5.04E-05	1.05	0.63	<0.01	-1.48E-05	1.81	0.02	0.02	-2.92E-04	1.16	0.98	<0.01	-3.57E-05	1.99	0.09	<0.01
2006	-6.52E-05	1.16	0.73	<0.01	-5.21E-05	1.92	0.11	<0.01	-3.04E-04	1.21	0.96	<0.01	-5.50E-05	2.00	0.14	<0.01
2007	-5.39E-05	1.13	0.61	<0.01	-2.05E-05	1.90	0.04	<0.01	-2.54E-04	1.26	0.98	<0.01	-3.74E-05	1.98	0.08	<0.01
2008	-4.81E-05	1.11	0.59	<0.01	-2.35E-06	1.85	0.00	0.81	-2.22E-04	1.23	0.98	<0.01	-1.82E-05	1.95	0.02	0.05
2009	-4.94E-05	1.13	0.72	<0.01	-1.10E-05	1.89	0.01	0.19	-2.25E-04	1.27	0.96	<0.01	-5.27E-05	1.99	0.10	<0.01
2010	-4.33E-05	1.16	0.57	<0.01	-2.21E-05	1.95	0.03	0.02	-2.13E-04	1.32	0.95	<0.01	-6.90E-05	2.08	0.19	<0.01
2011	-4.01E-05	1.17	0.53	<0.01	-9.07E-06	1.94	0.01	0.37	-1.95E-04	1.34	0.99	<0.01	-3.90E-05	2.03	0.08	<0.01
2012	-5.73E-05	1.27	0.64	<0.01	-7.75E-06	2.00	0.01	0.51	-1.90E-04	1.36	0.93	<0.01	-3.70E-05	2.01	0.06	<0.01
2013	-4.18E-05	1.26	0.55	<0.01	-1.16E-05	2.04	0.01	0.21	-1.89E-04	1.42	0.93	<0.01	-6.05E-05	2.09	0.15	<0.01
2014	-5.33E-05	1.32	0.49	<0.01	-2.29E-05	2.07	0.02	0.08	-2.18E-04	1.42	0.96	<0.01	-4.14E-05	1.96	0.06	<0.01
2015	-3.66E-05	1.30	0.36	<0.01	-1.59E-05	2.12	0.01	0.16	-1.86E-04	1.45	0.56	<0.01	-5.95E-05	2.06	0.16	<0.01
2016	-2.71E-05	1.30	0.20	<0.01	4.78E-06	2.10	<0.01	0.66	-1.75E-04	1.49	0.99	<0.01	-1.84E-05	1.98	0.01	0.11
2017	-3.79E-05	1.38	0.37	<0.01	-8.22E-06	2.13	<0.01	0.53	-1.62E-04	1.50	0.92	<0.01	-4.59E-05	2.00	0.09	<0.01
2018	-2.36E-05	1.35	0.13	<0.01	1.65E-05	2.10	0.01	0.32	-1.51E-04	1.52	0.96	<0.01	-1.57E-05	1.94	0.01	0.17
2019	-2.77E-05	1.43	0.14	<0.01	-1.00E-05	2.24	<0.01	0.47	-1.97E-04	1.59	0.95	<0.01	-5.03E-05	2.09	0.05	<0.01
2020	-1.55E-05	1.43	0.07	<0.01	-1.85E-05	2.32	0.01	0.05	-1.74E-04	1.62	0.75	<0.01	-6.91E-05	2.15	0.14	<0.01
2021	-2.09E-05	1.51	0.14	<0.01	9.69E-06	2.26	<0.01	0.32	-2.34E-04	1.70	0.86	<0.01	-1.92E-05	2.06	0.01	0.08

Table 6. The linear regression analysis of the tidal range and mean water discharge at four gauging stations in the VMD covers the period from 2000 to 2021 during the rising limb period.

	Tan Chau				My Thuan				Chau Doc				Can Tho			
Year	Slope	Intercept	R^2	P-	Slope	Intercept	R^2	P-	Slope	Intercept	R^2	P-	Slope	Intercept	R^2	P-
2000	-3.00E-05	0.74	0.75	<0.01	-8.30E-05	2.25	0.58	<0.01	-5.73E-05	0.43	0.75	<0.01	-6.77E-05	2.08	0.53	<0.01
2001	-1.90E-05	0.46	0.59	<0.01	-6.35E-05	2.03	0.60	<0.01	-4.79E-05	0.36	0.69	<0.01	-7.33E-05	2.17	0.46	<0.01
2002	-2.76E-05	0.65	0.74	<0.01	-6.66E-05	2.06	0.53	<0.01	-7.32E-05	0.50	0.84	<0.01	-5.25E-05	1.97	0.47	<0.01
2003	-2.31E-05	0.53	0.60	<0.01	-5.72E-05	1.94	0.32	<0.01	-7.97E-05	0.49	0.77	<0.01	-8.57E-05	2.27	0.27	<0.01
2004	-3.66E-05	0.80	0.86	<0.01	-5.34E-05	2.01	0.33	<0.01	-8.28E-05	0.54	0.82	<0.01	-6.17E-05	2.07	0.36	<0.01
2005	-4.21E-05	0.93	0.91	<0.01	-5.56E-05	2.15	0.24	<0.01	-1.36E-04	0.87	0.91	<0.01	-6.55E-05	2.11	0.41	<0.01
2006	-3.95E-05	0.86	0.87	<0.01	-6.92E-05	2.34	0.47	<0.01	-1.39E-04	0.86	0.90	<0.01	-5.74E-05	2.07	0.50	<0.01
2007	-5.52E-05	1.13	0.91	<0.01	-6.10E-05	2.30	0.23	<0.01	-1.22E-04	0.77	0.73	<0.01	-5.76E-05	2.05	0.49	<0.01
2008	-5.53E-05	1.15	0.92	<0.01	-6.72E-05	2.39	0.51	<0.01	-1.59E-04	0.98	0.90	<0.01	-4.64E-05	1.91	0.22	<0.01
2009	-4.76E-05	1.05	0.68	<0.01	-5.39E-05	2.23	0.26	<0.01	-1.34E-04	0.90	0.78	<0.01	-5.69E-05	2.06	0.31	<0.01
2010	-6.14E-05	1.28	0.81	<0.01	-5.28E-05	2.22	0.33	<0.01	-2.10E-04	1.29	0.78	<0.01	-5.38E-05	2.08	0.49	<0.01
2011	-4.58E-05	1.13	0.88	<0.01	-5.15E-05	2.35	0.58	<0.01	-1.33E-04	1.04	0.85	<0.01	-5.50E-05	2.07	0.67	<0.01
2012	-6.15E-05	1.38	0.90	<0.01	-5.75E-05	2.43	0.33	<0.01	-1.89E-04	1.28	0.85	<0.01	-5.78E-05	2.10	0.47	<0.01

	Tan Chau				My Thuan				Chau Doc				Can Tho			
Year	Slope	Intercept	R^2	P-	Slope	Intercept	R^2	P-	Slope	Intercept	R^2	P-	Slope	Intercept	R^2	P-
2013	-5.55E-05	1.34	0.70	<0.01	-5.08E-05	2.42	0.40	<0.01	-1.58E-04	1.17	0.73	<0.01	-5.00E-05	2.04	0.48	<0.01
2014	-6.03E-05	1.48	0.88	<0.01	-4.89E-05	2.43	0.26	<0.01	-2.07E-04	1.45	0.88	<0.01	-4.95E-05	1.94	0.46	<0.01
2015	-6.18E-05	1.48	0.48	<0.01	-9.93E-05	2.94	0.28	<0.01	-3.13E-04	1.86	0.65	<0.01	-2.64E-05	1.84	0.35	<0.01
2016	-8.18E-05	1.78	0.83	<0.01	-4.52E-05	2.43	0.19	<0.01	-2.07E-04	1.43	0.57	<0.01	-5.49E-05	2.11	0.34	<0.01
2017	-7.21E-05	1.72	0.91	<0.01	-4.42E-05	2.56	0.25	<0.01	-2.36E-04	1.59	0.77	<0.01	-6.33E-05	2.18	0.21	<0.01
2018	-6.55E-05	1.77	0.96	<0.01	-4.58E-05	2.66	0.42	<0.01	-1.86E-04	1.45	0.85	<0.01	-4.42E-05	2.04	0.57	<0.01
2019	-6.92E-05	1.90	0.88	<0.01	-2.76E-05	2.45	0.17	<0.01	-1.89E-04	1.38	0.72	<0.01	-4.04E-05	2.03	0.31	<0.01
2020	-4.61E-05	1.56	0.34	<0.01	-7.94E-06	2.26	0.01	0.65	-2.71E-04	1.77	0.57	<0.01	-4.29E-05	2.13	0.11	<0.01
2021	-5.94E-05	1.75	0.69	<0.01	-3.87E-05	2.60	0.10	<0.01	-1.87E-04	1.45	0.48	<0.01	-7.18E-05	2.33	0.12	<0.01

Table 7. The linear regression analysis of the tidal range and mean water discharge at four gauging stations in the VMD covers the period from 2000 to 2021 during the receding limb period.

	Tan Chau				My Thuan				Chau Doc				Can Tho			
Year	Slope	Intercept	R^2	P-	Slope	Intercept	R^2	P-	Slope	Intercept	R^2	P-	Slope	Intercept	R^2	P-
2000	-9.80E-06	0.23	0.48	<0.01	-6.86E-05	1.79	0.72	<0.01	-5.73E-05	0.43	0.96	<0.01	-6.95E-05	2.28	0.61	<0.01
2001	-2.17E-05	0.46	0.84	<0.01	-5.81E-05	1.76	0.71	<0.01	-4.79E-05	0.36	0.99	<0.01	-6.73E-05	2.34	0.55	<0.01
2002	-1.73E-05	0.40	0.67	<0.01	-4.75E-05	1.69	0.57	<0.01	-7.32E-05	0.50	0.99	<0.01	-6.12E-05	2.22	0.44	<0.01
2003	-2.45E-05	0.52	0.74	<0.01	-5.75E-05	1.82	0.50	<0.01	-7.97E-05	0.49	1.00	<0.01	-5.40E-05	2.10	0.70	<0.01
2004	-3.46E-05	0.70	0.83	<0.01	-6.77E-05	1.98	0.69	<0.01	-8.28E-05	0.54	0.99	<0.01	-6.57E-05	2.32	0.47	<0.01
2005	-2.36E-05	0.52	0.78	<0.01	-4.93E-05	1.95	0.47	<0.01	-1.36E-04	0.87	0.99	<0.01	-8.81E-05	2.60	0.45	<0.01
2006	-4.46E-05	0.89	0.86	<0.01	-5.47E-05	2.04	0.44	<0.01	-1.39E-04	0.86	0.99	<0.01	-6.63E-05	2.32	0.52	<0.01
2007	-4.88E-05	0.98	0.85	<0.01	-4.30E-05	2.01	0.35	<0.01	-1.22E-04	0.77	0.99	<0.01	-1.02E-04	2.67	0.33	<0.01
2008	-5.87E-05	1.13	0.87	<0.01	-4.60E-05	2.02	0.35	<0.01	-1.59E-04	0.98	0.98	<0.01	-4.31E-05	2.12	0.21	<0.01
2009	-6.16E-05	1.23	0.91	<0.01	-3.56E-05	1.92	0.33	<0.01	-1.34E-04	0.90	0.97	<0.01	-6.38E-05	2.21	0.50	<0.01
2010	-6.75E-05	1.32	0.83	<0.01	-4.94E-05	2.19	0.28	<0.01	-2.10E-04	1.29	0.97	<0.01	-7.14E-05	2.33	0.38	<0.01
2011	-3.99E-05	0.97	0.79	<0.01	-4.15E-05	2.12	0.53	<0.01	-1.33E-04	1.04	0.99	<0.01	-6.62E-05	2.35	0.63	<0.01
2012	-6.86E-05	1.41	0.85	<0.01	-4.21E-05	2.15	0.21	<0.01	-1.89E-04	1.28	0.95	<0.01	-6.78E-05	2.25	0.31	<0.01
2013	-5.61E-05	1.31	0.86	<0.01	-3.95E-05	2.21	0.30	<0.01	-1.58E-04	1.17	0.98	<0.01	-6.84E-05	2.35	0.46	<0.01
2014	-5.65E-05	1.34	0.78	<0.01	-3.83E-05	2.18	0.13	0.01	-2.07E-04	1.45	0.96	<0.01	-6.60E-05	2.28	0.21	<0.01
2015	-5.50E-05	1.34	0.72	<0.01	-2.51E-05	2.17	0.03	0.45	-3.13E-04	1.86	0.16	<0.01	-9.35E-05	2.42	0.06	0.08
2016	-7.83E-05	1.72	0.85	<0.01	-3.74E-05	2.35	0.13	<0.01	-2.07E-04	1.43	0.91	<0.01	-5.93E-05	2.14	0.26	<0.01
2017	-8.33E-05	1.86	0.90	<0.01	-2.49E-05	2.25	0.12	<0.01	-2.36E-04	1.59	0.84	<0.01	-4.91E-05	2.09	0.46	<0.01
2018	-6.01E-05	1.60	0.93	<0.01	-2.45E-05	2.21	0.27	<0.01	-1.86E-04	1.45	0.97	<0.01	-9.43E-05	2.84	0.54	<0.01
2019	-6.92E-05	1.83	0.95	<0.01	-1.61E-05	2.20	0.07	0.12	-1.89E-04	1.38	0.97	<0.01	-4.55E-05	2.09	0.30	<0.01
2020	-6.11E-05	1.78	0.88	<0.01	-2.50E-05	2.41	0.11	0.02	-2.71E-04	1.77	0.85	<0.01	-3.28E-05	2.02	0.21	<0.01
2021	-7.20E-05	1.96	0.86	<0.01	-6.75E-05	2.84	0.30	<0.01	-1.87E-04	1.45	0.92	<0.01	-3.76E-05	2.07	0.32	<0.01